Excitonic Interactions Mediated Symmetry-Breaking Charge Separation in Perylenediimide Multichromophoric Architectures

A thesis submitted for the degree of

Doctor of Philosophy

in

Chemistry

by

Aniruddha Mazumder

IPHD18003

Indian Institute of Science Education and Research
Thiruvananthapuram (IISER TVM),
Thiruvananthapuram – 695551
Kerala, India

January 2026

Declaration

I hereby declare that the Ph.D. thesis entitled **"Excitonic Interactions Mediated Symmetry-Breaking Charge Separation in Perylenediimide Multichromophoric Architectures"** is an independent work carried out by me at the School of Chemistry, Indian Institute of Science Education and Research Thiruvananthapuram (IISER TVM), under the supervision of **Prof. Mahesh Hariharan** and it has not been submitted anywhere else for any other degree, diploma or title. In keeping with the general practice of reporting the scientific observations, due acknowledgements have been made wherever the work described is based on the findings of other investigators.

Place: IISER Thiruvananthapuram **Aniruddha Mazumder**

Date: 08.01.2026

Certificate

This is to certify that the work embodied in the thesis entitled **"Excitonic Interactions Mediated Symmetry-Breaking Charge Separation in Perylenediimide Multichromophoric Architectures"** has been carried out by **Aniruddha Mazumder (IPHD18003)** under my supervision at the School of Chemistry, Indian Institute of Science Education and Research Thiruvananthapuram (IISER TVM) and the same has not been submitted elsewhere for a degree.

Place: IISER Thiruvananthapuram
Date: 08.01.2026

Prof. Mahesh Hariharan
(Thesis Supervisor)

Dedicated

To My Beloved

Grandmother, mother, father and brother

"Allow yourselves to dream and then chase after those dreams. That will always require effort and sacrifice, but be persistent!"

—Lionel Messi

Acknowledgements

My Ph.D. thesis represents the outcome of years of dedication, research, and personal growth, made possible through the support and guidance of numerous individuals and institutions. I am sincerely grateful to all those who have played a role in shaping this journey.

First and foremost, I am deeply grateful to my thesis advisor, Prof. Mahesh Hariharan, for his unwavering support, expert guidance, and constant encouragement throughout this journey. His thoughtful insights and patient mentorship have been instrumental in shaping my Ph.D. research and overall growth as a scholar.

I sincerely thank Prof. J. N. Moorthy, Director of IISER Thiruvananthapuram, for ensuring access to excellent infrastructure and research facilities. I am also grateful to the current and former Heads of the School of Chemistry for supporting my research through the CIL and IISER TVM facilities. I sincerely appreciate the guidance of my doctoral committee members, Prof. K. George Thomas and Prof. Reji Varghese, whose valuable feedback and continued support have greatly enriched my research journey. I would also like to acknowledge all the School of Chemistry faculty members for their exceptional teaching during my integrated Ph.D. coursework.

I am also grateful to Prof. R. S. Swathi, Professor, IISER TVM, whose collaboration and discussions have been enlightening and motivating. I particularly appreciate Prof. Swathi's constructive suggestions and shared knowledge on understanding the noncovalent interactions in perylenediimide aggregates through symmetry-adapted perturbation theory (SAPT). Also, I thank Prof. Bernd Engels, University of Würzburg, for allowing me to work with him for a short term on understanding the intersystem crossing mechanism in a core-twisted single molecule. I am also thankful to Dr. Brijith Thomas of New York University for the opportunity to collaborate on an engaging project focused on investigating the solid-state packing and structural properties of disordered organic materials. I am highly indebted to Prof. M. M. Shaijumon, IISER TVM, for allowing me to work with him on perylenediimide-based polyimides as organic cathodes in sodium-ion batteries.

I am deeply obliged to all past and present Hariharan group members: Dr. Nanditha G. N., Dr. Bappa G., Dr. Swati D., Dr. Aasif K., Dr. Indrajit G., Dr. Remya R., Dr. Ebin S., Dr. Devika S., Dr. Athira T. J., Ms. Amalu M., Dr. Lijina M. P., Dr. Swathi Krishna P. E., Mr. Amal K. H., Dr. Niyas M. A., Ms. Ambili R. V., Ms. Hridya P., Mr. Vishnu V., Ms. Meera M., Mr. Alfy

B., Mr. Deepu G., Mr. Krishna P., Mr. Dilip P. S., Ms. Kavya V., Mr. Jibin S., Mr. Philip D. M., Ms. Anjana V. M., Ms. Suvarna S. C., Ms. Tessy P., Ms. Raniya P., Mr. Jeswin S., Ms. Akshaya N., Ms. Keerthy P. S., Mr. Vivek V. D., Mr. Akhilesh K. U., Mr. Sohan D. J., Ms. Pallavi P. D., Ms. Hruidya C. B., Ms. Diana T., Mr. Lukhmanul H. K., Mr. Hanock B., Ms. Anitta B., Ms. Anjana S. K., Ms. Agaja K., Ms. Fathima T., Ms. Najuma N., Mr. Sharath D., Mr. Amalnadh T., Mr. Tamizharasan T., Mr. Abhijith M., Ms. Sona S., Mr. Gokul G., Mr. Ariharasudhan R., Ms. Megha S., Ms. Aswathy H., Ms. Greeshma G., Ms. Dhanushya P., Mr. Jagannathan V., Ms. Aarjoo J., Ms. Sujitha S., Mr. Devanath M., B., Mr. Avanindhra, Mr. Anjelo J., Mr. Anzil B. M. and Ms. Meera Jacob for the endless support, care, motivation and joyful moments during my Ph.D. work. On a special note, I thank Ms. Kavya V. and Mr. Philip D. M. for contributing to the ultrafast transient absorption and single-molecule fluorescence measurements presented in my doctoral work. I would like to give special thanks to Dr. Ebin S. and Dr. Devika S. for being outstanding mentors. Their early guidance, thought-provoking discussions, and foundational lessons in research have impacted my academic journey. I would like to extend my heartfelt thanks to the BS-MS and project students, Ms. Raniya P., Ms. Pallavi P. D., Mr. Aivin C. T., Mr. Noel B., and Mr. Jasim M., for their valuable contributions to the research presented in this thesis. I would also like to thank Dr. Soumya Biswas, Dr. Aditesh Mondal, Dr. Probal Nag, Dr. Anook N. E. A., Dr. Livin P., Dr. Ajaykumar M. P., Mr. Muhammed Raees and Mr. Debarghya Sarkar for the experimental help and constructive discussions regarding my doctoral research work.

I sincerely thank the administrative staff of IISER Thiruvananthapuram for their steadfast support in managing logistics and administrative tasks, which played a vital role in the smooth conduct of my doctoral studies. I am particularly grateful to Mr. Adarsh B. for his help with NMR experiments; Mr. Nibith K. for GC-MS, elemental, and FT-IR analyses; Mr. Alex P. A. for the XPS analysis; Mr. Kiran, Ms. Athira S., and Ms. Ansumol for MALDI-TOF measurements; Mr. Aneesh for SEM analysis; and Mr. Pradeep K. G. and Mr. Prem K. for HRMS support. I also extend my gratitude to all the teaching and non-teaching staff, especially those in the library, IT, purchase, finance, and mess departments, for their timely assistance. I am deeply thankful to IISER Thiruvananthapuram for the financial support during my doctoral research, and I truly appreciate their continued investment in my academic and professional development.

On a personal note, I am deeply thankful to my friends and peers who have offered moral support and companionship throughout this journey. I thank my integrated PHD18

batchmates who have been a constant source of motivation for me. I would also like to thank my Paagal Log friends' group, Ms. Megha R., Ms. Preetika V., Mrs. Ann T. B., Ms. Kavya V., Mr. Mehul T., Mr. Prajoy M., Mr. Jibin S., Mr. Philip D. M. and Mr. Abhishek S., who have stood beside me during the entire Ph.D. journey. In this line, I am thankful to my badminton group of friends, Ms. Neenu J., Mrs. Aswathy R., Ms. Aarcha S. and Mr. Shamil R. for always making my stay at IISER TVM pleasant. I am deeply thankful to Ms. Megha R. for being a passionate friend and constant companion, whose unwavering support and encouragement have been truly indispensable throughout my Ph.D. journey.

I am profoundly indebted to my family for their endless support and boundless love. Their belief in me and the sacrifices they have made have been the foundation upon which this research journey was built. The encouragement and patience of my parents, Dr. Amalendu M. and Mrs. Sampa M., have continually inspired me to persevere. I also extend my heartfelt thanks to my brother, Mr. Anindya M., whose constant motivation, love and support have helped me to complete my Ph.D. journey successfully.

- Aniruddha Mazumder

Preface

Symmetry-breaking charge separation (SB-CS) is a photoinduced process where a pair of identical chromophores forms a charge separated state (CSS) with the hole and electron on different chromophores, i.e., C–C + $h\nu \rightarrow C^{\bullet+}–C^{\bullet-}$, upon photoexcitation. The SB-CS process occurs in systems ranging from the chlorophyll pigment-protein in photosynthetic reaction centres to organic photovoltaic devices (OPVs). Recently, SB-CS materials have found widespread applications in artificial photosynthesis and OPVs due to the possibility of minimal energy loss during charge separation (<100 mV), when used as an active layer in organic solar cells. A thorough understanding of the photophysical processes (exciton formation, energy transfer, and charge separation) in molecular multichromophoric assemblies and their precise dependence on the chromophoric spatial arrangement, π-overlap, and intermolecular distances is quintessential for the design of efficient solar energy harvesting systems. Fundamentally, the SB-CS rate mainly depends on the strength of excitonic coupling between the individual chromophores and the solvent dielectric environment. Excitonic coupling in chromophores arises via the interaction of the transition dipoles during photoexcitation. Excitonic coupling is responsible for various photophysical processes like energy transfer, splitting of excited-state energy levels and delocalization of excitation across molecules. Further, the solvent dielectric medium assists in faster SB-CS by lowering the energy of the CSS beyond the locally excited-state via dipole-dipole interactions. Chapter 1 will introduce the fundamental concepts of excitonic coupling and SB-CS. The role of intramolecular excitonic interactions in modulating the SB-CS rates in monomeric solutions will be discussed in great detail. Due to the close molecular packing, multichromophoric systems show shorter interplanar distances (*d*) between the individual chromophores in the aggregated /solid-state. Therefore, the intermolecular short-range charge transfer (CT)-mediated coupling operative within π-π distances of $d \leq 6$ Å becomes dominant in the solid-state and contributes to the overall photophysical properties of the chromophore. The interference between the long-range Coulombic and short-range CT coupling, giving rise to the total excitonic coupling, modulates the photophysical properties in solution- and solid-states.

Achieving faster charge separation in organic multichromophoric systems capable of mimicking the electron transfer events in natural photosynthesis has been an exhilarating research topic for several decades. In chapter 2, we demonstrate the orientation-controlled acceleration of SB-CS in a synthetically designed angular (**A-PDI$_2$**) versus linear (**L-PDI$_2$**)

perylenediimide dimer. The solvent-dependent emission measurements of **A-PDI₂** display enhanced fluorescence quenching and lower fluorescence quantum yields in polar solvents compared to **L-PDI₂**. Dielectric-dependent femtosecond transient absorption (fsTA) measurements reveal ultrafast SB-CS in **A-PDI₂** (τ_{CS} = 6.3 ps) with charge separation ~20 times faster than in **L-PDI₂** (τ_{CS} = 127.9 ps). The nanosecond transient absorption (nsTA) measurements of **A-PDI₂** in ACE corroborate the population of triplet excited-states via the charge recombination (CR) pathway with a significant triplet quantum yield of ϕ_T = 35.9%. Contrastingly, the nsTA measurements of linear **L-PDI₂** reveal a negligible triplet population (ϕ_T < 1%). The theoretically computed Coulombic coupling strength in **A-PDI₂** ($|J_{Coul}|$ = 14.9 cm^{-1}) and **L-PDI₂** ($|J_{Coul}|$ = 438.4 cm^{-1}) sheds light on the critical role of dimer orientations on the rate of SB-CS. Therefore, the precise control over the molecular design and structure can be used to achieve weakly coupled multichromophoric dimers capable of accelerating intramolecular SB-CS.

Molecular trimers are important model systems to understand the effect of exciton delocalization and electronic coupling, controlling the excited-state relaxation dynamics and the concomitant photophysical properties. Chapter 3 demonstrates triplet excited-state population in a weakly coupled perylenediimide trimer (**PDI-T**) via intramolecular SB-CS at the single-molecule level. The fragment-based excited-state analysis provides evidence for the occurrence of CT states in the **PDI-T** trimer. The weak Coulombic coupling prevalent between the individual monomer units favours ultrafast charge separation over excimer state formation. The single-molecule fluorescence intensity trajectories of **PDI-T** in a nonpolar polystyrene matrix (ε = 2.60) exhibit prolonged fluorescence with infrequent dark states, representing the triplet and/or the CT states. In contrast, **PDI-T** shows erratic blinking dynamics resulting in low photon counts in poly(vinyl alcohol) matrix (ε = 7.80), corroborating the feasibility of charge separation in a polar dielectric environment. In agreement with the single-molecule measurements, fsTA measurements of **PDI-T** reveal ultrafast SB-CS (τ_{CS} < 5 ps) in polar tetrahydrofuran (ε = 7.58) and acetone (ε = 20.70). The nsTA measurements further reveal the population of triplet excited-states following charge separation in **PDI-T**. The negative free energy change (ΔG_{CS}) in **PDI-T** renders SB-CS feasible and accelerates charge separation in a polar dielectric medium. The correlation between the excited-state photophysics of **PDI-T** obtained at the single-molecule and ensemble levels provides a comprehensive understanding of the triplet generation mechanism and the SB-CS dynamics. Therefore, molecular trimers with

weak excitonic coupling are desirable for ultrafast SB-CS and triplet populations, having potential applications in optoelectronic devices.

Achieving efficient charge generation with minimal energy loss in the solid-state remains a fundamental challenge in developing high-performance organic optoelectronic devices. The generation of electron-hole radical pair at the active layer of organic photovoltaics through SB-CS has a crucial role in enhancing opencircuit voltage (V_{oc}) and thereby increasing power conversion efficiency. However, the need for solvent polarity stabilizing the CSS limits the scope for SB-CS in the solid-state. In chapter 4, we investigate SB-CS in thin films of two multichromophoric PDI derivatives (**PDI$_2$** and **PDI$_3$**) in a nonpolar polymethyl methacrylate (PMMA, ε = 2.8-3.2) polymer matrix. Steady-state spectroscopic investigations in thin films in PMMA reveal that **PDI$_2$** and **PDI$_3$** form J-type aggregates in the solid-state, showing broad red-shifted excitation and emission profiles. The solid-state fsTA measurements confirm ultrafast SB-CS occurring within τ_{CS} < 110 fs. The optimized dimer structures of the PDI aggregates corroborate the formation of favourable J-type slip-stacked architectures. Theoretical calculations validate the role of through-space long-range intermolecular excitonic communication and short-range π-π interactions in the solid-state molecular packing driving the ultrafast charge separation process in **PDI$_2$** and **PDI$_3$**. Therefore, multichromophoric architectures with slip-stacked PDI fragments enable ultrafast SB-CS even in a nonpolar PMMA polymer matrix, thus providing a framework for designing next-generation organic materials capable of efficient solid-state charge generation.

Table of Contents

List of Figures

List of Tables

List of Schemes

Abstract **1**

1. Introduction to Excitonic Interactions and Symmetry-Breaking Charge Separation (SB-CS): Role of Intramolecular and Intermolecular Excitonic Coupling in SB-CS **3**

1.1. Introduction 3

1.2. Molecular Exciton Theory; Kasha Model and Beyond 5

1.3. Symmetry-Breaking Charge Separation (SB-CS) 12

1.3.1. History of SB-CS 15

1.3.2. Key Factors Controlling SB-CS 16

1.3.2.1. Dielectric Medium Modulated Photoinduced SB-CS 16

1.3.2.2. Excitonic Coupling Mediated SB-CS 18

1.4. SB-CS in PDI Multichromophoric Architectures in the Isolated Monomeric State 23

1.4.1. Intramolecular Excitonic Interactions Modulating SB-CS in PDI Multimers 24

1.5. SB-CS in PDI Constructs in the Solid-State 30

1.5.1. Intermolecular Excitonic Interactions Modulating SB-CS in PDI Chromophores in the Solid-State 31

1.6. Aim and Objectives of the Thesis 35

2. Accelerating Symmetry-Breaking Charge Separation in an Angular versus Linear Perylenediimide Dimer through the Modulation of Coulombic Coupling **37**

2.1. Introduction 38

2.2. Results and Discussion 40

2.2.1. Dimer Molecules and the Optimized Structures 40

2.2.2. Steady-State Photophysical Properties of the Dimers 41

2.2.3. Solvent-Dependent Optical Properties of the Dimers 41

2.2.4. Femtosecond Transient Absorption Measurements of L-PDI_2 42

2.2.5. Femtosecond Transient Absorption Measurements of A-PDI_2 45

2.2.6. Nanosecond Transient Absorption Measurements of A-PDI_2 47

2.2.7. Rehm-Weller Analysis for the Dimers 48

2.2.8. DFT Calculated HOMO-LUMO Energies of the Dimers 48

2.2.9. Fragment-Based Excited-State Analysis 49
2.2.10. Excitonic Coupling Calculations 50
2.2.11. TDDFT Calculations 51
2.2.12. Proposed Jablonski Diagram 51
2.3. Conclusion 52
2.4. Experimental Section 53
2.4.1. Syntheses and Characterization 53
2.5. Additional Figures and Tables 57
2.6. Appendix 77
2.6.1. Materials and Methods 77
2.6.2. Computational Analysis 77
2.6.3. TheoDORE Analysis 78
2.6.4. Coulombic Coupling Calculation 78
2.6.5. Femtosecond Transient Absorption (fsTA) Measurement 79
2.6.6. Nanosecond Transient Absorption (nsTA) Measurement 79
2.6.7. Global Analysis 80
2.6.8. Electrochemistry 81
2.6.9. Rehm-Weller Analysis 82
2.6.10. Triplet Quantum Yield (ϕ_T) Measurements 82
3. Symmetry-Breaking Charge Separation Mediated Triplet Population in a Weakly Exciton Coupled Perylenediimide Trimer at the Single-Molecule Level 85
3.1. Introduction 86
3.2. Results and Discussion 88
3.2.1. Trimer Molecule and the Optimized Structure 88
3.2.2. Steady-State Photophysical Properties of PDI-T 89
3.2.3. Solvent-Dependent Optical Properties of PDI-T 90
3.2.4. HOMO-LUMO Energy, Excited-State Geometry and TDDFT Energies 91
3.2.5. Fragment-Based Excited-State and Excitonic Coupling Analyses 92
3.2.6. Rehm-Weller Analysis for PDI-T 92
3.2.7. Single-Molecule Fluorescence Measurements of PDI-T 93
3.2.8. Femtosecond Transient Absorption Measurements of PDI-T 95
3.2.9. Nanosecond Transient Absorption Measurements of PDI-T 98
3.2.10. Proposed Jablonski Diagram 99
3.3. Conclusion 100

3.4. Experimental Section 100
3.4.1. Syntheses and Characterization 100
3.5. Additional Figures and Tables 102
3.6. Appendix 120
3.6.1. Materials and Methods 120
3.6.2. Computational Analysis 120
3.6.3. TheoDORE Analysis 120
3.6.4. Coulombic Coupling Calculation 121
3.6.5. Femtosecond Transient Absorption (fsTA) Measurement 121
3.6.6. Nanosecond Transient Absorption (nsTA) Measurement 122
3.6.7. Global Analysis 122
3.6.8. Electrochemistry 122
3.6.9. Rehm-Weller Analysis 122
3.6.10. Single-Molecule Fluorescence Measurements 122
3.6.11. Triplet Quantum Yield (ϕ_T) Measurements 123
4. Ultrafast Symmetry-Breaking Charge Separation in Thin Films of J-Aggregated Perylenediimide Multimers in a Nonpolar Solid-State Environment 125
4.1. Introduction 125
4.2. Results and Discussion 127
4.2.1 PDI Multimers and the Optimized Structures 127
4.2.2. Steady-State Photophysical Properties of the PDI Multimers in Thin Films in PMMA 128
4.2.3. Femtosecond Transient Absorption Measurements of PDI_2 and PDI_3 Thin Films in PMMA 129
4.2.4. Fluorescence Lifetime Measurements of PDI_2 and PDI_3 Thin Films in PMMA . 131
4.2.5. Aggregate Geometry Optimization and Excitonic Coupling Calculations 132
4.2.6. Proposed Jablonski Diagram 133
4.3. Conclusion 134
4.4. Experimental Section 134
4.4.1. Syntheses and Characterization 134
4.5. Additional Figures and Tables 135
4.6. Appendix 141
4.6.1. Materials and Methods 141
4.6.2. DOSY NMR Measurement 141

4.6.3. Femtosecond Transient Absorption (fsTA) Measurement 142
4.6.4. Fluorescence Lifetime Imaging Microscopy 142
4.6.5. Computational Analysis..... 143
4.6.6. Coulombic Coupling Calculation 143
4.6.7. Charge Transfer-Mediated Coupling Calculation 143
5. Conclusion and Outlook 145
Bibliography 147
List of Publications..... 159
Workshops and Conferences..... 161
Copyrights and Permissions..... 163

List of Figures

No.	Title	Page No.
1.1	a) Schematic depicting excitation energy and electron transfer pathways where chromophores are arranged in two-dimensional planar distribution. b) The process of energy harvesting in an antenna system is represented as a funnel, where high-energy (short-wavelength) light is absorbed by outer antenna pigments, and the resulting excitation energy is progressively funnelled toward lower-energy pigments situated near the reaction centre. b) Reprinted with permission from ref (3). Copyright (2017) American Chemical Society.	3
1.2	Illustrations of natural light-harvesting assemblies: a) Architectural organization of the photosynthetic apparatus in purple non-sulfur bacteria. b) Structural model depicting the light-harvesting complex 2 (LH2). c) Schematic of excitation energy flow within the interconnected LH1 and LH2 complexes network. Reprinted with permission from ref (6). Copyright (2022) Springer Nature.	4
1.3	The absorption spectra of a set of naphthyl dimers linked by a norbornyl bridge are presented alongside that of a monomeric reference chromophore (shown as a dashed trace). The spectral features of the dimers exhibit two distinct absorption bands, with the separation between them corresponding to the magnitude of electronic coupling between the left and right naphthyl units. This splitting signifies that the excitation is delocalized across both chromophores, characteristic of a molecular exciton. Reprinted with permission from ref (22). Copyright (1993) American Chemical Society.	6
1.4	Schematic representation of exciton splitting for a molecular dimer and correlation between slip angle (θ), rotational angle (α) and the orientation factor (κ). Reprinted with permission from ref (28). Copyright (2018) John Wiley & Sons, Inc.	8
1.5	A schematic illustration depicting how the absorption (in blue) and	9

	fluorescence (in red) spectra shift upon the aggregation of cyanine dye monomers into H- and J-type aggregates. Reprinted with permission from ref (27). Copyright (2017) IOP Publishing.	
1.6	Molecular orbitals (MOs) corresponding to a) large interplanar separations (≥ 6 Å), where no significant orbital interaction is observed, and b) smaller interplanar distances (≤ 6 Å), where evident orbital overlap occurs. Reprinted with permission from ref (30). Copyright (2023) The Royal Society of Chemistry.	10
1.7	a) t_h and b) t_e within a π-stacked perylene dimer (interplanar distance of 3.5 Å) are plotted as functions of transverse displacement, derived from energy level splitting calculated using DFT. The DFT computed HOMO and LUMO isosurfaces of perylene are shown in c) and d), respectively. e) The product of t_h and t_e, which is proportional to the charge transfer coupling (J_{CT}), and f) the unscreened Coulombic interaction is both shown as a function of transverse displacements, determined from atomic transition charge densities obtained via TDDFT calculations. The red and blue regions denote J-aggregate and H-aggregate interactions, respectively. The sign conventions for t_h and t_e were defined according to the symmetry operations under which the TDM of the dimer remains symmetric. Reprinted with permission from ref (36). Copyright (2017) American Chemical Society.	11
1.8	a) A schematic representation depicting the charge separation and ensuing electron transfer steps within the purple bacterial RC. The red arrows mark the electron transfer routes along with their respective time constants. The green-coloured spheres positioned at the center of the chlorin rings denote the magnesium atoms present in bacteriochlorophyll (BChl). In this context, P refers to a dimer of BChl, while B_A and B_B represent monomeric BChl units. H_A and H_B are bacteriopheophytins (BPhs), Q_A and Q_B correspond to ubiquinone molecules, and Fe refers to a non-heme iron center. b) The transient absorption spectrum of biperylenylpropane recorded in ACN displays distinct photophysical features that can be	13

	attributed to the radical ion pair species. c) A conceptual illustration of a basic organic bilayer photovoltaic device, where a conventional donor and an acceptor material are layered in a sandwich-like orientation. The operating mechanism involves SB-CS, enabling efficient charge generation. Reprinted with permission from ref (10). Copyright (2022) American Chemical Society.	
1.9	The structural geometry of 'special pairs' in different RCs. Reprinted with permission from ref (10). Copyright (2022) American Chemical Society.	14
1.10	a) The molecular geometries of the SubPc monomer and the μ-OSubPc$_2$ dimer obtained through DFT optimizations. b) Illustration depicting how the excited-state dynamics of μ-OSubPc$_2$ vary with changes in solvent dielectric properties. Reprinted with permission from ref (53). Copyright (2021) John Wiley & Sons, Inc.	16
1.11	a) Molecular structure of (R,R)-Cy-PDI$_2$. b) The fsTA spectra of (R,R)-Cy-PDI$_2$ in TOL, THF, and ACE showing the excited-state dynamics upon photoexcitation at λ_{ex} = 470 nm (Top row). EAS reconstructed from global analysis of the fsTA data of (R,R)-Cy-PDI$_2$ (Bottom row). Reprinted with permission from ref (65). Copyright (2023) American Chemical Society.	17
1.12	a) The molecular dynamics simulations and b) fsTA spectra of the various host-guest complexes with Na^+ ion in DCM (left column: 18C6; middle column: 18C4; right column: 16C4). c) Molecular structures of bis-ANI, ANI and NI. d) The fsTA spectra of the *bis*-ANI compound in medium polar THF (left) and in polar ACE (right). Reprinted with permission from: a) and b) ref (71). Copyright (2019) The Royal Society of Chemistry; c) and d) ref (72). Copyright (2022) The Royal Society of Chemistry.	19
1.13	Molecular structure of perylenediimide and the different positions where substitutions can be accomplished.	24
1.14	a) Molecular structures of the Ref-PDI and Sp-PDI$_2$, where "R" represents the 3-pentyl group. The X-ray crystal structure shows near-orthogonal arrangement of the two PDI units in Sp-PDI$_2$. b)	26

	Absorption and emission spectra of Ref-PDI and Sp-PDI_2 in TOL. c) Dependence of the absolute values of $\|J_{coul}\|$ and $\|J_{CT}\|$ on the rotational angle (θ) separating the PDI monomer units. (Top) fsTA) spectra of Sp-PDI_2 recorded in d) TOL, e) THF, and f) ACN, illustrating the excited-state processes following photoexcitation at 440 nm. (Bottom) SAS derived through target analysis of the fsTA measurements for Sp-PDI_2. Reprinted with permission from ref (70). Copyright (2021) American Chemical Society.	
1.15	a) Chemical structures of the monomer (1), dimer (2), and trimer (3) are shown, where R denotes a 4′-tert-butylphenoxy substituent and the rotation angle between adjacent chromophores is approximately 15°. b) The fsIR spectra of compound 1 at 10 ps, alongside those of its charged counterparts (bottom), as well as spectra for compounds 2 (middle) and 3 (top) at three distinct time delays recorded in DCM. The IR-active vibrational modes in the excited-state clearly capture the characteristics of the mixed state in 2 and the SB-CS state in 3, owing to their heightened sensitivity to electron density variations across chromophores. In contrast, electronic transitions often yield broad and overlapping features, making them less suitable for such differentiation. Reprinted with permission from ref (67). Copyright (2022) Springer Nature.	28
1.16	Schematic diagram showing the through-bond and through-space excitonic interactions promoting intramolecular and intermolecular SB-CS, respectively, in multichromophoric molecular architectures.	35
2.1	Molecular structures of a) **L-PDI_2** and b) **A-PDI_2**. Ground-state optimized structures of c) **L-PDI_2** and d) **A-PDI_2** obtained at the B3LYP-D3/6-311+G(d,p) level of theory. e) Normalized UV-vis absorption spectra of PDI monomer, **L-PDI_2** and **A-PDI_2** in TOL. f) Normalized emission spectra (λ_{ex} = 480 nm) of PDI monomer, **L-PDI_2** and **A-PDI_2** in TOL.	40
2.2	The fsTA spectra of **L-PDI_2** showing the excited-state dynamics upon photoexcitation (λ_{ex} = 495 nm) in a) TOL and b) ACE. EAS	43

	reconstructed from global analysis of **L-PDI$_2$** with c) A → GS model for TOL and d) A → B → GS model for ACE; where A is the singlet excited-state, B is the CSS, and GS is the ground-state. Relative population profile of the excited-states fitted using above kinetic models in e) TOL and f) ACE.	
2.3	(Top row) fsTA spectra of **A-PDI$_2$** in a) TOL and b) ACE showing the excited-state dynamics upon photoexcitation. (Middle row) EAS reconstructed from global analysis of **A-PDI$_2$** with A → B → C → GS kinetic model, where A is the singlet excited-state, B is the relaxed singlet excited-state in case of TOL and the CSS in case of ACE, C is the triplet excited-state, and GS is the ground-state (λ_{ex} = 480 nm). (Bottom row) Relative population profile of the excited-states fitted using kinetic models. c) nsTA spectra of **A-PDI$_2$** in (top row) N_2-purged ACE and (middle row) O_2-purged ACE. (Bottom row) Single-wavelength decay kinetics fitted at 510 nm yielding the triplet excited-state lifetime in **A-PDI$_2$**.	45
2.4	Hole-electron correlation plots showing the localized/delocalized Frenkel exciton or charge transfer nature of the S_1, S_2, S_3 and S_4 excited-states in a) **L-PDI$_2$** and b) **A-PDI$_2$** obtained through fragment-based excited-state analysis. The nature of the excitations is defined by the CT and PR values.	49
2.5	Proposed Jablonski diagram summarizing the excited-state dynamics of **A-PDI$_2$** (green) and **L-PDI$_2$** (blue) upon photoexcitation under the influence of nonpolar TOL (left) and polar ACE (right); SB-CSS = symmetry-broken charge separated state, (S_0) = ground-state, (S_1) = locally excited first singlet state, $(S_1)_{rel}$ = relaxed first singlet excited-state, and T_3 = third triplet excited-state. The coloured dotted arrows denote non-radiative decay pathways and coloured solid arrows indicate fluorescence.	52
A2.1	^{1}H-NMR spectrum of **L-PDI$_2$** in $CDCl_3$.	57
A2.2	^{13}C-NMR spectrum of **L-PDI$_2$** in $CDCl_3$.	57
A2.3	MALDI mass spectrum of **L-PDI$_2$** with the highlighted molecular mass.	58

A2.4	The FT-IR spectrum of **L-PDI₂** in KBr disks.	58
A2.5	^{1}H-NMR spectrum of **A-PDI₂** in $CDCl_3$.	59
A2.6	^{13}C-NMR spectrum of **A-PDI₂** in $CDCl_3$.	59
A2.7	MALDI mass spectrum of **A-PDI₂** with the highlighted molecular mass.	60
A2.8	The FT-IR spectrum of **A-PDI₂** in KBr disks.	60
A2.9	Centroid-centroid distance ($d_{PDI\text{-}PDI}$) in the ground-state optimized structures of a) **L-PDI₂** and b) **A-PDI₂**.	61
A2.10	UV-vis absorption spectra of a) **L-PDI₂** and b) **A-PDI₂** recorded in various solvents. Emission spectra of c) **L-PDI₂** and d) **A-PDI₂** showing solvent dependence; panels e) and f) present the corresponding normalized emission spectra for **L-PDI₂** and **A-PDI₂**, respectively.	61
A2.11	a) Concentration-dependent UV-vis absorption spectra and b) absorption maxima (λ_{max}^{Abs} = 535 nm) versus concentration plot of **L-PDI₂** in TOL.	62
A2.12	a) Concentration-dependent UV-vis absorption spectra and b) absorption maxima (λ_{max}^{Abs} = 528 nm) versus concentration plot of **A-PDI₂** in TOL.	62
A2.13	a) Concentration-dependent UV-vis absorption spectra and b) absorption maxima (λ_{max}^{Abs} = 520 nm) versus concentration plot of **A-PDI₂** in ACE.	63
A2.14	a) Concentration-dependent UV-vis absorption spectra and b) absorption maxima (λ_{max}^{Abs} = 528 nm) versus concentration plot of **L-PDI₂** in ACE.	63
A2.15	UV-vis absorption changes of **L-PDI₂** upon a) chemical oxidation by adding antimony pentachloride ($SbCl_5$) and b) chemical reduction by adding cobaltocene ($CoCp_2$) in ACE.	64
A2.16	Global analysis fits for selected fsTA wavelengths of **L-PDI₂** (λ_{ex} = 495 nm) in a) TOL using A → GS kinetic model and b) ACE using A → B → GS kinetic model. Fitted results are shown using solid line profiles.	64
A2.17	Nanosecond transient absorption spectra of **L-PDI₂** in N_2-purged	65

	solution of a) TOL and b) ACE.	
A2.18	UV-vis absorption changes of **A-PDI$_2$** upon a) chemical oxidation by adding antimony pentachloride ($SbCl_5$) and b) chemical reduction by adding cobaltocene ($CoCp_2$) in ACE.	65
A2.19	Global analysis fits for selected fsTA wavelengths of **A-PDI$_2$** (λ_{ex} = 480 nm) in a) TOL and b) ACE using A → B → C → GS kinetic model. Fitted results are shown using solid line profiles.	66
A2.20	a) The nsTA decay of $[Ru(bpy)_3]^{2+}$ monitored at 370 nm. b) Time-resolved growth trace at 530 nm showing the formation of the triplet excited-state of β-carotene (^{3}β-carotene*) upon mixing $[Ru(bpy)_3]^{2+}$ with β-carotene in methanol, providing evidence for triplet-triplet energy transfer (TTET) from the ruthenium complex to β-carotene. c) Kinetic trace depicting the generation of ^{3}β-carotene* in a mixture of **A-PDI$_2$** and β-carotene in ACE, further confirming the occurrence of TTET from **A-PDI$_2$** to β-carotene in a polar solvent environment.	66
A2.21	Nanosecond transient absorption measurements of **A-PDI$_2$** in TOL in a) N_2-purged solution, b) O_2-purged solution. c) Nanosecond transient absorption decay profiles of **A-PDI$_2$** in TOL.	67
A2.22	a) The nsTA decay of $[Ru(bpy)_3]^{2+}$ monitored at 370 nm. b) Time-resolved growth trace at 530 nm showing the formation of the triplet excited-state of β-carotene (^{3}β-carotene*) upon mixing $[Ru(bpy)_3]^{2+}$ with β-carotene in methanol, providing evidence for triplet-triplet energy transfer (TTET) from the ruthenium complex to β-carotene. c) Kinetic trace depicting the generation of ^{3}β-carotene* in a mixture of **A-PDI$_2$** and β-carotene in TOL, further confirming the occurrence of TTET from **A-PDI$_2$** to β-carotene.	67
A2.23	Optimized structure of **A-PDI$_2$** showing core-twist.	68
A2.24	a) Cyclic voltammetry data and b) differential pulse voltammograms of **L-PDI$_2$** in DCM using Fc/Fc^+ coupled Ag/Ag^+ electrode.	68

A2.25	a) Cyclic voltammetry data and b) differential pulse voltammograms of **A-PDI$_2$** in DCM using Fc/Fc$^+$ coupled Ag/Ag$^+$ electrode.	69
A2.26	**L-PDI$_2$** fragments used for the TheoDORE and Coulombic coupling calculations.	69
A2.27	**A-PDI$_2$** fragments used for the TheoDORE and Coulombic coupling calculations.	70
A2.28	Hole-electron isosurface distribution showing the localized/delocalized Frenkel exciton or charge transfer nature of the S_1, S_2, S_3 and S_4 excited-states in **L-PDI$_2$**.	70
A2.29	Hole-electron isosurface distribution showing the localized/delocalized Frenkel exciton or charge transfer nature of the S_1, S_2, S_3 and S_4 excited-states in **A-PDI$_2$**.	71
A2.30	TDDFT calculated natural transition orbitals (NTOs) of the first singlet excited-state (S_1) of **L-PDI$_2$**. The corresponding weightages of the NTOs are mentioned. N.B.- HONTO is the highest occupied natural transition orbital and LUNTO is the lowest unoccupied natural transition orbital.	71
A2.31	TDDFT calculated natural transition orbitals (NTOs) of the first singlet excited-state (S_1) of **A-PDI$_2$**. The corresponding weightages of the NTOs are mentioned. N.B.- HONTO is the highest occupied natural transition orbital and LUNTO is the lowest unoccupied natural transition orbital.	72
A2.32	Transition dipole moment (TDM) vectors for the S_0 to S_1 transition in **L-PDI$_2$**.	72
A2.33	Transition dipole moment (TDM) vectors for the S_0 to S_1 transition in **A-PDI$_2$**.	73
A2.34	TDDFT calculated energies of the charge transfer (CT), locally excited S_1, and triplet (T_3) excited-states of **L-PDI$_2$** and **A-PDI$_2$** at the CAM-B3LYP-D3/6-311+G(d,p) level of theory in vacuum.	73
A2.35	The fsTA spectra of a) **L-PDI$_2$** and b) **A-PDI$_2$** obtained at 0.9 ps time delay in TOL and ACE solvents. The similar nature of the ESA	74

	bands shows the population of a locally excited singlet state in **L-PDI$_2$** and **A-PDI$_2$** upon initial photoexcitation.	
3.1	Molecular structures of a) ref-PDI and b) **PDI-T**. Ground-state optimized structure of **PDI-T** shown in c) side view and d) top view (3-pentyl group substituted with methyl group to minimize computational cost).	88
3.2	a) Normalized UV-vis absorption and emission spectra of ref-PDI (black) and **PDI-T** (red) in TOL. Inset shows the zoomed absorption spectra of ref-PDI and **PDI-T**, and a shoulder peaking at ≈ 535 nm was observed for **PDI-T**. b) Solvent-dependent normalized UV-vis absorption spectra of **PDI-T** in TOL (ε = 2.38), THF (ε = 7.58) and ACE (ε = 20.70). Inset shows the zoomed solvent-dependent absorption spectra of **PDI-T.** c) Solvent-dependent emission spectra of **PDI-T** display the significant quenching of the fluorescence intensity in polar THF and ACE solvents. Inset shows the zoomed-in solvent-dependent normalized emission spectra of **PDI-T.**	89
3.3	Representative FLIM images of **PDI-T** in a) PS and b) PVA. FIT traces of **PDI-T** in c) PS and d) PVA. e) Representative antibunching measurement of **PDI-T** in PS. f) The single-molecule fluorescence lifetime double histogram of **PDI-T** in PS and PVA.	93
3.4	(Top row) FsTA spectra of **PDI-T** in a) TOL, b) THF, and c) ACE showing the excited-state dynamics upon photoexcitation. (Bottom row) EAS reconstructed from global analysis of **PDI-T** with A → B → C → GS model for TOL (left), THF (center) and ACE (right), where A is the singlet excited-state, B is the CT state in case of TOL and, the CSS in the case of THF and ACE, C is the triplet excited-state, and GS is the ground-state (λ_{ex} = 480 nm).	95
3.5	Proposed Jablonski diagram consolidating the excited-state dynamics of **PDI-T** upon photoexcitation under the influence of nonpolar and polar dielectric media; SB-CS = symmetry-breaking charge separation, CT = charge transfer state, CSS = charge separated state, CR = charge recombination, S_0 = ground-state, S_1 =	99

	first singlet excited-state, S_3 = third singlet excited-state and T_1 = first triplet excited-state.	
A3.1	^{1}H-NMR spectrum of **PDI-T** in $CDCl_3$.	102
A3.2	^{13}C-NMR spectrum of **PDI-T** in $CDCl_3$.	102
A3.3	MALDI mass spectrum of **PDI-T** with the highlighted molecular mass.	103
A3.4	a) The entire FT-IR spectrum of **PDI-T** and b) the enlarged fingerprint region to pinpoint the similarity of **PDI-T** with the PDI monomer.	103
A3.5	Melting point tube with the **PDI-T** sample and the measurement indicated the melting point of **PDI-T** to be >300 ºC.	104
A3.6	Centroid to centroid distances depicted in the ground-state optimized geometry of **PDI-T** in vacuum**.**	104
A3.7	a) Concentration-dependent UV-vis absorption spectra and b) absorption maxima (λ_{max}^{Abs} = 523 nm) versus concentration plot of **PDI-T** in TOL.	104
A3.8	a) Concentration-dependent UV-vis absorption spectra and b) absorption maxima (λ_{max}^{Abs} = 517 nm) versus concentration plot of **PDI-T** in THF.	105
A3.9	a) Concentration-dependent UV-vis absorption spectra and b) absorption maxima (λ_{max}^{Abs} = 515 nm) versus concentration plot of **PDI-T** in ACE.	105
A3.10	HOMO-LUMO isosurface (isovalue = 0.01 a.u) obtained from the ground-state optimized geometry of **PDI-T** at B3LYP-D3/6-311+G(d,p) level of theory in vacuum.	106
A3.11	Ground-state optimized geometries of **PDI-T** in a) TOL, b) THF and c) ACE using IEFPCM model at the B3LYP-D3/6-311G+(d,p) level of theory.	106
A3.12	One-dimensional relaxed potential energy surface (PES) of **PDI-T** scan as a function of dihedral angle**.**	107
A3.13	S_1-state optimized geometry of **PDI-T** in vacuum at the CAM-B3LYP-D3/6-31G level of theory.	107

A3.14	TDDFT calculated natural transition orbitals (NTOs) of the first singlet excited-state (S_1) of **PDI-T**. The corresponding weightages of the NTOs and the wavelength are mentioned.	108
A3.15	TDDFT calculated natural transition orbitals (NTOs) of the third singlet excited-state (S_3) of **PDI-T**. The corresponding weightages of the NTOs and the wavelength are mentioned.	108
A3.16	**PDI-T** fragments used for the Coulombic coupling and TheoDORE analyses**.**	109
A3.17	a) Hole-electron correlation plots showing the localized or delocalized Frenkel exciton or charge transfer nature for the S_1, S_3, S_4 and S_5 excited-states of **PDI-T** and the b) corresponding hole-electron isosurface distribution of these excited-states. The nature of the excitations is defined by the CT and PR values.	109
A3.18	a) Cyclic voltammetry data and b) differential pulse voltammograms of **PDI-T** in DCM using Fc/Fc^+ coupled Ag/Ag^+ electrode.	110
A3.19	Representative FITs of **PDI-T** in PS measured for 300 s. The intensity threshold is defined by the blue line in the FITs.	110
A3.20	Representative FITs of **PDI-T** in PVA measured for 300 s. The intensity threshold is defined by the blue line in the FITs.	111
A3.21	The fluorescence lifetime distribution of **PDI-T** in a) PS and b) PVA matrices.	111
A3.22	Representative antibunching measurements of **PDI-T** in PS matrix.	112
A3.23	a) UV-vis absorption changes of **PDI-T** upon the addition of antimony pentachloride ($SbCl_5$) and b) difference absorption spectra of **PDI-T** obtained by subtracting ground-state absorption from that of chemically oxidized radical cation species in ACE.	112
A3.24	a) UV-vis absorption changes of **PDI-T** upon the addition of cobaltocene ($CoCp_2$) and b) difference absorption spectra of **PDI-T** calculated by subtracting the absorption of the neutral ground-state from that of the chemically generated radical anion in ACE.	113

A3.25	Global analysis fits for selected fsTA wavelengths of **PDI-T** (λ_{ex} = 480 nm) in TOL using A → B → C → GS kinetic model. Fitted results are shown using solid line profiles.	113
A3.26	Global analysis fits for selected fsTA wavelengths of **PDI-T** (λ_{ex} = 480 nm) in THF using A → B → C → GS kinetic model. Fitted results are shown using solid line profiles.	114
A3.27	Global analysis fits for selected fsTA wavelengths of **PDI-T** (λ_{ex} = 480 nm) in ACE using A → B → C → GS kinetic model. Fitted results are shown using solid line profiles.	114
A3.28	The stacked plot of the global analysis fitted CSS kinetic trace in ACE (top) and THF (middle) and CT kinetic trace in TOL (bottom), showing the distinct transient spectral signature of the radical cation and radical anion in **PDI-T**.	115
A3.29	(Top row) FsTA spectra of **PDI-T** in a) TOL, b) THF, and c) ACE showing the excited-state dynamics upon photoexcitation. (Bottom row) EAS reconstructed from global analysis of **PDI-T** with A → B → C → GS model for TOL (left), THF (center) and ACE (right), where A is the singlet excited-state, B is the CT state in case of TOL and, the CSS in the case of THF and ACE, C is the triplet excited-state, and GS is the ground-state (λ_{ex} = 532 nm).	115
A3.30	Nanosecond transient absorption measurements of **PDI-T** in N_2 purged solution of a) TOL, b) THF and c) ACE.	116
A3.31	Nanosecond transient absorption measurements of **PDI-T** in O_2 purged solution of a) TOL, b) THF and c) ACE.	116
A3.32	a) Nanosecond transient absorption decay profiles of **PDI-T** in a) TOL, b) THF and c) ACE at 510 nm.	116
A3.33	a) The nsTA decay of $[Ru(bpy)_3]^{2+}$ monitored at 370 nm. b) Time-resolved growth trace at 530 nm showing the formation of the triplet excited-state of β-carotene (^{3}β-carotene*) upon mixing $[Ru(bpy)_3]^{2+}$ with β-carotene in methanol, providing evidence for triplet-triplet energy transfer from the ruthenium complex to β-carotene.	117
A3.34	Time-resolved nsTA traces illustrating the growth of the triplet excited-state of β-carotene (^{3}β-carotene*) upon interaction with	117

	PDI-T, thereby validating the occurrence of triplet-triplet energy transfer from **PDI-T** to β-carotene in a) TOL, b) THF, and c) ACE.	
4.1	Molecular structures of a) **PDI_2** and b) **PDI_3**. Optimized structures of c) **PDI_2** and d) **PDI_3** showing the core-twist in the PDI multimers.	127
4.2	Fluorescence excitation spectra of a) **PDI_2** and b) **PDI_3**, and emission spectra of c) **PDI_2** and d) **PDI_3** in DIOX and thin films in PMMA.	128
4.3	fsTA spectra of a) **PDI_2** and d) **PDI_3** in thin films in PMMA showing the excited-state dynamics upon photoexcitation. EAS reconstructed from global analysis of the fsTA data of b) **PDI_2** and e) **PDI_3** with the A → B → GS kinetic model, where A is the CSS, B is the CSS_{rel}, and GS is the ground-state (λ_{ex} = 480 nm). Relative population profile of the excited-states fitted using the above kinetic models in c) **PDI_2** and f) **PDI_3**.	129
4.4	The optimized structures of a) **PDI_2** aggregate and b) **PDI_3** aggregate were obtained using a dimer model at the B3LYP-D3/6-31G level of theory in a vacuum (3-pentyl group substituted with methyl group to minimize computational cost). c) Schematic energy profile diagram summarizing the excited-state dynamics of **PDI_2** and **PDI_3** in (left) solution as monomer and (right) thin films in PMMA; S_0 = ground-state, S_1* = singlet excited-state; CSS = charge separated state; CSS_{rel} = relaxed charge separated state; T_n = triplet excited-state. N.B.- The solution-state photophysics is adapted from the previously reported energy profile diagrams in sections 2.2.12 and 3.2.10.	132
A4.1	a) 2D-DOSY NMR spectrum and b) diffusion coefficient fit obtained from DOSY NMR spectrum of **PDI_2** in $CDCl_3$.	135
A4.2	a) 2D-DOSY NMR spectrum and b) diffusion coefficient fit obtained from DOSY NMR spectrum of **PDI_3** in $CDCl_3$.	135
A4.3	a) Kubelka-Munk transformed normalized absorption spectra of **PDI_2** and **PDI_3** thin films in PMMA matrix. b) Normalized emission spectra of **PDI_2** and **PDI_3** thin films in PMMA matrix.	136

A4.4	Global analysis fits for selected fsTA wavelengths (λ_{ex} = 480 nm) of a) **PDI$_2$** and b) **PDI$_3$** thin films in PMMA matrix using A → B → GS kinetic model. Fits are shown as solid lines.	136
A4.5	fsTA spectra of a) **PDI$_2$** and d) **PDI$_3$** in thin films in PS showing the excited-state dynamics upon photoexcitation. EAS reconstructed from global analysis of the fsTA data of b) **PDI$_2$** and e) **PDI$_3$** with the A → B → GS kinetic model, where A is the hot S_1 state, B is the $(S_1)_{rel}$ state, and GS is the ground-state (λ_{ex} = 480 nm). Relative population profile of the excited-states fitted using the above kinetic models in c) **PDI$_2$** and f) **PDI$_3$**.	137
A4.6	a) Fluorescence lifetime decay and b) FLIM image of **PDI$_2$** thin film.	137
A4.7	a) Fluorescence lifetime decay and b) FLIM image of **PDI$_3$** thin film.	138
A4.8	a) **PDI$_2$** and b) **PDI$_3$** dimer fragments used for the Coulombic coupling calculations.	138
A4.9	HOMO and LUMO isosurfaces of **PDI$_2$** aggregate, obtained from the ground-state optimized dimer geometry. N.B.- isovalue = 0.02 a.u.	139
A4.10	HOMO and LUMO isosurfaces of **PDI$_3$** aggregate, obtained from the ground-state optimized dimer geometry. N.B.- isovalue = 0.02 a.u.	139

List of Tables

No.	Title	Page No.
2.1	Time constants (τ), rate constants (k), driving forces (ΔG) for SB-CS and triplet quantum yields (ϕ_T) of **L-PDI$_2$** and **A-PDI$_2$** in TOL (ε = 2.38) and ACE (ε = 20.70) solvents.	44
A2.1	Geometric parameters at S_0 optimized geometry of **L-PDI$_2$** and **A-PDI$_2$**.	74
A2.2	Steady-state photophysical properties of **L-PDI$_2$** and **A-PDI$_2$** in different solvents.	74

A2.3	Summary of redox potentials and HOMO/LUMO calculations of **L-PDI$_2$** and **A-PDI$_2$** (CH_2Cl_2, 298 K, ε_{SP} = 8.93).	75
A2.4	Vertical excitation energies for the low-lying singlet excited-states computed at the ground-state optimized geometry of **L-PDI$_2$** and **A-PDI$_2$** (TD-CAM-B3LYP-D3/6-311+G(d,p) level of theory) in vacuum.	75
A2.5	TDDFT calculated energies of the charge transfer (CT), locally excited S_1, and triplet (T_3) excited-states of **L-PDI$_2$** and **A-PDI$_2$** at the CAM-B3LYP-D3/6-311+G(d,p) level of theory in vacuum. N.B.- The T_3 excited-state was the low-lying triplet state near to S_1 state energy in **L-PDI$_2$** and **A-PDI$_2$**.	76
3.1	Time constants (τ), rate constants (k), driving forces (ΔG) for SB-CS and triplet quantum yields (ϕ_T) of **PDI-T** in different dielectric media.	97
A3.1	Geometric parameters at S_0 and S_1 optimized geometries of **PDI-T**.	118
A3.2	Steady-state photophysical properties of **PDI-T** in different solvents.	118
A3.3	Vertical excitation energies computed at the ground-state optimized geometry of **PDI-T** (TD-CAM-B3LYP-D3/6-311G+(d,p) level of theory) in vacuum.	118
A3.4	Vertical excitation energies computed for the $S_0 \rightarrow S_1$ transition at the ground-state optimized geometry of **PDI-T** in different solvents using IEFPCM model (TD-CAM-B3LYP-D3/6-311G+(d,p) level of theory).	119
A3.5	Summary of redox potentials and HOMO/LUMO calculations of **PDI-T** (CH_2Cl_2, 298 K, ε_{SP} = 8.93).	119
A4.1	The theoretically computed J_{Coul}, J_{CT} and J_{Total} interaction values in **PDI$_2$** and **PDI$_3$** aggregates.	140
A4.2	The computed low-lying singlet excited-state energies and the corresponding oscillator strengths (f) in **PDI$_2$** and **PDI$_3$** aggregates at the CAM-B3LYP-D3/DEF2-TZVP level of theory.	140

List of Schemes

No.	Title	Page No.
2.1	Synthesis scheme of a) PDI, NO_2-PDI and NH_2-PDI; b) **L-PDI$_2$** and c) **A-PDI$_2$**.	39
3.1	Synthesis scheme of a) PDI, NO_2-PDI and NH_2-PDI; and b) **PDI-T**.	87

Abstract

Excitonic interactions are crucial in modulating the photodeactivation pathways in organic multichromophoric systems. Symmetry-breaking charge separation (SB-CS) is an excited-state photodeactivation process where a pair of identical chromophores absorb a photon to form a charge separated state with the hole and electron on adjacent chromophores. SB-CS rates are highly dependent on the excitonic coupling between two chromophores. The interference between the long-range Coulombic coupling (J_{Coul}) and the short-range charge transfer (CT)-mediated coupling (J_{CT}) in a multichromophoric system plays a vital role in modulating the charge separation and charge recombination rates. In my doctoral thesis, the effect of intra and intermolecular excitonic coupling on the SB-CS rates will be demonstrated for perylenediimide (PDI)-based multimers at the isolated monomeric and aggregated states.

Chapter 1 will introduce the excitonic coupling concept and the SB-CS process. In chapter 2, the effect of weak intramolecular excitonic coupling accelerating SB-CS in PDI dimers will be discussed. Two PDI dimers with different orientations (linear and angular) were prepared to investigate the role of orientation-modulating excitonic coupling essential for faster SB-CS rates. Further in chapter 3, SB-CS mediated triplet excited-state population in a weakly coupled PDI trimer will be explained. Single-molecule fluorescence spectroscopy was employed to probe the emission intensity fluctuations due to the combined effect of charge separation and triplet state population. Finally, chapter 4 will demonstrate ultrafast SB-CS in thin films of J-aggregated PDI multimers in a nonpolar solid-state environment modulated through intermolecular excitonic coupling and strong π-π interactions.

Chapter 1

Introduction to Excitonic Interactions and Symmetry-Breaking Charge Separation (SB-CS): Role of Intramolecular and Intermolecular Excitonic Coupling in SB-CS

1.1. Introduction

Sunlight is the most sustainable energy source available on Earth, and developing efficient ways to harness solar energy could satisfy the growing energy needs in our world. Along the long history of evolution, mother nature has devised methods and strategies to perfect the electron and energy transfer reactions in the photosynthesis pigments for obtaining efficient

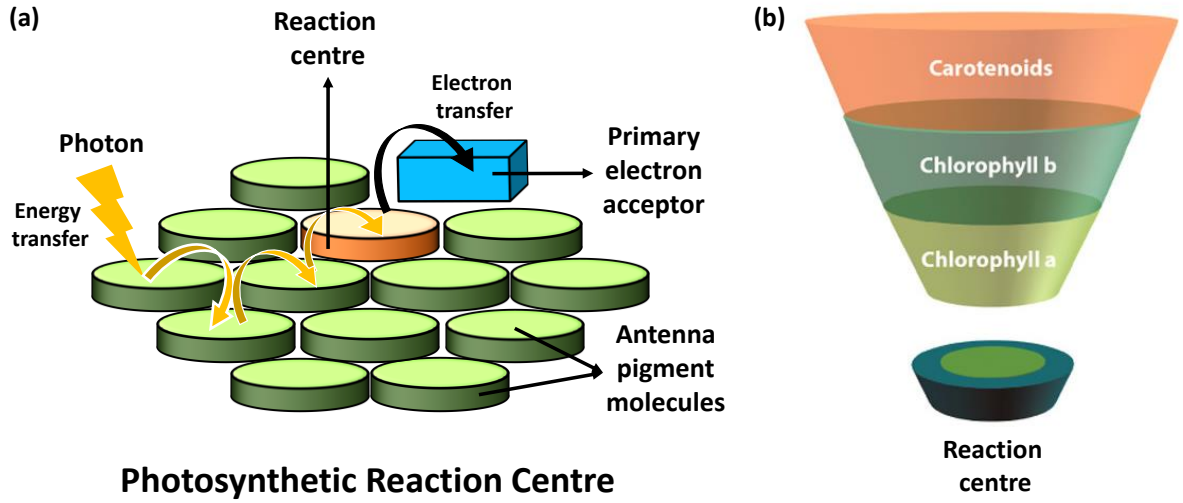

Figure 1.1: a) Schematic depicting excitation energy and electron transfer pathways where chromophores are arranged in two-dimensional planar distribution. b) The process of energy harvesting in an antenna system is represented as a funnel, where high-energy (short-wavelength) light is absorbed by outer antenna pigments, and the resulting excitation energy is progressively funnelled toward lower-energy pigments situated near the reaction centre. b) Reprinted with permission from ref (3). Copyright (2017) American Chemical Society.

chemical transformation and energy conversion pathways up to ~100% efficiencies.[1,2] Antenna pigment aggregates within the photosynthetic complex in natural photosynthesis are responsible for capturing incident sunlight and temporarily storing excitation energy (Figure 1.1). The excitation energy is subsequently directed to the reaction centre (RC), a complex structure where pigments and proteins are meticulously organized within a supportive biological matrix. A long-lived charge separated state (CSS) is generated within this reaction centre across the membrane. This event commences with symmetry-breaking charge separation, which initiates a cascade of electron transfer events associated with transmembrane proton translocation. The transformation of light energy into chemical energy through ATP production, is facilitated by the resultant electrochemical proton gradient.[3,4]

The light-harvesting complexes (LHC), also known as pigment-protein assemblies in photosynthetic organisms such as plants, algae, and bacteria, play a critical role in capturing the solar energy and directing the excitation energy to the RC. Although notable structural diversity exists for LHC antennas, the architecture of the RCs remains relatively conserved. The photosynthetic apparatus in the purple phototrophic bacteria is composed of two major pigment-protein assemblies: the core complex (RC-LH1) and the peripheral complex (LH2).[5,6] The RC unit is embedded within LH1, and several LH2 complexes encircle this RC-LH1 unit, thereby forming an extended two-dimensional array (Figure 1.2a). X-ray crystallography-

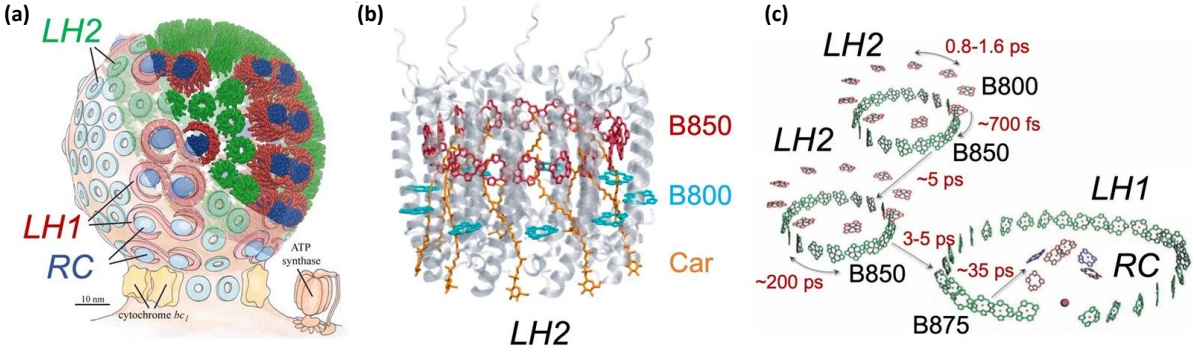

Figure 1.2: Illustrations of natural light-harvesting assemblies: a) Architectural organization of the photosynthetic apparatus in purple non-sulfur bacteria. b) Structural model depicting the light-harvesting complex 2 (LH2). c) Schematic of excitation energy flow within the interconnected LH1 and LH2 complexes network. Reprinted with permission from ref (6). Copyright (2022) Springer Nature.

derived structural insights into LH2 from the purple non-sulfur photosynthetic bacterium *Rhodopseudomonas acidophila*, strain 10050, provide the pigment-protein arrangement in LH2 (Figure 1.2b).[7] LH2 comprises 27 bacteriochlorophyll (BChl) molecules arranged in two concentric circular rings, B800 and B850, according to their characteristic absorption peaks. The B800 ring in LH2 contains nine relatively isolated BChls; meanwhile, the B850 ring includes 18 closely packed, strongly excitonically coupled BChls (Figure 1.2c). The different optical properties in B800 and B850 arise from the variations in pigment spacing and alignment, though both the rings are composed of the same BChl pigments. The sub-nanometer distances in the B850 ring give rise to pronounced excitonic interactions. After the absorption of solar energy, the excitation energy is transferred within and between the LH2 units, finally directing toward the RC. The energy transfer initially happens from B800 to B850 pigments, then transfers to neighbouring LH2 complexes (~5 ps). The LH1 subsequently absorbs the excitation energy within ~3–5 ps at a slightly lower energy (~870–880 nm).[8] Finally, the excitation energy is funnelled towards the RC-specific chlorophyll pairs ("special pair", P) from LH1 within approximately 30-40 ps (Figure 1.2c).[9] Ultimately, rather than transferring the excitation energy to adjacent pigments, these so-called "special pairs" (P) instigate a sequence of electron-transfer processes in RC via symmetry-breaking excited-state charge separation.[10] One of the exciting aspects of the energy transfer sequence is that it proceeds with a near-unity quantum efficiency. Although, all the pigment units are chemically identical BChl molecules, their precise spatial organization allows nature to fine-tune excitonic coupling leading to the highly optimized directional energy flow throughout the light-harvesting network.[11,12]

1.2. Molecular Exciton Theory; Kasha Model and Beyond

The advancement of next-generation photovoltaic and artificial photosynthesis technologies relies on understanding how molecular structure influences physical properties in molecular assemblies. Interest in molecular aggregates was ignited by the independent discoveries of Scheibe and Jelley in the 1930s,[13,14] which laid the foundation for decades of research spanning both fundamental and applied science.[15–19] In their pioneering work, Scheibe and Jelley noticed a significant bathochromic shift in the absorption spectra of concentrated solutions of 1,1′-

diethyl-2,2′-cyanine chloride (also known as pseudoisocyanine or PIC). Further to explain the electronic transitions in molecular crystals, Davydov later introduced the exciton theory.[20] Subsequently, building on this framework, Kasha formulated the molecular exciton theory, which correlates the photophysical behaviour of excitonically coupled systems to their spatial arrangements. Kasha's idea was particularly relevant for understanding the pigment-protein organization in photosynthetic light-harvesting complexes.[16,21]

When multiple chromophores are excited by light, the generated transition dipole moments (TDMs) can interact, leading to the photophysical phenomenon known as excitonic

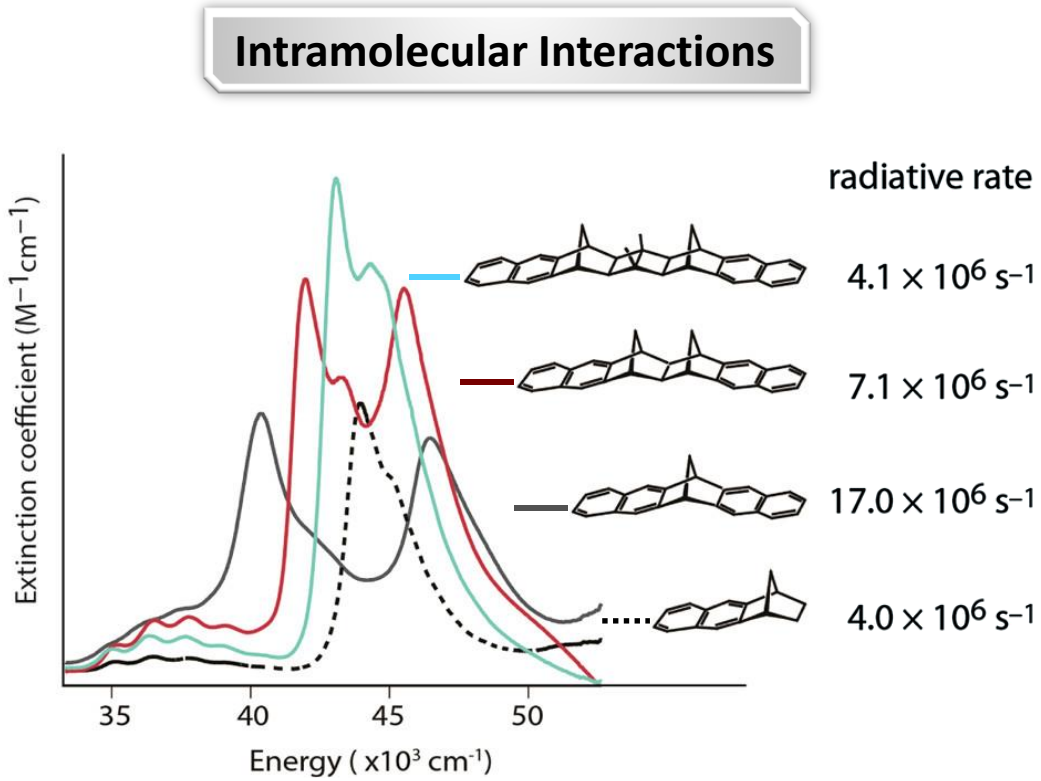

Figure 1.3: The absorption spectra of a set of naphthyl dimers linked by a norbornyl bridge are presented alongside that of a monomeric reference chromophore (shown as a dashed trace). The spectral features of the dimers exhibit two distinct absorption bands, with the separation between them corresponding to the magnitude of electronic coupling between the left and right naphthyl units. This splitting signifies that the excitation is delocalized across both chromophores, characteristic of a molecular exciton. Reprinted with permission from ref (22). Copyright (1993) American Chemical Society.

coupling. The interactions between the TDMs facilitate the exchange of electronic excitation energy between the chromophoric units. The excitonic coupling can arise due to intramolecular as well as intermolecular interactions. Figure 1.3 shows an example of a molecular exciton interaction in a series of norbornyl-bridged naphthalene chromophores.[22] We observe that as the number of naphthyl moieties increases from one to two, the absorption spectra exhibit splitting of the absorption maxima and an increase in the radiative rate. The strong excitonically coupled dinaphthyl dimer (~890 cm^{-1}) shown in grey trace results in the delocalization of excitation energy over both chromophores; therefore, energy splitting in the absorption band compared to the monomer naphthyl spectrum is observed (Figure 1.3). As the number of norbornyl bridges increases, the distance between the two naphthyl units increases, and the absorption behaviour becomes similar to that of the monomer, which is also manifested in the radiative rates. The splitting of the absorption band in the dinaphthyl dimer arises due to the intramolecular through-space electronic communication between the naphthalene moieties. However, we also infer that for dimers having large interchromophoric distances, the excitonic interaction vanishes and resembles the monomer photophysics.

The molecular exciton theory formulated by Kasha in 1960s was based on the point dipole approximation.[21] The transition densities later simplified as TDM vectors were considered point dipoles, and the interactions between the TDM vectors led to the excitonic coupling responsible for the unique photophysical signatures observed in the excited-state dynamics of multichromophoric systems upon photoexcitation. The simplified yet impactful model of interacting transition dipoles arranged in various geometries has sparked a wave of scientific breakthroughs in evaluating long-range Coulomb interactions (J_{Coul}). The ideal dipole approximation is employed to estimate the J_{Coul} interactions and can be represented as:[21,23,24]

$$J_{Coul} = \frac{\mu^2(\cos\alpha - 3\cos^2\Theta)}{4\pi\varepsilon_0 R^3} \qquad \text{(Eq 1.1)}$$

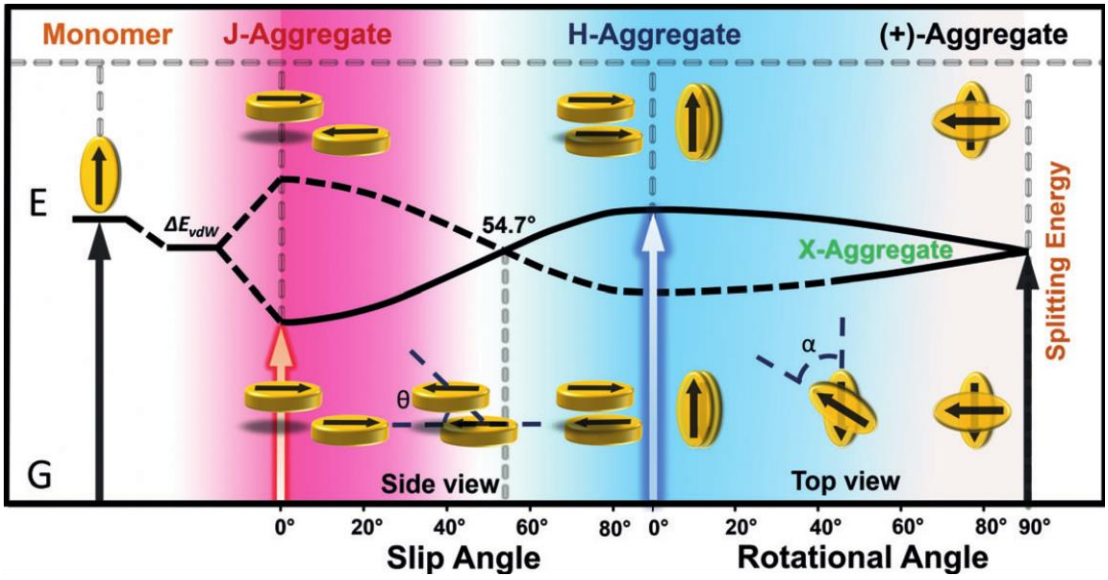

Figure 1.4: Schematic representation of exciton splitting for a molecular dimer and correlation between slip angle (θ), rotational angle (α) and the orientation factor (κ). Reprinted with permission from ref (28). Copyright (2018) John Wiley & Sons, Inc.

In this context, μ denotes the magnitude of the TDM vectors associated with the chromophores, R signifies the intermolecular distance, θ is defined as the angle between the polarization direction of the dipole and the vector linking the centers of the two molecules, α corresponds to the dihedral angle between their molecular planes, and ε_0 represents the permittivity of free space. The term $(\cos\alpha - 3\cos^2\theta)$ defines the orientation factor (κ).

Molecular aggregates are classified by Kasha's exciton model into H- and J-types, based on the spatial orientation of their TDM vectors. H-aggregates (H denotes hypsochromic) are formed through the face-to-face stacking of chromophores (Figure 1.4). The face-to-face arrangement leads to the splitting of the excitonic energy levels due to Coulombic interactions. Due to energy level splitting, the transition to the lower energy excitonic state becomes optically forbidden due to a net dipole moment cancellation; meanwhile, transitions to the higher energy state are allowed. The photophysical manifestation of the excitonic energy level splitting appears as a blue-shifted absorption maximum and either weak or no fluorescence emission in the aggregate relative to the monomer (Figure 1.4). The optical properties of H-aggregates from cyanine dye monomers are shown in Figure 1.5.[25–27]

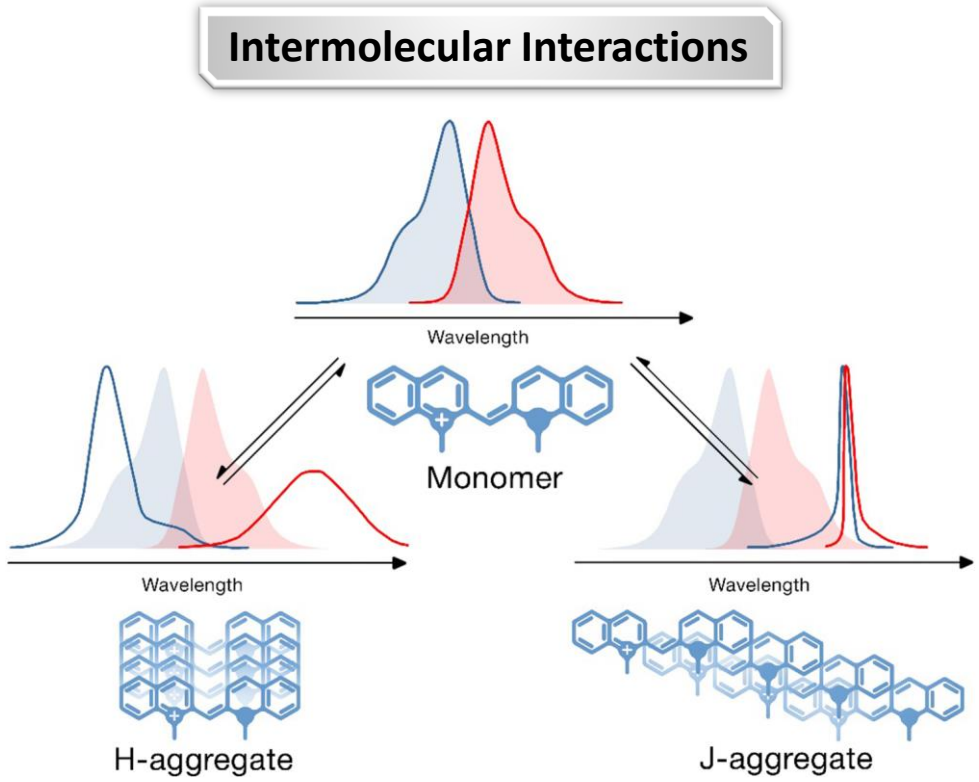

Figure 1.5: A schematic illustration depicting how the absorption (in blue) and fluorescence (in red) spectra shift upon the aggregation of cyanine dye monomers into H- and J-type aggregates. Reprinted with permission from ref (27). Copyright (2017) IOP Publishing.

On the other hand, J-aggregates (named after Jelley) exhibit a head-to-tail arrangement of the chromophores. The splitting of the excitonic energy level enables transitions to the lower excitonic state with a net dipole moment. The lower energy state transitions are characterized by red-shifted absorption as well as red-shifted enhanced emission bands compared to the monomer (Figure 1.4). An example of the optical properties of the J-aggregate of cyanine dye is shown in Figure 1.5. In addition to the well-known H- and J-type aggregates, Kasha also proposed the existence of a distinct category of aggregates characterized by cross-oriented transition dipoles and electronically degenerate states, arising from negligible Coulombic interactions (Figure 1.4).[28] Yet another class of aggregates is the magic angle-stacked aggregates, where parallelly arranged slip-stacked molecular aggregates with a slip angle of 54.7º (magic angle) between the transition dipoles are proposed to display monomer-like

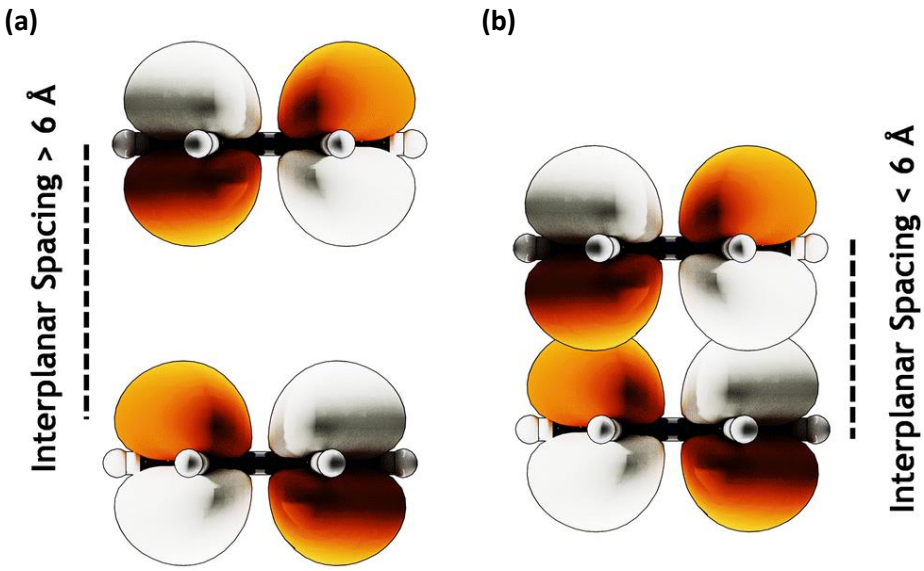

Figure 1.6: Molecular orbitals (MOs) corresponding to a) large interplanar separations (≥ 6 Å), where no significant orbital interaction is observed, and b) smaller interplanar distances (≤ 6 Å), where evident orbital overlap occurs. Reprinted with permission from ref (30). Copyright (2023) The Royal Society of Chemistry.

properties (Figure 1.4).[29] Nevertheless, the salient dipole-dipole excitonic model of Kasha fails to account for the orbital interactions among the chromophoric units in closely-packed chromophoric arrangements (d ≈ 3.5 Å), and therefore requires advanced electronic coupling models to describe the overall photophysics of an aggregate.

Intramolecular excitonic coupling holds profound impact on the excited-state dynamics in covalently bonded multichromophoric systems. Previously it has been observed that the combination of through-bond and through-space excitonic interactions contribute to the overall charge separation dynamics in covalently bound multichromophoric systems.[10] However, the through-space interactions dominate over the through-bond interactions in molecular multimers with the individual monomers exhibiting small interchromophoric distances.[30] In molecular aggregates where the interchromophoric spacing is sufficiently small, significant orbital overlap between neighbouring units can occur, thereby facilitating short-range excitonic coupling, as illustrated in Figure 1.6.[31] Spano and co-workers expanded Kasha's molecular exciton model through the incorporation of short-range charge transfer (CT)-mediated coupling

(J_{CT}).[32] In π-π stacked multichromophoric architectures ($d \leq 6$ Å), both the short-range and long-range interactions contribute to the optical properties of the molecule. The J_{CT} interactions can be estimated as:

$$J_{CT} = \frac{-2t_e t_h}{E_{CT} - E_{S_1}} \qquad \text{(Eq 1.2)}$$

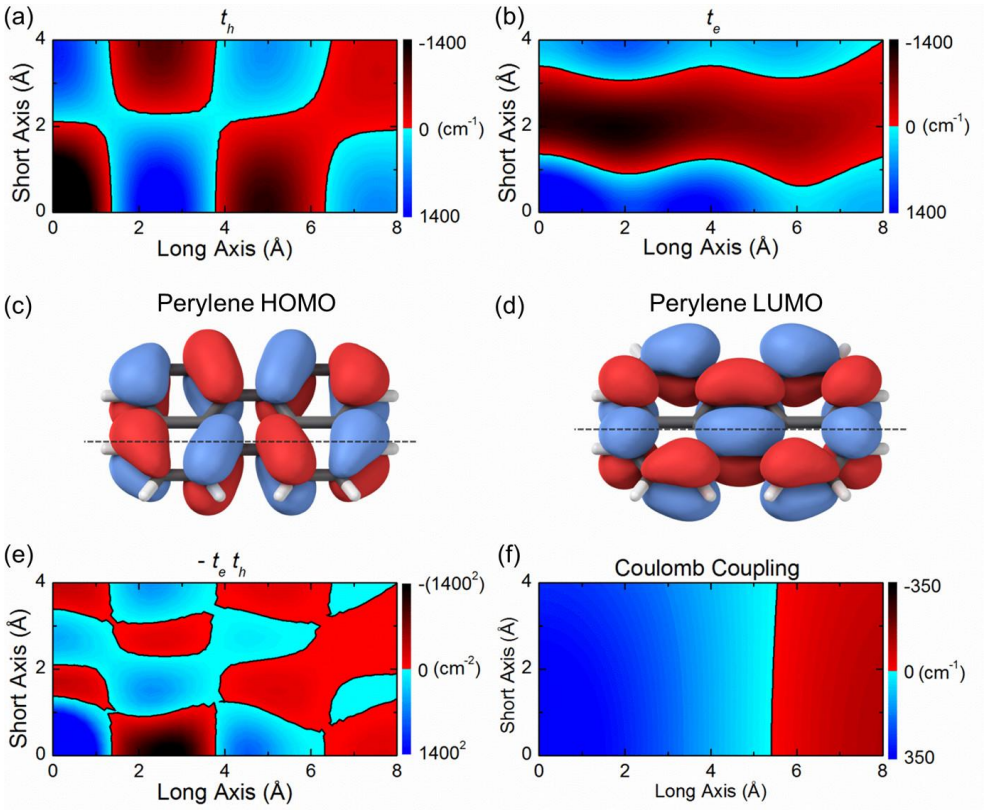

Figure 1.7: a) t_h and b) t_e within a π-stacked perylene dimer (interplanar distance of 3.5 Å) are plotted as functions of transverse displacement, derived from energy level splitting calculated using DFT. The DFT computed HOMO and LUMO isosurfaces of perylene are shown in c) and d), respectively. e) The product of t_h and t_e, which is proportional to the charge transfer coupling (J_{CT}), and f) the unscreened Coulombic interaction is both shown as a function of transverse displacements, determined from atomic transition charge densities obtained via TDDFT calculations. The red and blue regions denote J-aggregate and H-aggregate interactions, respectively. The sign conventions for t_h and t_e were defined according to the symmetry operations under which the TDM of the dimer remains symmetric. Reprinted with permission from ref (36). Copyright (2017) American Chemical Society.

In this context, t_e and t_h represent the transfer integrals for electrons and holes, respectively, while E_{CT} and E_{S_1} correspond to the energies of the CT state and the lowest singlet excited-state. The magnitude of excitonic coupling facilitated through the CT pathway in molecular systems is particularly sensitive to the slip angle (θ) and rotational displacement (α) between chromophores, due to the critical dependence on the relative phase alignment of the interacting molecular orbitals.[32–35] The CT interactions are intrinsically difficult to predict, primarily due to the variable spatial distribution of frontier molecular orbitals (FMOs), which is influenced by the symmetry and elemental makeup of the molecular scaffold.[31] Specifically, electron and hole coupling arise from the spatial overlap between the LUMOs and HOMOs of adjacent molecules, respectively. The total coupling (J_{Total}) in a multimer/molecular aggregate is the consolidated effect of short-range charge transfer and long-range Coulombic couplings, and can be represented as:

$$J_{Total} = J_{Coul} + J_{CT} \quad \text{(Eq 1.3)}$$

In closely-packed chromophoric systems ($d \leq 6$ Å), the net excitonic coupling is defined by the interference of charge transfer and Coulombic couplings terms. The strong interplay between the J_{Coul} and J_{CT} contributes to the overall photophysical behaviour of chromophoric assemblies.[36] The sensitivity in J_{Coul} and J_{CT} interactions with respect to displacements along the long and short axes for a π-stacked perylene dimer is given in Figure 1.7.

1.3. Symmetry-Breaking Charge Separation (SB-CS)

Symmetry-breaking charge separation (SB-CS) is a photoinduced excited-state phenomenon where a pair of identical chromophores absorb a photon to form a CSS with the hole and electron on adjacent chromophores.[10,37–39] SB-CS plays a vital role in both natural photosynthetic light-harvesting assemblies and the development of next-generation organic photovoltaic (OPV) technologies.[40,41] The main factors controlling the rate of SB-CS are: electronic coupling intrinsic to the chromophoric structure and the surrounding dielectric microenvironment.[42–45] SB-CS is the integral process which triggers the electron transfer events in photosynthetic bacteria, algae, and plants, converting solar energy into chemical energy.[46,47] The BChl dimer known as ‘special pair’ (P) in the RCs converts the absorbed solar energy to

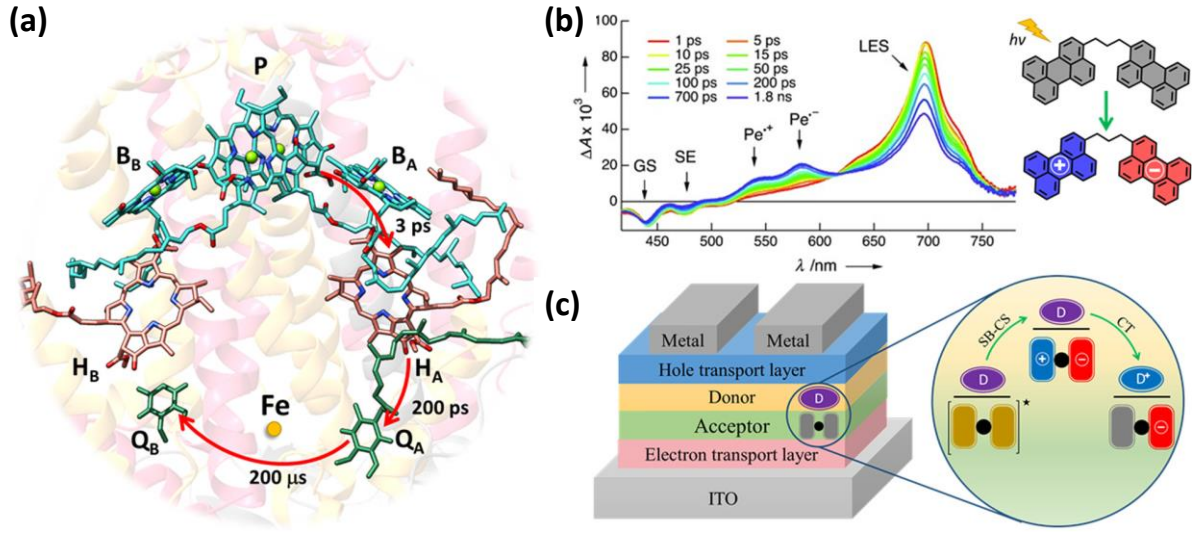

Figure 1.8: a) A schematic representation depicting the charge separation and ensuing electron transfer steps within the purple bacterial RC. The red arrows mark the electron transfer routes along with their respective time constants. The green-coloured spheres positioned at the center of the chlorin rings denote the magnesium atoms present in bacteriochlorophyll (BChl). In this context, P refers to a dimer of BChl, while B_A and B_B represent monomeric BChl units. H_A and H_B are bacteriopheophytins (BPhs), Q_A and Q_B correspond to ubiquinone molecules, and Fe refers to a non-heme iron center. b) The transient absorption spectrum of biperylenylpropane recorded in ACN displays distinct photophysical features that can be attributed to the radical ion pair species. c) A conceptual illustration of a basic organic bilayer photovoltaic device, where a conventional donor and an acceptor material are layered in a sandwich-like orientation. The operating mechanism involves SB-CS, enabling efficient charge generation. Reprinted with permission from ref (10). Copyright (2022) American Chemical Society.

CSS, and each sequential electron-transfer process decreases the free energy and stabilizes the reactive radical ion pair by enlarging the spatial separation between the pigments. Figure 1.8a shows the stepwise electron transfer events occurring within the purple bacterial RC (PDB ID: 1M3X, *Rhodobacter sphaeroides*). These 'special pairs' are weak excitonically coupled bichromophoric systems found in purple bacteria, photosystem I and photosystem II (Figure 1.9).

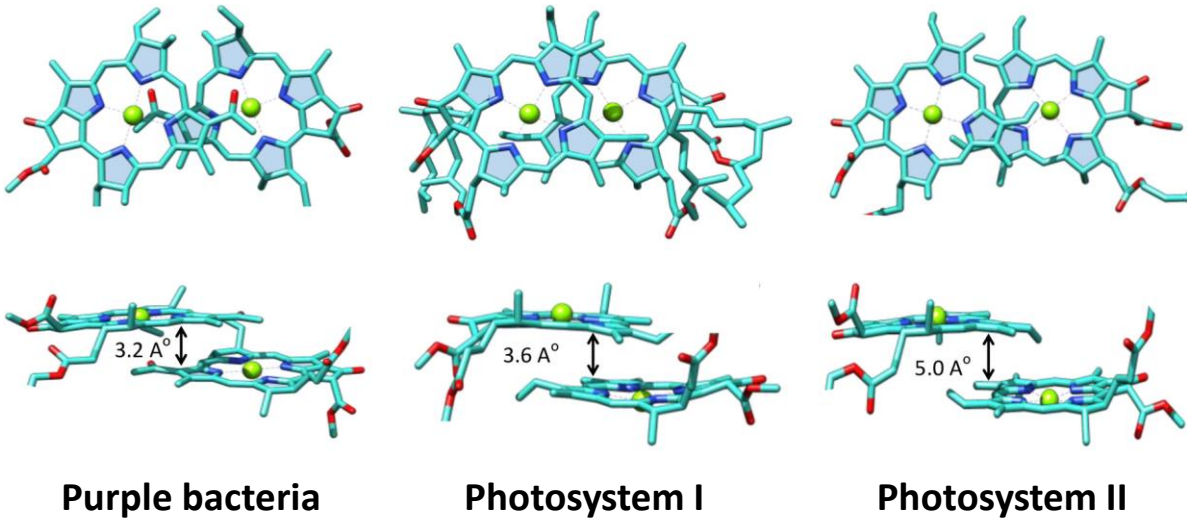

Figure 1.9: The structural geometry of 'special pairs' in different RCs. Reprinted with permission from ref (10). Copyright (2022) American Chemical Society.

Previously, the SB-CS process has been widely explored in weakly coupled multichromophoric systems.[48–54] Figure 1.8b shows the SB-CS process in a perylene dimer linked covalently by a propane bridge in acetonitrile, ACN (SE: stimulated emission, GS/GSB: ground-state bleach, $Pe^{\bullet+}$: perylene radical cation, $Pe^{\bullet-}$: perylene radical anion, LE/LES: locally excited-state). Upon photoexciting the perylene dimer, the LE state decays to form the CSS with the coexistence of both perylene radical cation and radical anion (Figure 1.8b). Charge separation takes place when the initially symmetric excited-state of the dimer is disrupted by either intramolecular vibrations or dynamic changes in the surrounding dielectric medium.[48] The development of molecular constructs that can demonstrate ultrafast charge separation and slow charge recombination is essential for the effective functioning of photovoltaic devices.

OPVs have recently garnered significant attention as a renewable source of energy, with a reported power conversion efficiency of ~18%.[55] OPVs rely on light absorption, exciton generation, charge separation, and carrier transport similar to natural photosynthesis.[56,57] The ability of the OPVs to incorporate a wide range of colour-absorbing materials and fabricate transparent devices has attracted the commercial solar device market.[57] However, the performance of OPVs is often limited due to the energetic and structural disorders.[57,58] The open-circuit voltage (V_{oc}) determined for organic solar cells usually shows a smaller value

when compared to the inorganic counterparts. The reduced V_{oc} arises from the significant energy offset between the optical band gap and the CSS.[58] To enhance the V_{oc} without negatively affecting other critical device metrics such as the short-circuit current (J_{sc}) or the fill factor (FF), it is crucial to reduce the energetic requirement that drives charge separation.[59] SB-CS holds significant potential for advancing OPVs, enabling the formation of CSS with energy losses below 100 mV, markedly lower than the ~500 mV or more typically required in traditional donor-acceptor architectures.[60] Therefore, utilizing SB-CS materials as an active layer in OPVs could be beneficial for developing more efficient optoelectronic devices.[40] Figure 1.8c illustrates a basic representation of a bilayer organic solar cell, where a typical donor and an acceptor capable of SB-CS are arranged in a sandwich-like arrangement. Upon absorbing light, a localized singlet excited-state is generated, which then evolves into a CSS via SB-CS. Subsequently, the donor molecule donates an electron to the SB-CS type acceptor, as depicted in Figure 1.8c.

1.3.1. History of SB-CS

The photogeneration of free charge carriers via exciton-exciton interactions was primitively demonstrated for the first time in 1963 by Jarnagin and co-workers in anthracene crystals.[61] Since then, researchers have made extensive efforts to understand the SB-CS process in organic systems. Subsequently in 1968, Lippert and co-worker showed the broad and featureless fluorescence spectra of 9,9'-dianthryl molecule in high-polar solvents. Further, they concluded that the orthogonal dianthryl molecule undergoes structural planarization in the excited-state, leading to excitonic coupling, favouring charge separation (a non-radiative pathway), manifested through the nature of the fluorescence spectra.[62] Later in 1975, Mataga and co-workers employed picosecond flash spectroscopy to probe the solvent-induced intramolecular electron transfer in 9,9'-bianthryl molecule after photoexcitation. The authors stated that the effects of the solvent dielectric constant upon the fluorescence quantum yield and lifetime of 9,9'-bianthryl denote the decrease of the radiative transition probability with the increase in the solvent polarity, which could be due to the photoinduced charge separation.[63] Bianthryl dimers initially served as a perfect testbed for probing SB-CS in multichromophoric assemblies.

However, researchers have moved to a broader range of chromophoric classes with tailored SB-CS properties in pursuit of better visible light-absorbing dyes.

1.3.2. Key Factors Controlling SB-CS

1.3.2.1. Dielectric Medium Modulated Photoinduced SB-CS

The SB-CS rates are highly sensitive to the electronic coupling between the individual chromophores and the surrounding dielectric microenvironment.[10,42,43] Through carefully designed experimental conditions, scientists have figured out the acceleration of SB-CS in polar dielectrics due to the lowering of the CSS energy beyond the locally excited singlet state formed upon photoexcitation.[53,64] Meech and co-workers have displayed the occurrence of excimer-mediated SB-CS in a μ-oxo-subphthalocyanine dimer (μ-OSubPc$_2$). The optimized structure showed the B-B distance as 2.65 Å, and the shortest distance between π-systems is 3.6 Å (Figure 1.10a). The short distance favours strong electronic coupling between the

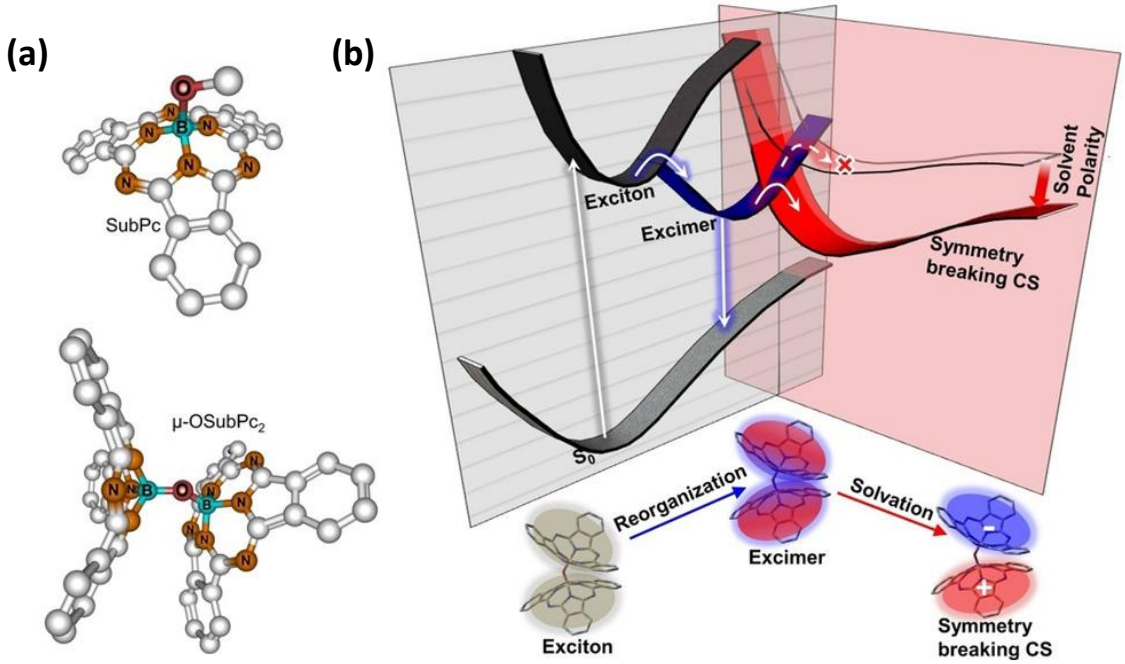

Figure 1.10: a) The molecular geometries of the SubPc monomer and the μ-OSubPc$_2$ dimer obtained through DFT optimizations. b) Illustration depicting how the excited-state dynamics of μ-OSubPc$_2$ vary with changes in solvent dielectric properties. Reprinted with permission from ref (53). Copyright (2021) John Wiley & Sons, Inc.

subphthalocyanine moieties, forming an excimer state. In highly polar solvents such as dimethylformamide (DMF), fluctuations in solvent orientation generate an asymmetry that facilitates the rapid transformation of the excimer into a CSS. In a nonpolar solvent like toluene (TOL), radiative transitions to the ground-state are observed as excimer emission (Figure 1.10b).[53] Hariharan and co-workers recently reported the solvent polarity-dependent SB-CS in a helically chiral perylenediimide bichromophore ((R,R)Cy-PDI$_2$). The molecular structure of (R,R)Cy-PDI$_2$ is shown in Figure 1.11a. Significant fluorescence quenching was observed for (R,R)Cy-PDI$_2$ in high polar solvents with fluorescence quantum yields, ϕ_F = 55% in nonpolar TOL and ϕ_F = 10% and 3% in tetrahydrofuran (THF) and acetone (ACE), respectively. Solvent polarity-induced conformational changes were observed in (R,R)Cy-PDI$_2$, where a reversal in the vibronic intensities of the $A_{0\text{-}0}$ and $A_{1\text{-}0}$ bands with excimer emission was observed. With increasing solvent polarity from THF, a moderately polar solvent, to ACE, a highly dipolar medium, (R,R)Cy-PDI$_2$ adopts a conformation that exhibits enhanced H-type electronic coupling. Strong dispersion interactions between the PDI moieties under more polar conditions could drive this structural change. Solvent dielectric-dependent femtosecond transient absorption (fsTA) measurements of (R,R)Cy-PDI$_2$ were performed in TOL, THF and ACE (Figure 1.11b). After photoexcitation at 470 nm, (R,R)Cy-PDI$_2$ in TOL populates the locally excited singlet state, which radiatively decays to the ground-state. Meanwhile, in polar solvents

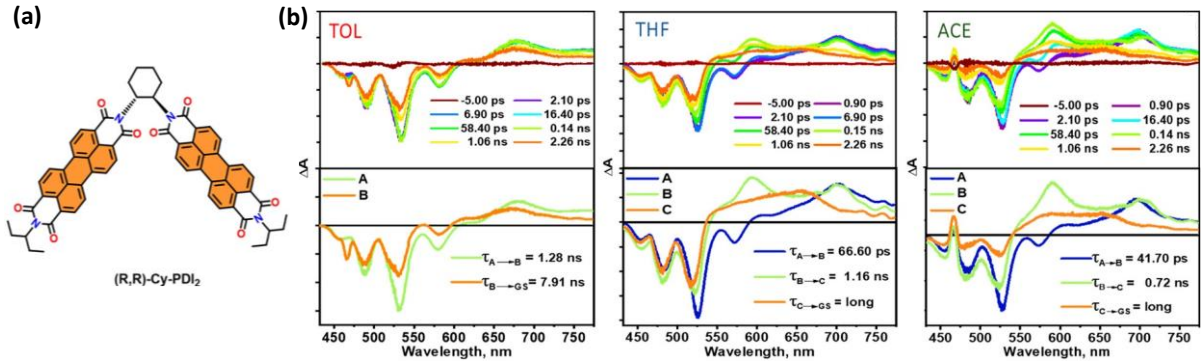

Figure 1.11: a) Molecular structure of (R,R)-Cy-PDI$_2$. b) The fsTA spectra of (R,R)-Cy-PDI$_2$ in TOL, THF, and ACE showing the excited-state dynamics upon photoexcitation at λ_{ex} = 470 nm (Top row). EAS reconstructed from global analysis of the fsTA data of (R,R)-Cy-PDI$_2$ (Bottom row). Reprinted with permission from ref (65). Copyright (2023) American Chemical Society.

like THF and ACE, distinct excited-state absorption (ESA) peaks corresponding to radical cation and radical anion species of (R,R)Cy-PDI_2 were observed (Figure 1.11b). The simultaneous existence of charge-ion species in the fsTA measurements corroborates SB-CS operative in the excited-dynamics of (R,R)Cy-PDI_2, limited by solvent polarity. This work demonstrates the crucial role of the dielectric medium in modulating SB-CS dynamics and the structural conformational changes.[65] In another example by D'Souza and co-workers, the solvent polarity-dependent SB-CS dynamics in a far-red absorbing bisstyryl-BODIPY dimer (2) were investigated. The dimer 2 exhibited significant fluorescence quenching from nonpolar TOL to highly polar DMSO, indicating the possibility of solvent-dependent SB-CS operating in the excited-state dynamics. Ultrafast fsTA measurements in TOL and DMSO probed the excited-state dynamics of dimer 2. The fsTA-derived species-associated spectra (SAS) of 2 in TOL showed the population of hot singlet and a relaxed singlet excited-state, without any indication of SB-CS events. Whereas, the SAS in DMSO exhibited characteristic ESA closely resembling the absorption features deduced for the charge separated species from the spectroelectrochemical studies, confirming SB-CS. The authors concluded that under the influence of polar DMSO, fast charge separation within 5-6 ps was observed in the dimer 2.[66]

1.3.2.2. Excitonic Coupling Mediated SB-CS

It has long been known that excitonic coupling within a chromophore modulates the charge separation dynamics in multichromophoric systems.[10] Weak coupling has been rationalized to accelerate or promote charge separation, while strong coupling often leads to undesired trap states like excimer formation.[67] The BChl dimers in the RCs of purple bacteria, photosystem I and photosystem II, show weak excitonic coupling, favouring the sequential electron transfer events in natural photosynthesis (*vide supra*, Figure 1.9).[68,69] Strong coupling typically leads to delocalized exciton states or excitonic splitting, often preventing charge localization. In weakly coupled systems, excitations are more localized; thus, CT can be more directional. When two identical (or similar) acceptor or donor units are present, the excitation can lead to a situation where a CSS is energetically degenerate in two orientations. The symmetry can then break, with one configuration preferred due to dynamic fluctuations (solvent, phonons,

etc.).[64,70] Therefore, designing multichromophoric systems with weak excitonic coupling is imperative to promote efficient SB-CS.

Previously, the effect of electronic coupling on the SB-CS rates has been explored in various classes of chromophores. Perylene has shown promising results for efficient SB-CS among the rylene family. Vauthey and co-workers have examined a set of bichromophoric systems composed of two identical perylene (Pe) units linked via various crown-ether

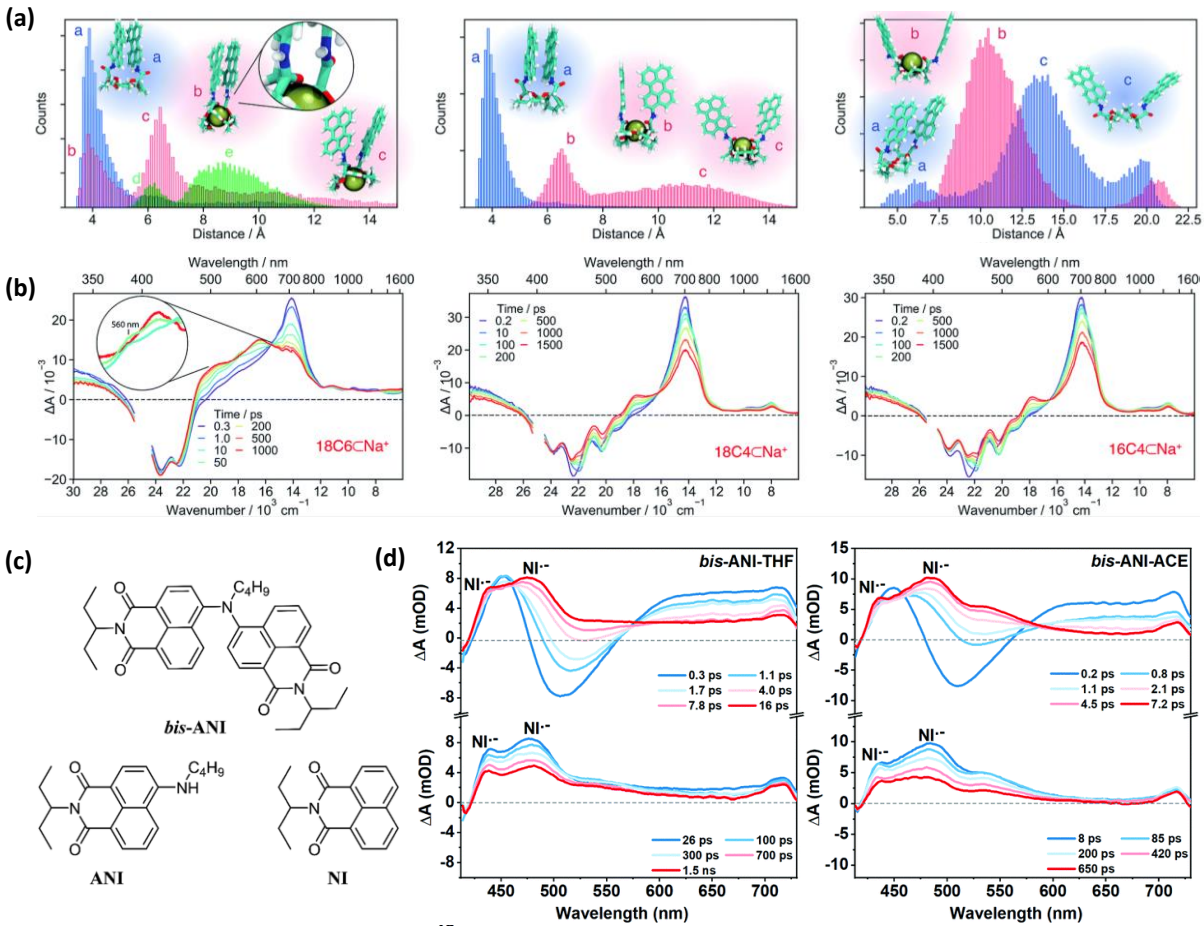

Figure 1.12: a) The molecular dynamics simulations and b) fsTA spectra of the various host-guest complexes with Na^+ ion in DCM (left column: 18C6; middle column: 18C4; right column: 16C4). c) Molecular structures of *bis*-ANI, ANI and NI. d) The fsTA spectra of the *bis*-ANI compound in medium polar THF (left) and in polar ACE (right). Reprinted with permission from: a) and b) ref (71). Copyright (2019) The Royal Society of Chemistry; c) and d) ref (72). Copyright (2022) The Royal Society of Chemistry.

scaffolds, including 18C6, 18C4, and 16C4. They have probed the binding of these bichromophores with cations of various sizes (Ba^{2+} and Na^{2+}), to uncover the cation binding-induced conformational changes modulating the excited-state dynamics. The study demonstrated that these bichromophoric systems enable systematic tuning of electronic coupling across a broad range by simply altering the size and structural characteristics of the macrocyclic linker. Due to the high conformational flexibility inherent in all three crown ethers, the excited-states of these bichromophores eventually relax into intramolecular excimers, which in turn prevent the formation of a CSS. Interestingly, the electronic interactions between the chromophores could be further adjusted through complexation with one or two metal cations. The binding of cations changes the ground-state molecular conformation and weakens the coupling between the chromophores. It also restricts the close approach of the perylene units, effectively suppressing excimer generation. Consequently, the system favours the formation of a symmetry-broken charge separated state upon photoexcitation. In essence, the molecular dynamics (MD) simulations support the idea that cation coordination promotes conformational control (Figure 1.12a), which reduces the electronic coupling and favours SB-CS (Figure 1.12b), helping to rationalize the experimental photophysical results observed in perylene attached 18C6, 18C4 and 16C4 crown-ether chromophores in dichloromethane (DCM).[71]

Ryleneimides, such as monoimides, diimides, and triimides, have a tunable π-conjugated scaffold with well-defined symmetry and electron affinity. These properties make them ideal candidates for studying SB-CS. The rigid planar structure, tunable electronic coupling, and ability to form multichromophoric assemblies offered by these molecules enable the generation of degenerate or near-degenerate CSS crucial for SB-CS, especially in low dielectric environments. Xia, Shinokubo, Kuang, Fukui and co-workers showed SB-CS in a nitrogen-bridged naphthalenemonoimide dimer (*bis*-ANI, Figure 1.12c). Electronic coupling between two identical naphthalenemonoimide moieties greatly influences the charge separation process and is strongly dependent on solvent polarity. The fsTA spectra of *bis*-ANI shown in Figure 1.12d demonstrate the ultrafast formation of the naphthalenemonoimide radical cation ($NI^{\bullet+}$) and radical anion ($NI^{\bullet-}$) species. The authors noted that strong electronic coupling in the ground-state geometry promotes efficient CT. Conversely, in the excited-state,

a near-orthogonal arrangement weakens this coupling, minimizing orbital overlap between the two naphthalenemonoimide units and favouring the formation of a CSS.[72] In another contribution by Koner, De, Datta and co-workers, the authors reported the occurrence of ultrafast SB-CS in ortho-substituted perylenemonoimide (PMI)-acetylene systems (o-PMI-ac), where the chromophores were linked through a phenyl spacer at various substitution sites (*ortho*, *meta*, and *para*). Their investigation also included a self-dimerized PMI and a PMI trimer substituted at the 1,3,5-positions on a phenyl ring, enabling systematic modulation of molecular twist and electronic delocalization. The excitonic interactions within the PMI units in the regioisomers was attributed to the difference in the relaxation mechanism in these multichromophoric PMI systems. The authors stated that the twisted conformation was responsible for the weak electronic coupling essential for efficient SB-CS.[43] Xia and co-workers reported a prolonged SB-CS state (k_{CS}/k_{CR} > 1800 in DMF) in a null-exciton coupled nonconjugated triperyleno[3,3,3]propellane triimides (TPPTI). The long-range Coulombic coupling (J_{Coul}) was calculated to be 1.67 cm^{-1}, meanwhile the short-range CT-mediated coupling (J_{CT}) was estimated to be -0.33 cm^{-1} in TPPTI. As a consequence, the overall electronic coupling according to Eq 1.3 becomes J_{Total} = 1.34 cm^{-1}. Additional computational studies indicated that the null-exciton character of TPPTI displays a preferential hole-transfer coupling, which may promote rapid SB-CS in polar solvent environments.[73] Scientists have also shown interest in investigating SB-CS in higher-analogous rylenediimide molecules like terrylenediimide (TDI). Wasielewski, Young and co-workers have designed a spiro-fused TDI dimer ($sTDI_2$), undergoing intramolecular singlet fission (SF) in nonpolar TOL, whereas, in polar 2-methyltetrahydrofuran, incoherent SB-CS is observed through the stabilization of the CT trap state. The authors stated that the significant contribution of the CT state in the excited-state dynamics of $sTDI_2$ could be due to the excitonic coupling as a result of the spiro bond connectivity. This work serves as an essential milestone to obtain deeper insights into molecular design for tuning SF and SB-CS properties.[74]

Multichromophoric pyrene derivatives have also been investigated in the past for SB-CS. The team led by Vauthey and co-workers synthesized a pyrene (Py) derivative where two Py moieties are linked via an amide bridge to an 18-crown-6 macrocycle. The average distance between the two Py subunits was controlled by binding cations of different sizes (Mg^{2+} and

Ba^{2+}). Py is well-known to form excimer states upon photoexcitation, which was also observed in Py_2, where the shorter Py-Py distance promotes strong electronic coupling leading to excimer formation. The binding studies showed that $Py_2 \subset Ba^{2+}$ exhibits a large distance between the Py moieties, offering negligible electronic coupling where charge separation was not observed. However, cation binding with Mg^{2+} demonstrated intermediate coupling which favoured SB-CS to be operative in the Py_2. This significant work shows how we can fine-tune the electronic coupling in chromophores like pyrene to undergo SB-CS, which intrinsically favours excimer formation.[75] Carefully designed BODIPY-based multichromophores have shown potential to exhibit efficient SB-CS. Han, Donato, Zhao and co-workers have reported a series of BODIPY dimers (BB-1, BB-2, BB-3, BB-4, BB-5, and BB-6) exhibiting SB-CS induced intersystem crossing (ISC). The absence of clear charge separation signatures and the loss of red-shifted emission in polar solvents could be attributed to the strong electronic interaction between the two BODIPY units in the non-orthogonal configurations of BB-5 and BB-6. The near-orthogonal orientation of the BB-1, BB-3, and BB-4 dimers leads to weaker electronic coupling, which in turn favours charge recombination-induced ISC to form the triplet excited-states.[76] Multimers based on diketopyrrolopyrrole core have been previously investigated for SB-CS dynamics. Guldi, Sastre-Santos and co-workers have demonstrated electronic coupling-dependent excited-state dynamics in different dithienylphenylene spacer-connected diketopyrrolopyrrole, *ortho*-DPP (*o*-DPP), *meta*-DPP (*m*-DPP), and *para*-DPP (*p*-DPP). Among the DPP dimers studied, the *o*-DPP dimer demonstrated the highest efficiency for intramolecular SF, achieving a triplet quantum yield (TQY) of 40% in benzonitrile. In contrast, the TQYs for the *meta*- and *para*-substituted analogues (*m*-DPP and *p*-DPP) were significantly lower, estimated at 11% and 0%, respectively, under identical solvent conditions. The superior SF performance of *o*-DPP is attributed to an optimal level of electronic coupling between its two DPP units. The coupling is strong enough to facilitate efficient SF, yet sufficiently weak to allow decoherence of the correlated triplet pair state $^1(T_1T_1)$. The lack of spatial overlap in *p*-DPP, leading to weaker electronic coupling, favoured SB-CS and shuts down intramolecular SF. This work coveys the importance of solvent polarity controlling the CT character in diketopyrrolopyrrole multimers, which is essential in mediating the electronic coupling required for either SB-CS or SF.[77] Thompson, Bradforth, and co-workers developed

two distinct bichromophoric systems based on dipyrrin frameworks: one system (1) comprised two BODIPY units connected via a single bond at their meso-positions, while the other (2) consisted of a pair of dipyrrin ligands coordinated around a Zn^{2+} ion, forming a tetrahedral complex. The molecular arrangements adopted in this work minimizes the exciton coupling between the two dipyrrins by reducing the orbital overlap. According to the authors, the two dipyrrin units adopt orthogonal orientations in both molecular structures; however, the nature of their linkage differs between structures 1 and 2. In structure 1, the dipyrrins are directly bonded via a C–C single bond, resulting in a minimum inter-fragment distance of 1.49 Å. In contrast, in structure 2, the nearest approach between the dipyrrins occurs through an inter-ligand nitrogen-nitrogen (N–N) interaction, with a separation of 3.39 Å. These structural variations significantly influence the extent of electronic coupling, leading to an enhanced CT rate in the meso-linked dimer 1, approximately ten times faster than that observed for the zinc-coordinated dipyrrin complex 2.[60]

1.4. SB-CS in PDI Multichromophoric Architectures in the Isolated Monomeric State

Perylene-3,4,9,10-bis(dicarboximide) (PDI) derivatives are a well-established family of organic chromophores known for their strong absorption in the visible region, large molar extinction coefficients and high fluorescence quantum yields. Due to their excellent electron-accepting properties, high charge transport ability, and remarkable thermal and photochemical stability, PDIs are utilized in various organic electronic applications.[28,78] The optical characteristics and redox behaviour of PDI chromophores can be effectively modulated through appropriate functionalization at the perylene core. In contrast, modifications at the imide position exert only a minor effect on these properties.[79] Importantly, PDIs are capable of forming stable radical cations and anions, with strong transient absorption signatures. The rigid, planar π-conjugated framework of PDIs complements efficient electronic communication between the adjacent PDI units, making them ideal candidates for studying SB-CS in multi chromophoric assemblies.[54,64,80] Due to these salient features, PDI serves as a highly versatile chromophore, enabling the design of a wide variety of covalently linked multichromophoric systems. By introducing diverse linkers or spacers at the bay, ortho or imide positions (Figure

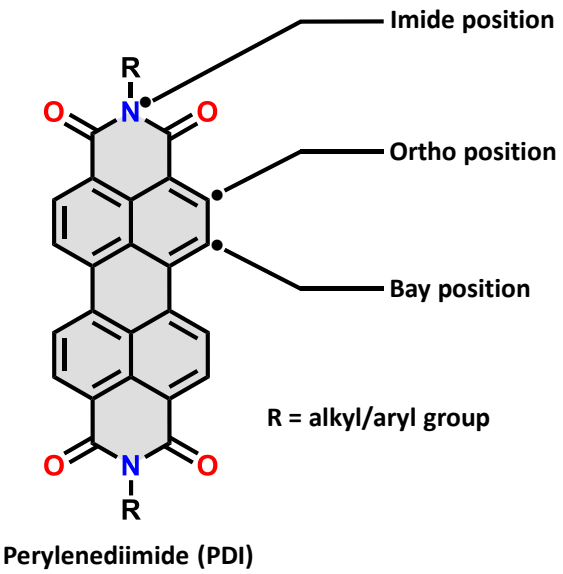

Figure 1.13: Molecular structure of perylenediimide and the different positions where substitutions can be accomplished.

1.13), the interchromophore coupling can be tailored for desired excited-state properties. Over the years, various PDI-based multichromophoric systems have been designed, explicitly focusing on homo-multimers to achieve SB-CS in these systems in the isolated monomeric state in solutions.

1.4.1. Intramolecular Excitonic Interactions Modulating SB-CS in PDI Multimers

• Bichromophoric PDI Architectures

Wasielewski and co-workers reported the first example of SB-CS in a PDI-based multichromophore in cofacial (*cof*-5PDI$_2$) and linear dimers (*lin*-5PDI$_2$) of a green PDI chlorophyll analogue in 2002. The parallel cofacial structural feature of *cof*-5PDI$_2$ is an example of Kasha's H-aggregate model, where the higher energy level has higher oscillator strength due to dipole-dipole coupling of the TDM vectors of the individual PDI units. The absorption spectrum of *cof*-5PDI$_2$ in TOL corroborated the theoretical prediction with the higher energy band maximum at 632 nm having the highest oscillator strength. However, the same exciton model predicts *lin*-5PDI$_2$ to exhibit a dominant transition to the lower energy

exciton state (experimental absorption maxima at 704 nm) due to the end-to-end orientation of the transition dipole moments. Ultrafast transient absorption measurements of *cof*-5PDI$_2$ strongly indicated the occurrence of SB-CS between the PDI units in both TOL and 2-methyltetrahydrofuran. Meanwhile, *lin*-5PDI$_2$ showed the formation of the CSS (PDI$^{\bullet+}$-PDI$^{\bullet-}$) only in polar 2-methyltetrahydrofuran. This work provided an initial platform to understand the effect of excitonic interactions on the SB-CS dynamics in PDI bichromophoric architectures.[78] Subsequently, the explicit effect of electronic coupling modulating the intramolecular electron transfer dynamics in donor-bridge-acceptor PDI multimers with a phenyl group as a bridge was shown for the first time by Adams and co-workers in 2004. The authors have theoretically estimated the electronic coupling matrix element (V) through ab initio quantum chemical models. The electronic coupling value for the homo-dimer without any phenyl bridge showed V = 50.7 cm^{-1}, which was largely consistent with V = 97 cm^{-1} obtained via intramolecular electron transfer dynamics *vs.* the solvent dielectric constant fits. Even though the computed coupling values for the larger dimers are significantly smaller, they suggest that the bridging unit becomes increasingly crucial in facilitating electronic coupling as the multimer size increases, particularly when multiple phenyl rings are involved.[80] Further, Janssen and co-workers rationalized that the fate of the CSS depends on the extent of electronic coupling between the individual monomers. According to the authors, the generation of triplet excited-states through the radical pair intersystem crossing (RP-ISC) pathway necessitates weak electronic interaction between the donor and acceptor units, enabling a spin flip within the CT state. On the other hand, the spin-orbit intersystem crossing (SO-ISC) pathway is accompanied by a concurrent change in spin-orbit momentum. It is promoted when strong electronic coupling between the radical ion pair exists. In their work, the cofacially stacked PDI dimer connected by a xanthene linker exhibits strong coupling due to the close vicinity (~4.5 Å) and parallel arrangement of the PDI fragments, which results in enhanced ISC in the dimer relative to monomeric PDI through the SO-ISC mechanism.[81] In another example, by Würthner, Wasielewski and co-workers reported intramolecular SB-CS mediated triplet population in a PDI cyclophane molecule (Cy-PBI) with low electronic coupling matrix element V = 15 cm^{-1} and high reorganization energy λ = 0.75 eV. The authors stated that Cy-PBI's charge separation process is endergonic in a nonpolar solvent like TOL, yielding a high

fluorescence quantum yield for Cy-PBI. Encapsulation of electron-rich guest species inside the Cy-PBI host framework significantly alters the excited-state deactivation route, resulting in ultrafast intermolecular charge separation occurring within a few picoseconds. This process gives rise to the guest's radical cation and the radical anion of the PDI unit.[82] In their quest to

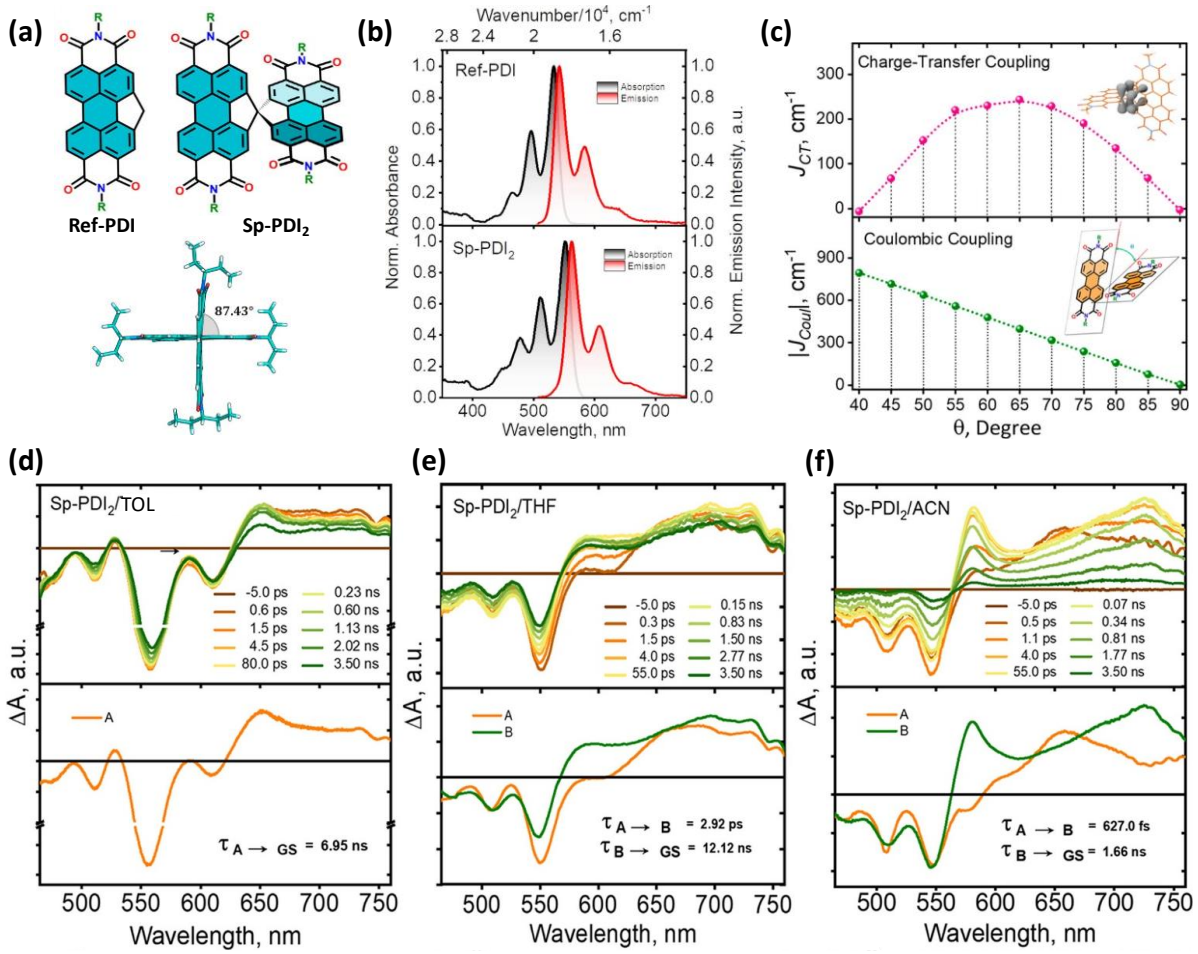

Figure 1.14: a) Molecular structures of the Ref-PDI and Sp-PDI$_2$, where "R" represents the 3-pentyl group. The X-ray crystal structure shows near-orthogonal arrangement of the two PDI units in Sp-PDI$_2$. b) Absorption and emission spectra of Ref-PDI and Sp-PDI$_2$ in TOL. c) Dependence of the absolute values of $|J_{Coul}|$ and $|J_{CT}|$ on the rotational angle (θ) separating the PDI monomer units. (Top) fsTA) spectra of Sp-PDI$_2$ recorded in d) TOL, e) THF, and f) ACN, illustrating the excited-state processes following photoexcitation at 440 nm. (Bottom) SAS derived through target analysis of the fsTA measurements for Sp-PDI$_2$. Reprinted with permission from ref (70). Copyright (2021) American Chemical Society.

understand the extent of electronic coupling modulating the rate of SB-CS in organic multichromophoric architectures, researchers have pushed their limits to design novel systems with desired electronic properties to obtain faster charge separation dynamics. Hariharan and co-workers have recently reported the photophysics of a null-exciton coupled spiro PDI dimer, Sp-PDI_2 (Figure 1.14a). The X-ray crystal structure shows a near-orthogonal arrangement of the two PDI units in Sp-PDI_2 with a dihedral angle of 87.43°. The UV-vis absorption and emission spectra of Ref-PDI and Sp-PDI_2 in TOL (Figure 1.14b) indicated the null-type electronic coupling with similar absorption and emission profiles. The theoretically estimated dependence of the absolute values of $|J_{Coul}|$ and $|J_{CT}|$ on the rotational angle (θ) separating the PDI monomer units, confirms the negligible $|J_{Coul}|$ and $|J_{CT}|$ at the perpendicular orientation (Figure 1.14c). The dielectric-dependent fsTA measurements confirmed ultrafast SB-CS in moderately polar THF (τ_{CS} = 2.92 ps) and highly polar ACN (τ_{CS} = 627 fs) with distinct $PDI^{\bullet+}$ and $PDI^{\bullet-}$ ESA peaks (Figure 1.14d-f). The Sp-PDI_2 dimer shows negligible long-range Coulombic coupling due to the PDI units' perpendicular orientation via spiro linkage. The destructive interference between the π-orbitals leads to a negligible short-range CT coupling. The total null coupling localizes the initially formed exciton in one of the PDI units, facilitating faster charge separation.[70]

- **Trichromophoric PDI Architectures**

Xia, Wu and co-workers realized SB-CS in a nonpolar solvent by modulating the interchromophore coupling in PDI trimers connected via phenyl bridges in the bay position. The mixing between the S_1 and CT states was improved by the effect of "bridge resonance" through the phenyl bridge, resulting in the clear detection of the CT absorption band in the UV-vis spectra of both the PDI dimers, along with negative free energies of charge separation (ΔG_{CS}) in $CHCl_3$ and TOL.[83] Wasielewski, Stoddart, Würthner and co-workers have reported a rigid PDI triangle connected by a cyclohexane bridge, where the rigid architecture reduces the electronic coupling between the PDI subunits, thereby kinetically favouring ultrafast SB-CS over intramolecular excimer formation. The fsTA measurements of the PDI triangle molecule in DCM show ultrafast charge separation to form the CSS ($PDI^{+\bullet}$–$PDI^{-\bullet}$) within τ_{CS} = 12.0 ± 0.2 ps. Moreover, the authors demonstrated that complete electron delocalization

occurs across the three PDI fragments arranged in a triangular configuration, indicating rapid electron transfer between neighbouring redox centers.[64] A significant contribution regarding the effect of null-aggregates accelerating SB-CS was shown by Wasielewski and co-workers. A slip-stacked PDI dimer (compound 2) and a trimer (compound 3), exhibiting null-type excitonic characteristics, were synthesized to investigate how vibronic coupling influences

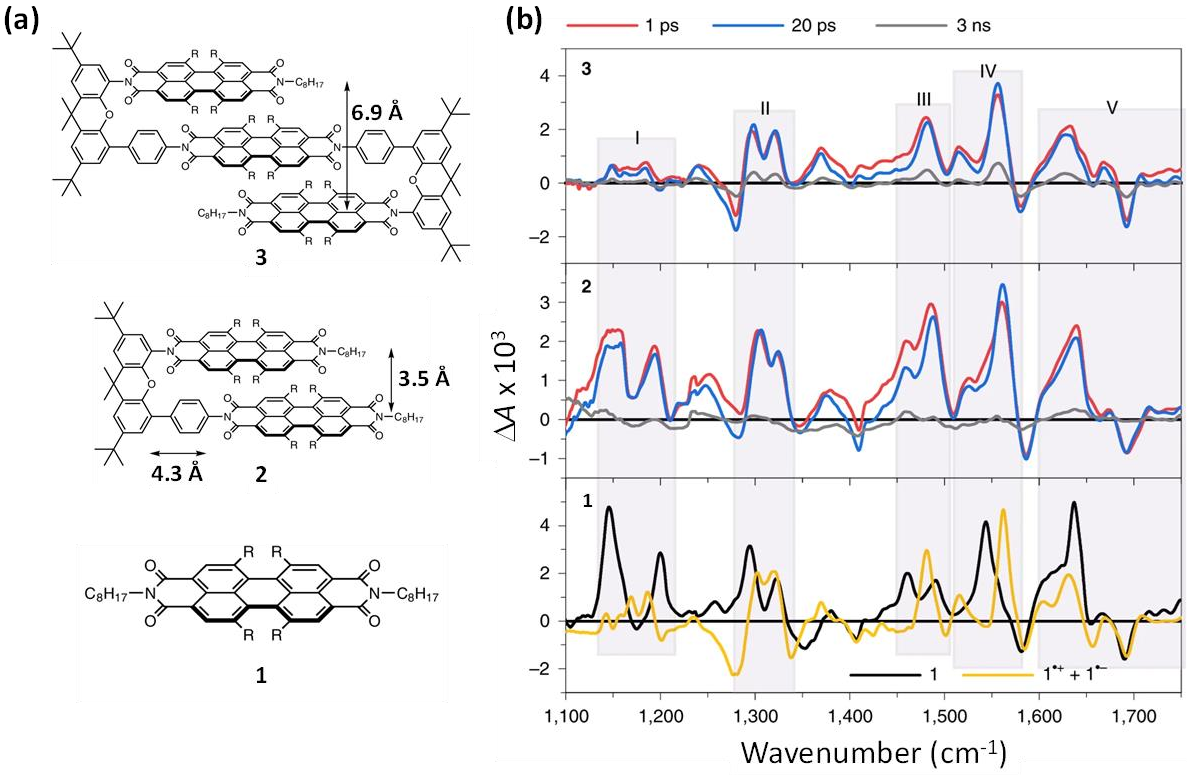

Figure 1.15: a) Chemical structures of the monomer (1), dimer (2), and trimer (3) are shown, where R denotes a 4′-tert-butylphenoxy substituent and the rotation angle between adjacent chromophores is approximately 15°. b) The fsIR spectra of compound 1 at 10 ps, alongside those of its charged counterparts (bottom), as well as spectra for compounds 2 (middle) and 3 (top) at three distinct time delays recorded in DCM. The IR-active vibrational modes in the excited-state clearly capture the characteristics of the mixed state in 2 and the SB-CS state in 3, owing to their heightened sensitivity to electron density variations across chromophores. In contrast, electronic transitions often yield broad and overlapping features, making them less suitable for such differentiation. Reprinted with permission from ref (67). Copyright (2022) Springer Nature.

coherent SB-CS (Figure 1.15a). Ultrafast methods, including fsTA and time-resolved infrared along with vibrational coherence (VC) spectroscopies, were employed to unravel the fast formation of a mixed excited-state between neighbouring PDI units in dimer 2. This process, driven by vibronic coupling along high-frequency vibrational modes, occurs within 200 fs. In contrast, for PDI trimer 3, incoherent SB-CS unfolds through electron or hole transfer from the initially formed coherent FE/CT mixed state to a more distant PDI unit, occurring over a timescale of 2-3 ps. The authors explained that in PDI trimer 3, the incoherent SB-CS is expedited by low-frequency vibrational motions between the chromophores, which act to disrupt the initially formed mixed excited-state. The intermediate mixed electronic state accelerates SB-CS and is responsible for ultrafast SB-CS in trimer 3 which is three orders of magnitude than in dimer 2. Femtosecond infrared (fsIR) absorption measurements were carried out to probe the characteristic peaks from the FE and PDI radical ion pair (Figure 1.15b). The instrument response of the fsIR instrument (~500 fs) limited the observation of FE state evolution to the mixed FE/CT state in 2 and 3. Analyses across five distinct spectral windows confirmed that compound 2 exhibits a hybrid FE/CT character, while compound 3 promptly evolves into a completely dissociated CSS. Region I (1,135-1,212 cm^{-1}) includes the contributions from both FE and radical ion states, compound 2 exhibits broad and intense signals spanning the entire range, while the spectra of compound 3 closely resemble those of a pure CSS. Region III (1,442-1,500 cm^{-1}) features the characteristic peaks of the FE state at 1,459 cm^{-1} and charged species at 1,482 cm^{-1}, compound 2 shows signals corresponding to both, whereas compound 3 presents a relatively flat absorption profile with a weak signal in the FE region that decays quickly (Figure 1.15b). This work showcases the powerful utility of fsIR technique to probe the ultrafast charge separation dynamics in multichromophoric systems.[67]

- **Tetrachromophoric PDI Architectures**

In pursuing more efficient light-harvesting systems, researchers have progressively advanced from studying molecular dimers and trimers to exploring molecular tetramers for desired charge separation dynamics. In an exemplary work, Ma, Song, Yang and co-workers designed two PDI-based tetramers with a fused (COTh-FPDI) and non-fused (COTh-*α*PDI)

saddle-shaped cyclooctatetrathiophene bridge; to compare the strength of interchromophore electronic coupling favouring SF and/or SB-CS. The flexible linking in COTh-αPDI greatly relaxes the inter-PDI geometry due to steric effect, leading to weak inter-PDI electronic coupling and electronic relaxation dominated by ultrafast SB-CS (τ_{CS} ~100 fs). Contrastingly, in the case of COTh-FPDI with fused linker, inter-PDI geometry was determined by the topological characteristics of the COTh core, leading to strong inter-PDI electronic coupling and CT-mediated inter-PDI SF (τ_{SF} ~150 ps, TQY ~150%). This work demonstrates a novel strategy to enable SF/SB-CS in molecular multimers by tuning the interchromophore electronic coupling by attaching fused rigid or flexible covalent linkers.[84] Xia, Tang, Wan and co-workers explored the dependency of electronic coupling on the SB-CS rates in a V-type twisted PDI dimer (PM-PDI$_2$) and a PDI tetramer derivative possessing a tetrahedral 3D architecture with four PDI units (PM-PDI$_4$). The authors attributed the variation in SB-CS rates observed in DMF, where k_{CS} (PM-PDI$_4$)/k_{CS} (PM-PDI$_2$) = 5.4, to differences in the excited-state geometries of the two molecules, which in turn influence the strength of electronic coupling. Using the generalized Mulliken-Hush approach, the electronic coupling values were determined to be 118.56 cm^{-1} for PM-PDI$_4$ and 43.55 cm^{-1} for PM-PDI$_2$. These calculated coupling magnitudes indicate a more efficient charge separation process in PM-PDI$_4$ than PM-PDI$_2$, aligning well with the charge separation rate constants derived from the fsTA measurements.[85]

1.5. SB-CS in PDI Constructs in the Solid-State

Achieving SB-CS in the solid-state is highly desirable for improving the performance of the organic optoelectronic devices by enabling efficient charge generation without traditional donor-acceptor interfaces. The solvent polarity and molecular reorganization can readily facilitate excited-state symmetry-breaking and stabilize the CSS, leading to efficient SB-CS in solution-state. Unlike in solution, the solid-state poses a significantly more constrained and complex environment. Along this line, achieving SB-CS in the solid-state is quite challenging due to the absence of solvent-induced dielectric stabilization, reduced conformational flexibility, and the strong influence of intermolecular packing and crystalline order. Factors like these can hinder the energetic degeneracy and local asymmetry required to drive the charge localization process in symmetric chromophores. PDI derivatives are well-known for

demonstrating diverse SB-CS pathways in solution through strategic substitution at the bay and imide positions, allowing the tuning of their electronic coupling and the excited-state energy landscape.[10,37] Nevertheless, the translation of such dynamics into the solid-state domain remains underexplored. Achieving a precise balance between the electronic coupling, molecular packing, and dielectric microenvironment in the bulk, favouring SB-CS, is non-trivial. Excessively strong π–π stacking may lead to undesired excimer trap state formation, while too weak an interaction may prevent any electronic communication altogether. Further, the absence of controlled asymmetry in the solid-state molecular environment can limit the thermodynamic driving force for SB-CS. These challenges highlight the need for in-depth exploration into solid-state molecular organization, aggregate formation type (H- *vs.* J-aggregates), and interface engineering to replicate or even enhance the SB-CS mechanisms observed in the solution-state.[38,67]

1.5.1. Intermolecular Excitonic Interactions Modulating SB-CS in PDI Chromophores in the Solid-State

Wasielewski and co-workers demonstrated the first example of solid-state SB-CS in PDI chromophores in 2020. The study focused on probing the excited-state behaviour of polycrystalline thin films composed of 1,6,7,12-tetra(phenoxy)perylene-3,4:9,10-bis(dicarboximide), where the imide nitrogen positions were functionalized with either n-octyl chains (octyl-tpPDI) or hydrogen atoms (H-tpPDI). Detailed X-ray structural analysis revealed π-π stacking in both octyl-tpPDI and H-tpPDI thin films. H-tpPDI exhibited a higher degree of slip-stacked packing arrangement and intermolecular hydrogen bonding to its adjacent molecules than octyl-tpPDI. FsTA measurements were carried out in solid-state films to investigate the excited-state dynamics of octyl-tpPDI and H-tpPDI thin films. Octyl-tpPDI exhibited an excimer-like state, which prevents complete charge separation. Unlike octyl-tpPDI, H-tpPDI displays a rapid emergence of the anionic signal at 785 nm, indicating that ultrafast charge separation occurs for a subset of molecules within the ~300 fs timeframe defined by the instrument's response. The authors suggest that although these thin films exist in a relatively nonpolar solid-state setting, PDIs are known to exhibit significant quadrupole moments that become more pronounced with shorter alkyl substituents at the imide positions.

This “alkyl chain effect” is attributed to variations in molecular packing in the solid-state. In such environments, PDI units may effectively act as solvents for one another; thus, octyl-tpPDI likely resides in a less polar microenvironment than its hydrogen-substituted counterpart. This difference potentially explains the much more rapid SB-CS observed in H-tpPDI. The capacity of PDI units to self-solvate stabilizes the CT state and promotes faster SB-CS. The authors concluded that the favourable through-space short-range π-π interactions in H-tpPDI film enable ultrafast SB-CS. In contrast, the strong dipolar coupling in octyl-tpPDI film leads to an excimer-like state with CT character.[86] Subsequently, in 2022, Zhang and co-workers reported intermolecular SB-CS in a PDI derivative in the aggregated state in a binary DMF/water solvent mixture. The authors stated that the hydrophobic effect induced by water forces the PDI molecules to stack in a columnar fashion in the aggregate structure. The columnar aggregation helped achieve the appropriate excitonic coupling between the PDI monomers needed for facile charge separation in the solid-state.[87] Further, Wasielewski, Young and co-workers demonstrated the effect of hydrogen bonding on intermolecular SB-CS in tetra(phenoxy)perylenediimide (tpPDI) single crystals. The authors have investigated the photoinduced excited-state dynamics of single crystals of *N*,*N*-di(*n*-propyl)-tpPDI (C_3-tpPDI), *N*-(*n*-propyl)-tpPDI (C_3H-tpPDI), and H-tpPDI using transient absorption microscopy (TAM) and time-resolved fluorescence microscopy (TRFM). The presence of CT features from the TAM data and the emission observed by TRFM with the same lifetimes strongly suggests that exciting the crystals populates a mixed electronic state comprised of the singlet exciton and CT state. However, the relative contributions of the singlet and CT character varied. This variation is attributed to the structural differences among the crystals, due to the varied hydrogen-bonding sites in the three molecular systems, thereby modulating the intermolecular interactions between the individual chromophores within the single crystals. The excited-state was assigned to a mixed state rather than an excimer-like state as the absorption and emission spectra of the crystals maintained their vibronic structure and the emission lifetimes did not exhibit the longer lifetimes (>5 ns), characteristic of PDI excimers. This work elucidated the role of H-bonding sites in facilitating intermolecular SB-CS in organic single crystals.[88] In a separate study, Koner, Wasielewski, Young, and co-workers demonstrated the occurrence of intermolecular SB-CS in both aggregated solutions and solid-state thin films of two

multichromophoric PMI compounds, $Bz(PMI)_3$ and $Bz(PMI)_4$. In these structures, the PMI units were modified by introducing a benzene moiety through an acetylene linkage. The fsTA and nanosecond transient absorption (nsTA) measurements were performed in solution-state (monomer) in DCM as well as aggregated state in ACN and solid-state thin films. The fsTA measurements corroborated the SB-CS process in aggregated and thin-film states of $Bz(PMI)_3$ and $Bz(PMI)_4$. In contrast, charge separation was not observed in monomeric solutions in DCM. The distinct excited-state behaviour was attributed to the excitonic interactions between the intermolecular PMIs associated with π-π stacking within the aggregates and the solid films.[89] Very recently, Wang, Wang, Xu, Fan and co-workers showed that the SB-CS rate constants can be significantly improved in ultrasmall organic nanocrystals (NCs). Symmetric PDI dimers were freeze assembled into ultrasmall (sub-5 nm) NCs with ordered molecular stacking. Two aza-annulated PDI multichromophoric systems connected either via *para* (*p*-BDNP) or *meta* (*m*-BDNP) positions in a phenyl bridge were synthesized and ultrasmall NCs were achieved from them (*p*-5 nm and *m*-5 nm). In the monomeric molecular state, *p*-BDNP exhibited faster intramolecular charge separation than *m*-BDNP due to a more delocalized CSS. Whereas, fsTA spectroscopy corroborated charge separation to be accelerated in ultrasmall NCs, about 20 times going from *p*-BDNP to *p*-5 nm and about 254 times going from *m*-BDNP to *m*-5 nm. The authors concluded that the para-substitution bridge of *p*-BDNP promotes the coplanarity between the two PDI units, enhancing the intermolecular π–π interactions. This facilitates electron transfer from one PDI unit to the adjacent PDI unit, leading to a more delocalized CSS. The ultrasmall *p*-5 nm NC showed ultrafast SB-CS due to the strengthened in-plane lamellar stacking of *p*-BDNP providing a facile electron transport channel along the direction of the π–π stacking. However, the twisted packing of the PDI unit in *m*-BDNP limited the electron transport due to the lack of continuous charge transport channels in *m*-5 nm NC.[90]

1.6. Aim and Objectives of the Thesis

A thorough understanding of the effect of excitonic interactions modulating the SB-CS dynamics as a function of the relative intramolecular and intermolecular spatial orientation of the distinct chromophoric assembly is fundamental to the development of high-performance optoelectronic systems. This thesis aims to achieve various angular and linear chromophoric arrangements and probe the concomitant SB-CS dynamics in different dielectric environments at both isolated monomeric and solid-state levels, modulated by through-bond and through-space excitonic interactions (Figure 1.16). Chapter 2 explores the orientation-controlled acceleration of SB-CS in a synthetically designed angular (**A-PDI$_2$**) versus linear (**L-PDI$_2$**) PDI dimer. The current work suggests that the Coulombic coupling strength in **A-PDI$_2$** ($|J_{Coul}|$ = 14.9 cm^{-1}) and **L-PDI$_2$** ($|J_{Coul}|$ = 438.4 cm^{-1}) is the crucial factor modulating the SB-CS rates in the PDI dimers. The 3rd chapter demonstrates the SB-CS mediated triplet excited-state population in a weakly coupled PDI trimer (**PDI-T**) at the single-molecule level. This work shows the fluctuations in fluorescence of **PDI-T** in a nonpolar polystyrene matrix (ε = 2.60) with prolonged fluorescence and infrequent dark states, representing the triplet and/or the charge transfer states. In contrast, in a poly(vinyl alcohol) matrix (ε = 7.80), erratic blinking dynamics resulting in low photon counts were observed, corroborating the feasibility of charge

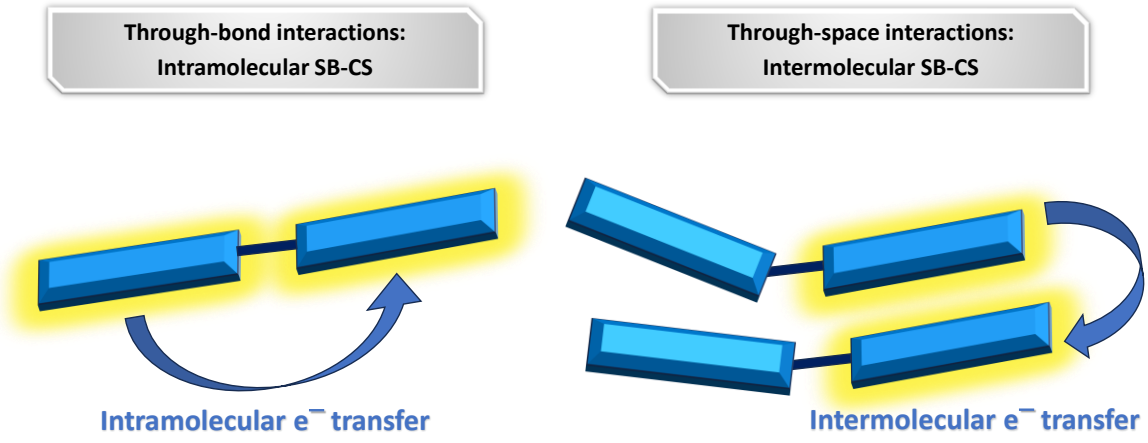

Figure 1.16: Schematic diagram showing the through-bond and through-space excitonic interactions promoting intramolecular and intermolecular SB-CS, respectively, in multichromophoric molecular architectures.

separation in a polar environment. Chapter 4 showcases the ultrafast SB-CS in thin films of J-aggregated PDI multimers (**PDI_2** and **PDI_3**) in a nonpolar polymer matrix. Electronic coupling calculations revealed the role of through-space electronic communication and strong π–π interactions promoting ultrafast charge separation in **PDI_2** and **PDI_3** aggregates.

Chapter 2

Accelerating Symmetry-Breaking Charge Separation in an Angular versus Linear Perylenediimide Dimer through the Modulation of Coulombic Coupling

Abstract

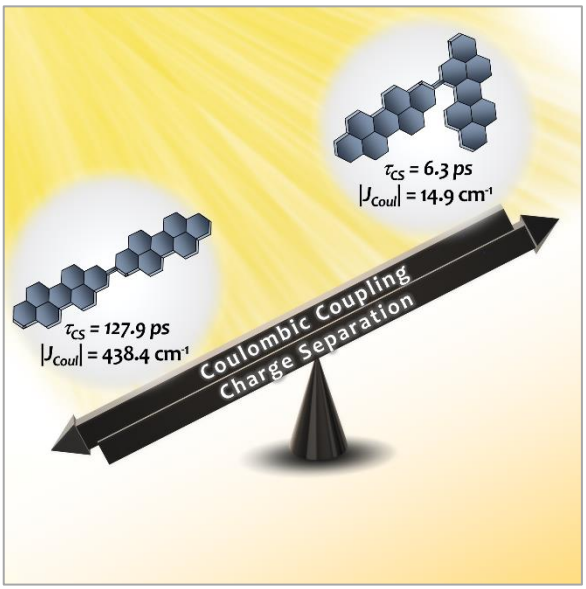

Achieving faster charge separation in organic systems capable of mimicking the electron transfer events in natural photosynthesis has been an exhilarating research topic for several decades. Herein, we demonstrate the orientation-dependent acceleration of symmetry-breaking charge separation (SB-CS) in an angular (**A-PDI$_2$**) versus linear (**L-PDI$_2$**) perylenediimide dimer. Femtosecond transient absorption measurements reveal ultrafast SB-CS in **A-PDI$_2$** (τ_{CS} = 6.3 ps) with charge separation ~20 times faster than in **L-PDI$_2$** (τ_{CS} = 127.9 ps). Nanosecond transient absorption measurements establish the negligible population of triplet excited-states in **L-PDI$_2$** (ϕ_T < 1%), whereas a significant triplet excited-state population (ϕ_T = 35.9%) is quantified in **A-PDI$_2$**. The theoretically computed Coulombic coupling strength in **A-PDI$_2$** ($|J_{Coul}|$ = 14.9 cm^{-1}) and **L-PDI$_2$** ($|J_{Coul}|$ = 438.4 cm^{-1}) is rationalized as the crucial factor modulating the SB-CS rates. The current investigation could be beneficial for designing light harvesting materials capable of faster charge separation for efficient optoelectronic devices.

2.1. Introduction

Multichromophoric systems are of potential interest for charge separation (CS) and light harvesting in artificial photosynthesis and related optoelectronic applications.[91] Designing multichromophoric systems with efficient architectures similar to natural photosynthetic systems could achieve near unity efficiency in energy transfer and charge transfer (CT) processes.[92] The last few decades have seen the rise of perylenediimide (PDI) and its derivatives as a superior chromophore for charge transport,[78,93,94] electron acceptors in organic photovoltaic devices (OPVs)[95–98] and applications in singlet fission.[99] Among the different excited-state processes in PDI multimers, understanding the symmetry-breaking charge separation (SB-CS) pathway is particularly interesting owing to its relevance in OPVs.[60,100,101] SB-CS materials are particularly well-suited for use in OPVs due to their ability to generate CSS with minimal energy loss, typically under 100 mV, unlike conventional donor-acceptor systems, which often incur losses of 500 mV or more during charge separation.[10,40,60]

SB-CS is an excited-state phenomenon where a pair of identical chromophores absorb a photon to form a CSS with the hole and electron on adjacent chromophores.[10,38,67,102] SB-CS finds varied applications in synthetic light harvesting systems as well as emerging optoelectronic devices.[41,60,100,101] The SB-CS rate is highly dependent on the electronic coupling and the surrounding dielectric microenvironment.[10,42–45,103] Through extensive efforts, scientists have figured out the acceleration of SB-CS in polar dielectrics due to the lowering of the CSS energy beyond the locally excited singlet state.[10,53,64] Wasielewski and co-workers showed acceleration of SB-CS in a PDI trimer through vibronic coupling in the coherent dimer intermediate.[67] Xia and co-workers demonstrated the faster CS in a *para*-phenylene bridged N-annulated PDI dimer compared to the *meta*-connected dimer due to inherent destructive overlap between the wave function via the meta-substituted linker.[104] The effect of excitonic coupling moderating the SB-CS dynamics has been previously demonstrated in pyrene and perylene multichromophoric systems by Vauthey and co-workers.[71,75] Optimum electronic coupling was identified as the critical factor responsible for faster and more efficient CS, whereas strong coupling led to undesirable decay pathways, such as excimer formation, hindering the CS

process.[75] However, the precise understanding of the effect of different dimeric orientations on the SB-CS dynamics has received less attention.

Our previous research on the diverse CS dynamics associated with different PDI dimers including flexible as well as rigid structures, urged us to explore the influence of different chromophore orientations modulating the SB-CS rate.[70,105] Herein, we show the acceleration of SB-CS in an angular (**A-PDI$_2$**) *vs*. linear (**L-PDI$_2$**) PDI dimer, through the modulation of chromophore orientation. Femtosecond transient absorption measurements characterize the symmetry-breaking charge separation (SB-CS) process in **A-PDI$_2$** and **L-PDI$_2$**. Coulombic

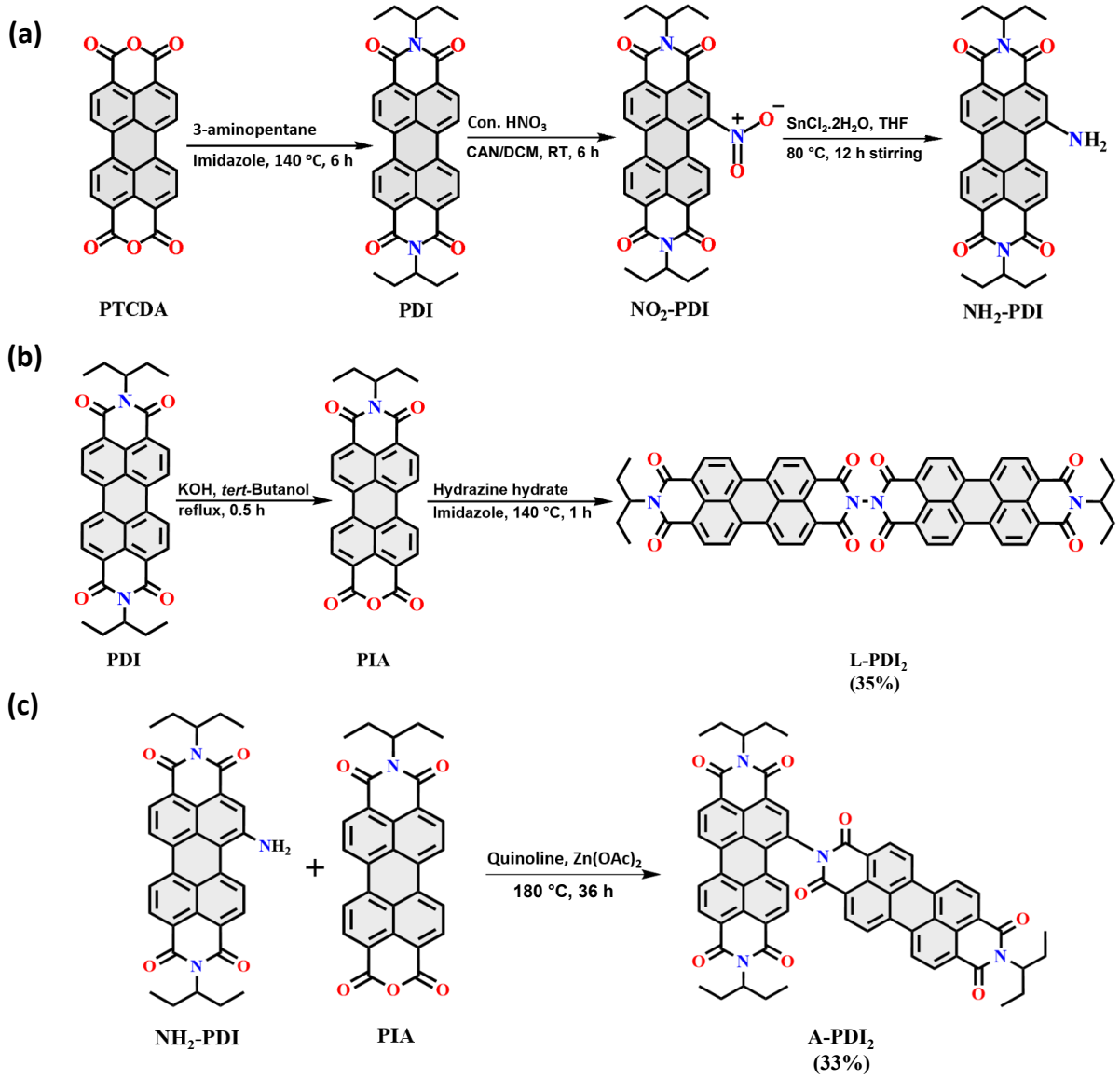

Scheme 2.1: Synthesis scheme of a) PDI, NO_2-PDI and NH_2-PDI; b) **L-PDI$_2$** and c) **A-PDI$_2$**.

coupling interactions and charge localization/delocalization properties are theoretically estimated to understand the role of chromophore orientation modulating the excited-state dynamics in **A-PDI$_2$** and **L-PDI$_2$**.

2.2. Results and Discussion

2.2.1. Dimer Molecules and the Optimized Structures

L-PDI$_2$ and **A-PDI$_2$** (Figure 2.1a and 2.1b) were prepared and characterized according to the previously reported and modified methods (Scheme 2.1 and Figures A2.1-A2.8).[106,107] The ground-state structures were optimized in the gas phase using density functional theory (DFT) at the B3LYP-D3/6-311+G(d,p) level, carried out with the Gaussian 16 software package. The ground-state optimized geometry of **L-PDI$_2$** shows the end-to-end linear arrangement of the two PDI fragments with the molecular planes arranged perpendicular to each other (Figure 2.1c). **L-PDI$_2$** exhibited a planar π-core with a dihedral angle (θ) of 89.9° between the two PDI fragments. On the other hand, **A-PDI$_2$** exhibits angular orientation of the two PDI fragments with a dihedral angle of 68.8° (Figure 2.1d). The bay-substituted PDI fragment in **A-PDI$_2$**

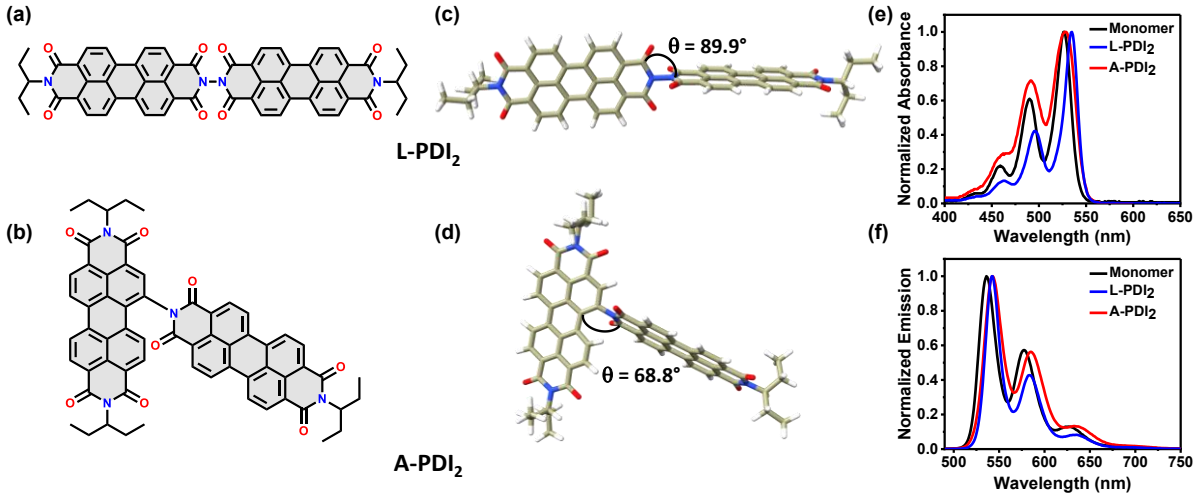

Figure 2.1: Molecular structures of a) **L-PDI$_2$** and b) **A-PDI$_2$**. Ground-state optimized structures of c) **L-PDI$_2$** and d) **A-PDI$_2$** obtained at the B3LYP-D3/6-311+G(d,p) level of theory. e) Normalized UV-vis absorption spectra of PDI monomer, **L-PDI$_2$** and **A-PDI$_2$** in TOL. f) Normalized emission spectra (λ_{ex} = 480 nm) of PDI monomer, **L-PDI$_2$** and **A-PDI$_2$** in TOL.

shows a π-core twisting of 20.3° due to the steric hindrance from the other PDI monomer fragment. The centroid-centroid distances ($d_{PDI\text{-}PDI}$) in the ground-state optimized structures of **L-PDI$_2$** and **A-PDI$_2$** were found to be 12.7 Å and 9.0 Å, respectively (Figure A2.9 and Table A2.1).

2.2.2. Steady-State Photophysical Properties of the Dimers

The steady-state optical properties of **L-PDI$_2$** and **A-PDI$_2$** were investigated and compared to the reference PDI monomer (Scheme 2.1).[108] UV-vis electronic absorption and fluorescence spectroscopic measurements for the samples were performed in TOL ($C_0 \approx 0.5$ μM). The UV-vis absorption spectrum of **L-PDI$_2$** in TOL exhibits a ~9 nm bathochromic shift in comparison to the PDI monomer with the absorption maximum at $\lambda_{max}^{Abs} \approx 535$ nm (Figure 2.1e and Table A2.2). The intensity ratio between the 0-0 and 0-1 vibronic transitions, expressed as $A_{0\text{–}0}/A_{0\text{–}1}$, was determined for **L-PDI$_2$** and monomer to understand the excitonic coupling prevalent in **L-PDI$_2$**. Higher value of $A_{0\text{-}0}/A_{0\text{-}1}$ in **L-PDI$_2$** (2.37) with respect to PDI monomer (1.64), indicates strong J-type excitonic coupling between the PDI units in **L-PDI$_2$**, with high oscillator strength for the 0-0 vibronic band compared to the 0-1 band in the experimental absorption spectrum (Figure 1e).[32,106,109,110] Contrastingly, the UV-vis absorption spectrum of **A-PDI$_2$** in TOL (Figure 2.1e) shows a ~3 nm bathochromic shift ($\lambda_{max}^{Abs} \approx 529$ nm) and the slightly lower value of $A_{0\text{-}0}/A_{0\text{-}1}$ ratio in **A-PDI$_2$** (1.40) compared to the PDI monomer indicates weak H-type excitonic coupling in **A-PDI$_2$**.[32] The emission spectra of the PDI dimers ($\lambda_{ex} = 480$ nm, $C_0 \approx 0.5$ μM), **L-PDI$_2$** and **A-PDI$_2$**, exhibit a ~6-7 nm bathochromic shift compared to the PDI monomer emission spectrum, presumably due to the extended π-conjugation between the PDI units in the dimer moieties (Figure 2.1f).[111] **L-PDI$_2$** and **A-PDI$_2$** emission spectra reveal well-resolved vibronic features with the emission maxima at $\lambda_{max}^{Emi} \approx 542$ nm and 543 nm, respectively (Figure 2.1f).

2.2.3. Solvent-Dependent Optical Properties of the Dimers

Solvent-dependent UV-vis absorption and emission measurements were recorded to probe the effect of the local dielectric environment on the photophysical properties of **L-PDI$_2$** and **A-**

PDI₂ (Figure A2.10). Nonpolar TOL (ε = 2.38) and polar ACE (ε = 20.70) with varied dielectric constants were used for the measurements. The solvent-dependent UV-vis absorption spectra of **L-PDI₂** (Figure S10a) and **A-PDI₂** (Figure A2.10b) exhibit nearly unperturbed absorption features. Unlike absorption, the solvent-dependent emission properties of **L-PDI₂** and **A-PDI₂** showed contrasting characteristics. The solvent-dependent emission spectra of **L-PDI₂** in nonpolar TOL (Figure A2.10c) displayed enhanced emission intensity with high fluorescence quantum yield (ϕ_{FL}) of 95.4%. Similar ϕ_{FL} values have been previously reported for analogous PDI linear dimers by Langhals and co-worker.[106] Significant fluorescence quenching was observed for **L-PDI₂** while shifting from TOL to ACE (Figure A2.10c and A2.10e), and ϕ_{FL} was estimated to be 6.1% in ACE. Intriguingly, **A-PDI₂** exhibited enhanced emission quenching in all the solvents under investigation compared to **L-PDI₂**, with ϕ_{FL} of 63.0% in TOL and 1.0% in ACE (Figure A2.10d, A2.10f and Table A2.2). The lower ϕ_{FL} values of **L-PDI₂** and **A-PDI₂** in polar solvents compared to the PDI monomer ($\phi_{FL} \approx 98\%$)[108] indicates the presence of diverse non-radiative decay channels involved in the excited-state dynamics of the PDI dimers. Concentration-dependent UV-vis absorption measurements were carried out for **L-PDI₂** and **A-PDI₂** in TOL and ACE. Both the dimers follow Beer-Lambert's law, exhibiting the monomer nature even at concentrations as high as 10 μM in TOL (Figures A2.11 and A2.12). In ACE, **A-PDI₂** maintained a monomer nature till a concentration of 10 μM (Figure A2.13), while **L-PDI₂** showed aggregation behaviour above ~2 μM due to lesser solubility in polar ACE (Figure A2.14). Therefore, steady-state photophysical and transient absorption measurements for the dimers were carried out at ~0.5 μM and ~1.5 μM concentrations, respectively.

2.2.4. Femtosecond Transient Absorption Measurements of L-PDI₂

To obtain deeper insights into the non-radiative decay pathways of **L-PDI₂** and **A-PDI₂** responsible for the low fluorescence in polar dielectrics, we performed solvent dielectric-dependent femtosecond transient absorption (fsTA) measurements of **L-PDI₂** and **A-PDI₂** in nonpolar TOL (ε = 2.38) and polar ACE (ε = 20.70) solvents. After photoexciting **L-PDI₂** (C_0 ≈ 1.5 μM) at 495 nm in TOL, the fsTA spectra depict negative GSB at ~520 to 560 nm, SE at ~562 to 602 nm and ESA with positive features centered at ~670 nm (Figure 2.2a). The ~670

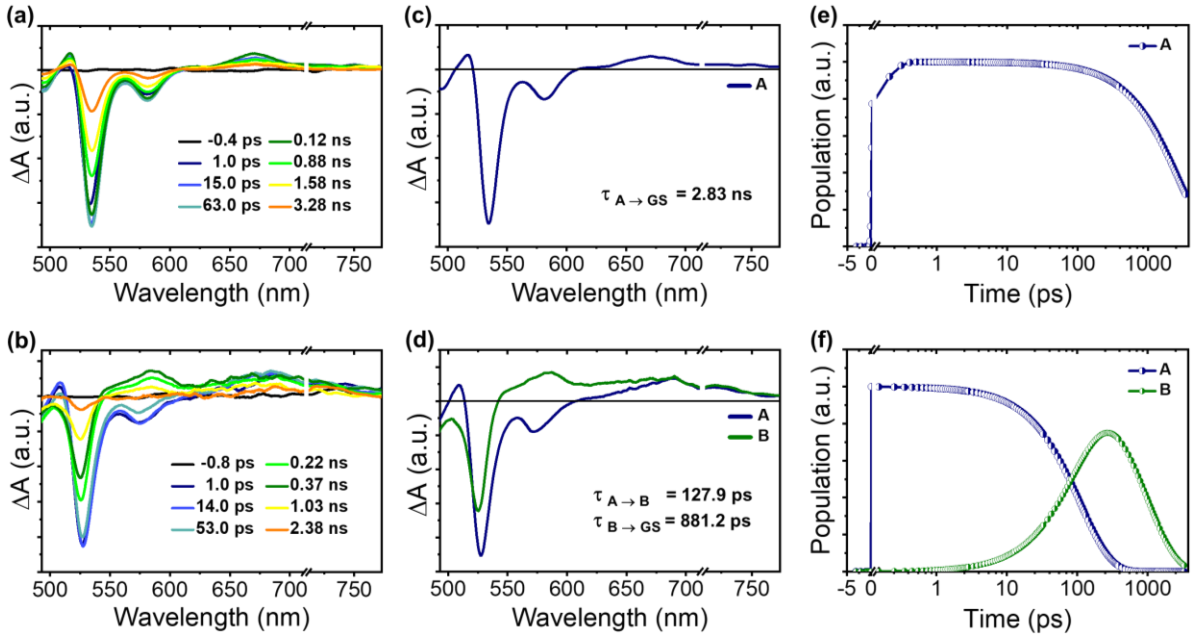

Figure 2.2: The fsTA spectra of **L-PDI$_2$** showing the excited-state dynamics upon photoexcitation (λ_{ex} = 495 nm) in a) TOL and b) ACE. EAS reconstructed from global analysis of **L-PDI$_2$** with c) A → GS model for TOL and d) A → B → GS model for ACE; where A is the singlet excited-state, B is the CSS, and GS is the ground-state. Relative population profile of the excited-states fitted using above kinetic models in e) TOL and f) ACE.

nm ESA represents the characteristic spectral signature of the locally excited singlet state (**^{1}L-PDI$_2$***) of the PDI chromophore.[64,70,85,111] Within higher time delays of 3.28 ns, GSB recovery was observed in **L-PDI$_2$**. On the other hand, **L-PDI$_2$** in polar ACE showed marked differences in the excited-state dynamics compared to that of **L-PDI$_2$** in TOL. Upon photoexcitation, the fsTA spectra of **L-PDI$_2$** in ACE ($C_0 \approx 1.5$ μM) exhibit negative GSB at ~514 to 556 nm, SE at ~559 to 601 nm and ESA centered at ~685 nm (Figure 2.2b). The initially populated **^{1}L-PDI$_2$*** state shows rapid decay to form a new transient species with ESA at ~586 and 690 nm, corresponding to the spectral signature of PDI monomer's radical cation (PDI$^{\bullet+}$) and radical anion (PDI$^{\bullet-}$), respectively (Figure A2.15a and A2.15b).[64,65,70,111] The simultaneous occurrence of PDI$^{\bullet+}$ and PDI$^{\bullet-}$ transient features represent the CSS, confirming the SB-CS in **L-PDI$_2$** in ACE.[78,111] At higher time delays of 2.38 ns, the CSS undergoes charge recombination (CR),

leading to ground-state recovery.

Global analysis of the fsTA data of **L-PDI₂** was performed to acquire the evolution-associated spectra (EAS) and the relative population profile of the excited-states for the aforementioned transformations.[112] Globally analyzed fits are plotted together with selected kinetic traces obtained at different wavelengths to demonstrate the quality of the fitting, as illustrated in Figure A2.16a and A2.16b. The EAS and the relative population profile of **L-PDI₂** in TOL (Figure 2.2c and 2.2e) demonstrated a single principal component (A). The component (A) is assigned to the locally excited singlet state (**^{1}L-PDI₂***). Ground-state recovery was observed with the decay of the **^{1}L-PDI₂*** state with a time constant of τ_A= 2.83 ns. However, in a polar solvent ACE, the EAS and relative population profile plot of **L-PDI₂** exhibit two principal components with prominent evidence of forming the CSS (Figure 2.2d and 2.2f). The first component (A) is attributed to the **^{1}L-PDI₂*** state, which undergoes CS (τ_{CS} = 127.9 ps) to form the CSS (component (B)) via SB-CS.[113] The origin of CS in **L-PDI₂** in the presence of polar ACE probably originates from the lowering of the CSS energy relative to the **^{1}L-PDI₂*** state energy.[10,111,114] The CSS in **L-PDI₂** decays to ground-state via CR with a time constant τ_{CR} = 881.2 ps. Table 2.1 presents the time constants (τ) and rate constants (k) for the CS and CR processes in **L-PDI₂** across different solvents, as determined by global analysis. Furthermore, nanosecond transient absorption (nsTA) measurements of **L-PDI₂** were performed to probe the fate of the CSS formed in ACE. Upon exciting the sample ($C_0 \approx$ 1.5 μM) at 532 nm with a laser

Table 2.1: Time constants (τ), rate constants (k), driving forces (ΔG) for SB-CS and triplet quantum yields (ϕ_T) of **L-PDI₂** and **A-PDI₂** in TOL (ε = 2.38) and ACE (ε = 20.70) solvents.

Dimer	Solvent	τ_{CS}[a] (ps)	k_{CS}[a] (s^{-1})	ΔG_{CS} (eV)	τ_{CR}[a] (ps)	k_{CR}[a] (s^{-1})	ΔG_{CR} (eV)	ϕ_T[b] (%)
L-PDI$_2$	TOL	-	-	+0.13	-	-	-2.43	-
	ACE	127.9	7.8 x 10^9	-0.18	881.2	1.1 x 10^9	-2.14	-
A-PDI$_2$	TOL	-	-	+0.19	-	-	-2.50	12.7
	ACE	6.3	1.6 x 10^{11}	-0.28	319.7	3.1 x 10^9	-2.64	35.9

[a] Obtained from fsTA measurements.

[b] Obtained from nsTA measurements.

pulse of 8-10 ns duration, the nsTA spectra of **L-PDI$_2$** (Figure A2.17a and A2.17b) show no evidence of any long-lived species, particularly triplet excited-states. Therefore, the CSS in **L-PDI$_2$** undergoes CR to repopulate the ground-state.

2.2.5. Femtosecond Transient Absorption Measurements of A-PDI$_2$

Having established the SB-CS dynamics in **L-PDI$_2$**, we further probed the excited-state decay pathways in the angular dimer, **A-PDI$_2$**. Upon photoexcitation at 480 nm, the fsTA spectra of **A-PDI$_2$** in nonpolar TOL ($C_0 \approx 1.5$ μM) exhibit negative GSB at ~500 to 560 nm, SE at ~562

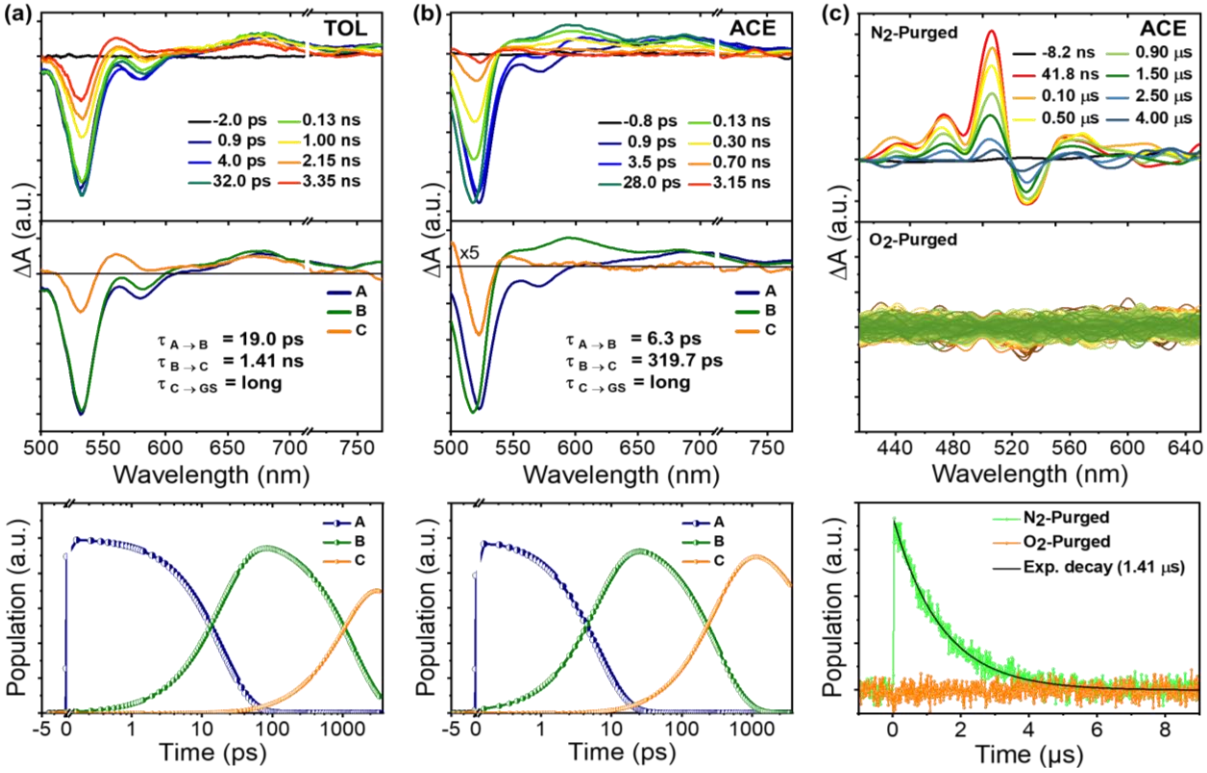

Figure 2.3: (Top row) fsTA spectra of **A-PDI$_2$** in a) TOL and b) ACE showing the excited-state dynamics upon photoexcitation. (Middle row) EAS reconstructed from global analysis of **A-PDI$_2$** with A → B → C → GS kinetic model, where A is the singlet excited-state, B is the relaxed singlet excited-state in case of TOL and the CSS in case of ACE, C is the triplet excited-state, and GS is the ground-state (λ_{ex} = 480 nm). (Bottom row) Relative population profile of the excited-states fitted using kinetic models. c) nsTA spectra of **A-PDI$_2$** in (top row) N_2-purged ACE and (middle row) O_2-purged ACE. (Bottom row) Single-wavelength decay kinetics fitted at 510 nm yielding the triplet excited-state lifetime in **A-PDI$_2$**.

to 600 nm and ESA with positive features centered at ~674 nm (Figure 2.3a-top). The ESA at ~674 nm represents the characteristic spectral signature of the locally excited singlet state (^{1}**A-PDI$_2$***).[64,85,111] At longer delay times around 3.35 ns, a distinct transient species emerged, exhibiting ESA centered at ~560 nm. This species demonstrated significant long lifetime, as its complete decay could not be captured within the 3.6 ns time window available in the fsTA experiment. Conversely, **A-PDI$_2$** in ACE shows entirely different excited-state dynamics compared to TOL. Upon photoexcitation at 480 nm, the fsTA spectra of **A-PDI$_2$** ($C_0 \approx 1.5$ μM) displayed negative GSB at ~501 to 553 nm, SE at ~555 to 595 nm and ESA centered at ~687 nm (Figure 2.3b-top). The initially populated ^{1}**A-PDI$_2$*** state exhibits ultrafast decay to form a new transient species with ESA at ~593 and 684 nm, corresponding to the CSS formed in **A-PDI$_2$** due to SB-CS (Figure A2.18a and A2.18b).[65,83,111] Notably, the CSS undergoes decay within a few hundred picoseconds, leading to the formation of a new, long-lived transient species characterized by ESA around 547 nm. The complete decay of this long-lived species could not be tracked within the time resolution of the fsTA experiment.

The kinetic components involved in the above-mentioned transformations were obtained by global analysis of the fsTA data of **A-PDI$_2$**.[112] The selected kinetic traces at different wavelengths are shown in Figure A2.19a and A2.19b to demonstrate the quality of the fitting. The EAS and the relative population profile of **A-PDI$_2$** in TOL shows three principal components (Figure 2.3a-middle and 2.3a-bottom). The first component (A) is assigned to a locally excited hot singlet state (^{1}**A-PDI$_2$***),[115] which undergoes rapid vibrational relaxation (τ_{VR} = 19.0 ps) to form the second principal component (B). The component (B) is attributed to the relaxed singlet excited-state in **A-PDI$_2$**. Eventually, component (B) decays within 1.41 ns to populate the third principal component (C) in the EAS of **A-PDI$_2$**. The component (C) was long-lived and the exact nature of the species could not be deciphered from fsTA measurements. On the contrary, the EAS of **A-PDI$_2$** in ACE provided clear evidence of the formation of the CSS (component (B)) via ultrafast CS from the initially populated ^{1}**A-PDI$_2$*** state (component (A)) with a time constant of 6.3 ps (Figure 2.3b-middle and 2.3b-bottom). The ultrafast CS detected in **A-PDI$_2$** in polar ACE might have resulted from the lowering of the CSS energies relative to the ^{1}**A-PDI$_2$*** state energy.[64,70,114] The CSS decays within 319.7 ps to form a long-lived species (component (C)), which could be a triplet excited-state formed via

CR in **A-PDI₂** (*vide infra*).[111,116] The time constants (τ) and rate constants (k) for the CS and CR processes in **A-PDI₂** across various solvents based on global analysis findings are mentioned in Table 2.1. The relatively weak ESA intensity of the $PDI^{\bullet-}$ compared to the $PDI^{\bullet+}$ in the fsTA spectra of **L-PDI₂** and **A-PDI₂** could arise due to the lower molar absorption coefficient (ε) for the radical anion species formed in the PDI dimers.[43,67,111]

2.2.6. Nanosecond Transient Absorption Measurements of A-PDI₂

Further, to characterize the long-lived species detected in the fsTA experiments, nsTA measurements of **A-PDI₂** were carried out in ACE and TOL ($C_0 \approx 1.5$ μM). After photoexcitation at 532 nm, the nsTA spectra of **A-PDI₂** in nitrogen-purged ACE exhibited intense ESA bands at ~437, 473, 506 and 557 nm (Figure 2.3c-top) corresponding to the triplet state absorption of PDI ($T_1 \rightarrow T_n$ transitions).[117–119] Along with ESA, GSB and/or SE was observed at ~518 to 546 nm in the nsTA spectra. The nsTA measurements in oxygen-purged ACE solution revealed a rapid decay of the ESA bands, confirming the nature of the observed long-lived species to be triplet manifolds in **A-PDI₂** following photoexcitation (Figure 2.3c-middle). Monoexponential fitting of the nsTA derived single-wavelength decay kinetics at 510 nm, yielded the triplet lifetime (τ_T) of **A-PDI₂** in ACE as 1.41 μs (Figure 2.3c-bottom). To measure the triplet quantum yield (ϕ_T) of **A-PDI₂**, triplet-triplet energy transfer experiments were performed with $[Ru(bpy)_3]^{2+}$ as a standard ($\phi_T \approx 100\%$ in methanol) and beta-carotene as the triplet energy acceptor.[119–121] **A-PDI₂** exhibited significant triplet population in ACE with a ϕ_T of 35.9% (Figure A2.20 and Table 2.1). The triplet population pathway in **A-PDI₂** in ACE arises from the CR mechanism via the SB-CS process,[122–125] which was unobserved in the linear dimeric analogue **L-PDI₂**. The higher CR rate observed for **A-PDI₂** in ACE ($k_{ACE}^{CR} = 3.1 \times 10^9$ s^{-1}) indicates that the spin-orbit charge transfer intersystem crossing (SOCT-ISC) mechanism could be the most likely pathway for triplet state formation.[111,116] The nsTA spectra of **A-PDI₂** in nitrogen-purged TOL show weak ESA bands corresponding to triplet state absorption with a τ_T of 1.22 μs (Figure A2.21). The low triplet yield ($\phi_T = 12.7\%$) observed for **A-PDI₂** in TOL (Figure A2.22) probably originates from the core-twisting of the PDI fragment in the dimer structure (Figure A2.23). Previously, our group demonstrated twist-

induced triplet population in core-substituted PDI derivatives and a linear dependence of core-twist to the triplet quantum yield was observed.[126]

2.2.7. Rehm-Weller Analysis for the Dimers

Rehm-Weller formulation was implemented to estimate the free energy changes of CS (ΔG_{CS}) and CR (ΔG_{CR}) processes in **L-PDI$_2$** and **A-PDI$_2$** in TOL and ACE to understand the thermodynamic feasibility of the observed SB-CS process in the PDI dimers (Table 2.1).[127] The essential parameters for the Rehm-Weller formulation were obtained through cyclic voltammetry (CV) and differential pulse voltammetry (DPV) experiments (Table A2.3). Glassy carbon and Ag/Ag^+ electrodes served as the working and reference electrodes, respectively, in the electrochemical measurements.[111] Two consecutive reversible reduction waves were observed in the voltammograms of **L-PDI$_2$** (E_1(red) = −0.98 V and E_2(red) = −1.23 V; Figure A2.24a and A2.24b). While, the angular **A-PDI$_2$** exhibited three consecutive reversible reduction waves in the voltammograms (E_1(red) = −1.02 V, E_2(red) = −1.20 V and E_3(red) = −1.30 V; Figure A2.25a and A2.25b). The ΔG_{CS} obtained for **L-PDI$_2$** in TOL and ACE are +0.13 eV and -0.18 eV, respectively (Table 2.1). Meanwhile, **A-PDI$_2$** exhibited $\Delta G_{CS} \approx$ +0.19 eV and -0.28 eV in TOL and ACE, respectively. The positive ΔG_{CS} for **L-PDI$_2$** and **A-PDI$_2$** in TOL confirms the infeasibility of the SB-CS process compared to ACE. Moreover, the enhanced negative ΔG_{CS} for **A-PDI$_2$** (-0.28 eV) compared to **L-PDI$_2$** (-0.18 eV) corroborates the higher feasibility and efficiency of the SB-CS process experimentally observed for **A-PDI$_2$** in ACE. The higher feasibility of the CR process in **A-PDI$_2$** ($\Delta G_{CR} \approx$ -2.64 eV), in contrast to **L-PDI$_2$** ($\Delta G_{CR} \approx$ -2.14 eV) in ACE, probably contributes to the higher triplet yield in **A-PDI$_2$** (*vide supra*).

2.2.8. DFT Calculated HOMO-LUMO Energies of the Dimers

Quantum chemical calculations were carried out on theoretical models of **L-PDI$_2$** and **A-PDI$_2$** to unveil the key structural aspects controlling the SB-CS process and the concomitant triplet population dynamics in the PDI dimers. Time-dependent density functional theory (TDDFT) was employed to compute the vertical excitation energies (VEEs) at the CAM-B3LYP-D3/6-

311+G(d,p) level of theory in vacuum. The VEE calculations of **L-PDI₂** reveal the first singlet excited-state (S_1) with the highest oscillator strength (*f*), while **A-PDI₂** shows the S_1 and S_2 states with significant *f*. The VEEs and the corresponding *f* values of the low-lying singlet excited-states for **L-PDI₂** and **A-PDI₂** are provided in Table A2.4. DFT calculated FMO energies at the CAM-B3LYP-D3/6-311+G(d,p) level of theory in vacuum depicts the HOMO-LUMO energies of **L-PDI₂** as E_{HOMO} = -7.41 eV and E_{LUMO} = -2.91 eV. **A-PDI₂** shows similar HOMO-LUMO energies as **L-PDI₂** with E_{HOMO} = -7.33 eV and E_{LUMO} = -3.05 eV. The minimized HOMO-LUMO energy gap in both the dimers ($\Delta E_{HOMO-LUMO}$ = 4.50 eV for **L-PDI₂** and 4.28 eV for **A-PDI₂**) compared to the PDI monomer ($\Delta E_{HOMO-LUMO}$ = 4.62 eV) occurs due to the extended π-conjugation between the two PDI units in the dimers.[107]

2.2.9. Fragment-Based Excited-State Analysis

The nature of the low-lying singlet excited-states contributing to the SB-CS process was characterized by fragment-based excited-state analysis implemented in TheoDORE.[128,129] **L-**

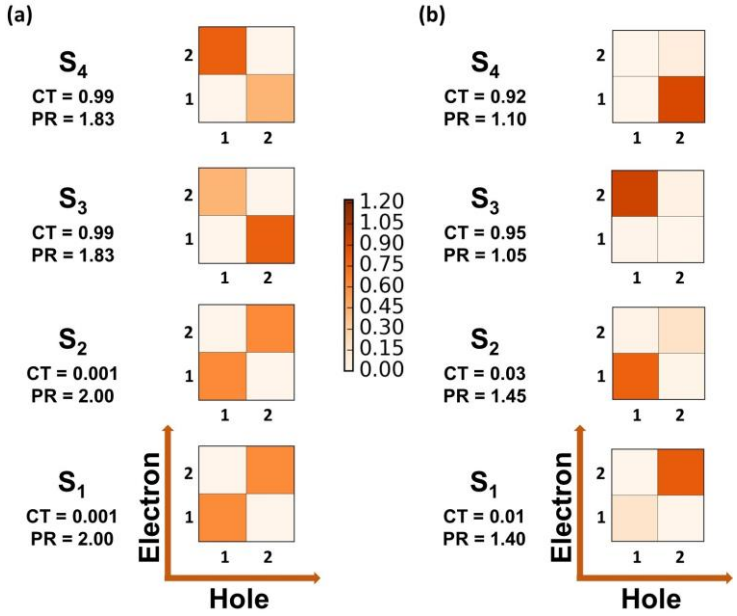

Figure 2.4: Hole-electron correlation plots showing the localized/delocalized Frenkel exciton or charge transfer nature of the S_1, S_2, S_3 and S_4 excited-states in a) **L-PDI₂** and b) **A-PDI₂** obtained through fragment-based excited-state analysis. The nature of the excitations is defined by the CT and PR values.

PDI₂ and **A-PDI₂** were fragmented into two separate PDI units for the analysis (Figures A2.26 and A2.27). The participation ratio (PR) quantifies how broadly the excitation energy is distributed across various molecular fragments, while the CT value helps classify the character of excited-states. CT values span from 0 to 1, where a value below 0.2 typically indicates a Frenkel exciton (FE) state, and a value exceeding 0.8 signifies a charge transfer state. The S_1 and S_2 states in **L-PDI₂** are delocalized Frenkel states with a CT value of 0.001 and PR of 2.00 for both states (Figures 2.4a and A2.28). The degenerate S_3 and S_4 states in **L-PDI₂** exhibit pure CT character with CT values of 0.99 and 0.99, respectively. The delocalized nature of the CT states (S_3 and S_4) in **L-PDI₂** was confirmed by the PR value of 1.83 (Figures 2.4a and A2.28). Analogously, the S_1 and S_2 states in **A-PDI₂** show Frenkel exciton character with a CT value of 0.01 and 0.03, respectively (Figures 2.4b and A2.29). Intriguingly, unlike **L-PDI₂**, the Frenkel states (S_1 and S_2) in **A-PDI₂** exhibit localized exciton nature with a PR value of 1.40 and 1.45. The higher energy singlet states in **A-PDI₂**, S_3 and S_4, are localized CT states with a CT value of 0.95 and 0.92 and a PR value of 1.05 and 1.10, respectively (Figures 2.4b and A2.29). The delocalization of the CT excitons along the two PDI units in **L-PDI₂** could be responsible for the slow CR process under the solvation in polar ACE.[130,131] Furthermore, the CT excitons in **A-PDI₂** are localized in a particular PDI unit, which probably reduces the lifetime of the CSS and accelerates the CR process in ACE.[132]

2.2.10. Excitonic Coupling Calculations

To understand the role of electronic coupling intrinsic to the spatial chromophore orientation modulating the SB-CS rates, we have theoretically estimated the long-range Coulombic coupling (J_{Coul}) interactions in **L-PDI₂** and **A-PDI₂**. Due to the insignificant orbital overlap in the PDI dimers investigated in this work, the short-range charge transfer interactions are approximated to be negligible and does not contribute to the overall photophysics for the dimers (Figures A2.30 and A2.31).[103] As a prerequisite to J_{Coul} estimation, we have calculated and visualized the transition dipole moment (TDM) vectors for the ground-state absorption in the dimers. The TDM vector orientation in **L-PDI₂** shows a linear head to tail arrangement with the TDM lying in the molecular plane along the long axis of each PDI fragment (Figure A2.32). While, **A-PDI₂** exhibits angular orientation (x-arrangement) between the two TDM vectors

with rotational offset of 60.4° (Figure A2.33). The **L-PDI$_2$** and **A-PDI$_2$** dimers were fragmented into two separate PDI units (Figures A2.26 and A2.27), and J_{Coul} interactions were investigated for the singlet excited-state with highest oscillator strength at the CAM-B3LYP/DEF2-TZVP level of theory using excitation energy transfer (EET)[24,133] method in Gaussian 16. **L-PDI$_2$** exhibited strong Coulombic coupling interactions with $|J_{Coul}|$ = 438.4 cm^{-1}, while **A-PDI$_2$** showed weak Coulombic coupling amounting to 14.9 cm^{-1}. Our theoretically estimated J_{Coul} interaction strengths are in good agreement with the experimentally observed excitonic coupling for **L-PDI$_2$** ($A_{0\text{-}0}/A_{0\text{-}1}$ = 2.37) and **A-PDI$_2$** ($A_{0\text{-}0}/A_{0\text{-}1}$ = 1.40). The lower strength of J_{Coul} interaction due to the angular orientation in **A-PDI$_2$** accelerates CS and favours faster SB-CS over **L-PDI$_2$**.[32,103,109]

2.2.11. TDDFT Calculations

To further gain insights into how molecular geometry modulates the energies of the locally excited S_1, CT, and triplet excited-states, we performed TDDFT analysis for the PDI dimers at the CAM-B3LYP-D3/6-311+G(d,p) level of theory in vacuum (Figure A2.34 and Table A2.5). In **L-PDI$_2$**, the low-lying CT state (E_{CT} = 3.64 eV) and the T_3 state (E_{T3} = 2.61 eV) has a sizeable energy gap (ΔE_{CT-T3} = 1.03 eV), and lies above the S_1 state (E_{S1} = 2.57 eV). The pre-broken symmetry and the core-twist in **A-PDI$_2$** (*vide supra*), due to the C-N bond connectivity between the two PDI units, stabilize the CT (E_{CT} = 3.08 eV) and the T_3 states (E_{T3} = 2.56 eV), with the T_3 lying below the S_1 state (E_{S1} = 2.60 eV, Figure A2.34).[126] Under the influence of polar ACE, the CT state stabilizes below the S_1 state, accelerating the CS process in **A-PDI$_2$**,[134] and the minimal energetic offset between the CT and T_3 states (ΔE_{CT-T3} = 0.52 eV) could favour the population of the triplet excited-states via CR in **A-PDI$_2$**.[135]

2.2.12. Proposed Jablonski Diagram

Figure 2.5 depicts a schematic energy level diagram consolidating the photoexcited dynamics of **L-PDI$_2$** and **A-PDI$_2$** in varied dielectric mediums. Upon photoexcitation, **L-PDI$_2$** and **A-PDI$_2$** populate the locally excited singlet state in TOL and ACE (Figure A2.35a and A2.35b). **L-PDI$_2$** in nonpolar TOL relaxes to the ground-state via radiative decay. Meanwhile, **L-PDI$_2$** forms the CSS in polar ACE, which eventually decays to the ground-state via CR. On the other

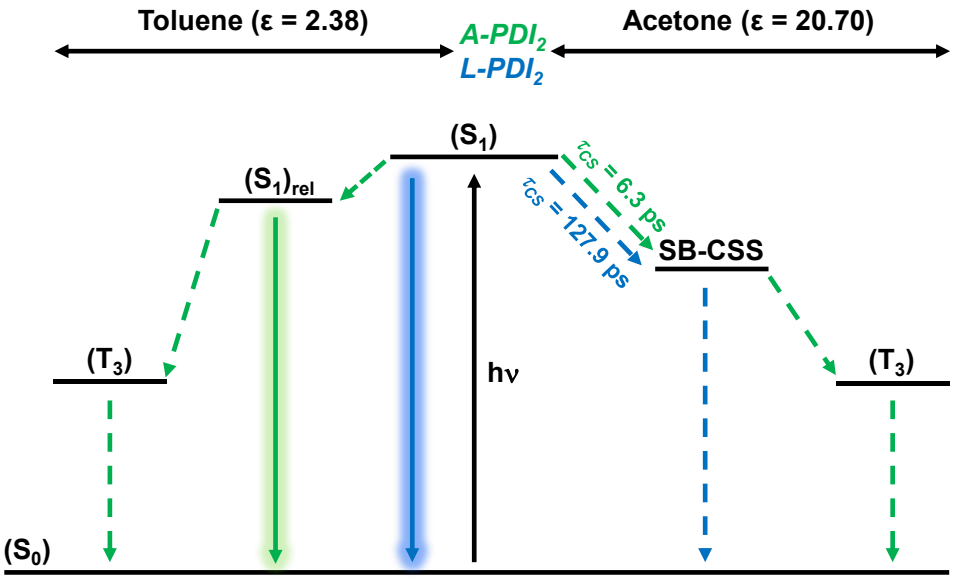

Figure 2.5: Proposed Jablonski diagram summarizing the excited-state dynamics of **A-PDI₂** (green) and **L-PDI₂** (blue) upon photoexcitation under the influence of nonpolar TOL (left) and polar ACE (right); SB-CSS = symmetry-broken charge separated state, (S_0) = ground-state, (S_1) = locally excited first singlet state, $(S_1)_{rel}$ = relaxed first singlet excited-state, and T_3 = third triplet excited-state. The coloured dotted arrows denote non-radiative decay pathways and coloured solid arrows indicate fluorescence.

hand, **A-PDI₂** in TOL populates triplet excited-states via the relaxed singlet excited-state. Whereas, **A-PDI₂** exhibits ultrafast SB-CS in ACE, which recombines to populate the triplet excited-states in significant yield.

2.3. Conclusion

In summary, we have deciphered the orientation-controlled acceleration of symmetry-breaking charge separation in a synthetically designed angular (**A-PDI₂**) versus linear (**L-PDI₂**) perylenediimide dimer. UV-vis absorption spectra showed weaker excitonic coupling in **A-PDI₂** than in **L-PDI₂**. The solvent-dependent emission measurements of **A-PDI₂** displayed enhanced fluorescence quenching and lower fluorescence quantum yields in polar solvents compared to **L-PDI₂**. Dielectric-dependent fsTA measurements indicated the faster SB-CS process in **A-PDI₂** with ultrafast CS time constant of τ_{CS} = 6.3 ps (k_{CS} = 1.6 x 10^{11} s^{-1}) in ACE.

Comparatively, **L-PDI$_2$** exhibited slower SB-CS (τ_{CS} = 127.9 ps, k_{CS} = 7.8 x 10^9 s^{-1}) with CS time constant ~20 times slower than **A-PDI$_2$** in ACE. The nsTA measurements of **A-PDI$_2$** in ACE corroborated the population of triplet excited-states via the CR pathway with a significant triplet quantum yield of ϕ_T = 35.9%. Contrastingly, the nsTA measurements of linear **L-PDI$_2$** revealed a negligible triplet population (ϕ_T < 1%). The estimated negative ΔG_{CS} values for the PDI dimers render SB-CS feasible and accelerate the CS process under the influence of polar ACE. Fragment-based excited-state analysis in TheoDORE imparted evidence for the occurrence of CT states in both the dimers contributing to the SB-CS process. The computed strength of Coulombic coupling interactions in **L-PDI$_2$** and **A-PDI$_2$** sheds light on the critical role of dimer orientations on the rate of SB-CS. Therefore, this investigation could be highly beneficial for realizing a guiding principle towards designing SB-CS materials capable of faster charge separation for optoelectronic devices.

2.4. Experimental Section

2.4.1. Syntheses and Characterization

Synthesis of PDI: The compound was prepared according to a reported method.[136] PTCDA (5 g) and imidazole (125 g) were heated to 140 °C until a homogeneous melt formed. 3-Aminopentane (3.7 g, 2.5 equiv.) was added dropwise under N_2, and the mixture was refluxed for 6 h. After cooling, the reaction mixture was washed with 1 N HCl/ethanol (40:60, v/v). The precipitate was filtered, purified by column chromatography (DCM:petroleum ether), affording the product as a dark red solid (5.75 g, 85%).

M.p. > 300 °C.

^{1}H NMR (500 MHz, $CDCl_3$, ppm) δ = 8.66 (d, J = 8.0 Hz, 4H), 8.60 (d, J = 8.1 Hz, 4H), 5.11 – 5.03 (m, 2H), 2.34 – 2.17 (m, 4H), 1.95 (m, 4H), 0.93 (t,12H).

^{13}C NMR (125 MHz, $CDCl_3$, ppm) δ = 134.7, 131.7, 129.8, 126.7, 123.7, 123.2, 57.9, 25.2, 11.6.

HRMS (APCI) m/z calculated for $C_{34}H_{31}N_2O_4$ $[(M+H)^+]$: 531.2283; found 531.2271.

IR (KBr): cm^{-1} = 2966, 2934, 2876, 1699, 1659, 1595, 1578, 1456, 1434, 1406, 1339, 1252,

1198, 1090, 852, 809, 746.

Synthesis of NO_2-PDI: Following a reported method,[107,137] PDI (900 mg, 1.6 mmol) was dissolved in DCM (100 mL), and conc. HNO_3 (0.1 M, 3.0 mL) along with cerium(IV) ammonium nitrate (CAN, 1.2 g, 2.2 mmol) were added. The reaction was stirred at room temperature for 6 h under N_2. After neutralization with 10% KOH, the mixture was extracted with DCM. Purification by silica gel column chromatography (DCM as eluent) yielded a shiny red solid (829 mg, 95%).

M.p. > 300 °C.

^{1}H NMR (500 MHz, $CDCl_3$, ppm) δ = 8.74 (d, *J* = 7.6 Hz, 1H), 8.62–8.69 (m, 4H), 8.55 (d, *J* = 8.0 Hz, 1H), 8.18 (d, *J* = 7.6 Hz, 1H), 4.93-4.99 (m, 2H), 2.12-2.21 (m, 4H), 1.83-1.89 (m, 4H), 0.84 (t, *J* = 10 Hz, 12H).

^{13}C NMR (125 MHz, $CDCl_3$, ppm) δ = 147.70, 135.50, 132.95, 129.53, 129.38, 129.14, 127.95, 127.53, 126.68, 126.47, 124.53, 124.07, 58.24, 57.95, 24.99, 24.91, 11.33, 11.31.

HRMS (APCI) m/z calculated for $C_{36}H_{30}O_6N_3$ $[(M+H)^+]$; 576.2129; found 576.2112.

IR (KBr): cm^{-1} = 2963, 2947, 2878, 1705, 1659, 1597, 1535, 1458, 1404, 1335, 1250, 1204, 1088, 856, 810, 748.

Synthesis of NH_2-PDI: Tin(II) chloride dihydrate ($SnCl_2 \cdot 2H_2O$, 2.875 g, 12.7423 mmol) and NO_2-PDI (500 mg, 0.8686 mmol) were suspended in THF (50 mL) and stirred for 20 min. The mixture was then refluxed at 80 °C for 12 hr with continuous stirring. After completion, the solvent was removed under reduced pressure, and the residue was dissolved in ethyl acetate. The organic solution was washed successively with 10% NaOH and brine, dried over anhydrous Na_2SO_4, filtered, and concentrated. Purification by alumina column chromatography (ethyl acetate, 2:3 v/v) afforded NH_2-PDI in 80% yield.[111]

M.p. > 300 °C.

^{1}H NMR (500 MHz, $CDCl_3$, ppm) δ = 8.82 (d, J = 8.0 Hz, 1H), 8.61 (m, J = 7.6 Hz, 2H), 8.50 (m, J = 8.0 Hz, 2H), 8.42 (d, J = 7.6 Hz, 1H), 8.10 (s, 1H), 5.01 (m, J = 8.0 Hz, 4H), 2.19 (m, J = 8.0 Hz, 4H), 1.87 (m, J = 8.0 Hz, 4H), 0.85 (t, J = 5 Hz, 12H).

HRMS (APCI) m/z calculated for $C_{36}H_{32}O_4N_3$ $[(M+H)^+]$; 546.2395; found 546.2380.

Synthesis of PIA: PDI (1 g, 1.885 mmol) is stirred for 15 min under nitrogen in 15 mL of t-butanol with KOH (1.586 g, 28.275 mmol) followed by a further reflux of 15 min. After cooling, 2 mL of 2N HCl and 5 mL of acetic acid were added while stirring.[138] After that, a rotary evaporator was used to extract the solvent after washing with water. PIA (400 mg, 47%) was obtained by chromatographing the purple solid on a silica gel column with DCM/hexanes (90:10) as the mobile phase. The next step was performed without any further characterization of the product.

Synthesis of L-PDI$_2$: PIA (100 mg, 0.217 mmol), hydrazine hydrate (5.43 mg, 0.1085 mmol), and imidazole (354.56 mg) were heated under reflux with stirring (140 °C, 1 hr).[106] The solid precipitate was treated with methanol/water washing, dried (100 °C), and purified by silica gel column chromatography (neutral Al_2O_3, $CHCl_3$/ethanol (20/1) and then silica gel, $CHCl_3$/ethanol (20/1)) to give **L-PDI$_2$** (70 mg, 35%).

M.p. >300 °C

^{1}H NMR (500 MHz, $CDCl_3$, ppm) δ = 8.59 (s, 8H), 8.49-8.43 (d, 8H), 5.05-4.99 (m, 2H), 2.27-2.18 (m, 4H), 1.93-1.88 (m, 4H), 0.91-0.88 (t, 12H).

^{13}C NMR (125 MHz, $CDCl_3$, ppm) δ = 160.19, 160.13, 135.39, 133.69, 132.37, 123.58, 122.77, 122.39, 57.87, 29.71, 25.06, 11.44.

MS (MALDI-TOF) m/z calculated for $C_{58}H_{38}O_8N_4$ $[(M-H)^+]$; 917.26; found 917.70.

Synthesis of A-PDI$_2$: A-PDI$_2$ was synthesized in accordance with an established literature method.[107] To a 5 mL solution of quinoline, NH_2-PDI (110 mg, 0.20 mmol), PIA (92.29 mg, 0.20 mmol), and zinc acetate (20 mg, 0.0848 mmol) were added, and the mixture was stirred at 180 °C for 36 hr under an inert nitrogen atmosphere. After allowing the reaction to cool to ambient temperature, the resulting mixture was poured into 200 mL of 2 M aqueous HCl. The product was subsequently extracted three times using DCM, followed by drying over anhydrous sodium sulfate. Purification of the crude product was carried out using silica gel column chromatography with a petroleum ether/DCM eluent system (1:4 v/v), affording the desired compound as a pure product (67 mg, 33% yield).

M.p. >300 °C

^{1}H NMR (500 MHz, $CDCl_3$, ppm) δ = 8.74–8.61 (m, 11H), 8.47-8.38 (m, 3H), 8.13–8.12 (d,

1H), 5.05– 4.97 (m, 2H), 4.91–4.88 (m, 1H), 2.25–2.17 (m, 4H), 1.95–1.76 (m, 8H), 0.90–0.77 (t, 18H).

^{13}C NMR (125 MHz, $CDCl_3$, ppm) δ = 162.50, 135.38, 133.94, 133.11, 133.03, 131.67, 128.56, 128.32, 127.31, 126.09, 125.88, 125.47, 124.25, 122.92, 122.78, 122.35, 122.28, 121.43, 56.86, 23.90, 10.23.

MS (MALDI-TOF) m/z calculated for $C_{63}H_{48}O_8N_4$ $[(M+H)^+]$; 989.40; found 989.61.

2.5. Additional Figures and Tables

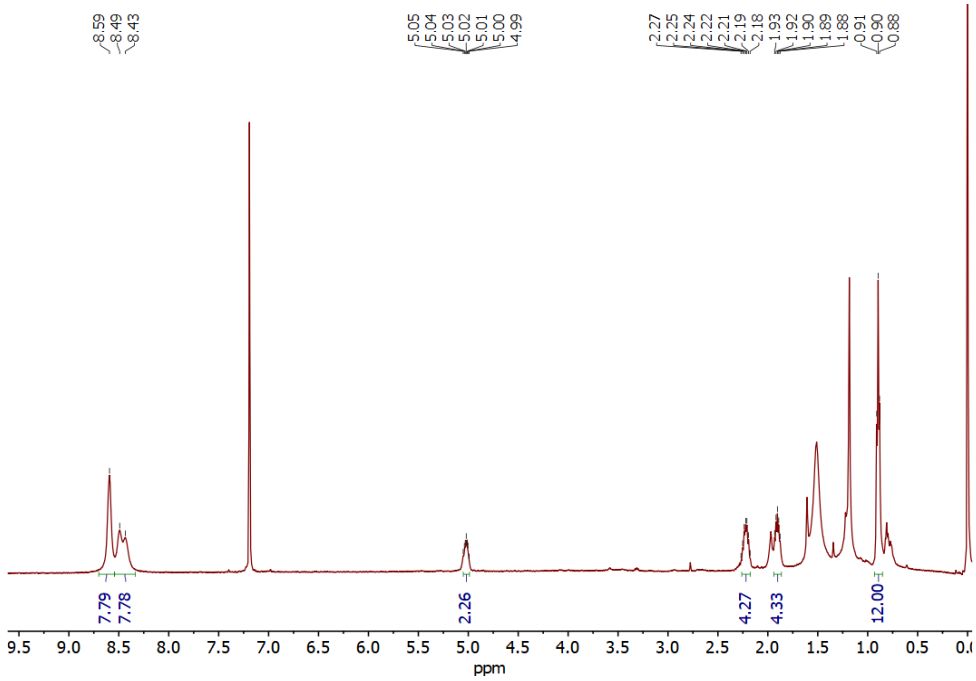

Figure A2.1: ^{1}H-NMR spectrum of **L-PDI$_2$** in $CDCl_3$.

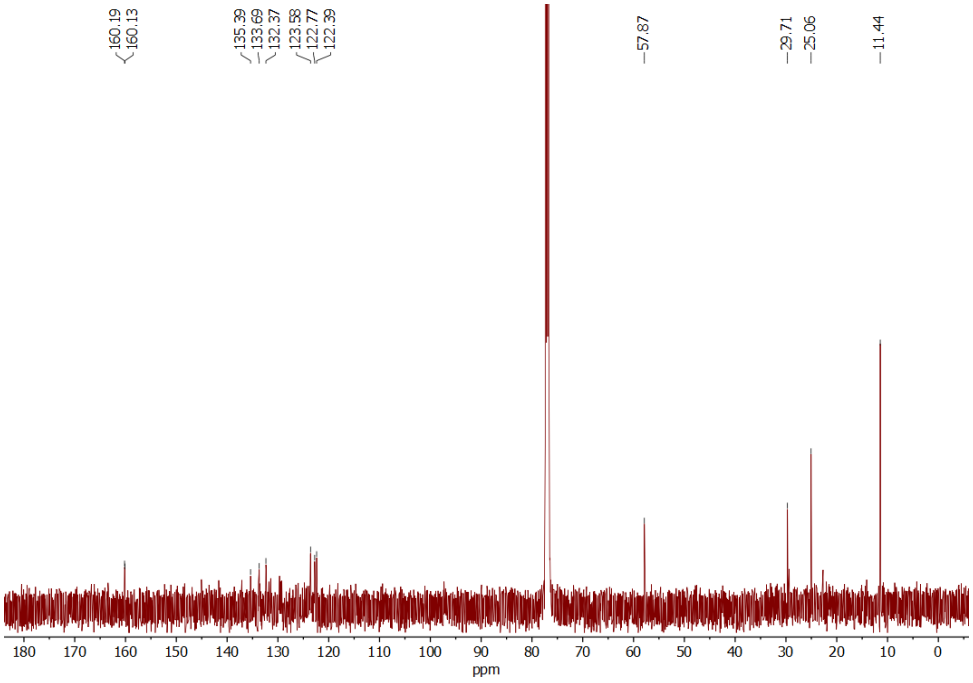

Figure A2.2: ^{13}C-NMR spectrum of **L-PDI$_2$** in $CDCl_3$.

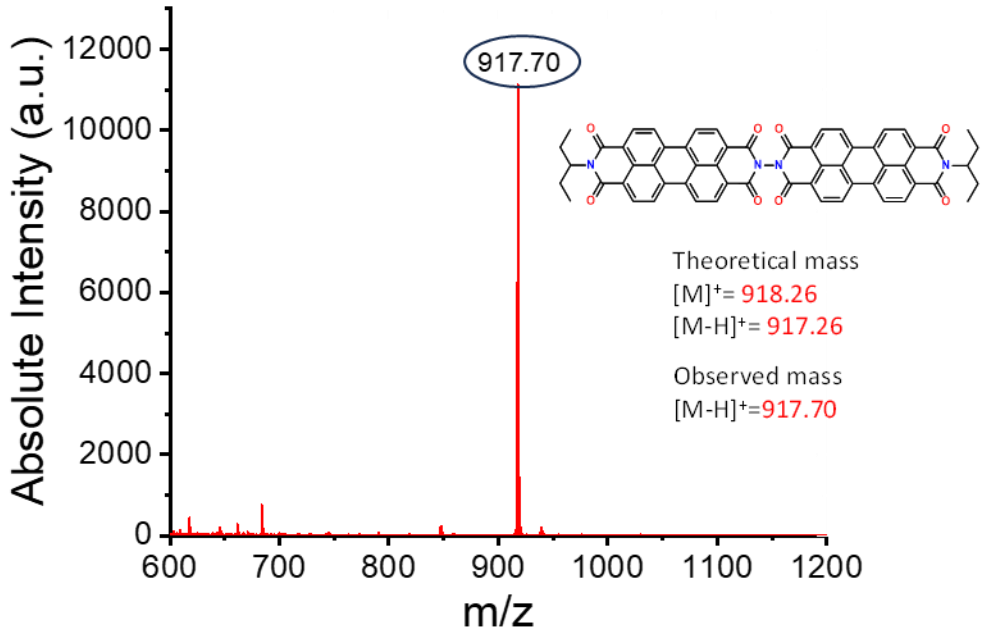

Figure A2.3: MALDI mass spectrum of **L-PDI$_2$** with the highlighted molecular mass.

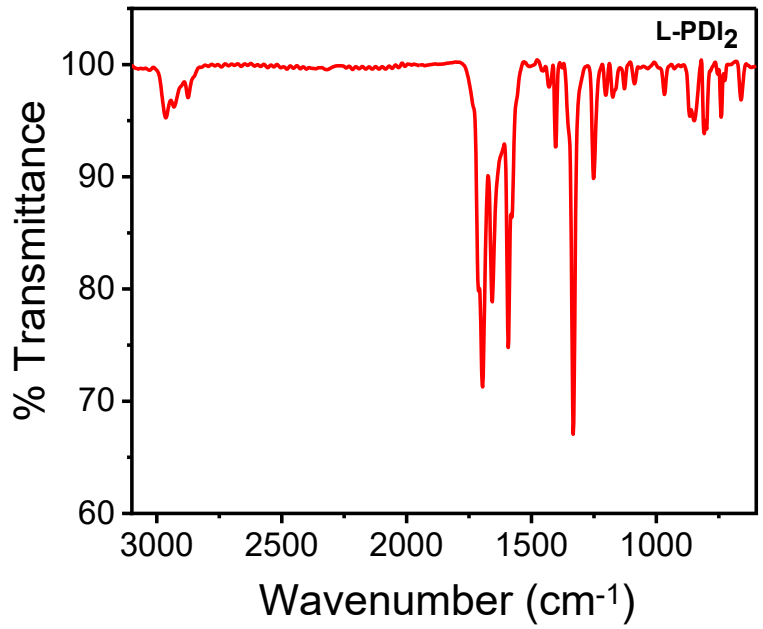

Figure A2.4: The FT-IR spectrum of **L-PDI$_2$** in KBr disks.

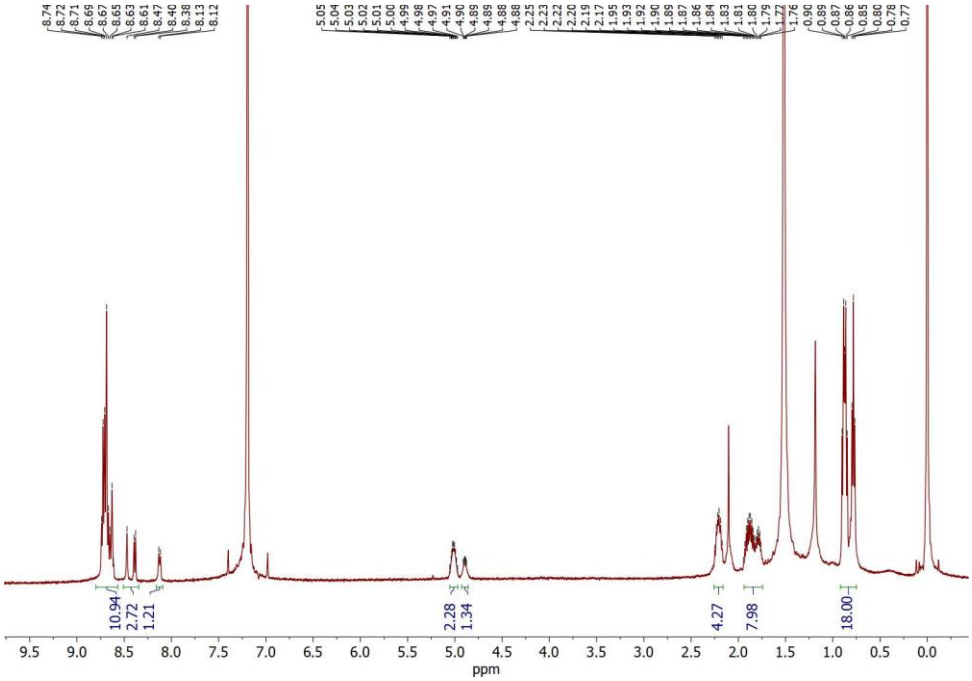

Figure A2.5: ^{1}H-NMR spectrum of **A-PDI$_2$** in $CDCl_3$.

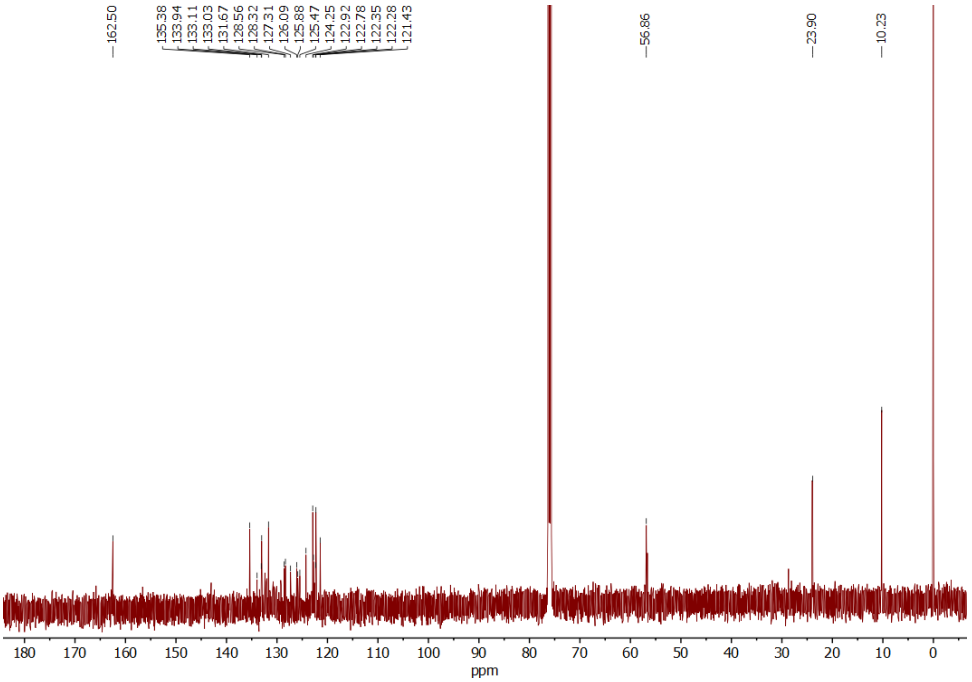

Figure A2.6: ^{13}C-NMR spectrum of **A-PDI$_2$** in $CDCl_3$.

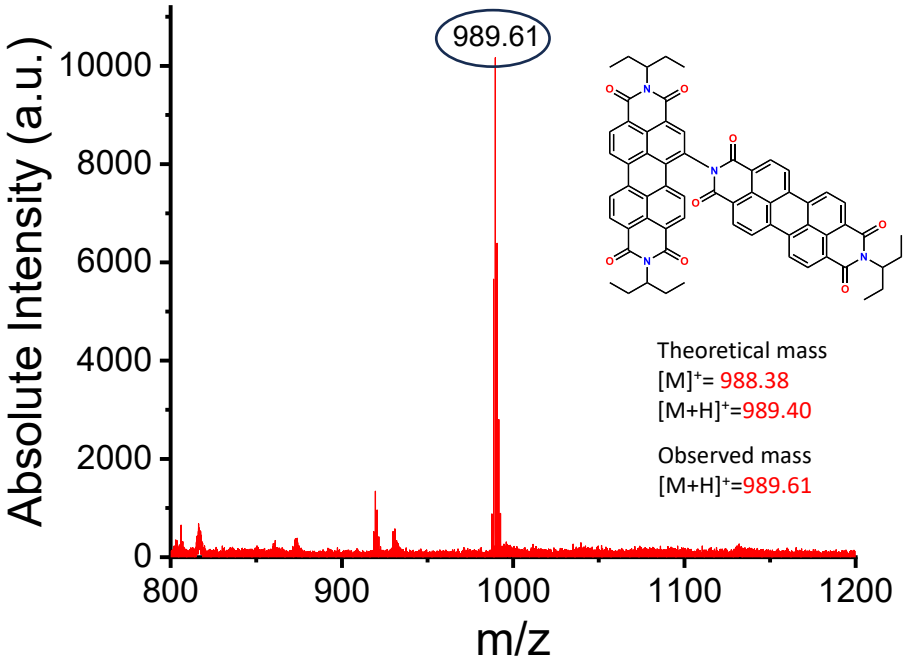

Figure A2.7: MALDI mass spectrum of **A-PDI$_2$** with the highlighted molecular mass.

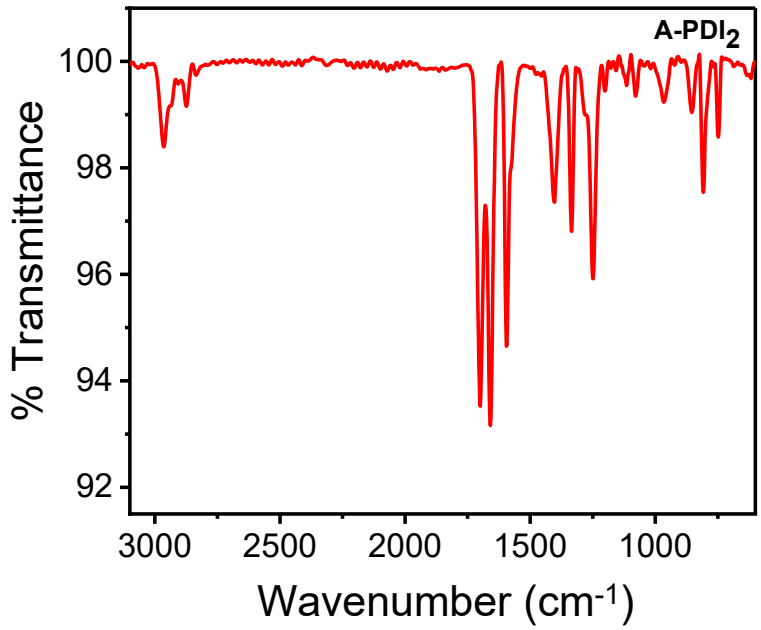

Figure A2.8: The FT-IR spectrum of **A-PDI$_2$** in KBr disks.

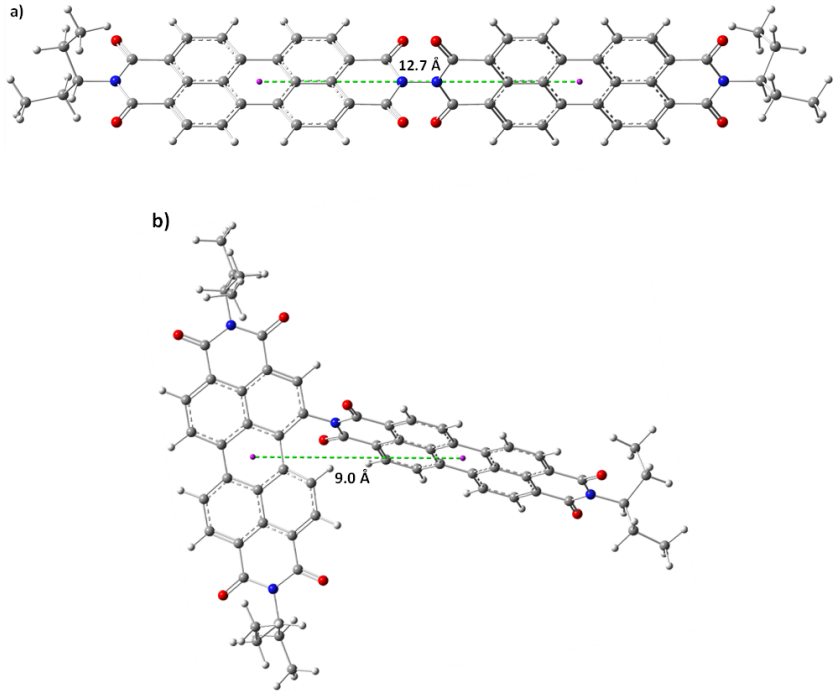

Figure A2.9: Centroid-centroid distance ($d_{PDI\text{-}PDI}$) in the ground-state optimized structures of a) **L-PDI$_2$** and b) **A-PDI$_2$**.

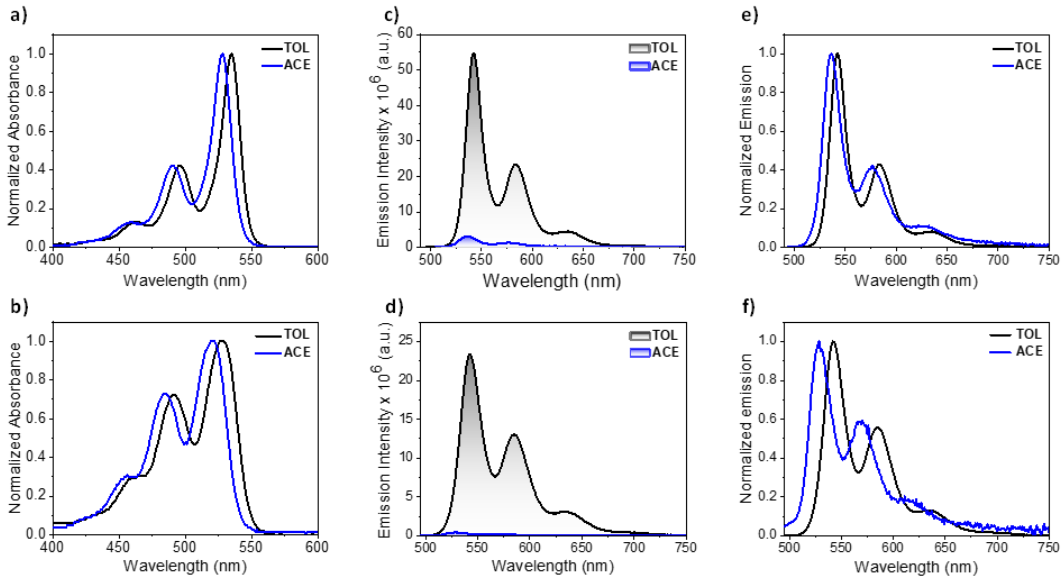

Figure A2.10: UV-vis absorption spectra of a) **L-PDI$_2$** and b) **A-PDI$_2$** recorded in various solvents. Emission spectra of c) **L-PDI$_2$** and d) **A-PDI$_2$** showing solvent dependence; panels e) and f) present the corresponding normalized emission spectra for **L-PDI$_2$** and **A-PDI$_2$**, respectively.

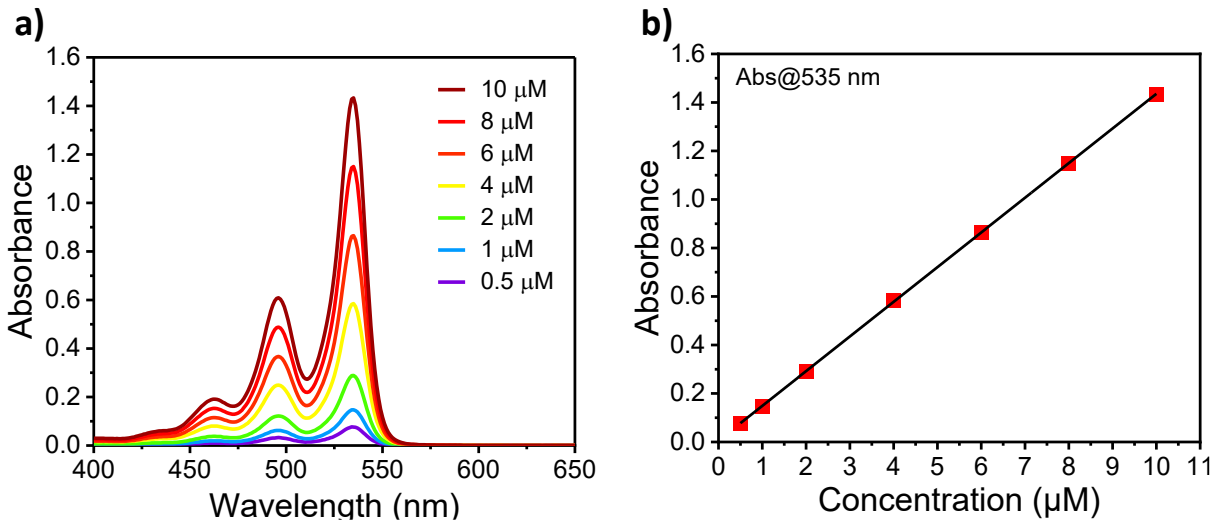

Figure A2.11: a) Concentration-dependent UV-vis absorption spectra and b) absorption maxima (λ_{max}^{Abs} = 535 nm) versus concentration plot of **L-PDI₂** in TOL.

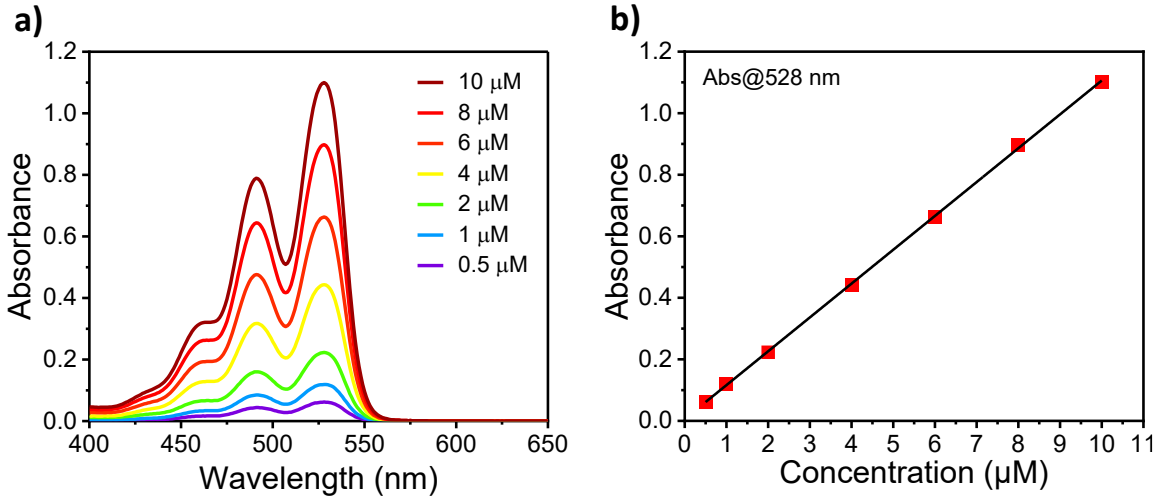

Figure A2.12: a) Concentration-dependent UV-vis absorption spectra and b) absorption maxima (λ_{max}^{Abs} = 528 nm) versus concentration plot of **A-PDI₂** in TOL.

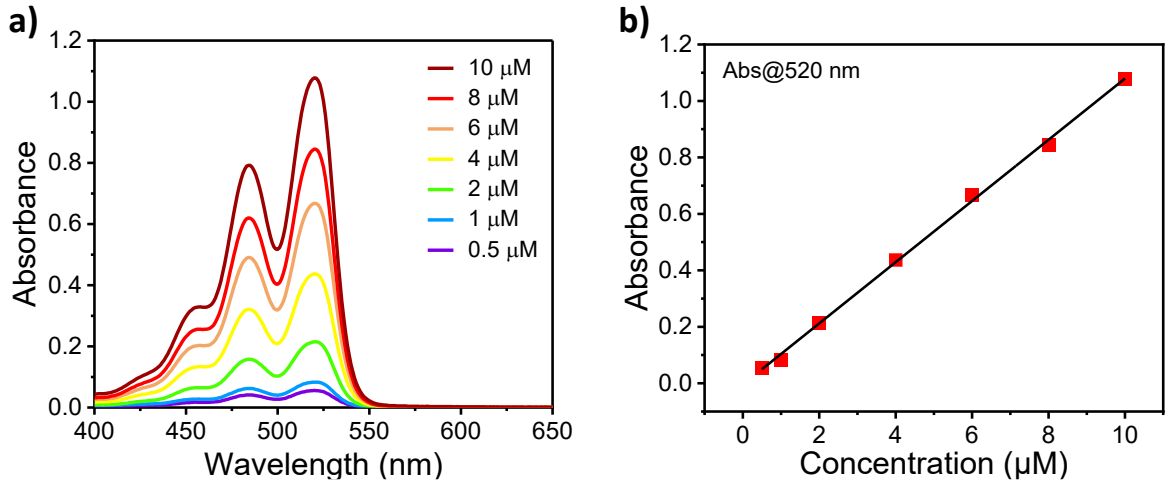

Figure A2.13: a) Concentration-dependent UV-vis absorption spectra and b) absorption maxima (λ_{max}^{Abs} = 520 nm) versus concentration plot of **A-PDI₂** in ACE.

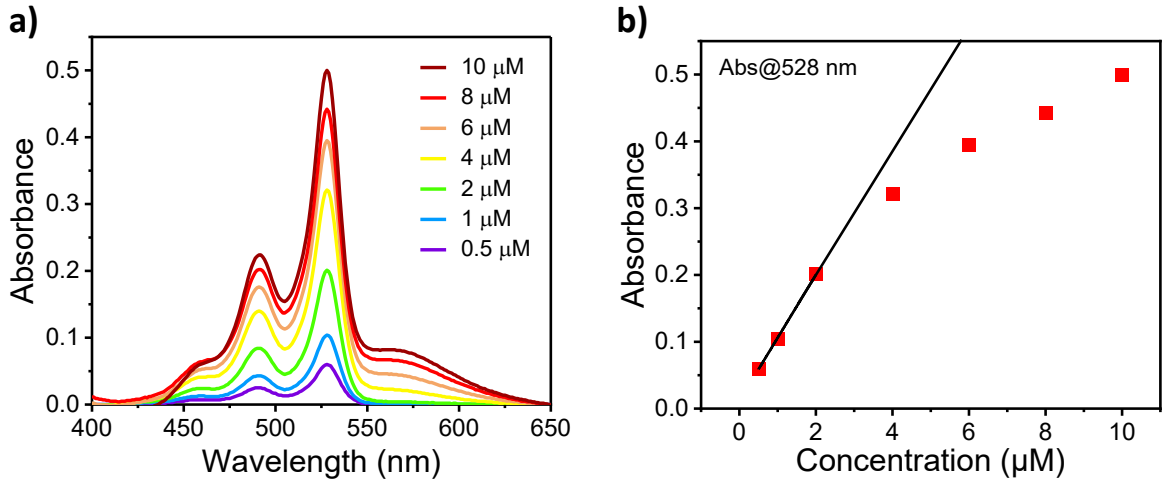

Figure A2.14: a) Concentration-dependent UV-vis absorption spectra and b) absorption maxima (λ_{max}^{Abs} = 528 nm) versus concentration plot of **L-PDI₂** in ACE.

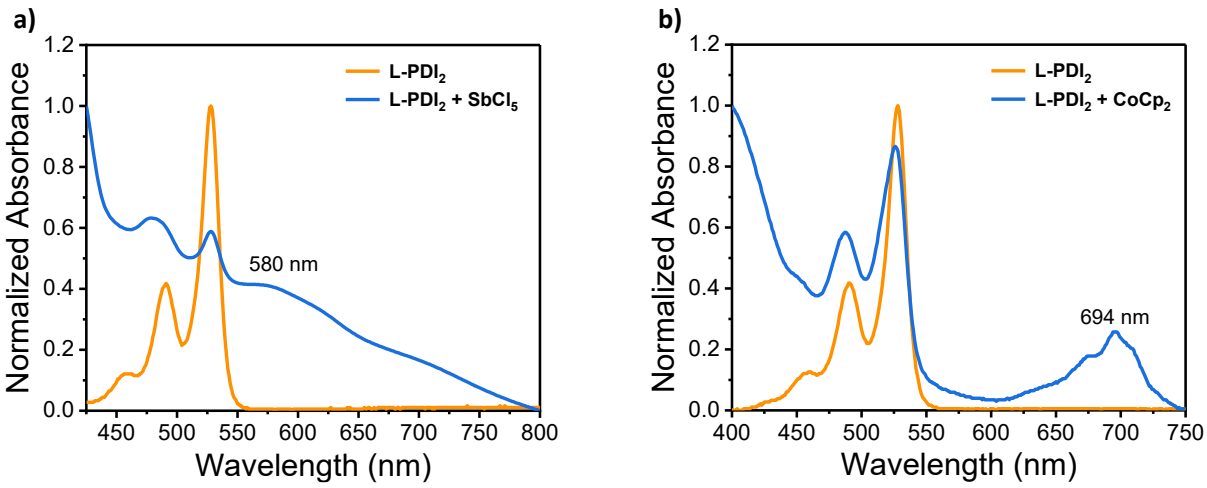

Figure A2.15: UV-vis absorption changes of **L-PDI₂** upon a) chemical oxidation by adding antimony pentachloride ($SbCl_5$) and b) chemical reduction by adding cobaltocene ($CoCp_2$) in ACE.

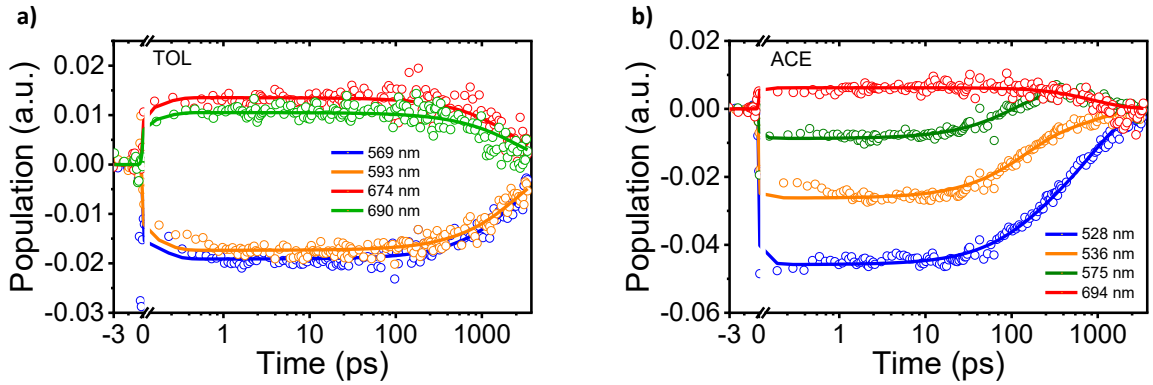

Figure A2.16: Global analysis fits for selected fsTA wavelengths of **L-PDI₂** (λ_{ex} = 495 nm) in a) TOL using A → GS kinetic model and b) ACE using A → B → GS kinetic model. Fitted results are shown using solid line profiles.

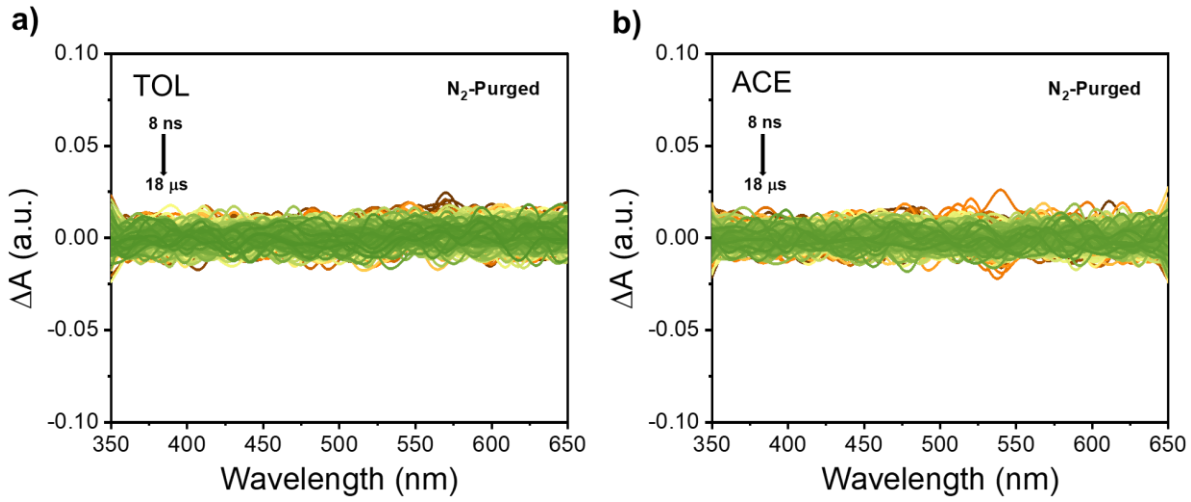

Figure A2.17: Nanosecond transient absorption spectra of **L-PDI$_2$** in N_2-purged solution of a) TOL and b) ACE.

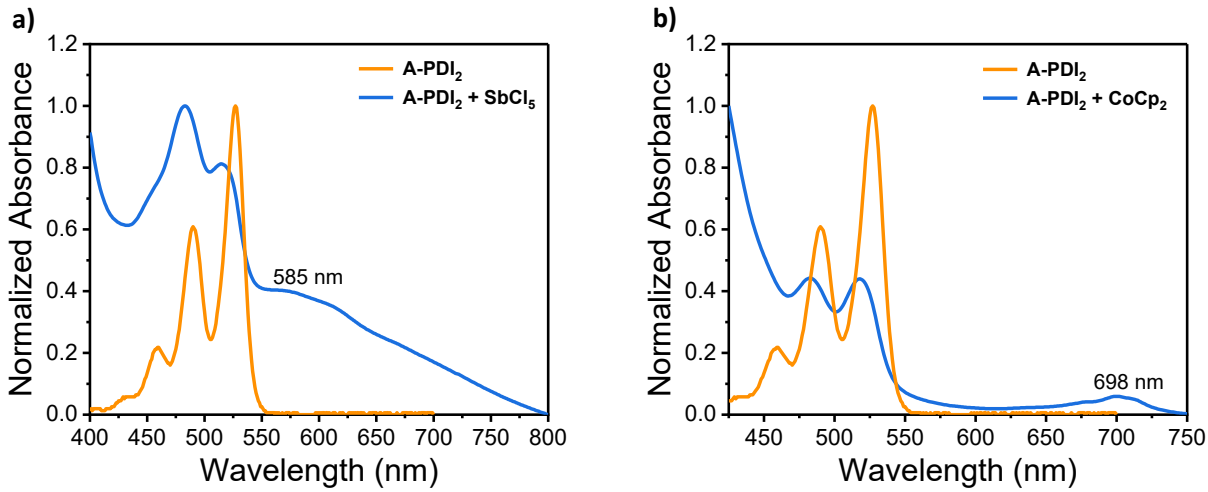

Figure A2.18: UV-vis absorption changes of **A-PDI$_2$** upon a) chemical oxidation by adding antimony pentachloride ($SbCl_5$) and b) chemical reduction by adding cobaltocene ($CoCp_2$) in ACE.

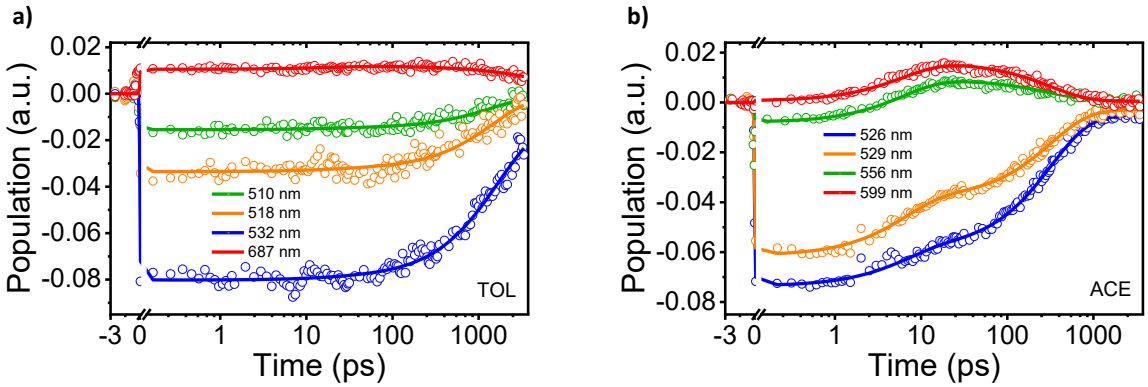

Figure A2.19: Global analysis fits for selected fsTA wavelengths of **A-PDI2** (λ_{ex} = 480 nm) in a) TOL and b) ACE using A → B → C → GS kinetic model. Fitted results are shown using solid line profiles.

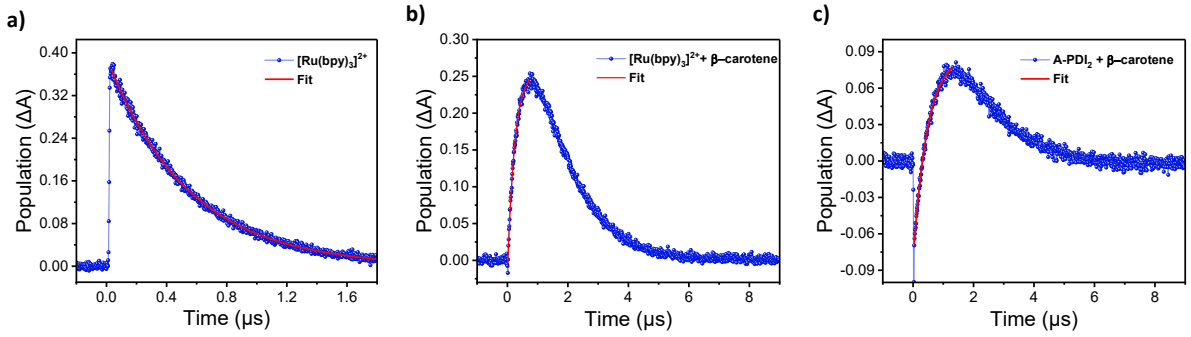

Figure A2.20: a) The nsTA decay of $[Ru(bpy)_3]^{2+}$ monitored at 370 nm. b) Time-resolved growth trace at 530 nm showing the formation of the triplet excited-state of β-carotene (^{3}β-carotene*) upon mixing $[Ru(bpy)_3]^{2+}$ with β-carotene in methanol, providing evidence for triplet-triplet energy transfer (TTET) from the ruthenium complex to β-carotene. c) Kinetic trace depicting the generation of ^{3}β-carotene* in a mixture of **A-PDI2** and β-carotene in ACE, further confirming the occurrence of TTET from **A-PDI2** to β-carotene in a polar solvent environment.

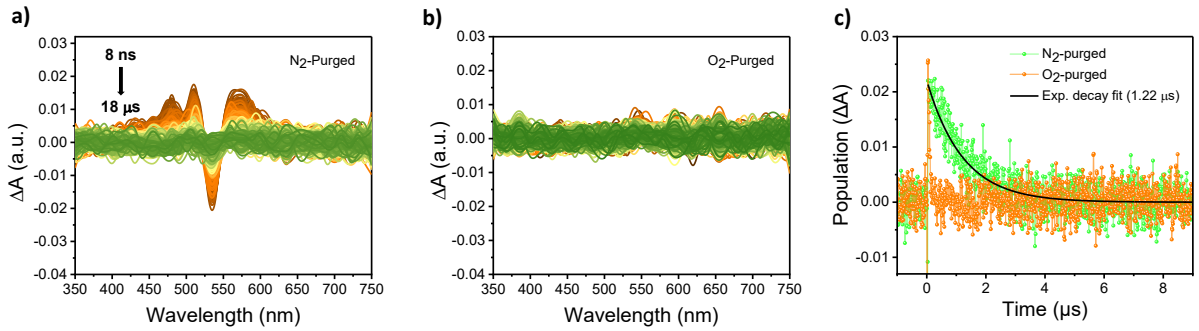

Figure A2.21: Nanosecond transient absorption measurements of **A-PDI$_2$** in TOL in a) N_2-purged solution, b) O_2-purged solution. c) Nanosecond transient absorption decay profiles of **A-PDI$_2$** in TOL.

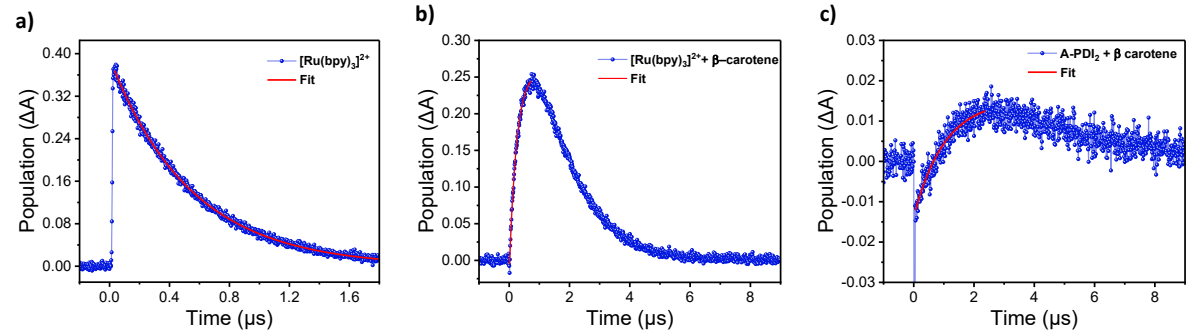

Figure A2.22: a) The nsTA decay of $[Ru(bpy)_3]^{2+}$ monitored at 370 nm. b) Time-resolved growth trace at 530 nm showing the formation of the triplet excited-state of β-carotene (^{3}β-carotene*) upon mixing $[Ru(bpy)_3]^{2+}$ with β-carotene in methanol, providing evidence for triplet-triplet energy transfer (TTET) from the ruthenium complex to β-carotene. c) Kinetic trace depicting the generation of ^{3}β-carotene* in a mixture of **A-PDI$_2$** and β-carotene in TOL, further confirming the occurrence of TTET from **A-PDI$_2$** to β-carotene.

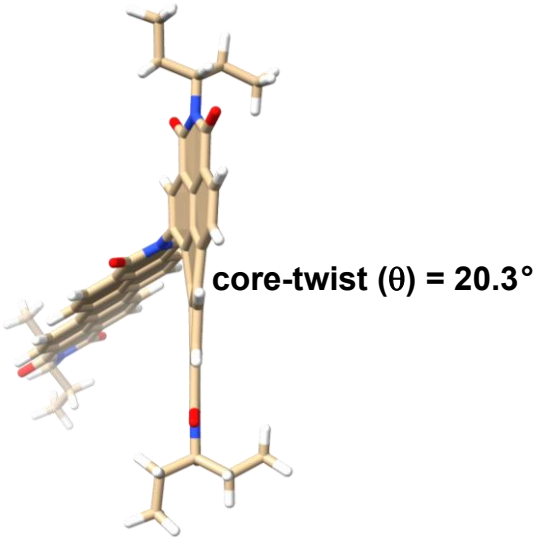

Figure A2.23: Optimized structure of **A-PDI$_2$** showing core-twist.

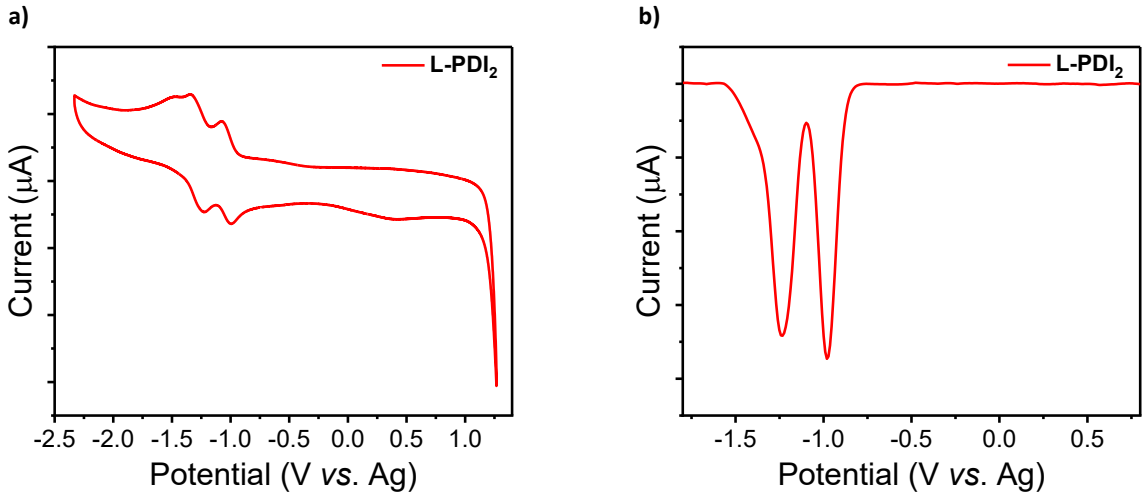

Figure A2.24: a) Cyclic voltammetry data and b) differential pulse voltammograms of **L-PDI$_2$** in DCM using Fc/Fc$^+$ coupled Ag/Ag$^+$ electrode.

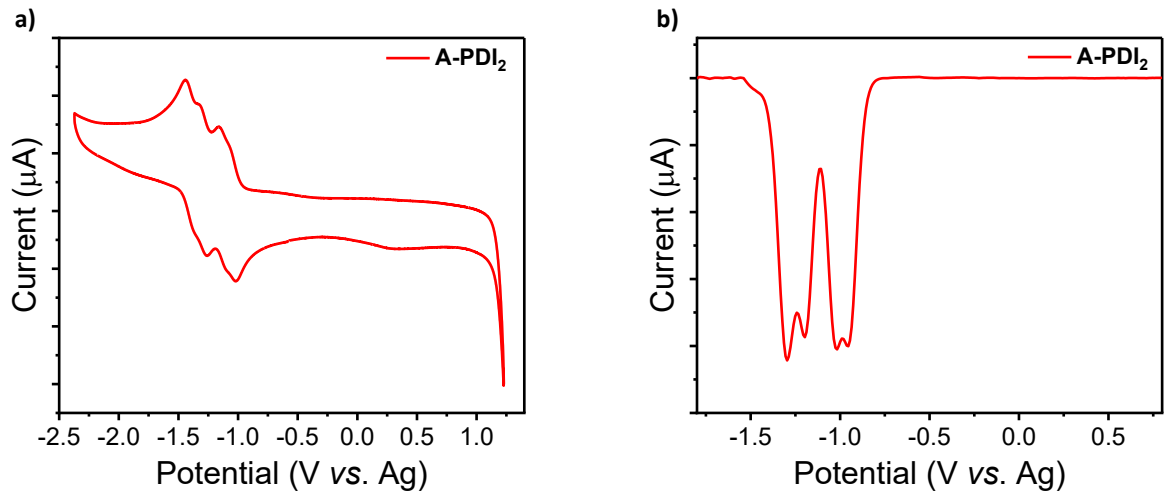

Figure A2.25: a) Cyclic voltammetry data and b) differential pulse voltammograms of **A-PDI$_2$** in DCM using Fc/Fc^+ coupled Ag/Ag^+ electrode.

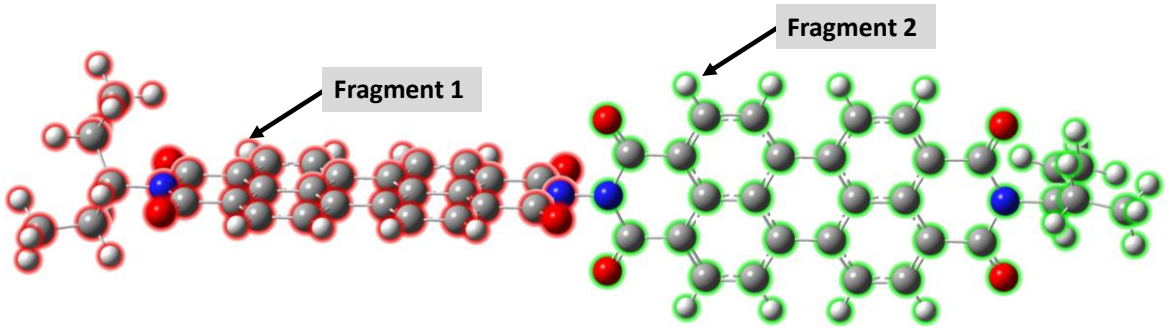

Figure A2.26: L-PDI$_2$ fragments used for the TheoDORE and Coulombic coupling calculations.

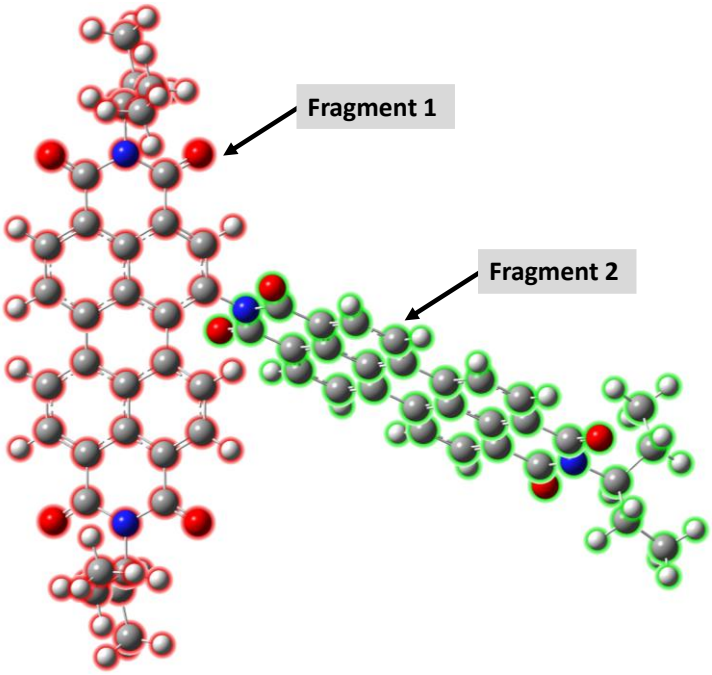

Figure A2.27: A-PDI$_2$ fragments used for the TheoDORE and Coulombic coupling calculations.

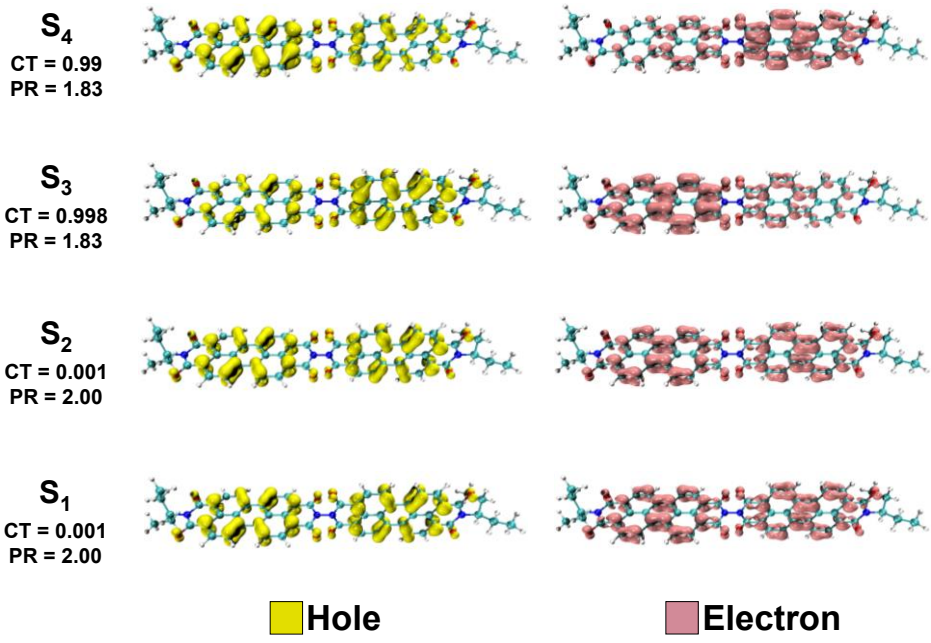

Figure A2.28: Hole-electron isosurface distribution showing the localized/delocalized Frenkel exciton or charge transfer nature of the S_1, S_2, S_3 and S_4 excited-states in **L-PDI$_2$**.

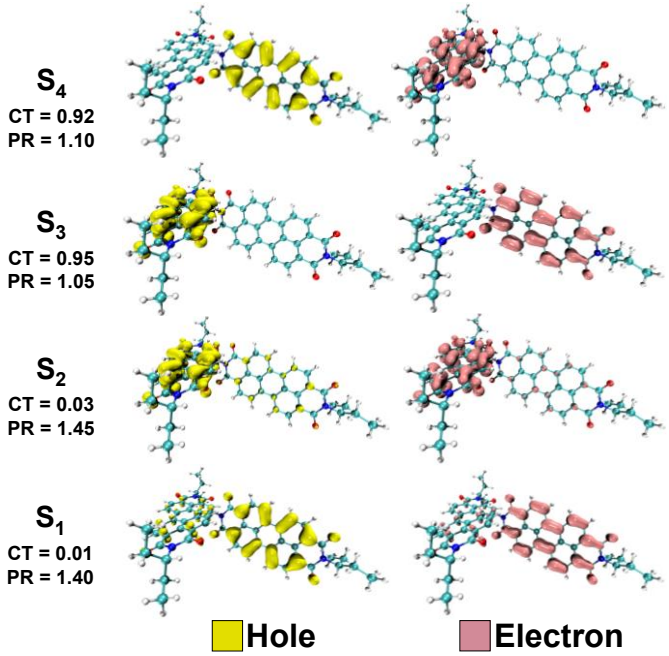

Figure A2.29: Hole-electron isosurface distribution showing the localized/delocalized Frenkel exciton or charge transfer nature of the S_1, S_2, S_3 and S_4 excited-states in **A-PDI2**.

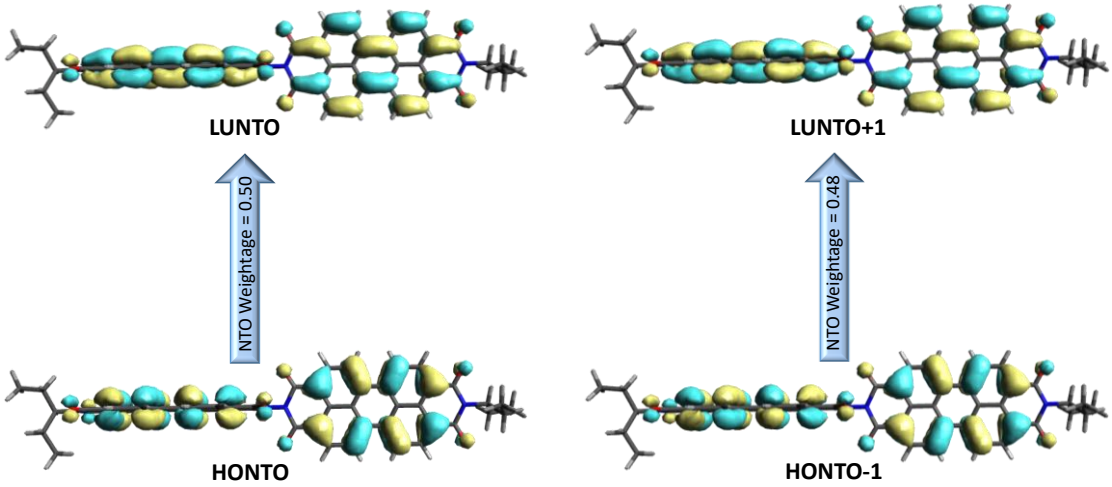

Figure A2.30: TDDFT calculated natural transition orbitals (NTOs) of the first singlet excited-state (S_1) of **L-PDI2**. The corresponding weightages of the NTOs are mentioned. N.B.- HONTO is the highest occupied natural transition orbital and LUNTO is the lowest unoccupied natural transition orbital.

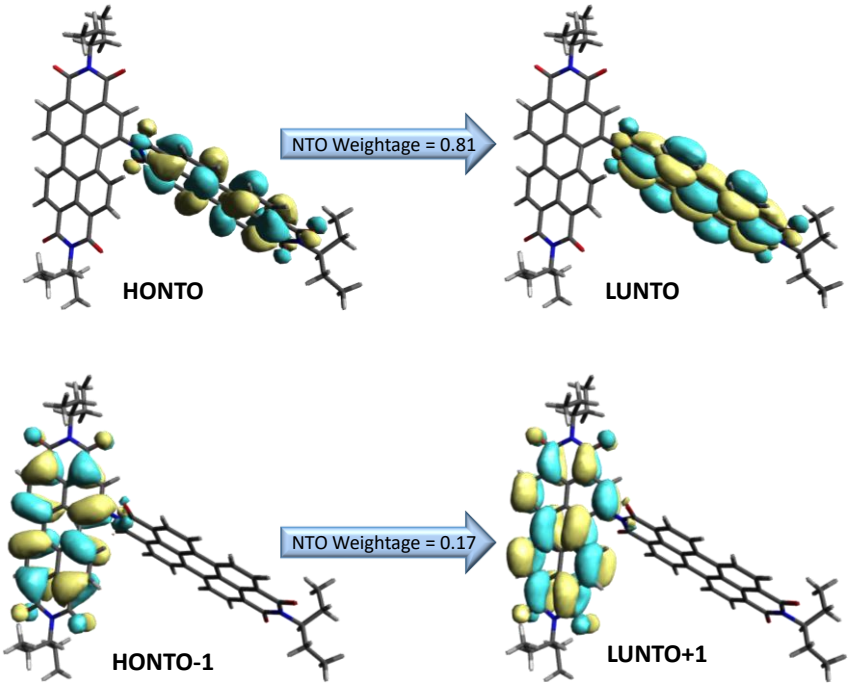

Figure A2.31: TDDFT calculated natural transition orbitals (NTOs) of the first singlet excited-state (S_1) of **A-PDI$_2$**. The corresponding weightages of the NTOs are mentioned. N.B.- HONTO is the highest occupied natural transition orbital and LUNTO is the lowest unoccupied natural transition orbital.

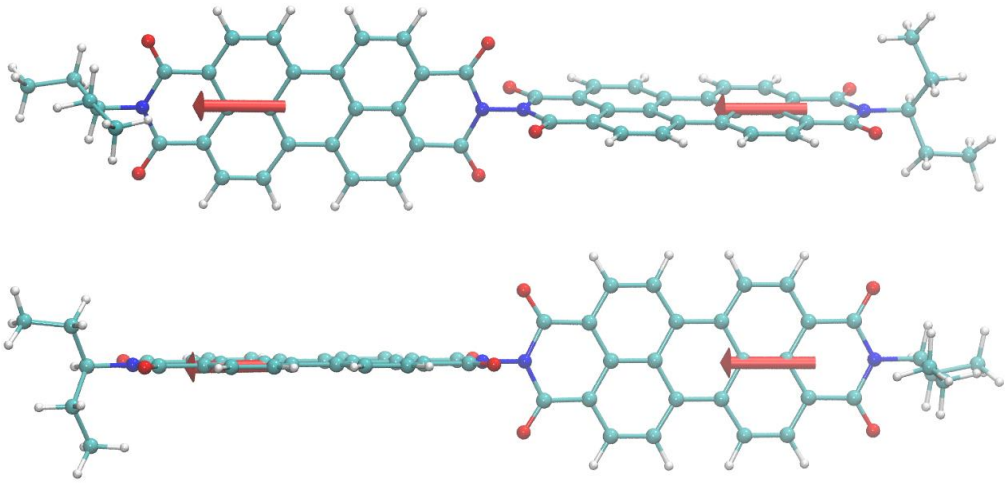

Figure A2.32: Transition dipole moment (TDM) vectors for the S_0 to S_1 transition in **L-PDI$_2$**.

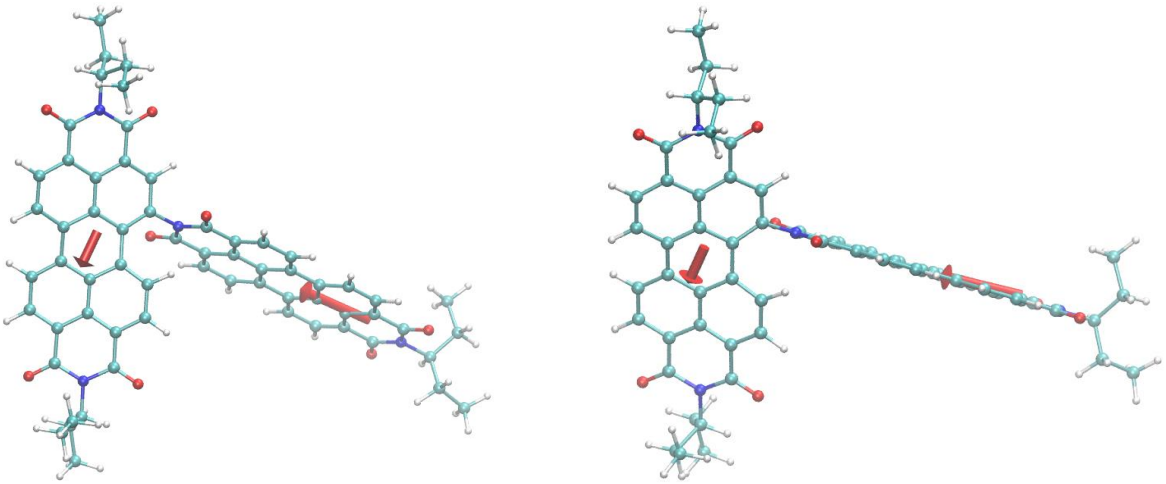

Figure A2.33: Transition dipole moment (TDM) vectors for the S_0 to S_1 transition in **A-PDI$_2$**.

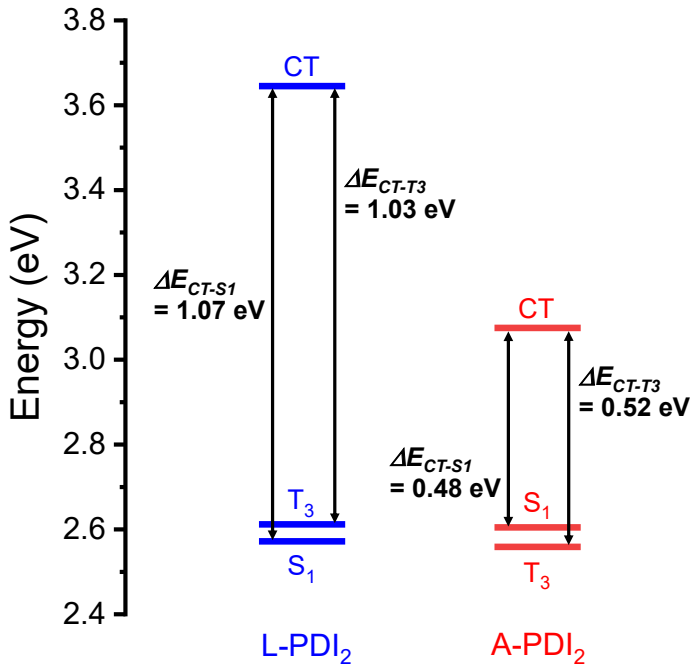

Figure A2.34: TDDFT calculated energies of the charge transfer (CT), locally excited S_1, and triplet (T_3) excited-states of **L-PDI$_2$** and **A-PDI$_2$** at the CAM-B3LYP-D3/6-311+G(d,p) level of theory in vacuum.

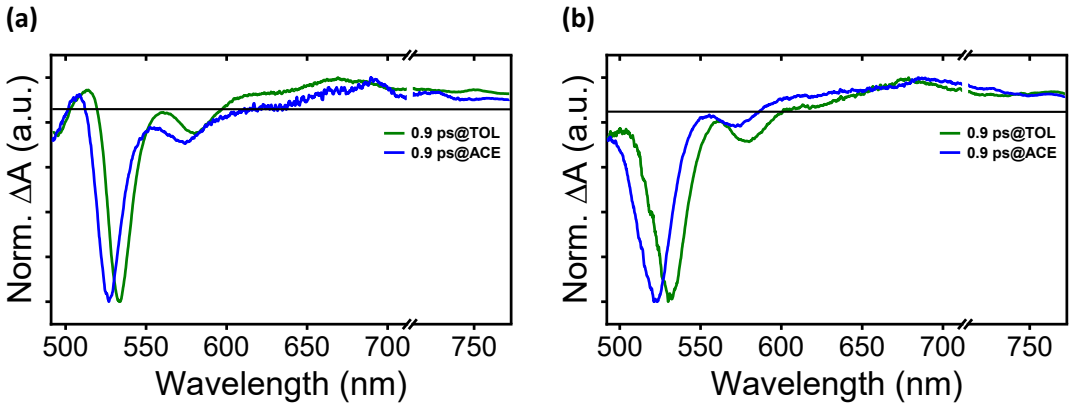

Figure A2.35: The fsTA spectra of a) **L-PDI₂** and b) **A-PDI₂** obtained at 0.9 ps time delay in TOL and ACE solvents. The similar nature of the ESA bands shows the population of a locally excited singlet state in **L-PDI₂** and **A-PDI₂** upon initial photoexcitation.

Table A2.1: Geometric parameters at S_0 optimized geometry of **L-PDI₂** and **A-PDI₂**.

Dimer	Dihedral angle, θ (°)	Core twist (°)	Centroid-to-centroid distance, $d_{PDI-PDI}$ (Å)
L-PDI₂	89.9	–	12.7
A-PDI₂	68.8	20.3	9.0

Table A2.2: Steady-state photophysical properties of **L-PDI₂** and **A-PDI₂** in different solvents.

Dimer	Solvent	Absorption Maxima, λ_{max}^{Abs} (nm)	Emission Maxima, λ_{max}^{Emi} (nm)	Quantum yield, ϕ_{FL} (%)
L-PDI₂	TOL	535	542	95.4
	ACE	528	536	6.1
A-PDI₂	TOL	529	543	63.0
	ACE	521	529	1.0

Table A2.3: Summary of redox potentials and HOMO/LUMO calculations of **L-PDI₂** and **A-PDI₂** (CH_2Cl_2, 298 K, ε_{SP} = 8.93).

Dimer	[a]E_1(red) (V)	[a]E_2(red) (V)	[a]E_3(red) (V)	λ_{onset} (nm)	E_g^{opt} (eV)	HOMO (eV)	LUMO (eV)	E_{00} (eV)
L-PDI₂	−0.98	−1.23	–	543.9	2.28	-6.10	-3.82	2.32
A-PDI₂	−1.02	−1.20	−1.30	543.9	2.28	-6.06	-3.78	2.36

[a] reduction potentials *vs*. Fc/Fc^+.

Table A2.4: Vertical excitation energies for the low-lying singlet excited-states computed at the ground-state optimized geometry of **L-PDI₂** and **A-PDI₂** (TD-CAM-B3LYP-D3/6-311+G(d,p) level of theory) in vacuum.

Dimer	Excited-state	Oscillator strength (*f*)	Energy (eV)	Wavelength (nm)
L-PDI₂	S_1	1.9	2.57	482
A-PDI₂	S_1	0.8	2.60	476
	S_2	1.0	2.67	464

Table A2.5: TDDFT calculated energies of the charge transfer (CT), locally excited S_1, and triplet (T_3) excited-states of **L-PDI$_2$** and **A-PDI$_2$** at the CAM-B3LYP-D3/6-311+G(d,p) level of theory in vacuum. N.B.- The T_3 excited-state was the low-lying triplet state near to S_1 state energy in **L-PDI$_2$** and **A-PDI$_2$**.

Excited-state	Energy (eV)	
	L-PDI$_2$	**A-PDI$_2$**
CT	3.64	3.08
S_1	2.57	2.60
T_3	2.61	2.56

2.6. Appendix

2.6.1. Materials and Methods

All reagents were obtained from commercial sources and used directly without additional purification. Reactions were performed in oven-dried glassware. Solvents were purified and dried following standard laboratory procedures before use. Thin-layer chromatography (TLC) was carried out on pre-coated silica gel 60 F254 aluminium plates (0.25 mm, Merck), with visualization under UV light at both short and long wavelengths. Column chromatography was conducted on silica gel (200-400 mesh) using solvent systems chosen according to the TLC mobility of the target compounds. Reported yields correspond to products confirmed to be both chromatographically and spectroscopically pure. Melting points were determined using a capillary melting point apparatus. ^{1}H and ^{13}C NMR spectra were recorded on a Bruker Advance DPX 500 MHz spectrometer with tetramethylsilane (TMS) as the reference standard. Mass spectra were obtained using a Bruker UltrafleXtreme MALDI-TOF/TOF instrument equipped for matrix-assisted laser desorption/ionization (MALDI). Photophysical studies were performed in quartz cuvettes with a 10 mm path length. UV-vis-NIR absorption spectra were collected on a Shimadzu UV-3600 spectrophotometer, and fluorescence measurements were recorded using a Horiba Jobin Yvon Fluorolog system. Fourier transform infrared (FT-IR) spectra were acquired on a Shimadzu IR Prestige-21 spectrometer with samples prepared as KBr pellets.

2.6.2. Computational Analysis

All the computational investigations were carried out in Gaussian 16 software package.[139] Geometry optimizations for the ground-state were carried out in the gas phase at the B3LYP-D3/6-311+G(d,p) level of theory. Vertical excitation energies along with oscillator strengths were obtained using time-dependent density functional theory (TDDFT) calculations at the CAM-B3LYP-D3/6-311+G(d,p) level. Long-range Coulombic coupling values were determined via the electronic energy transfer (EET) module implemented in Gaussian 16. Hole-electron distributions and natural transition orbital (NTO) isosurfaces for the **L-PDI$_2$** and **A-PDI$_2$** model compounds were analyzed using Multiwfn 3.8.[140] The resulting visualizations

were prepared with VMD version 1.9.3.[141]

2.6.3. TheoDORE Analysis

The nature of the excited-states in **L-PDI$_2$** and **A-PDI$_2$** were analyzed by fragment-based excited-state analysis using TheoDORE[128,129] at the ground-state optimized geometry. Each PDI monomer was considered as a fragment in both the dimers (Figures A2.26 and A2.27). To analyze the excited-state properties, three parameters were employed: the participation ratio (PR), the mean position (POS) of the initial (hole) and final (electron) orbitals, and the charge transfer character (CT). The PR indicates how many molecular fragments are involved in a given excitation and, in this study, spans values between 1 and 2. The POS denotes the average spatial location of the hole and electron for each excitation event. The CT parameter quantifies the extent of charge separation by measuring the contribution of transitions where the initial and final orbitals reside on different fragments. A CT value of 1 represents a fully charge separated state, while a CT of 0 corresponds to a Frenkel-type excitation. Additionally, electron-hole correlation plots were created to provide a visual and qualitative understanding of the nature of each excited-state in both dimer systems.

2.6.4. Coulombic Coupling Calculation

Electronic or resonance energy transfer (EET/RET) describes the mechanism by which excitation energy is relayed from a donor molecule in its excited-state to a neighboring acceptor molecule in the ground-state. Within the Gaussian 16 suite, EET computations are performed using a quantum mechanical framework grounded in DFT, applying a time-dependent variational methodology. This protocol involves carrying out excited-state calculations for each molecular fragment individually, followed by the evaluation of coupling interactions between all resultant excited-states. For singlet excitation energy transfer (SEET), the electronic coupling comprises of three terms,

$$V^{SEET} = V^{Coul} + V^{exch} + V^{ovlp} \qquad \text{(Eq 2.1)}$$

Where, V^{Coul} is the Coulombic coupling between electronic transitions, V^{exch} is the Dexter's exchange coupling and V^{ovlp} stems from the overlap between the donor-acceptor orbitals.

$$V^{Coul} = \iint dr_1 dr_2 \frac{\rho_D^{tr*}(r_1)\rho_A^{tr}(r_2)}{|r_1 - r_2|} \quad \text{(Eq 2.2)}$$

Where, $\rho_D^{tr}(r_1)$ and $\rho_A^{tr}(r_2)$ are the transition densities (the diagonal element of the density matrix) respectively of donor and acceptor.

TDDFT calculation was performed on **L-PDI$_2$** and **A-PDI$_2$** after defining each PDI monomer as a fragment (Figures A2.26 and A2.27) at the CAM-B3LYP/DEF2-TZVP level, and Coulombic coupling between the states was procured.[23,24,133]

2.6.5. Femtosecond Transient Absorption (fsTA) Measurement

Femtosecond transient absorption (fsTA) experiments were performed using a setup seeded by a Spectra-Physics Mai Tai SP mode-locked laser (86 MHz, 800 nm), which pumped a Spectra-Physics Spitfire Ace regenerative amplifier operating at 1 kHz with an output energy of 5.5 mJ. Part of the amplified beam was directed to a TOPAS optical parametric amplifier to generate the 440 nm pump pulses, while the remaining 800 nm light was sent through an optical delay line within an ExciPro pump-probe spectrometer. A sapphire crystal placed in this path produced a white-light continuum, which was split into probe and reference beams. Detection was carried out using a dual diode array detector, offering a spectral coverage of 200 nm and a maximum time delay of 3.6 ns. Sample solutions were held in a 1.2 mm path length rotating cuvette. The instrument response function (IRF), determined from the two-photon absorption of a 10% benzene/methanol mixture, was ~110 fs at 530 nm. An 80% neutral density filter was employed to control the excitation fluence, and the samples were photoexcited with 200 nJ, 100 fs pulses. The polarization between the pump and probe pulses was kept at ~54.7° magic angle, to maintain an isotropic signal for the sample. **L-PDI$_2$** and **A-PDI$_2$** were excited at 495 nm and 480 nm, respectively, for the fsTA measurements. Upon variations in laser intensity, the detected kinetic components remained unaffected, excluding singlet-singlet annihilation.[142]

2.6.6. Nanosecond Transient Absorption (nsTA) Measurement

Nanosecond transient absorption (nsTA) measurements were carried out using an Applied Photophysics LKS-60 laser kinetic spectrometer. Excitation was provided by the second harmonic output (532 nm, ~10 ns pulse width) of a Quanta Ray INDI-40-10 series pulsed

Nd:YAG laser. The kinetic decay profile recorded at 510 nm was analyzed by fitting to an exponential function using OriginPro software. The nsTA measurements of **L-PDI$_2$** and **A-PDI$_2$** were carried out on nitrogen-purged solutions of TOL and ACE.

2.6.7. Global Analysis

Global analysis of the fsTA data was carried out using Glotaran software. This involved evaluating the instrument response function and accounting for group velocity dispersion of the white light continuum, which facilitated accurate determination of decay lifetimes and dispersion-corrected spectra. A sequential kinetic model was applied during the global fitting process, allowing simultaneous examination across all wavelengths to obtain the EAS.[112]

Time-resolved spectroscopic measurements are recorded with respect to two variables: the spectral parameter, wavelength (λ), and the temporal delay (t) following the moment of photoexcitation. The model underlying the data matrix is a superposition of n_{comp} components given by the equation,

$$\Psi(\lambda, t) = \sum_{l=1}^{n_{comp}} c_l(t)\varepsilon_l(\lambda) \qquad \text{(Eq 2.3)}$$

where c_l and ε_l are the unknown concentration profile and spectrum of component, respectively.

An initial step in analyzing such datasets generally entails performing singular value decomposition to gain insights into the underlying spectral and kinetic components. Singular value decomposition (SVD) serves as a matrix decomposition method that assists in identifying the number of distinct spectral and temporal contributions within the dataset, providing crucial insight for constructing an appropriate initial kinetic model (Golub GH, Van Loan CF, 1996, Matrix Computations. 3rd edition. The Johns Hopkins University Press, Baltimore).

By applying a sequential fitting model to the fsTA dataset within the Glotaran platform, one obtains the SVD of the residual matrix, along with the extracted kinetic parameters, EAS, their normalized counterparts, and corresponding concentration profiles through an interactive graphical interface. In a sequential or unbranched unidirectional model, the associated spectra are called evolution associated spectra (EAS), and the model of equation 2.3 then reads as,

$$\Psi(\lambda, t) = \sum_{l=1}^{n_{comp}} c_l^{EAS}(t, \theta)EAS_l(\lambda) \qquad \text{(Eq 2.4)}$$

With successively increasing lifetimes, the EAS visualizes the spectral evolution. It is important to emphasize that the EAS reflect how the spectral features evolve over time and do not directly correspond to distinct chemical or physical entities. Rather, EAS captures the dynamic spectral variations linked to specific kinetic time constants.

2.6.8. Electrochemistry

Cyclic voltammograms and differential pulse voltammograms were performed at room temperature using an electrochemical workstation from CH Instruments, Inc. Electrochemical measurements were carried out using a single-compartment, three-electrode configuration comprising a glassy carbon electrode as the working electrode, a platinum wire serving as the counter electrode, and a silver wire functioning as the reference electrode. Before each experiment, the working and reference electrodes were polished on a felt pad with 0.05 μm Al_2O_3 suspension, followed by sonication in distilled water and ACE for approximately 3 minutes, and subsequent drying. The counter electrode Pt wire remained unstained and was cleaned by flame treatment. The supporting electrolyte, tetrabutylammonium hexafluorophosphate (TBAF), was pre-dried in the oven, and DCM was degassed before usage. All measurements were conducted under a nitrogen atmosphere. The concentration of TBAF used was typically 100 times that of the analyte The calibration of the instrument was carried out employing the ferrocene/ferrocenium (Fc/Fc^+) redox couple as an external reference, with measurements conducted under identical experimental conditions as those used for the samples. The potential $E_{Fc/Fc+}$ represents the Fc/Fc^+ redox couple potential relative to the Ag reference electrode. $E_{Fc/Fc+}$ is the potential of Fc/Fc^+ *vs*. Ag. The energy level of the Fc/Fc^+ redox couple was taken to be -4.8 eV relative to the vacuum level. HOMO and LUMO energies were calculated using the following equation.

$$E_g^{opt} = 1240/\lambda_{onset} \quad \text{(Eq 2.5)}$$

$$E_{LUMO} = -(E'_{red} + 4.8 - E_{Fc/Fc+}) \text{ eV} \quad \text{(Eq 2.6)}$$

$$E_{HOMO} = E_{LUMO} - E_g^{opt} \quad \text{(Eq 2.7)}$$

where E'_{red} are the experimentally measured reduction potentials *vs*. Ag/Ag^{+}. E_{LUMO} and E_{HOMO} are the corresponding LUMO and HOMO energy levels.

Redox titration

The redox titration measurements for **L-PDI$_2$** and **A-PDI$_2$** were carried out in ACE. For oxidation of both of the perylenediimide dimers, antimony pentachloride ($SbCl_5$) was used. Cobaltocene was used as the reducing agent.

2.6.9. Rehm-Weller Analysis

The free energy change (ΔG) for the charge separation and charge recombination were calculated employing the followed relations built on the Born dielectric continuum model.

$$\Delta G_{CS} = e[E_{ox} - E_{red}] - E_{00} + C + S \quad \text{(Eq 2.8)}$$

$$C = \frac{-e^2}{4\pi\epsilon_0}\left(\frac{1}{\epsilon_S r_{AD}}\right) \quad \text{(Eq 2.9)}$$

$$S = \frac{e^2}{4\pi\epsilon_0}\left(\frac{1}{r_D} + \frac{1}{r_A}\right)\left(\frac{1}{\epsilon_S} - \frac{1}{\epsilon_{SP}}\right) \quad \text{(Eq 2.10)}$$

$$\Delta G_{CR} = -(E_{00} + \Delta G_{CS}) \quad \text{(Eq 2.11)}$$

Where e is the charge of the electron, E_{ox} and E_{red} are the oxidation and reduction potentials, respectively, ϵ_0 is the permittivity of free space, ϵ_S is the static dielectric constant of the solvent, and ϵ_{SP} is the static dielectric constant of the solvent used for electrochemical measurements, r_{AD} is the donor-acceptor distance, r_D and r_A are the cation and anion hard-sphere radii, respectively (were approximated as $r_{AD}/2$) and E_{00} is the energy of the excited singlet (donor) state. At finite distances, the Coulombic attraction energy *(C)* between the radical ion-is given by a point-charge model as $(1/\epsilon_S r_{AD})$.

2.6.10. Triplet Quantum Yield (ϕ_T) Measurements

The triplet quantum yield (ϕ_T) of **A-PDI$_2$** was determined using triplet-triplet energy transfer to β-carotene, employing $[Ru(bpy)_3]^{2+}$ as a reference compound, which has a reported ϕ_T close

to 1.[119] As per literature procedures, optically matched solutions of $[Ru(bpy)_3]^{2+}$ in methanol and **A-PDI$_2$** in TOL and ACE, each with absorbance between 0.1 and 0.2 at 532 nm, were prepared. [119] Equal volumes of β-carotene in $CHCl_3$ were added to each solution. Upon photoexcitation, triplet energy transfer from either $[Ru(bpy)_3]^{2+}$ or **A-PDI$_2$** led to the formation of the β-carotene triplet state, which was monitored at 530 nm. The quantum yield values for **A-PDI$_2$** were calculated using a standard equation, where "Sam" and "Ref" denote the sample (**A-PDI$_2$**) and the reference ($[Ru(bpy)_3]^{2+}$), respectively. In this analysis, k_{obs} refers to the pseudo-first-order rate constant for the growth of the β-carotene triplet signal, while k_0 represents the decay rate constant of the donor triplet states in the absence of β-carotene, using solutions with equal absorbance.

$$\phi_T^{Sam} = \phi_T^{Ref} \times \frac{\Delta A^{Sam}}{\Delta A^{Ref}} \times \frac{k_{obs}^{Sam}}{k_{obs}^{Sam} - k_0^{Sam}} \times \frac{k_{obs}^{Ref} - k_0^{Ref}}{k_{obs}^{Ref}} \quad \text{(Eq 2.12)}$$

Chapter 3

Symmetry-Breaking Charge Separation Mediated Triplet Population in a Weakly Exciton Coupled Perylenediimide Trimer at the Single-Molecule Level

Abstract

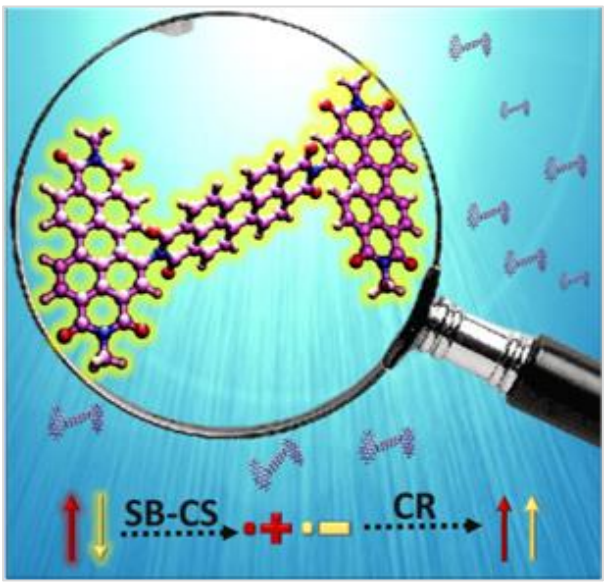

Herein, we demonstrate triplet excited-state population in a conformationally rigid perylenediimide trimer (**PDI-T**) via intramolecular symmetry-breaking charge separation (SB-CS) at the single-molecule level. The single-molecule fluorescence intensity trajectories of **PDI-T** in nonpolar polystyrene matrix (ε = 2.60) exhibit prolonged fluorescence with infrequent dark states, representing the triplet and/or the charge transfer states. In contrast, in a poly(vinyl alcohol) matrix (ε = 7.80), erratic blinking dynamics resulting in low photon counts were observed, corroborating the feasibility of charge separation in a polar environment. In agreement with the single-molecule measurements, transient absorption spectroscopy of **PDI-T** reveals ultrafast SB-CS (τ_{CS} < 5 ps) in polar THF (ε = 7.58) and ACE (ε = 20.70), with the population of the triplet excited-state through charge recombination. The current investigation shows the utility of rigid and weakly coupled molecular constructs in controlling triplet generation and SB-CS for potential applications in optoelectronic devices.

3.1. Introduction

The engineering of triplet excited-states[143–145] is essential for realizing potential applications in photocatalysis, photovoltaics, molecular logic gates, photodynamic therapy and triplet-triplet annihilation upconversion processes.[146,147] Perylenediimides (PDIs) and their derivatives are the sought-after materials for several optoelectronic and organic solar cell applications, owing to their excellent fluorescence quantum yields, thermal and photochemical stabilities.[106,148,149] Inherent to the molecular design, PDI-based multichromophoric systems exhibit triplet excited-state population via diverse excited-state photo-deactivation pathways.[145] The deactivation processes predominantly include intersystem crossing (ISC),[125,150] singlet fission (SF)[151–154] and charge recombination (CR)[58,116,155] decay channels. The efficiency of triplet generation in multichromophoric assemblies is often limited by other undesired deactivation pathways like excimer formation[53,65,156] and low SF yields.[151,157] To enhance the triplet yield for practical applications, alternate methods have to be developed. In this line, one of the most entrancing strategies is symmetry-breaking charge separation (SB-CS) mediated triplet population.[122,158] SB-CS is an excited-state process where a charge separated state (CSS) is formed by a pair of identical chromophores upon photoexcitation.[10,37,67,83,102,105,159] SB-CS is of great importance in natural photosynthetic light harvesting systems as well as emerging organic photovoltaics (OPVs).[40,41] SB-CS materials capable of triplet generation could potentially be beneficial for photoredox catalysis.[160]

Previously, at the single-molecule level, multichromophoric architectures have been explored extensively to understand excitation energy transfer and various electron transfer processes.[161,162] Single-molecule fluorescence microscopy (SMFM) measurements depict fluorescence on and off patterns (known as blinking) depending on the nature of the excited-states contributing to fluorescence.[163,164] The fluorescent states (on-states) are often called as bright states and the non-fluorescent states (off-states) are referred to as dark states. The dark states are usually attributed to the triplet state, photoisomers or generation of the charge transfer (CT)/charge separated state of the fluorophore of interest.[165] Understanding the dark states in organic fluorophores is crucial for the development and design of better emitters in imaging applications.[166] Albeit numerous reports on correlation of triplet excitons to the dark states in

PDI chromophores, the combination of CT/CSS and triplet states responsible for the dark off-states at the single-molecule level remains elusive.[65,158,167]

Our longstanding efforts to access long-lived triplet excitons in organic chromophores, motivated us to explore potential strategies for triplet generation in multichromophoric systems.[145,168] In this work, we reveal triplet excited-state population via ultrafast intramolecular SB-CS in a rigid perylenediimide trimer (**PDI-T**). The weak excitonically coupled **PDI-T** exhibits rigid ground- and excited-state structures, thereby suppressing the excimer formation channels.[64,75] SMFM measurements of **PDI-T** reveal contrasting blinking dynamics in a polar polyvinyl alcohol matrix compared to a nonpolar polystyrene matrix. In agreement with the single-molecule analysis, femtosecond and nanosecond transient absorption measurements of **PDI-T** at the ensemble level substantiate ultrafast SB-CS leading to the triplet state population in polar solvents.

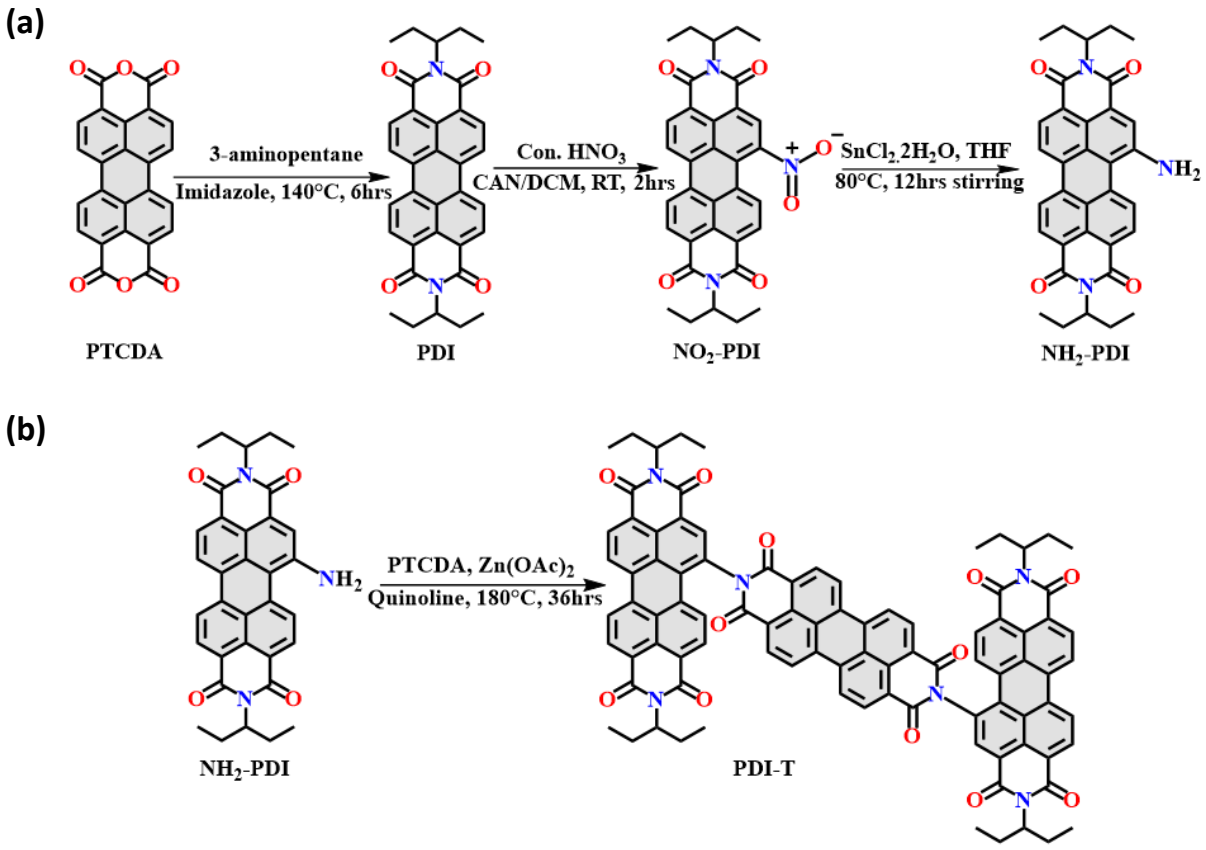

Scheme 3.1: Synthesis scheme of a) PDI, NO_2-PDI and NH_2-PDI; and b) **PDI-T**.

3.2. Results and Discussion

3.2.1 Trimer Molecule and the Optimized Structure

PDI-T was synthesized and characterized (Scheme 3.1 and Figures A3.1-A3.5) according to the previously reported and modified procedure,[107] starting from the parent PDI monomer (ref-PDI, Figures 3.1a and 3.1b). Density functional theory (DFT) was employed to perform ground-state geometry optimizations in vacuum at the B3LYP-D3/6-311G+(d,p) level of theory in Gaussian 16. The ground-state optimized geometry of **PDI-T** shows the central PDI bridge to have a planar π-core (Figure 3.1c), whereas the two terminal PDI units demonstrate a core-twist of 20.6° due to the resulting steric effects between the bay H atom and bulky PDI bridge (3-pentyl group was substituted with methyl group to lower the computational cost). The terminal and the central PDI units were found to be arranged in an edge-to-edge fashion with a dihedral angle (θ) of 70.3° and a centroid-centroid distance of $d_{\mathbf{PDI\text{-}PDI}}$ = 9.01 Å (Figures

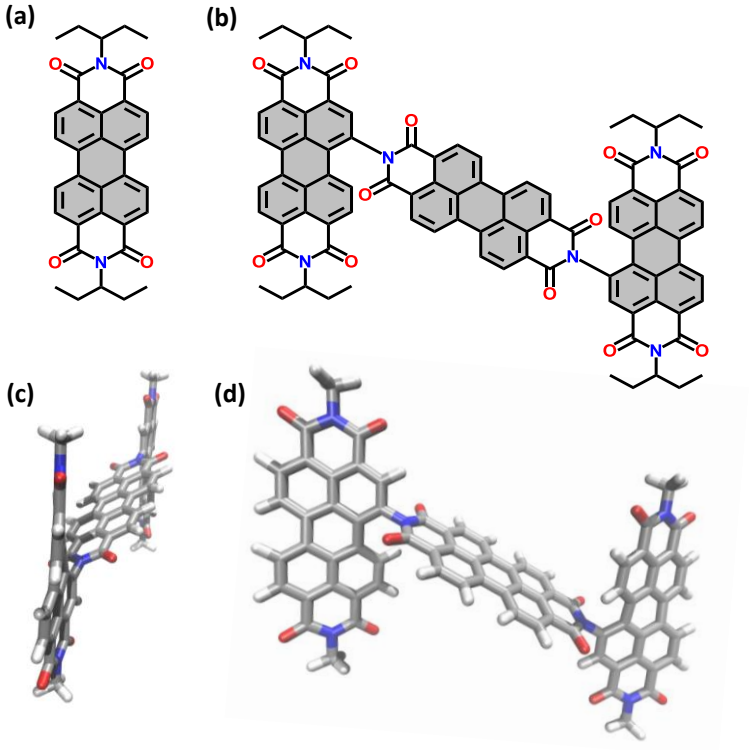

Figure 3.1: Molecular structures of a) ref-PDI and b) **PDI-T**. Ground-state optimized structure of **PDI-T** shown in c) side view and d) top view (3-pentyl group substituted with methyl group to minimize computational cost).

3.1d and A3.6). While the terminal PDI units demonstrate a large centroid-centroid distance of $d_{\mathbf{PDI\text{-}PDI}}$ = 18.03 Å (Figure A3.6 and Table A3.1).

3.2.2 Steady-State Photophysical Properties of PDI-T

The steady-state optical properties of **PDI-T**, and the parent compound (ref-PDI) were investigated by electronic absorption and fluorescence spectroscopic measurements in TOL (C_0 ≈ 0.5-1 μM). The UV-vis absorption spectrum of **PDI-T** exhibits a ≈ 4 nm hypsochromic shift in comparison to the parent ref-PDI monomeric unit with the absorption maximum at λ_{max}^{Abs} ≈ 523 nm (Figure 3.2a and Table A3.2) and a molar extinction coefficient (ε_{max}) of 90450 M^{-1} cm^{-1}. Additionally, broadening of the λ_{max}^{Abs} band of **PDI-T** was observed, and a unique red-shifted shoulder band was noticed at ≈ 535 nm (Figure 3.2a-inset). Shoulder absorption bands of red-shifted nature have been previously documented in various PDI derivatives, suggesting the effective mixing of the bright singlet excited-state (S_1) with the CT state[83] or the splitting of the locally excited-state due to excitonic coupling.[32,109,110]

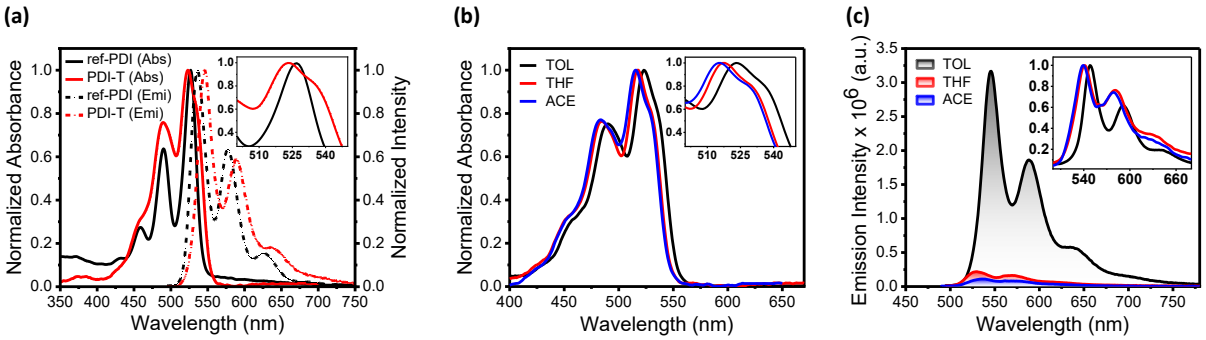

Figure 3.2: a) Normalized UV-vis absorption and emission spectra of ref-PDI (black) and **PDI-T** (red) in TOL. Inset shows the zoomed absorption spectra of ref-PDI and **PDI-T**, and a shoulder peaking at ≈ 535 nm was observed for **PDI-T**. b) Solvent-dependent normalized UV-vis absorption spectra of **PDI-T** in TOL (ε = 2.38), THF (ε = 7.58) and ACE (ε = 20.70). Inset shows the zoomed solvent-dependent absorption spectra of **PDI-T.** c) Solvent-dependent emission spectra of **PDI-T** display the significant quenching of the fluorescence intensity in polar THF and ACE solvents. Inset shows the zoomed-in solvent-dependent normalized emission spectra of **PDI-T.**

The emission spectrum of **PDI-T** in TOL (λ_{ex} = 480 nm, C_0 ≈ 0.5-1 μM) reveals well-resolved vibronic bands with the emission maximum at λ_{max}^{Emi} ≈ 546 nm (Figure 3.2a and Table A3.2). The emission maximum in **PDI-T** showcased a ≈ 9 nm bathochromic shift compared to ref-PDI (λ_{max}^{Emi} ≈ 537 nm, the emission spectrum of ref-PDI is reproduced adapting from the previously reported photophysical investigations on the parent PDI monomer).[108] Presumably, the extended π-conjugation between the three PDI units is manifested through the overall red-shift of the emission spectrum in **PDI-T**.

3.2.3 Solvent-Dependent Optical Properties of PDI-T

We carried out solvent-dependent UV-vis absorption and fluorescence measurements to comprehend the effect of the local dielectric environment moderating the excited-state optical properties of **PDI-T**. Three solvents of varied dielectric constants were used, *i.e.*, nonpolar TOL (ε = 2.38), moderately-polar THF (ε = 7.58) and highly-polar ACE (ε = 20.70). The solvent-dependent UV-vis absorption spectra of **PDI-T** display virtually similar spectra with ≈ 7 nm blue-shift for λ_{max}^{Abs} in ACE compared to TOL (Figure 3.2b).[169] Unlike the UV-vis absorption spectra, contrasting differences were observed in the solvent-dependent emission spectra of **PDI-T**. Significant quenching of the fluorescence emission intensity was observed while going from TOL to THF to ACE (Figure 3.2c) with ≈ 7-9 nm blue-shift for λ_{max}^{Emi} in polar solvents (Figure 3.2c-inset), and the fluorescence quantum yield (ϕ_{FL}) was calculated to be 10.4% in TOL, <1% in THF and <1% in ACE (Table A3.2). The lower ϕ_{FL} values of **PDI-T** compared to ref-PDI (ϕ_{FL} ≈ 98%)[108] and the solvent-dependent fluorescence quenching confirm the presence of other non-radiative decay channels involved in the excited-state dynamics of **PDI-T.** Additionally, UV-vis absorption spectra of **PDI-T** were recorded at varying concentrations in TOL, THF, and ACE to examine concentration-dependent behaviour. **PDI-T** shows the monomer nature following Beer-Lambert's law even at concentrations as high as 10 μM in all the solvents under investigation, and therefore all the ensemble level spectroscopic measurements were carried out at ≈ 0.5–3 μM concentrations of **PDI-T** (Figures A3.7-A3.9).

3.2.4 HOMO-LUMO Energy, Excited-State Geometry and TDDFT Energies

The DFT (B3LYP-D3/6-311G+(d,p)) calculated HOMO and LUMO energies of **PDI-T** were E_{HOMO}= -7.47 eV and E_{LUMO}= -3.29 eV, respectively. The significant stabilization of the HOMO occurs due to the extended π-conjugation between the three PDI units in **PDI-T**.[107] The electron density distribution in HOMO was found to be on the terminal PDI fragments, while LUMO exhibited electron density solely on the central PDI fragment (Figure A3.10). Further, solvent-dependent ground-state geometry optimizations of **PDI-T** were performed employing integral equation formalism polarizable continuum model (IEFPCM) at the DFT-B3LYP-D3/6-311G+(d,p) level of theory. The optimized ground-state structural parameters in the presence of solvent models are similar to each other with the core-twist of the terminal PDI fragments as 20.26° in TOL, 20.06° in THF and 20.04° in ACE (Figure A3.11). The above result indicates the rigidity of the ground-state conformation of **PDI-T** regardless of the local dielectric solvent medium. A one-dimensional relaxed potential energy surface (PES) scan as a function of dihedral between terminal PDI unit and central PDI unit, shows minimum energy conformation at θ=70° (Figure A3.12). The above result supports the restricted free rotation around C-N bonds in **PDI-T** and substantiates the rigidity of **PDI-T** ground-state structure.

Geometry optimization of the first singlet excited-state (S_1) in **PDI-T** was performed, to further probe the conformational rigidity of the S_1 state geometry. Figure A3.13 shows the S_1 optimized geometry at the CAM-B3LYP-D3/6-31G level of theory in vacuum. The S_1 optimized structure evidences core-twist of 18.0° (terminal PDIs) and a dihedral angle of 67.0° between the central and the terminal PDI units (Table A3.1). The S_1 optimized parameters were found to be similar to ground-state optimized parameters, and therefore, **PDI-T** is conformationally rigid and limits significant structural relaxation upon photoexcitation.

The vertical excitation energies (VEEs) calculated at CAM-B3LYP-D3/6-311G+(d,p) level of theory in vacuum reveal two bright states, S_1 and S_3, with significant oscillator strengths (*f*) for the **PDI-T** molecule, while the S_2 state exhibits zero oscillator strength (Table A3.3). The computed near-degenerate bright states in the VEE calculations explain the observation of the red-shifted shoulder band in the UV-vis absorption spectrum of **PDI-T** (*vide supra*). The near-degeneracy of the S_1 and S_3 states most probably arises from the weak

excitonic splitting of the locally excited energy level in **PDI-T**.[20,109] Further, computed natural transition orbitals (NTOs) demonstrate the locally excited nature of the $S_0 \rightarrow S_1$ and $S_0 \rightarrow S_3$ transitions, corroborating the probable population of both S_1 and S_3 states upon photoexcitation (Figures A3.14 and A3.15). The computed solvent-dependent VEEs of **PDI-T** show negligible change in the $S_0 \rightarrow S_1$ transition energies (Table A3.4).

3.2.5 Fragment-Based Excited-State and Excitonic Coupling Analyses

To obtain insights into the nature of different excited-states, fragment-based excited-state analysis was performed.[128,129] Three fragments, two terminal PDI**s**, and one central PDI were considered for the analysis (Figure A3.16). S_1 (f=0.99) and S_3 (f=1.51) are localized Frenkel states with CT values of 0.01 and 0.04, respectively (Figure A3.17a). Both the hole-electron isosurfaces are localized on the central PDI fragment in the S_1 state (PR=1.3), whereas in the S_3 state, they are localized on both the terminal PDI fragments (PR=2.6) (Figure A3.17b). Nearly degenerate S_4 (f=0.0) and S_5 (f=0.03) states possess pure CT state character with CT values of 0.95. For the S_4 and S_5 states, the hole is localized on the terminal PDI fragments, and the electron is localized on the central PDI fragment, respectively (Figure A3.17b). Long-range Coulombic coupling (J_{Coul}) interactions were calculated to investigate the excitonic interactions integral to the spatial orientation of the PDI subunits in **PDI-T**.[24,133] The trimer moiety was fragmented into three units and coupling values were investigated for the singlet excited-state with highest oscillator strength (Figure A3.16). The J_{Coul} value for fragments 1 and 2 was computed to be −2.69 cm^{-1}; and for the fragments 1 and 3 J_{Coul} was nearly zero. The obtained J_{Coul} values suggest weak excitonic interactions between the individual PDI units.

3.2.6 Rehm-Weller Analysis for PDI-T

Rehm-Weller formulation was employed to estimate the thermodynamic feasibility of CS and CR processes through the calculation of the free energy changes of CS (ΔG_{CS}) and CR (ΔG_{CR}) in **PDI-T** in solvents of varied dielectric constants (Table 3.1).[127] The essential parameters for Rehm-Weller formulation were obtained using cyclic voltammetry (CV) and differential pulse voltammetry (DPV) (Figure A3.18 and Table A3.5). The Ag/Ag^+ and glassy carbon electrodes were used as the reference and working electrodes, respectively.[65] **PDI-T** exhibits three consecutive reversible reduction waves in the voltammograms (E_1(red) = −1.02 V, E_2(red) =

−1.20 V and E_3(red) = −1.42 V)). The free energy change (ΔG_{CS}) for **PDI-T**, calculated using the Rehm-Weller equation, was found to be approximately +0.06 eV in TOL, −0.11 eV in THF, and −0.18 eV in ACE. The slightly positive ΔG_{CS} value in TOL indicates that complete charge separation is thermodynamically unfavourable in nonpolar medium, unlike in THF and ACE, where the negative values support spontaneous charge separation.

3.2.7 Single-Molecule Fluorescence Measurements of PDI-T

Having established the moderate fluorescence in nonpolar medium and significant quenching of fluorescence in the polar media for **PDI-T**, we carried out single-molecule fluorescence measurements to characterize the dark states responsible for the fluorescence quenching in **PDI-T** molecule under the influence of different dielectric environments. Polystyrene (PS, ε = 2.60) and polyvinyl alcohol (PVA, ε = 7.80) were employed as the polymeric analogues for the nonpolar and polar medium, respectively for the SMFM measurements. The samples for the SMFM experiments were prepared via spin-coating **PDI-T** in PS (nonpolar) and PVA (polar) matrices to incorporate the influence of varied solvent polarity and polarizability.[170] The

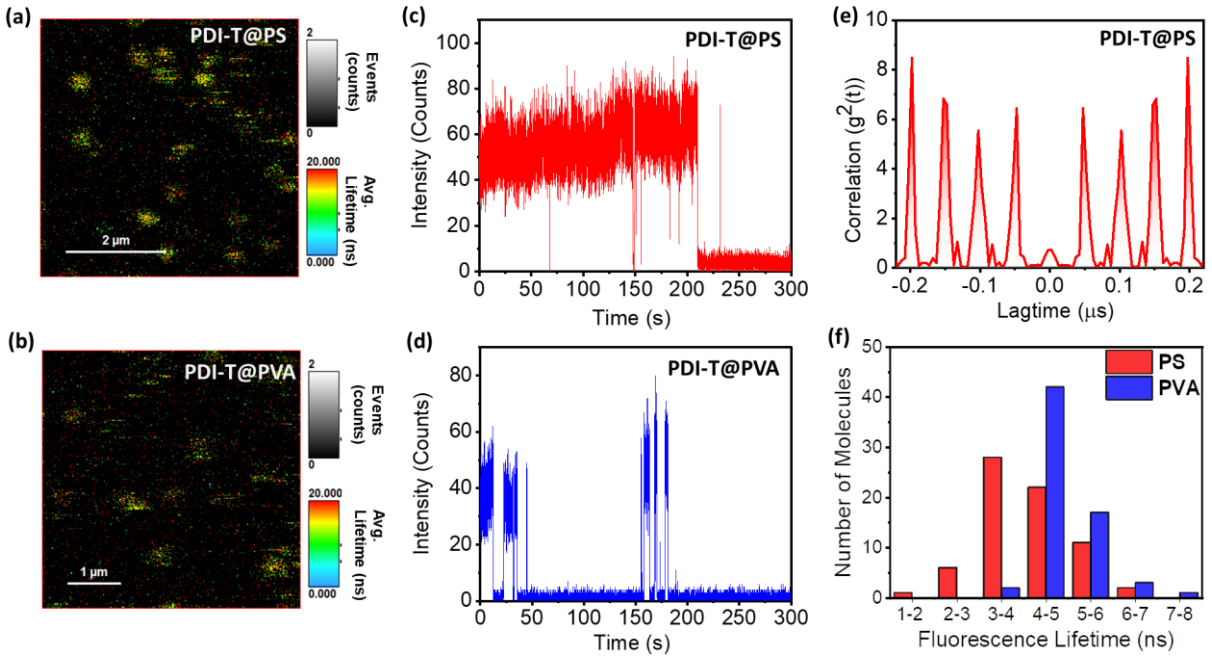

Figure 3.3: Representative FLIM images of **PDI-T** in a) PS and b) PVA. FIT traces of **PDI-T** in c) PS and d) PVA. e) Representative antibunching measurement of **PDI-T** in PS. f) The single-molecule fluorescence lifetime double histogram of **PDI-T** in PS and PVA.

fluorescence-lifetime imaging microscopy (FLIM) images were acquired for **PDI-T** in PS and PVA (Figures 3.3a and 3.3b). The fluorescence intensity trajectories (FITs) of the **PDI-T** molecule were recorded by exciting the sample at 510 nm with a repetition rate of 20 MHz (Figures A3.19 and A3.20). In PS, the FIT blinking patterns for 93 single molecules involve short and long off-states observed within a time frame of 300 s. Single-step and multistep FITs were also observed with a combination of long and short off-states for **PDI-T** in PS (Figure 3.3c). The on- and off-states for a given FIT are defined with an intensity threshold. Short off-states observed in the FITs could possibly be attributed to the population of triplet states. The long off-states are usually attributed to photoexcitation-induced radical ions or charge separated states.[65,163–165] In a nonpolar polymer medium like PS, the long off-states observed in **PDI-T** molecules could possibly be due to the radical pair generated from the population of the CT state. The single-step traces are probably the partially photobleached **PDI-T** molecules during the single-molecule fluorescence measurements.[165]

In a polar PVA matrix, the FIT traces for 133 molecules were acquired with a total time frame of 300 s. The FLIM image of **PDI-T** in PVA (Figure 3.3b) shows increased blinking, which is visible as the dark pixel lines in the scanning region of the sample. The duration of the fluorescence on-state for **PDI-T** in PVA is short compared to that in PS. The majority of the FITs (~65 molecules, Figure A3.20) of **PDI-T** in PVA depict short on-states resulting in low fluorescence intensity counts. The FITs for most single-molecule fluorescence measurements in PVA have erratic blinking patterns and disappear in the middle of the scan in FLIM images.[80] The lower fluorescence photon count and erratic blinking in PVA for **PDI-T** possibly arises due to the lowering of the ΔG_{CS}, facilitating CS in the polar matrix. Frequent off-states with variable duration (long and short) in the FITs of **PDI-T** in PVA matrix could be attributed to a combination of triplet and charge separated states (Figure 3.3d). The fluorescence lifetime distribution for **PDI-T** at the single-molecule level in PS (70 molecules, Figure A3.21a) depicts a broad distribution having the maximum centered at 3 to 4 ns (Figure 3.3f). The broad nature of the fluorescence lifetime distribution in PS could be attributed to a combined contribution of the free volume dynamics and core-twist in **PDI-T**.[56] In PVA, the fluorescence lifetime distribution is narrow compared to the fluorescence lifetime distribution in PS, with the maximum at 4 to 5 ns (Figure 3.3f). The change in fluorescence lifetime for

PDI-T in PVA compared to PS could possibly be attributed to the hydrogen bond networks in PVA restricting vibrations contributing to the non-radiative decay pathways. The deviation from the optical alignment is observed as a gradual decline in the fluorescence intensity in FITs.[171] Photon antibunching experiments are based on the sub-Poissonian nature of light and are conducted to verify the observation of a single emitter.[172] The second-order photon correlation analysis is employed to examine the photon coincidences in the molecular emitters. The antibunching measurements were carried out for **PDI-T** in PS and PVA matrices and the performed measurements gave antibunching data for **PDI-T** in PS (Figures 3.3e and A3.22).

3.2.8 Femtosecond Transient Absorption Measurements of PDI-T

To further characterize the nature of the short and long off-states observed in the SMFM measurements of **PDI-T**, we performed solvent dielectric-dependent femtosecond transient absorption (fsTA) measurements in TOL, THF and ACE ($C_0 \approx$ 2-3 μM, photoexcited at 480 nm with a 100 fs laser pulse). Upon photoexcitation, the fsTA spectra of **PDI-T** in TOL (ε = 2.38,

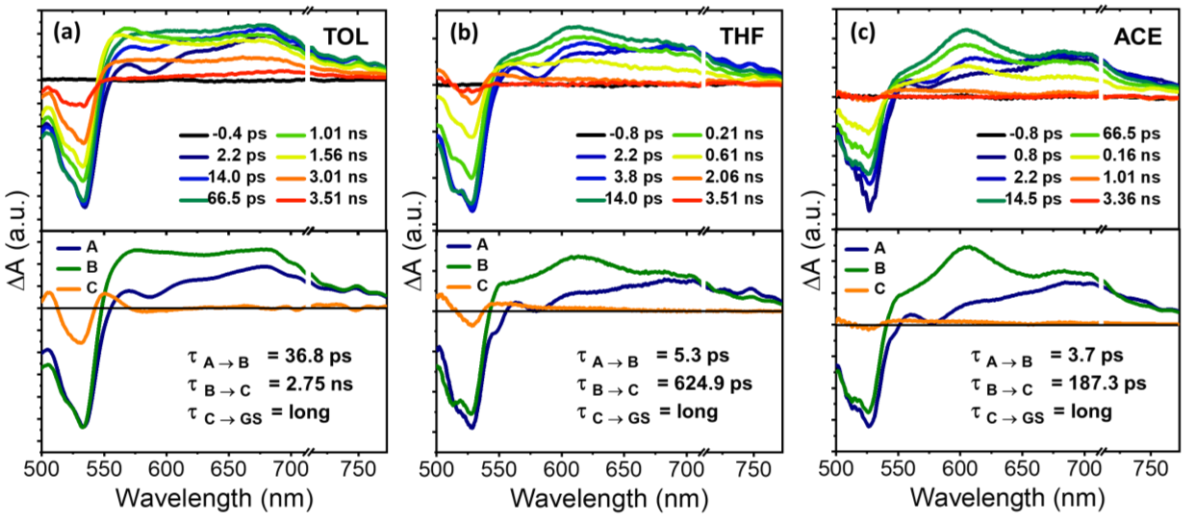

Figure 3.4: (Top row) FsTA spectra of **PDI-T** in a) TOL, b) THF, and c) ACE showing the excited-state dynamics upon photoexcitation. (Bottom row) EAS reconstructed from global analysis of **PDI-T** with A → B → C → GS model for TOL (left), THF (center) and ACE (right), where A is the singlet excited-state, B is the CT state in case of TOL and, the CSS in the case of THF and ACE, C is the triplet excited-state, and GS is the ground-state (λ_{ex} = 480 nm).

Figure 3.4a-top) depict negative GSB and/or SE at ≈ 500 to 550 nm and positive ESA centered at ≈ 682 nm. The ESA at ≈ 682 nm represents the distinct spectral feature of the singlet excited-state (**^{1}PDI-T***) of the parent ref-PDI monomer.[64,70,85] Within 36.8 ps, the **^{1}PDI-T*** state decays, and a new transient species exhibiting a broad ESA at ≈ 548 to 750 nm emerges. The newly formed transient species shows two peak maxima at ≈ 577 and 680 nm, relatively in line with the spectral signature of ref-PDI**'s** radical cation ($PDI^{\bullet+}$) and radical anion ($PDI^{\bullet-}$), respectively.[64,65,70,105] However, the ESA feature is broader than the typically observed spectroscopic signatures of CSS in PDI chromophores.[10] The broadening of the spectral trace could be due to the incomplete CS in **PDI-T** in TOL, which is assigned to a CT state.[78,83,173] At higher time delays, The CT state decays to give rise to a new species having positive ESA with a maximum at ≈ 550 nm. The newly emerging transient species was found to be long-lived and did not decay within the fsTA experimental time window of 3.6 ns.

Contrastingly, **PDI-T** in polar THF ($\varepsilon = 7.58$) and ACE ($\varepsilon = 20.70$) displays significantly different excited-state dynamics as compared to nonpolar TOL. Upon photoexcitation at 480 nm, the fsTA spectra of **PDI-T** in THF solution in the initial few picoseconds (Figure 3.4b-top) were characterized by fast decay of the **^{1}PDI-T*** state with GSB and/or SE as a negative feature at ≈ 500 to 548 nm and ESA as a positive feature at ≈ 682 nm. The **^{1}PDI-T*** state decays in ultrafast timescale to form a new transient species with ESA at ≈ 613 and 702 nm, corresponding to the unique spectral signature of the parent ref-PDI**'s** $PDI^{\bullet+}$ and $PDI^{\bullet-}$, respectively (Figures A3.23 and A3.24).[64,65,70,105] The coexistence of the $PDI^{\bullet+}$ and $PDI^{\bullet-}$ represents the CSS and recommends that SB-CS operate between the analogous monomeric PDI units in **PDI-T**. Eventually, the CSS decays within few hundreds of picoseconds and evolves to a new transient species exhibiting broad ESA feature having maximum at ≈ 545 nm which did not decay within the fsTA experimental time window. Likewise, fsTA measurements of **PDI-T** in ACE revealed GSB and/or SE at ≈ 500 to 547 nm and ESA corresponding to the **^{1}PDI-T*** state centered at ≈ 684 nm in the initial few picoseconds (Figure 3.4c-top). The locally excited **^{1}PDI-T*** state demonstrates ultrafast decay to give rise to the CSS having prominent $PDI^{\bullet+}$ and $PDI^{\bullet-}$ ESA features at ≈ 607 and 702 nm, respectively. At higher time delays, the appearance of a newly formed transient species was observed at ≈ 543 nm following the rapid

decay of the CSS. The new transient species detected in the fsTA spectra in ACE was concordant to the third species obtained in THF having positive broad ESA with maximum at ≈ 545 nm and long lifetime.

The EAS for the aforementioned transformations were obtained through global analysis of the fsTA data.[112] Figures A3.25, A3.26, and A3.27 present representative kinetic traces at various wavelengths overlaid with globally fitted curves, illustrating the accuracy of the fitting results. The EAS of **PDI-T** in TOL show three principal components (Figure 3.4a-bottom); the first component (A) is attributed to the locally excited singlet state (**^{1}PDI-T***). The **^{1}PDI-T*** component undergoes rapid decay (36.8 ps) to form the second principal component (B). Component (B) was assigned to a CT state (Figure A3.28). CT state corresponds to incomplete or partial charge separation, whereas complete charge separation between donor and acceptor moieties creates a CSS.[59,66,174–176] The observation of a CT state instead of a CSS in the excited-state dynamics of **PDI-T** in TOL, could be due to the higher energy of the CT state under the influence of a less polar dielectric medium.[105,124] The CT state (component (B)) decays within 2.75 ns, forming component (C) in the EAS (Figure 3.4a-bottom). Component (C) is a long-lived species and could be due to the population of triplet states in **PDI-T**.[139,177]

The EAS of **PDI-T** in THF and ACE showed distinct evidence of forming the CSS (component (B)) through ultrafast CS from the initially populated locally excited singlet state (component (A)) with time constants of 5.3 ps and 3.7 ps, respectively (Figures 3.4b-bottom, 3.4c-bottom and A3.28).[113] Ultrafast CS observed in **PDI-T** in the presence of polar dielectric

Table 3.1: Time constants (τ), rate constants (k), driving forces (ΔG) for SB-CS and triplet quantum yields (ϕ_T) of **PDI-T** in different dielectric media.

Solvent	τ_{CT} (ps)	τ_{CS} (ps)	k_{CS} (s^{-1})	ΔG_{CS} (eV)	τ_{CR} (ps)	k_{CR} (s^{-1})	ΔG_{CR} (eV)	ϕ_T (%)
TOL (ε=2.38)	36.8	-	-	+0.06	2750.0	3.6×10^8	−2.37	65.6
THF (ε=7.58)	-	5.3	1.9×10^{11}	−0.11	624.9	1.6×10^9	−2.21	29.8
ACE (ε=20.70)	-	3.7	2.7×10^{11}	−0.18	187.3	5.3×10^9	−2.16	22.2

environments could have originated from the lowering of the CSS energies relative to the **^{1}PDI-T*** state energy.[10,64,65,70,114,178] The CSS in **PDI-T** exhibits slow CR in THF solvent with a time constant of 624.9 ps to form the third component (C). While, in ACE the CSS undergoes fast CR (187.3 ps) to form component (C). We hypothesize that a triplet excited-state (component (C)) is populated in **PDI-T** through CR from the CSS in both THF and ACE (*vide infra*).[145] The global analysis derived fitted time constants (τ) and rate constants (k) of CT, CS, and CR processes in **PDI-T** in different solvents are provided in Table 3.1. Additionally, to investigate the possibility of excitation-dependent photophysics in **PDI-T**, we have recorded the fsTA spectra by photoexciting the sample at 532 nm in TOL, THF and ACE (Figure A3.29). The excited-state dynamics of **PDI-T** observed at 532 nm and 480 nm excitation were identical with similar time constants, and hence, we exclude the effects of different excitation wavelengths in **PDI-T** (refer to section 3.6.5 for more details).

3.2.9 Nanosecond Transient Absorption Measurements of PDI-T

Nanosecond transient absorption (nsTA) measurements of **PDI-T** were executed in solvents of varying polarity (TOL, THF, and ACE), to characterize the long-lived state (C) detected in fsTA experiments. Upon photoexcitation at 532 nm, the nsTA spectra of **PDI-T** in nitrogen-enriched TOL (C_0 ≈ 2-3 μM) exhibited positive ESA bands at ≈ 480, 513, and 570 nm (Figure A3.30a) characteristic of the PDI triplet state absorption ($T_1 \rightarrow T_n$ transitions).[117–119] Along with ESA, intense GSB and/or SE was observed at ≈ 523 to 553 nm. The nsTA spectra of **PDI-T** evidenced ESA bands at ≈ 510 and 571 nm in both THF and ACE solvents (Figures A3.30b and A3.30c). Rapid decay of the positive ESA bands was observed upon performing the nsTA measurements in oxygen-purged solutions, confirming the population of triplet manifolds in **PDI-T** upon photoexcitation (Figure A3.31a-c). The fitted triplet lifetimes (τ_T) for **PDI-T** were 2.48 μs in TOL, 3.15 μs in THF and 1.94 μs in ACE (Figure A3.32a-c). The triplet quantum yields (ϕ_T) of **PDI-T** in different solvents were calculated with $[Ru(bpy)_3]^{2+}$ as a standard (ϕ_T ≈ 100% in methanol).[119] **PDI-T** exhibited ϕ_T of 65.6%, 29.8%, and 22.2% in TOL, THF, and ACE solvents, respectively (Figures A3.33, A3.34 and Table 3.1). The obtained higher values of charge recombination rates for **PDI-T** (k_{TOL}^{CR} = 3.6 x 10^8 s^{-1}, k_{THF}^{CR} = 1.6 x 10^9 s^{-1} and k_{ACE}^{CR} = 5.3

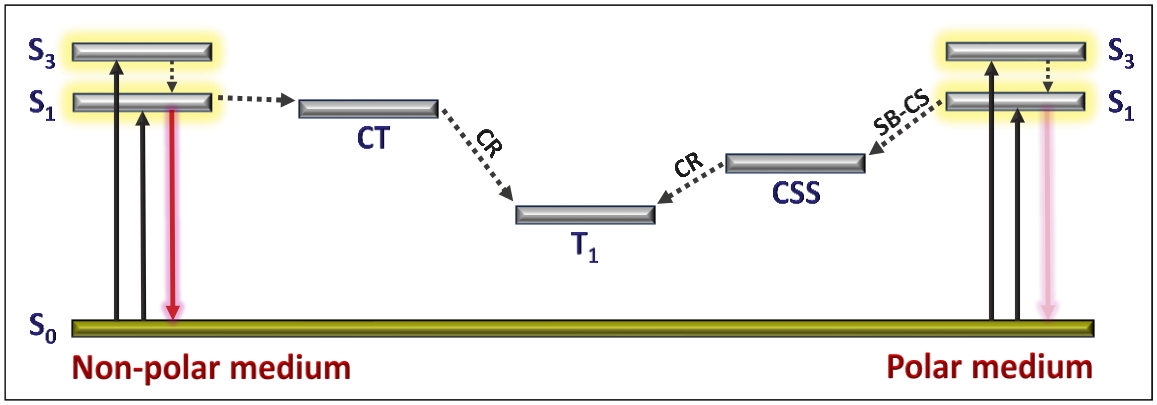

Figure 3.5: Proposed Jablonski diagram consolidating the excited-state dynamics of **PDI-T** upon photoexcitation under the influence of nonpolar and polar dielectric media; SB-CS = symmetry-breaking charge separation, CT = charge transfer state, CSS = charge separated state, CR = charge recombination, S_0 = ground-state, S_1 = first singlet excited-state, S_3 = third singlet excited-state and T_1 = first triplet excited-state.

x 10^9 s^{-1}), suggest spin-orbit charge transfer intersystem crossing (SOCT-ISC) mechanism as the most probable pathway for triplet population.[116,145] The CT recombination process for **PDI-T** in TOL is comparatively slower (2.75 ns) than the CR dynamics in THF (624.9 ps) and ACE (187.3 ps), therefore, spin-allowed relaxation to the ground-state and ISC to populate the triplet excited-state becomes competitive in TOL.[17] The slower CT recombination could be the probable reason for the higher ϕ_T in **PDI-T** in nonpolar TOL.[122,139,177]

3.2.10 Proposed Jablonski Diagram

Schematic Jablonski diagram summarizing the mechanism of triplet excited-state population in **PDI-T** upon photoexcitation in different dielectrics is shown in Figure 3.5. **PDI-T** populates triplet excited-states via CR from the CSS in polar dielectrics like THF, ACE and PVA. Whereas, in nonpolar TOL and PS, triplet states are largely generated via the CT state.[122,139,177]

3.3. Conclusion

In summary, we have synthesized a PDI-based rigid trimer, **PDI-T,** exhibiting symmetry-breaking charge separation mediated triplet population upon photoexcitation. Fragment-based excited-state analysis provides evidence for the occurrence of CT states in the **PDI-T** trimer. The weak Coulombic coupling prevalent between the individual monomer units favors CS over excimer formation.[64,104] At the single-molecule level, **PDI-T** demonstrates contrasting blinking patterns based on the polarity of the matrices. In a nonpolar polystyrene matrix, the observed short and long off-states in the FITs are attributed to the triplet and CT dark states, respectively. While, the FITs obtained in the presence of polar polyvinyl alcohol matrix were representative of a combination of charge separated and triplet dark states with long and frequent short off-states. FsTA and nsTA measurements of **PDI-T** revealed ultrafast CS (τ_{CS} = 3.7 ps in ACE and 5.3 ps in THF) preceding triplet excited-state population. Triplet-triplet energy transfer experiments corroborated the generation of triplet excited-states in **PDI-T**. Negative ΔG_{CS} in **PDI-T** renders SB-CS feasible and accelerates CS in the presence of polar dielectric medium. The correlation between the excited-state photophysics of **PDI-T** obtained at the single-molecule and ensemble levels provides comprehensive understanding of the triplet generation mechanism and the SB-CS dynamics. Therefore, this contribution could be highly beneficial for realizing various multichromophoric molecular constructs capable of efficient symmetry-breaking charge separation mediated triplet population for applications in single-molecule electronics.

3.4. Experimental Section

3.4.1. Syntheses and Characterization

Synthesis and characterization of PDI is detailed in section 2.4.1.[136]

Synthesis and characterization of NO_2-PDI is detailed in section 2.4.1.[107,137]

Synthesis and characterization of NH_2-PDI is detailed in section 2.4.1.[107]

Synthesis of PDI-T: PDI-T was synthesized by adopting a previously established method.[107] A reaction mixture consisting of NH_2-PDI (110 mg, 0.20 mmol), PTCDA (16.94 mg, 0.032

mmol), zinc acetate (20 mg, 0.0848 mmol), and 5 mL of quinoline was stirred at 180 °C for 36 hr under a nitrogen atmosphere. Upon completion, the mixture was allowed to return to room temperature and subsequently poured into 200 mL of 2 M aqueous HCl. The product was extracted three times with DCM and dried using anhydrous sodium sulfate. The resulting crude compound was subjected to purification via silica gel column chromatography using a petroleum ether and DCM solvent system (1:4 v/v), yielding the pure target molecule as a red solid (30 mg, 34% yield).

^{1}H NMR (500 MHz, $CDCl_3$, ppm) δ = 8.89–8.74 (m, 16H), 8.72–8.69 (m, 2H), 8.61–8.57 (m, 2H), 8.49–8.46 (m, 2H), 5.23–5.04 (m, 4H), 2.32–2.20 (m, 8H), 1.99–1.78 (m, 8H), 0.90–0.75 (m, 24H).

^{13}C NMR (125 MHz, $CDCl_3$, ppm) δ = 162.42, 162.39, 134.84, 134.82, 133.97, 133.95, 133.11, 132.37, 131.85, 131.76, 130.40, 129.13, 128.35, 127.32, 126.10, 126.06, 125.88, 124.28, 124.21, 123.50, 123.45, 123.10, 122.84, 122.72, 122.60, 122.41, 122.07, 56.86, 56.66, 30.90, 28.67, 28.34, 23.97, 23.91, 21.67, 13.10, 10.30, 10.24.

MS (MALDI-TOF) m/z calculated for $C_{92}H_{66}O_{12}N_6$ $[(M+H)^+]$; 1448.47; found 1448.21.

Elemental analysis calculated for $C_{92}H_{66}N_6O_{12}$: C, 67.95%; H, 4.80%; N 4.68%. Found: C, 67.96%; H, 4.87%; N, 4.77%.

3.5. Additional Figures and Tables

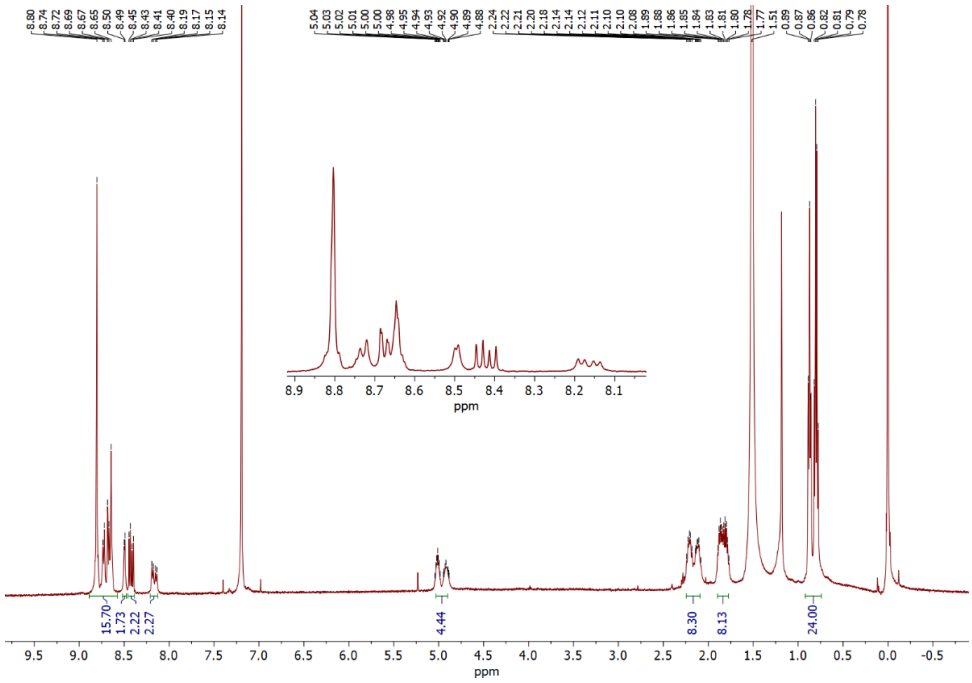

Figure A3.1: ^{1}H-NMR spectrum of **PDI-T** in $CDCl_3$.

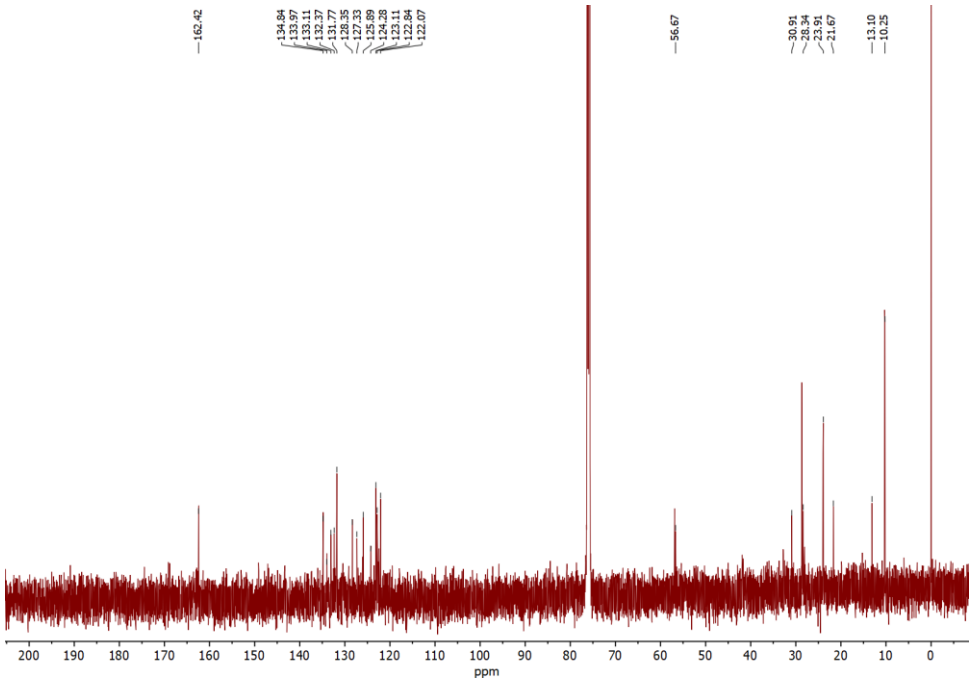

Figure A3.2: ^{13}C-NMR spectrum of **PDI-T** in $CDCl_3$.

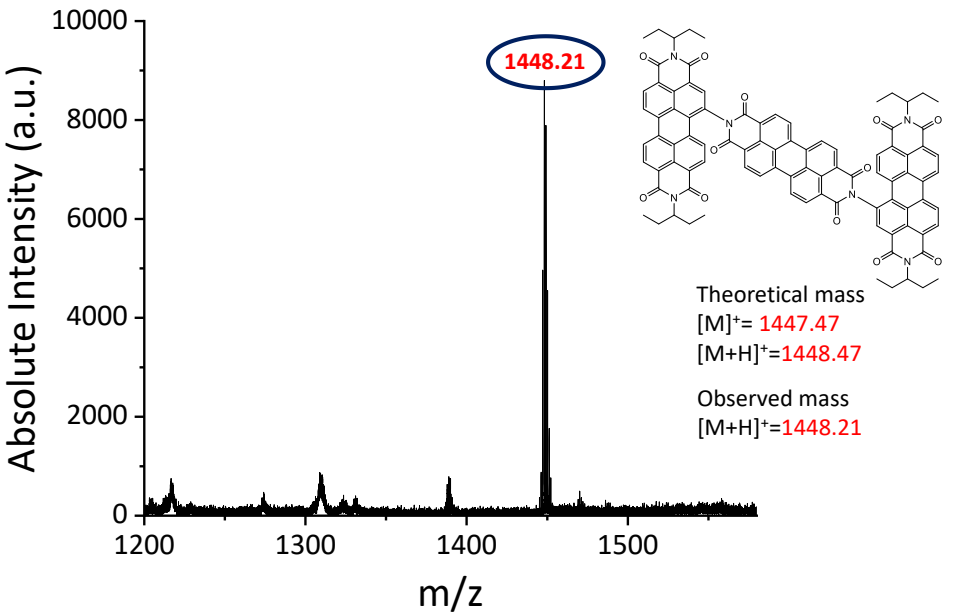

Figure A3.3: MALDI mass spectrum of **PDI-T** with the highlighted molecular mass.

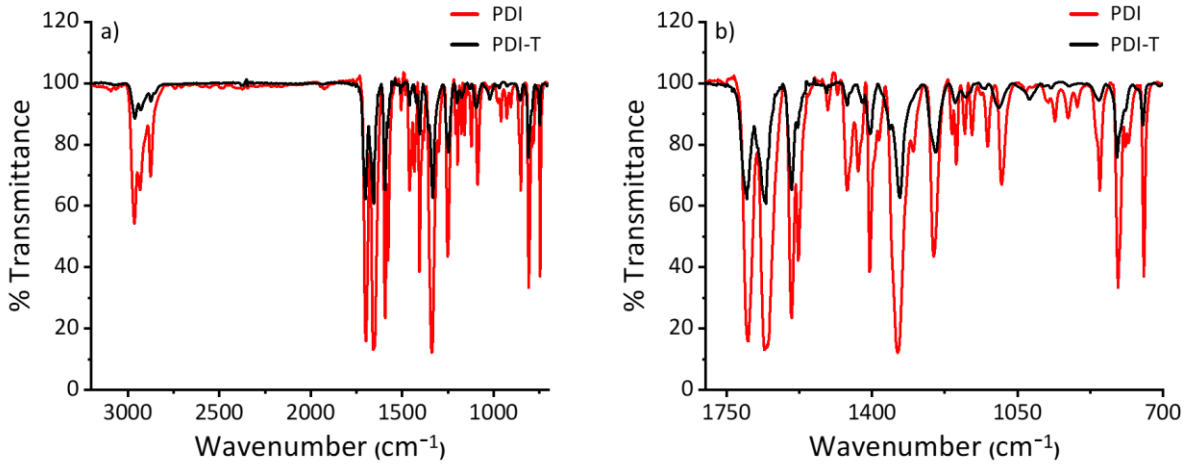

Figure A3.4: a) The entire FT-IR spectrum of **PDI-T** and b) the enlarged fingerprint region to pinpoint the similarity of **PDI-T** with the PDI monomer.

Powder nature retained at 300° C

Figure A3.5: Melting point tube with the **PDI-T** sample and the measurement indicated the melting point of **PDI-T** to be >300 ºC.

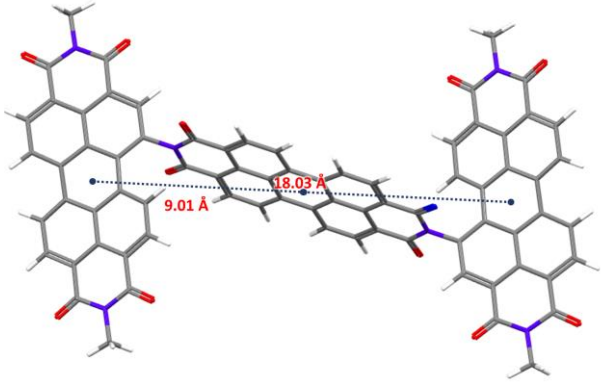

Figure A3.6: Centroid to centroid distances depicted in the ground-state optimized geometry of **PDI-T** in vacuum**.**

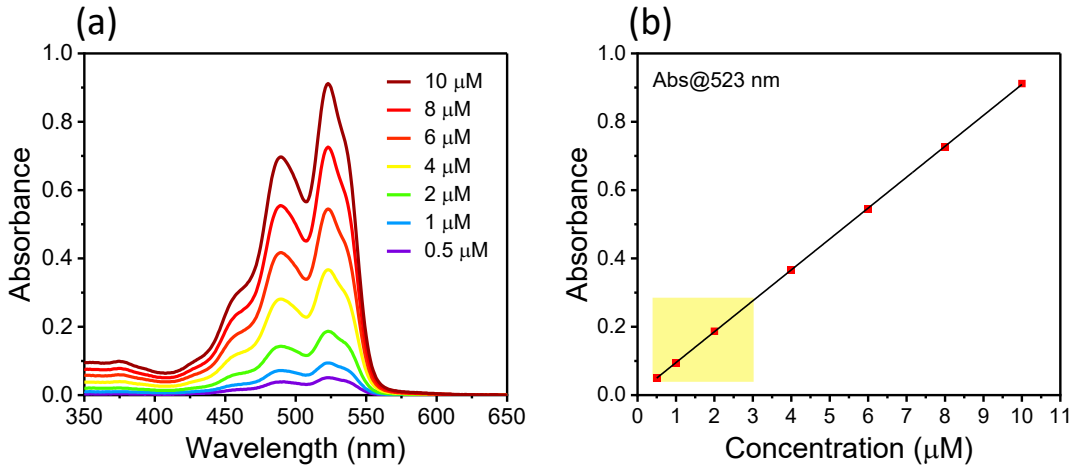

Figure A3.7: a) Concentration-dependent UV-vis absorption spectra and b) absorption maxima (λ_{max}^{Abs} = 523 nm) versus concentration plot of **PDI-T** in TOL.

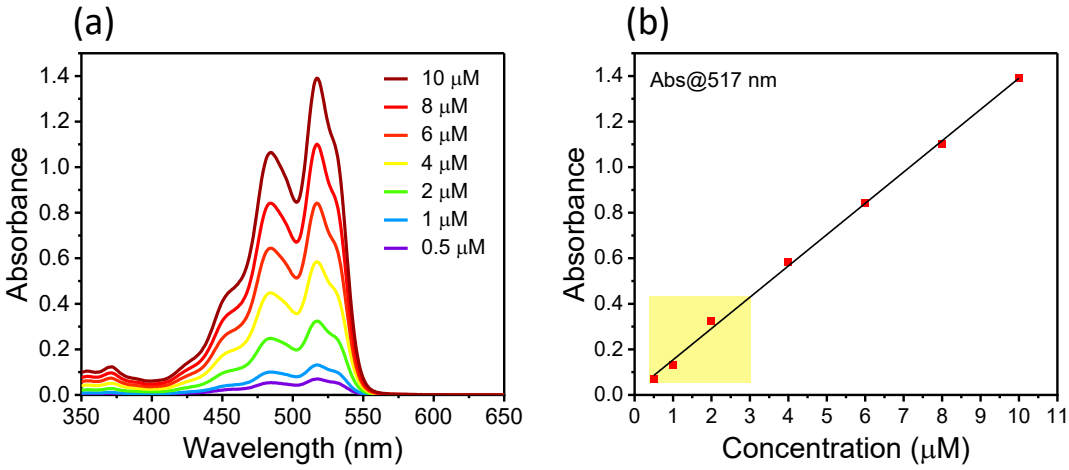

Figure A3.8: a) Concentration-dependent UV-vis absorption spectra and b) absorption maxima (λ_{max}^{Abs} = 517 nm) versus concentration plot of **PDI-T** in THF.

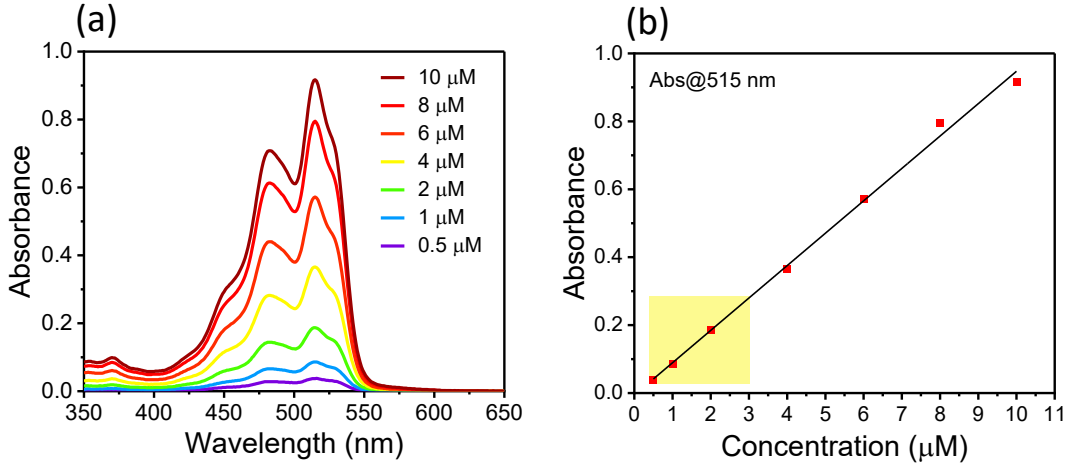

Figure A3.9: a) Concentration-dependent UV-vis absorption spectra and b) absorption maxima (λ_{max}^{Abs} = 515 nm) versus concentration plot of **PDI-T** in ACE.

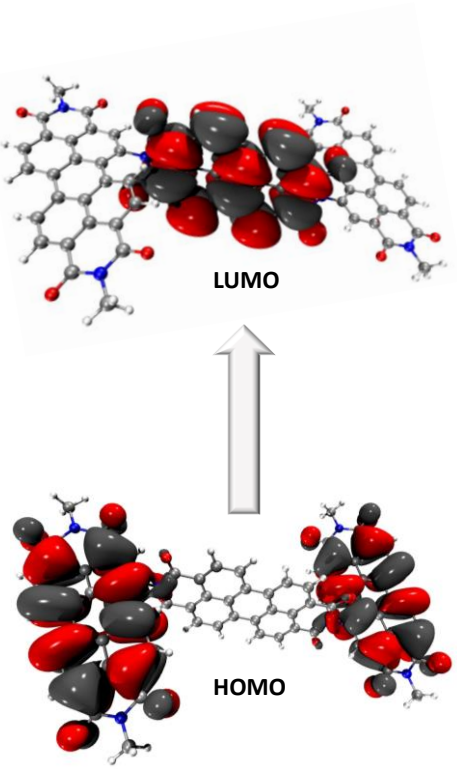

Figure A3.10: HOMO-LUMO isosurface (isovalue = 0.01 a.u) obtained from the ground-state optimized geometry of **PDI-T** at B3LYP-D3/6-311+G(d,p) level of theory in vacuum.

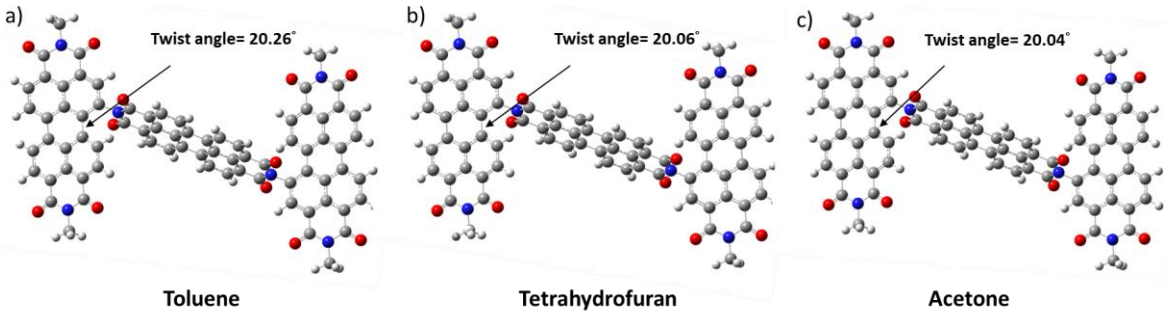

Figure A3.11: Ground-state optimized geometries of **PDI-T** in a) TOL, b) THF and c) ACE using IEFPCM model at the B3LYP-D3/6-311G+(d,p) level of theory.

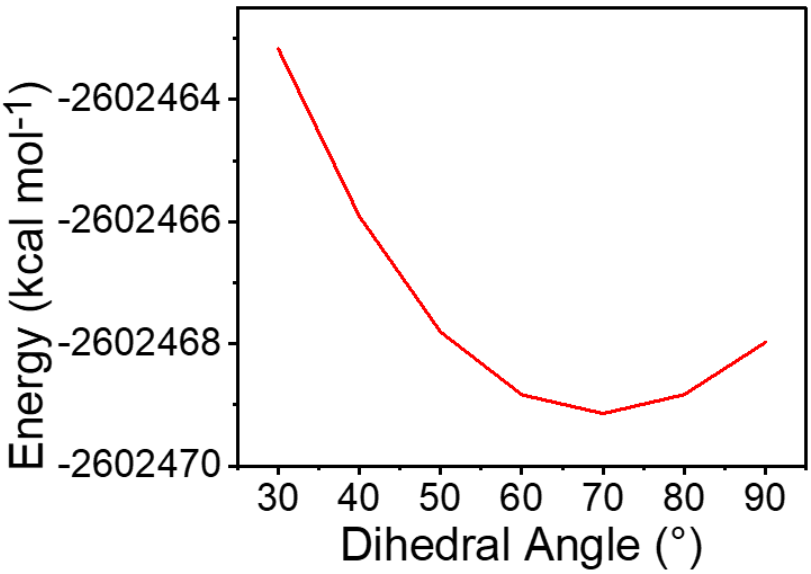

Figure A3.12: One-dimensional relaxed potential energy surface (PES) of **PDI-T** scan as a function of dihedral angle**.**

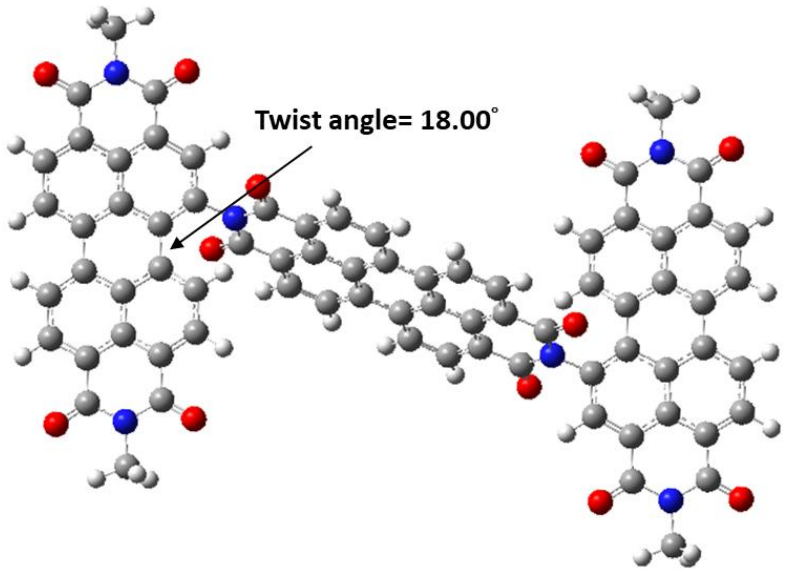

Figure A3.13: S_1-state optimized geometry of **PDI-T** in vacuum at the CAM-B3LYP-D3/6-31G level of theory.

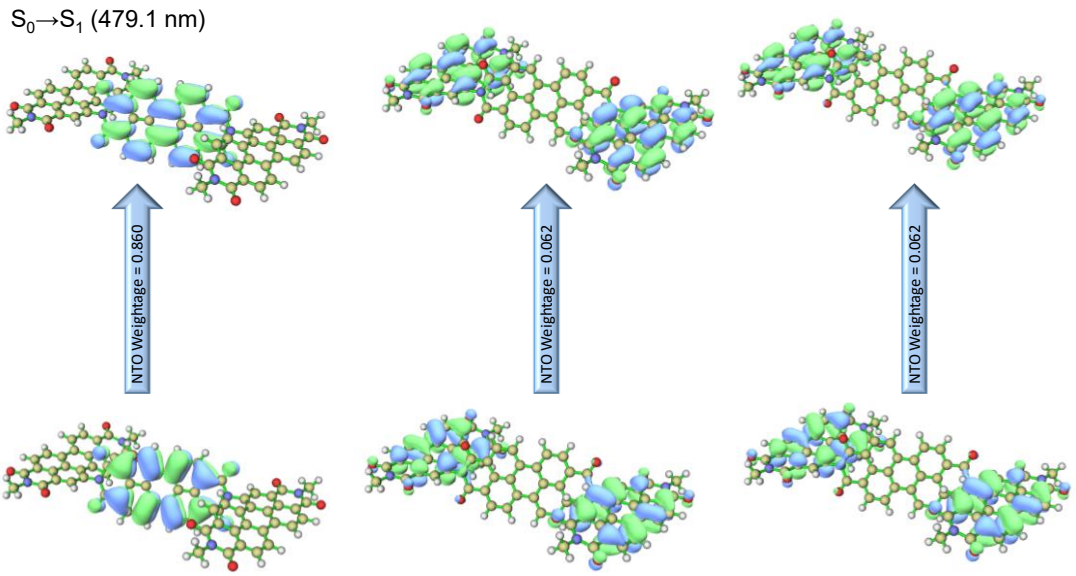

Figure A3.14: TDDFT calculated natural transition orbitals (NTOs) of the first singlet excited-state (S_1) of **PDI-T**. The corresponding weightages of the NTOs and the wavelength are mentioned.

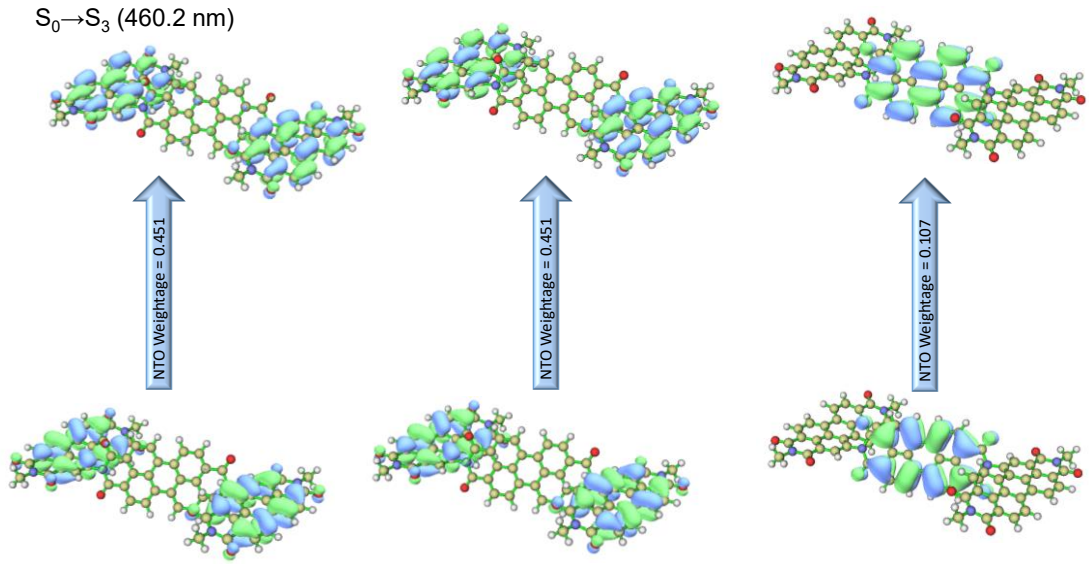

Figure A3.15: TDDFT calculated natural transition orbitals (NTOs) of the third singlet excited-state (S_3) of **PDI-T**. The corresponding weightages of the NTOs and the wavelength are mentioned.

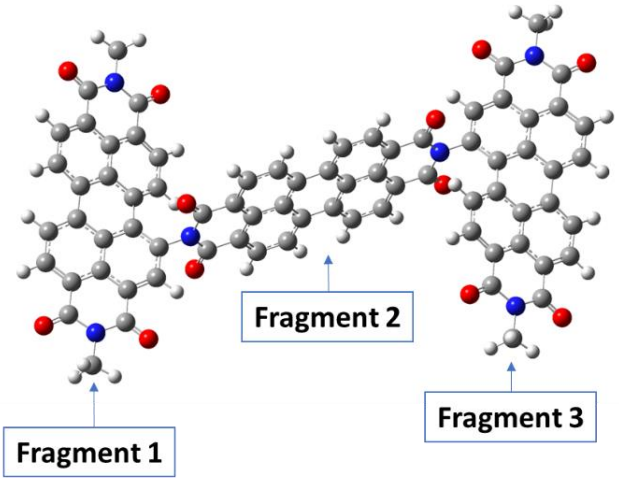

Figure A3.16: PDI-T fragments used for the Coulombic coupling and TheoDORE analyses**.**

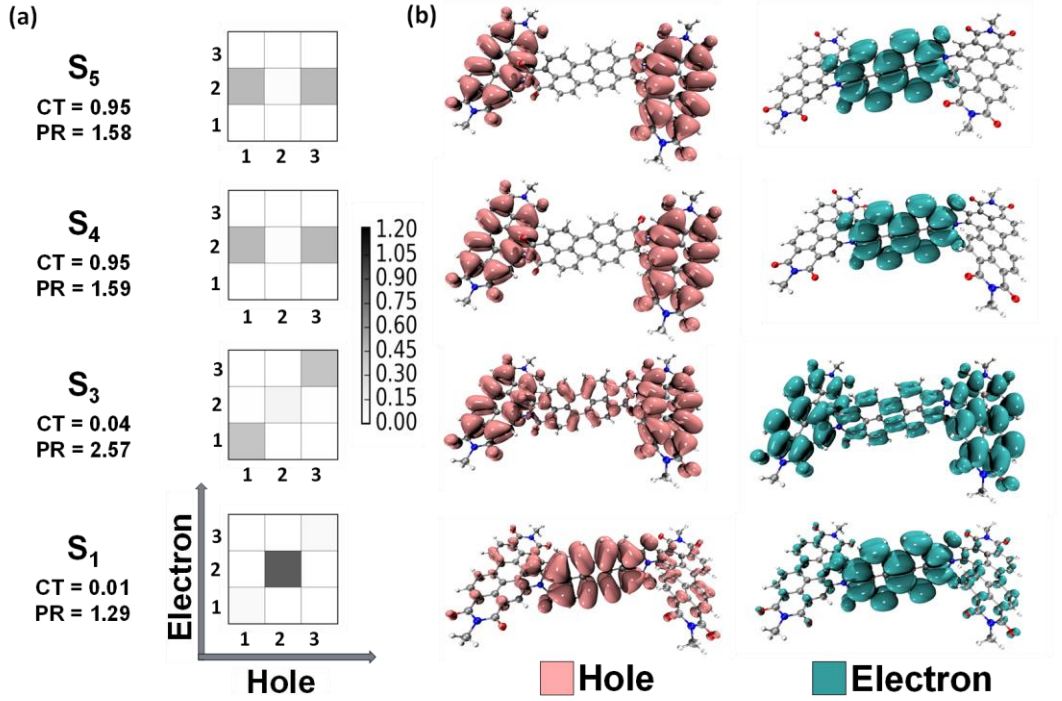

Figure A3.17: a) Hole-electron correlation plots showing the localized or delocalized Frenkel exciton or charge transfer nature for the S_1, S_3, S_4 and S_5 excited-states of **PDI-T** and the b) corresponding hole-electron isosurface distribution of these excited-states. The nature of the excitations is defined by the CT and PR values.

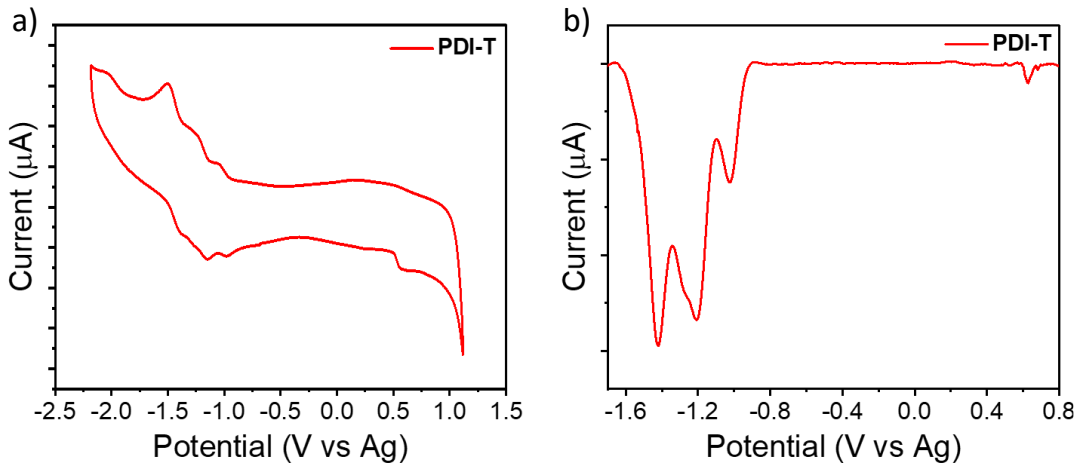

Figure A3.18: a) Cyclic voltammetry data and b) differential pulse voltammograms of **PDI-T** in DCM using Fc/Fc^+ coupled Ag/Ag^+ electrode.

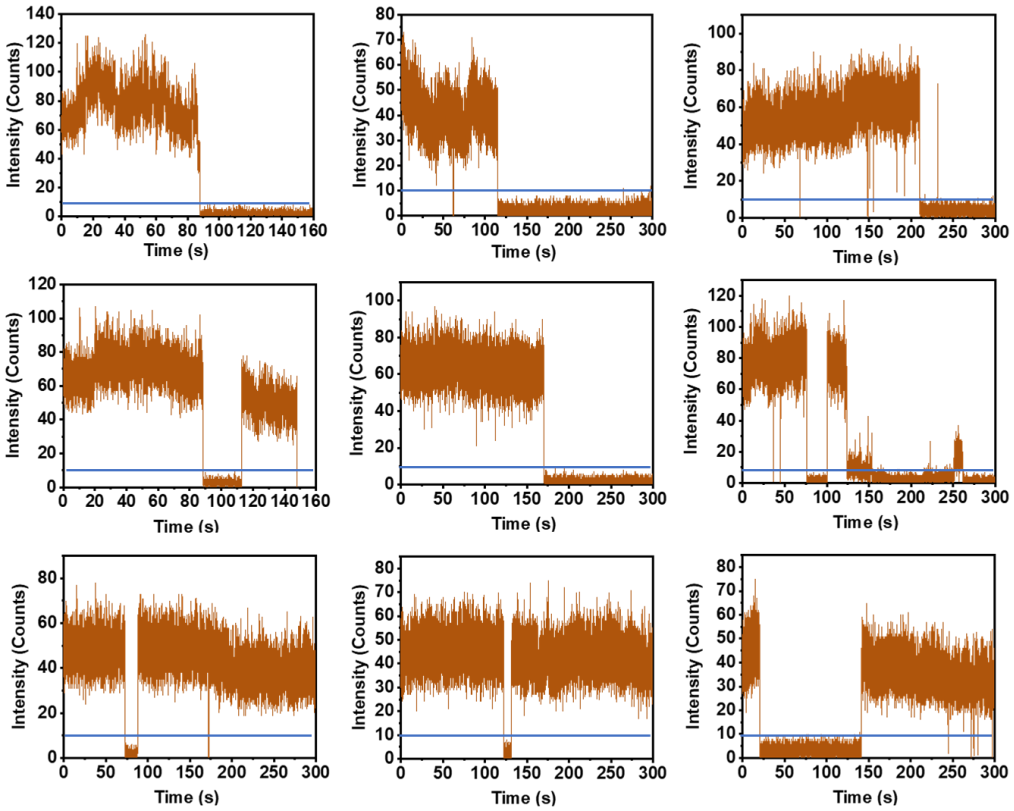

Figure A3.19: Representative FITs of **PDI-T** in PS measured for 300 s. The intensity threshold is defined by the blue line in the FITs.

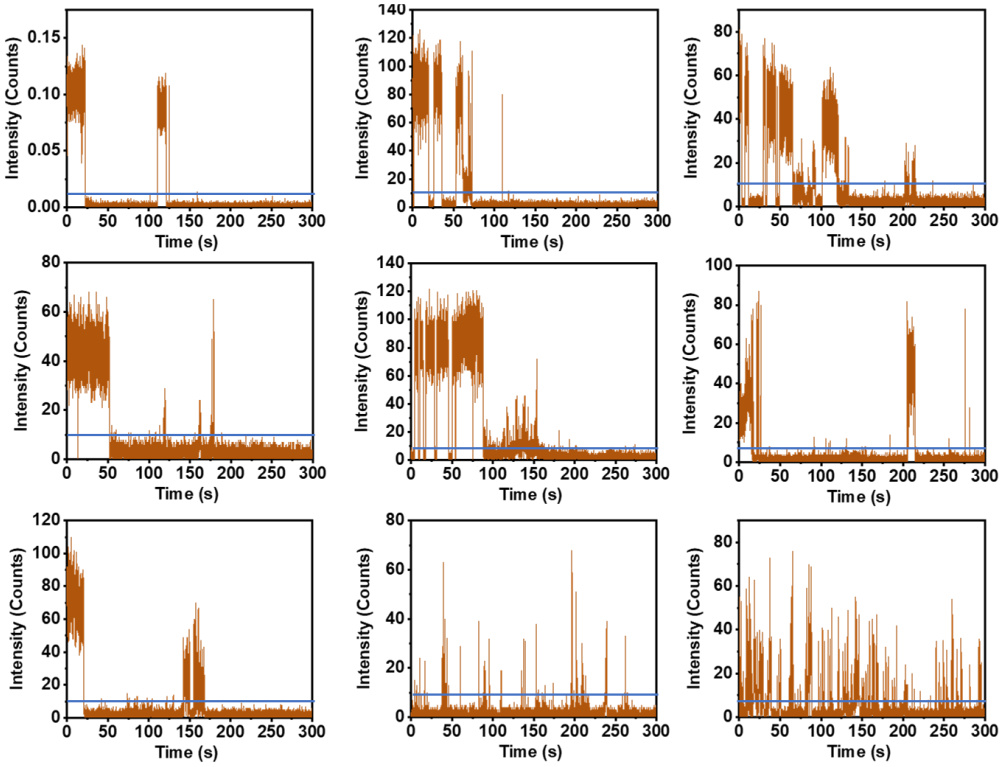

Figure A3.20: Representative FITs of **PDI-T** in PVA measured for 300 s. The intensity threshold is defined by the blue line in the FITs.

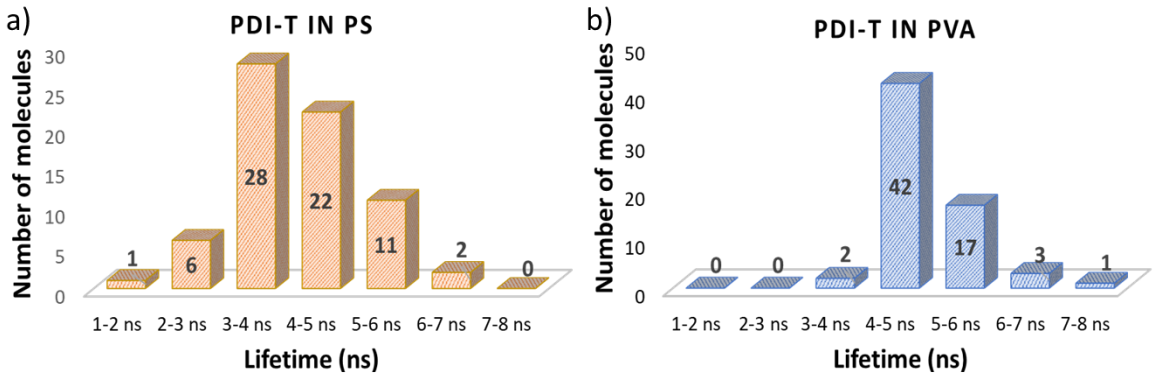

Figure A3.21: The fluorescence lifetime distribution of **PDI-T** in a) PS and b) PVA matrices.

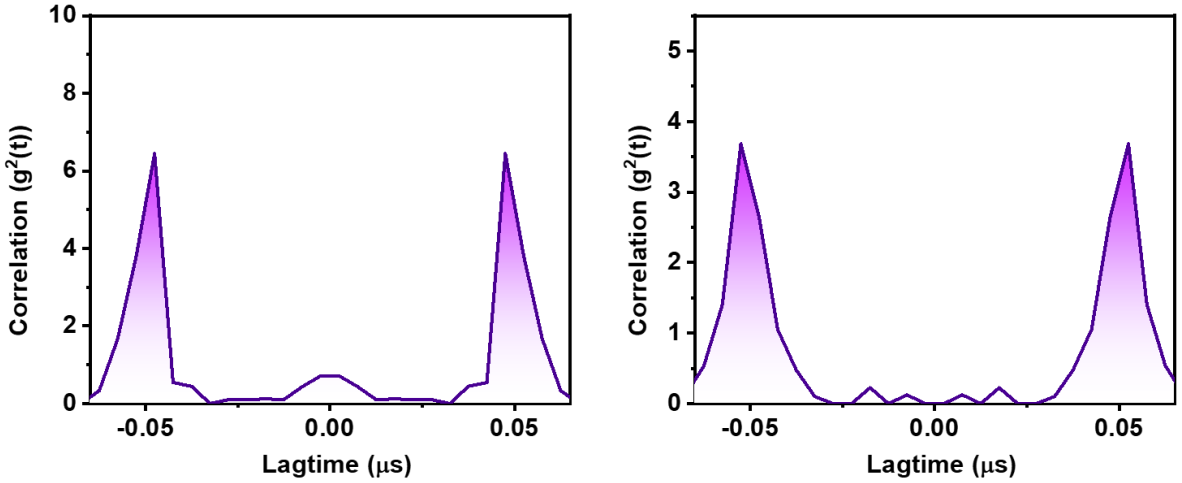

Figure A3.22: Representative antibunching measurements of **PDI-T** in PS matrix.

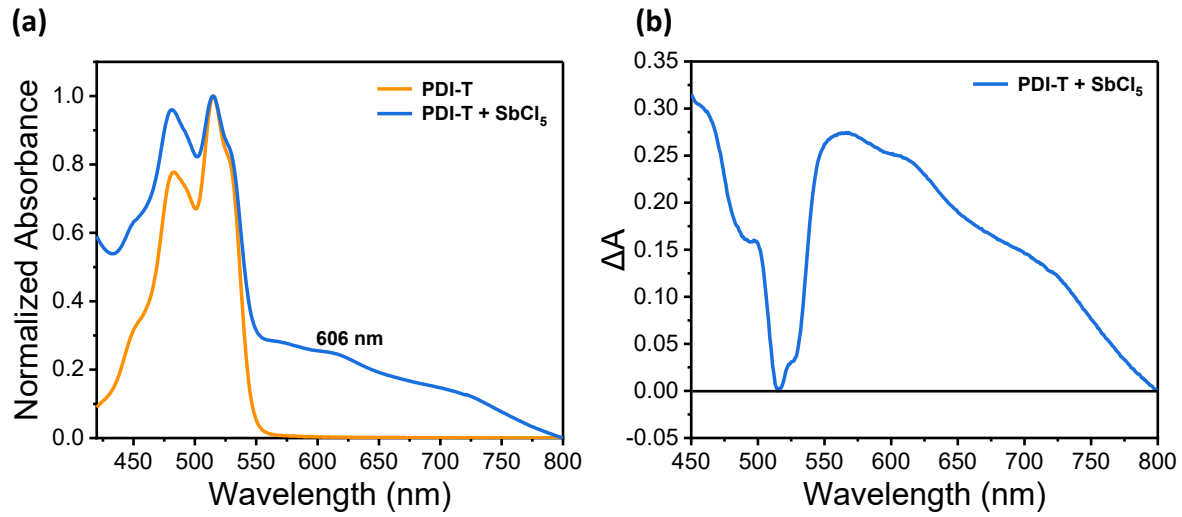

Figure A3.23: a) UV-vis absorption changes of **PDI-T** upon the addition of antimony pentachloride ($SbCl_5$) and b) difference absorption spectra of **PDI-T** obtained by subtracting ground-state absorption from that of chemically oxidized radical cation species in ACE.

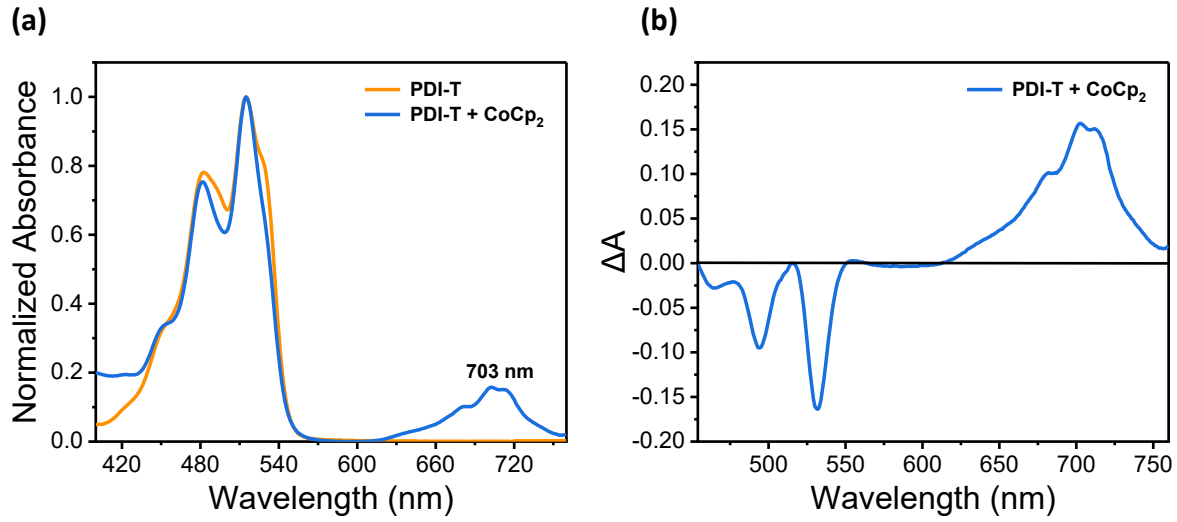

Figure A3.24: a) UV-vis absorption changes of **PDI-T** upon the addition of cobaltocene ($CoCp_2$) and b) difference absorption spectra of **PDI-T** calculated by subtracting the absorption of the neutral ground-state from that of the chemically generated radical anion in ACE.

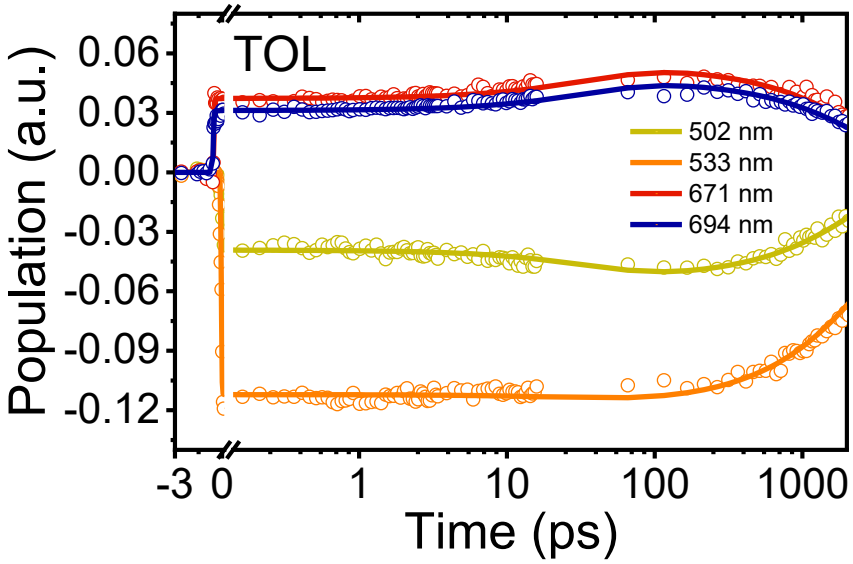

Figure A3.25: Global analysis fits for selected fsTA wavelengths of **PDI-T** (λ_{ex} = 480 nm) in TOL using A → B → C → GS kinetic model. Fitted results are shown using solid line profiles.

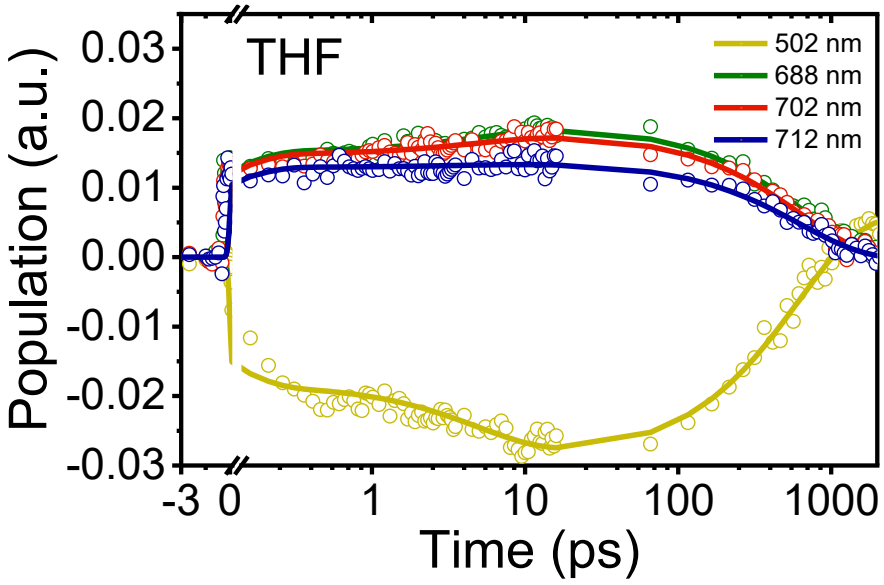

Figure A3.26: Global analysis fits for selected fsTA wavelengths of **PDI-T** (λ_{ex} = 480 nm) in THF using A → B → C → GS kinetic model. Fitted results are shown using solid line profiles.

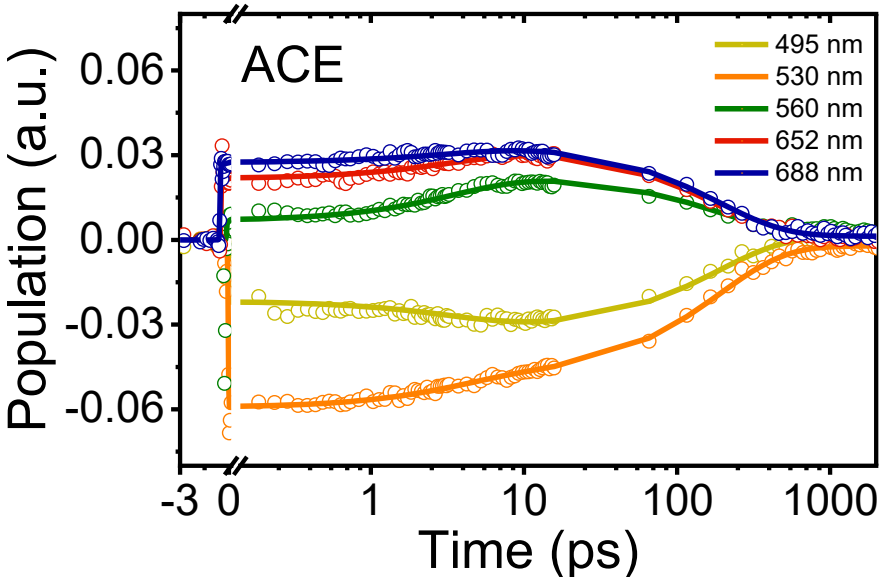

Figure A3.27: Global analysis fits for selected fsTA wavelengths of **PDI-T** (λ_{ex} = 480 nm) in ACE using A → B → C → GS kinetic model. Fitted results are shown using solid line profiles.

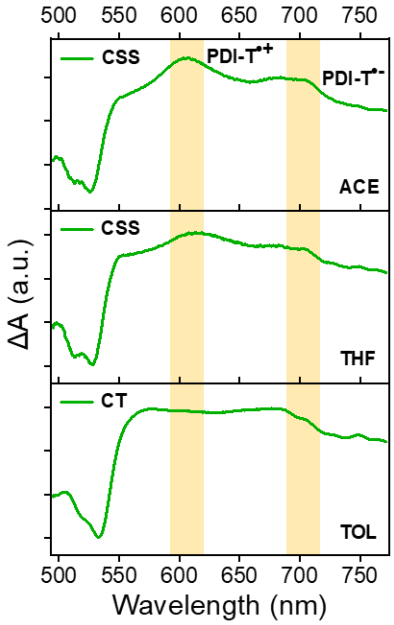

Figure A3.28: The stacked plot of the global analysis fitted CSS kinetic trace in ACE (top) and THF (middle) and CT kinetic trace in TOL (bottom), showing the distinct transient spectral signature of the radical cation and radical anion in **PDI-T**.

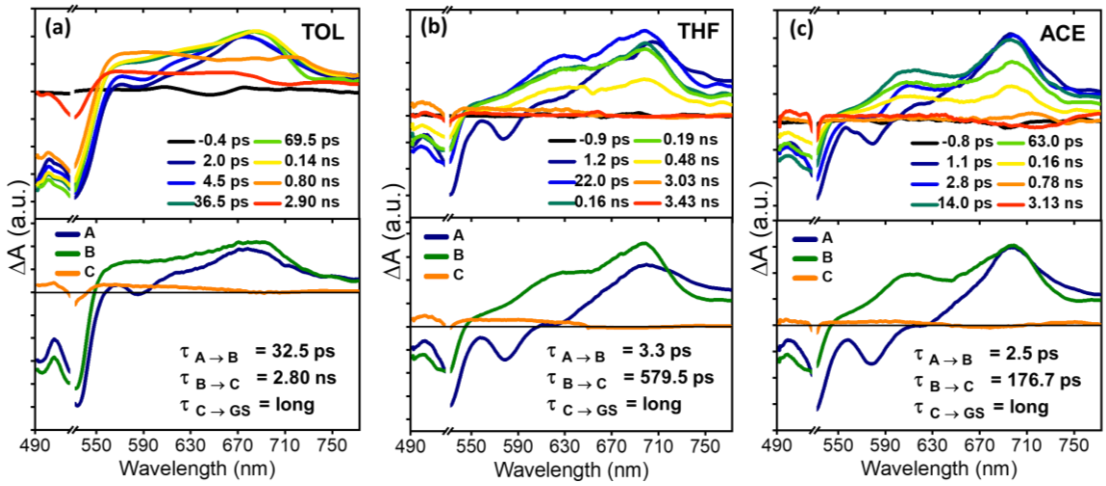

Figure A3.29: (Top row) FsTA spectra of **PDI-T** in a) TOL, b) THF, and c) ACE showing the excited-state dynamics upon photoexcitation. (Bottom row) EAS reconstructed from global analysis of **PDI-T** with A → B → C → GS model for TOL (left), THF (center) and ACE (right), where A is the singlet excited-state, B is the CT state in case of TOL and, the CSS in the case of THF and ACE, C is the triplet excited-state, and GS is the ground-state (λ_{ex} = 532 nm).

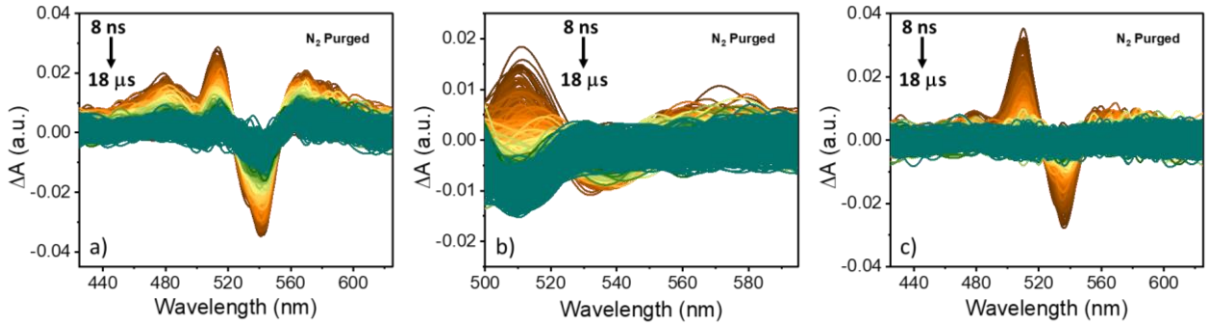

Figure A3.30: Nanosecond transient absorption measurements of **PDI-T** in N_2 purged solution of a) TOL, b) THF and c) ACE.

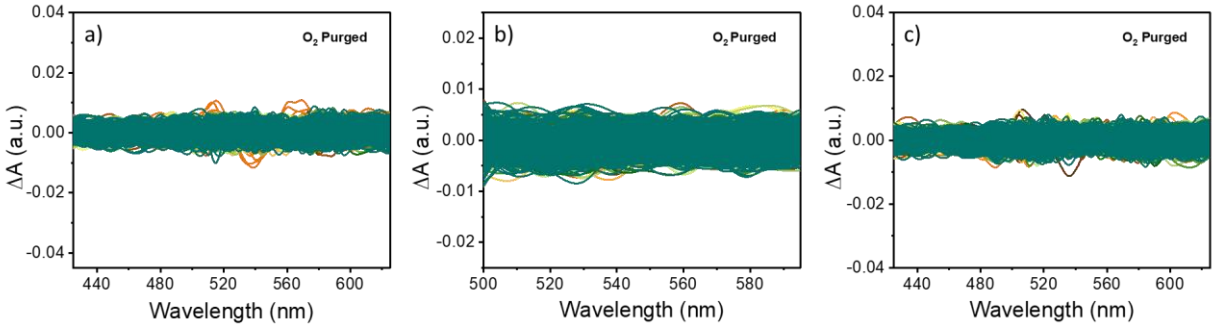

Figure A3.31: Nanosecond transient absorption measurements of **PDI-T** in O_2 purged solution of a) TOL, b) THF and c) ACE.

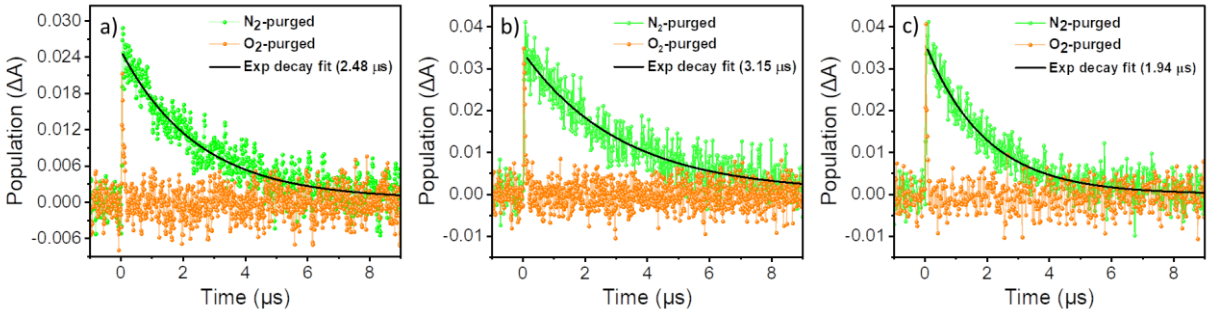

Figure A3.32: a) Nanosecond transient absorption decay profiles of **PDI-T** in a) TOL, b) THF and c) ACE at 510 nm.

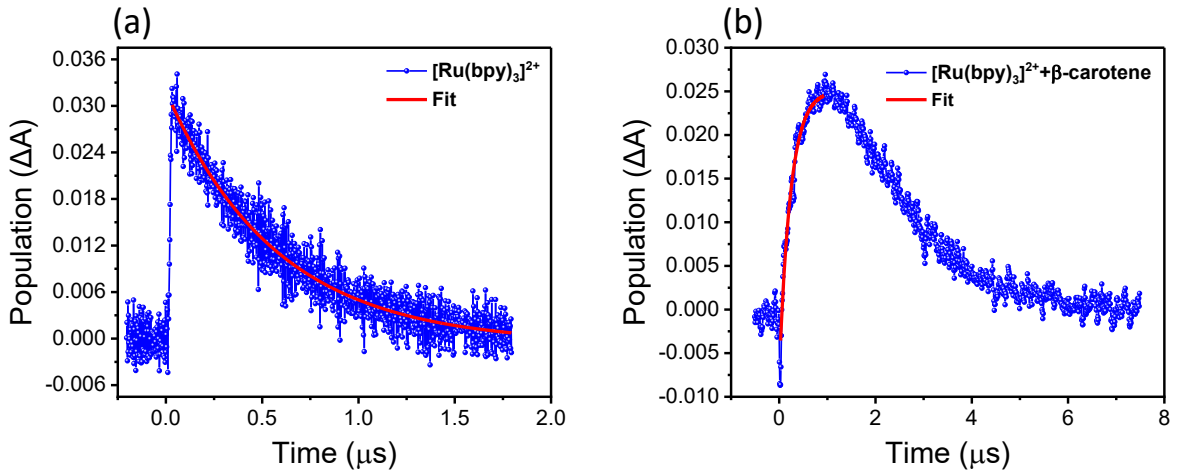

Figure A3.33: a) The nsTA decay of $[Ru(bpy)_3]^{2+}$ monitored at 370 nm. b) Time-resolved growth trace at 530 nm showing the formation of the triplet excited-state of β-carotene (^{3}β-carotene*) upon mixing $[Ru(bpy)_3]^{2+}$ with β-carotene in methanol, providing evidence for triplet-triplet energy transfer from the ruthenium complex to β-carotene.

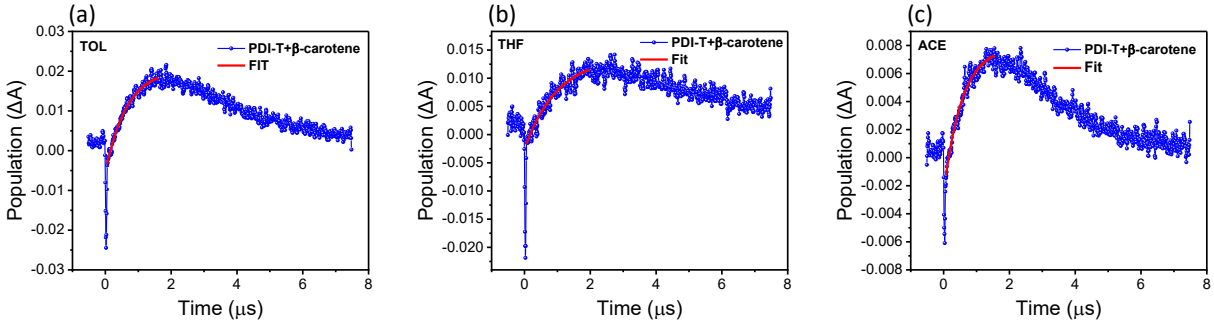

Figure A3.34: Time-resolved nsTA traces illustrating the growth of the triplet excited-state of β-carotene (^{3}β-carotene*) upon interaction with **PDI-T**, thereby validating the occurrence of triplet-triplet energy transfer from **PDI-T** to β-carotene in a) TOL, b) THF, and c) ACE.

Table A3.1: Geometric parameters at S_0 and S_1 optimized geometries of **PDI-T**.

Geometry	Bridge to terminal C-N bond distance (Å)	Dihedral angle, θ (°)	Core twist (°)	Centroid-to-centroid distance between terminal and bridge PDIs, $d_{PDI\text{-}PDI}$ (Å)	Centroid-to-centroid distance between two terminal PDIs, $d_{PDI\text{-}PDI}$ (Å)
S_0	1.44	70.3	20.6	9.01	18.03
S_1	1.44	67.0	18.0	9.02	18.03

Table A3.2: Steady-state photophysical properties of **PDI-T** in different solvents.

Solvent	Absorption Maxima (λ_{max}^{Abs})	Emission Maxima (λ_{max}^{Emi})	Quantum yield, ϕ_{FL} (%)
TOL	523 nm	546 nm	10.4
THF	517 nm	529 nm	<1
ACE	515 nm	535 nm	<1

Table A3.3: Vertical excitation energies computed at the ground-state optimized geometry of **PDI-T** (TD-CAM-B3LYP-D3/6-311G+(d,p) level of theory) in vacuum.

State	Oscillator strength (*f*)	Energy (eV)	Wavelength (nm)
S_1	0.99	2.588	479.11
S_2	0	2.670	464.36
S_3	1.51	2.694	460.20`

Table A3.4: Vertical excitation energies computed for the $S_0 \rightarrow S_1$ transition at the ground-state optimized geometry of **PDI-T** in different solvents using IEFPCM model (TD-CAM-B3LYP-D3/6-311G+(d,p) level of theory).

Solvent	Dielectric constant (ε)	Oscillator strength (f)	Energy (eV)	Energy (nm)
TOL	2.38	1.10	2.48	499.09
THF	7.58	1.11	2.49	498.07
ACE	20.7	1.12	2.49	497.31

Table A3.5: Summary of redox potentials and HOMO/LUMO calculations of **PDI-T** (CH_2Cl_2, 298 K, ε_{SP} = 8.93).

Compound	[a] E_1(red) (V)	[a] E_2(red) (V)	[a] E_3(red) (V)	λ_{onset} (nm)	E_g^{opt} (eV)	HOMO (eV)	LUMO (eV)	E_{00} (eV)
PDI-T	-1.02	-1.20	-1.42	548.67	2.26	-6.03	-3.77	2.31

[a] reduction potentials *vs*. Fc/Fc^+.

3.6. Appendix

3.6.1. Materials and Methods

Detailed information regarding the materials and methods used is given in section 2.6.1.

Concentration-Dependent UV-vis Absorption Measurements

A 50 μM 5 mL stock solution of **PDI-T** was prepared in TOL, THF and ACE solvents and was further diluted for concentration-dependent UV-vis absorption measurements. The shaded region in the absorption maxima versus concentration plot of **PDI-T** (Figures A3.7b-A3.9b) indicates the concentration region (0.5-3 μM) used for all the ensemble level photophysical measurements of **PDI-T**.

3.6.2. Computational Analysis

All the computational investigations were carried out in Gaussian 16 software package.[139] Ground-state geometry optimization in vacuum and solvents (IEFPCM model) and rigid PES scan were performed at B3LYP-D3/6-311+G(d,p) level of theory. The FMOs were obtained from the generated cube files of energy calculations. Vertical excitation energies along with oscillator strengths were obtained using time-dependent density functional theory (TDDFT) calculations at the CAM-B3LYP-D3/6-311+G(d,p) level. Geometry optimization of the first singlet excited-state (S_1) was carried out employing CAM-B3LYP-D3 functional and 6-31G basis set (a smaller basis set was used to reduce the computation cost and avoid convergence failure). In order to compute long-range Coulombic coupling, an electronic energy transfer (EET) module available in Gaussian 16 was utilized. HOMO-LUMO, hole-electron distributions and natural transition orbital (NTO) isosurfaces for the **PDI-T** model system were analyzed using Multiwfn 3.8.[140] The resulting visualizations were prepared with VMD version 1.9.3.[141]

3.6.3. TheoDORE Analysis

The theoretical details for the TheoDORE analysis are provided in previous section 2.6.3. The nature of the excited-states in **PDI-T** was analyzed using TheoDORE at the ground-state

optimized geometry. Each PDI monomer was considered as a fragment in the **PDI-T** trimer (Figure A3.16).

3.6.4. Coulombic Coupling Calculation

The detailed Coulombic coupling estimation methodology is provided in section 2.6.4. TDDFT calculation was performed on **PDI-T** after defining each PDI monomer as a fragment (Figure A3.16) at the CAM-B3LYP-D3/DEF2-TZVP level, and Coulombic coupling between the states was procured.[23,24,133]

3.6.5. Femtosecond Transient Absorption (fsTA) Measurement

The detailed fsTA instrumentation and experimental methods are provided in the previous section 2.6.5. For the fsTA measurement of **PDI-T**, the sample was excited with 480 nm, 200 nJ, and 100 fs pulses. Upon variations in laser intensity, the detected kinetic components remained unaffected, excluding singlet-singlet annihilation.[142]

To examine whether the excited-state dynamics of **PDI-T** are influenced by excitation wavelength, additional fsTA measurements were performed following photoexcitation at 532 nm in TOL, THF, and ACE. The obtained fsTA spectra is shown in Figure A3.29. The deconvoluted EAS of **PDI-T** in TOL (Figure A3.29a-bottom) display three components. The component A is attributed to the locally excited singlet state (^{1}**PDI-T***), decaying with 32.5 ps to form component B. Although the ESA for component B has spectral similarity to the radical cation ($PDI^{\bullet+}$) and radical anion ($PDI^{\bullet-}$) of **ref-PDI** monomer, the ESA feature is very broad and is assigned to a CT state. The CT state decays within 2.80 ns and forms component C, which is long-lived and is assigned to the triplet excited-state of **PDI-T**. However, the EAS of **PDI-T** in THF and ACE show the distinct evidence of forming the CSS representing the unique ESA spectral feature of $PDI^{\bullet+}$ and $PDI^{\bullet-}$ (component B) formed through the locally excited singlet state (component A) with time constants of 3.3 ps and 2.5 ps, respectively (Figure A3.29b and A3.29c). The CSS state decays within 579.5 ps and 176.7 ps in THF and ACE, respectively to form the third component C. Component C was found to be long-lived and is attributed to the triplet excited-state of **PDI-T**. The excited-state dynamics obtained after photoexciting **PDI-T** at 532 nm were identical to the photophysics observed at 480 nm

excitation with similar time constants. Therefore, excitation-dependent photophysics was not observed in **PDI-T**.

3.6.6. Nanosecond Transient Absorption (nsTA) Measurement

Instrumentation details and experimental methods for nsTA measurements are given in section 2.6.6. Nanosecond laser flash photolysis measurements were carried out on a nitrogen-purged solution of **PDI-T** in TOL, THF and ACE.

3.6.7. Global Analysis

Global analysis of the fsTA data was carried out using Glotaran software and is detailed in section 2.6.7.[112]

3.6.8. Electrochemistry

The details regarding the electrochemical measurements are mentioned in section 2.6.8.

Redox titration

The redox titration measurements for **PDI-T** were carried out in ACE. Antimony pentachloride ($SbCl_5$) was used to oxidize the perylenediimide trimer. Cobaltocene ($CoCp_2$) was used as the reducing agent. Difference absorption spectra of **PDI-T** were obtained by subtracting ground-state absorption from that of chemically oxidized radical cation and reduced radical anion species.

3.6.9. Rehm-Weller Analysis

The theoretical details regarding the Rehm-Weller analysis are given in section 2.6.9.

3.6.10. Single-Molecule Fluorescence Measurements

Fluorescence lifetime imaging microscopy (FLIM) and fluorescence intensity trajectories (FITs) were recorded using a PicoQuant MicroTime 200 (MT200) time-resolved fluorescence setup. This system was built on an inverted Olympus IX83 microscope, integrated with a piezo-controlled scanning stage (P-733.2CD, PI). Excitation of the sample was carried out with a 512

nm pulsed laser source (LDH-D-C-512, PicoQuant) operating at 20 MHz, and data acquisition was performed using a scan dwell time of 0.4 milliseconds. The emitted photons were captured through a 60× NA 1.2 water immersion objective (UplanSApo). Spectral selection was achieved using a primary dichroic mirror (zt405-442/510 rpc-UF3, Chroma) in combination with a 519 nm long-pass emission filter (FF01-519/LP, Semrock). A 50 μm pinhole was employed for spatial filtering of the emitted photons, which were subsequently collected by a single-photon avalanche photodiode (SPAD) detector from Excelitas. The resulting photon signals were then processed using a HydraHarp 400 time-correlated single-photon counting (TCSPC) system from PicoQuant. SymPhoTime64 software (PicoQuant) handled data recording and analysis. A mixture of **PDI-T** (~10^{-10} M) and a polystyrene (PS) matrix (2% w/v) in TOL was spin-coated on a coverslip of 0.13-0.16 mm thickness. The polyvinyl alcohol (PVA) sample was prepared according to the reported procedure. A freshly prepared mixture of PVA (2 mg/mL) and glycerol (10 μL) in distilled water was stirred at 90°C for 1 h. The sample solution of **PDI-T** was prepared in $CHCl_3$ (~10^{-12} M). The thin film was prepared by sandwiching the sample layer by alternatively spin coating the polymer solution. After preparation, the thin film sample was placed in a vacuum for 10 minutes.[179] Fluorescence lifetimes and FITs of **PDI-T** single molecules were obtained by exciting the sample at 512 nm (refer to Figures A3.19 and A3.20). The excitation laser operated with a power of ~0.12 μW and at a repetition rate of 20 MHz. Fluorescence lifetimes and FITs with a 15 ms bin time were acquired using SymPhoTime software. Photon antibunching measurements were conducted using the standard Hanbury Brown-Twiss interferometer configuration in the MicroTime200 from PicoQuant. Due to the low fluorescence intensity count for **PDI-T** in PVA, the photons collected were inadequate for a reliable antibunching correlation. The on- and off- events are separated from the fluorescence intensity trajectories by applying threshold (typically 3 times of standard deviation higher than the background noise level).[180] PS and PVA matrices were procured from Sigma-Aldrich.

3.6.11. Triplet Quantum Yield (ϕ_T) Measurements

To determine the triplet quantum yield (ϕ_T) of **PDI-T**, a method involving triplet-triplet energy transfer to β-carotene was employed, using $[Ru(bpy)_3]^{2+}$ as a reference compound with a

known ϕ_T of approximately 1, as reported in the literature.[119] Equal volumes of β-carotene dissolved in $CHCl_3$ were added to optically matched solutions of $[Ru(bpy)_3]^{2+}$ in methanol and **PDI-T** in TOL, THF, and ACE, each adjusted to have an absorbance between 0.1 and 0.2 at 532 nm. Upon excitation, both $[Ru(bpy)_3]^{2+}$ and **PDI-T** were capable of transferring triplet energy to β-carotene, leading to the formation of its triplet excited-state, which was monitored at 530 nm. The triplet quantum yields for **PDI-T** were calculated using the standard equation Eq 2.12, where the superscripts "Sam" and "Ref" refer to the sample (**PDI-T**) and the reference ($[Ru(bpy)_3]^{2+}$), respectively. Here, k_{obs} represents the pseudo-first-order rate constant for β-carotene triplet growth, while k_0 denotes the decay constant of the donor triplet state in the absence of β-carotene, with both measurements taken from solutions having identical absorbance.

Chapter 4

Ultrafast Symmetry-Breaking Charge Separation in Thin Films of J-Aggregated Perylenediimide Multimers in a Nonpolar Solid-State Environment

Abstract

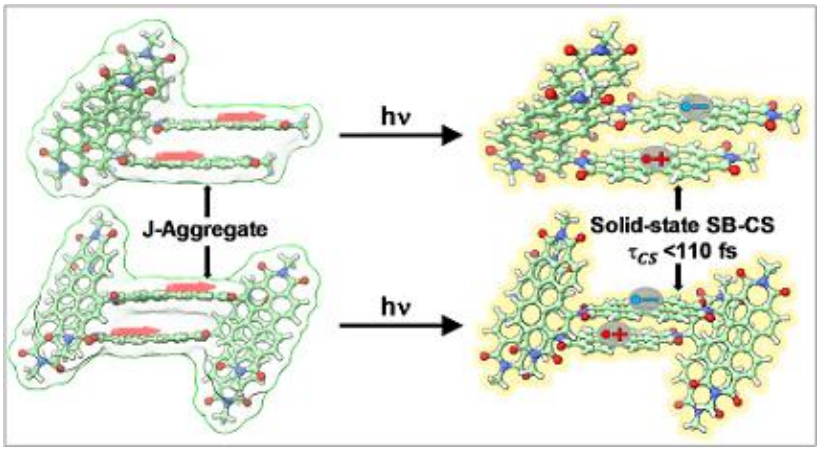

We demonstrate ultrafast symmetry-breaking charge separation (τ_{CS} <110 fs) in thin films of J-aggregated perylenediimide (PDI) multimers in a nonpolar polymethyl methacrylate polymer matrix (ε = 2.80-3.20). Theoretical calculations reveal the role of through-space electronic communication and π-π interactions promoting ultrafast charge separation in PDI multimers in the solid-state.

4.1. Introduction

Achieving efficient charge separation (CS) with minimal energy loss is a key challenge in advancing organic photovoltaic (OPV) devices.[10,40] Symmetry-breaking charge separation (SB-CS) has recently emerged as a prospective solution for generating hole-electron pairs in chromophoric assemblies without conventional donor-acceptor interfaces.[67,78,104] SB-CS takes advantage of asymmetry introduced by molecular packing or the surrounding environment to generate long-lived charge separated states (CSS) from photoexcited neutral chromophores, ultimately paving the way for improved

open-circuit voltages and better device performance.[38,39,48,70] Although SB-CS is well documented in solution-phase systems where solvent polarity helps stabilize the charge separated state, achieving it in the solid-state, without the aid of external dielectric stabilization, presents both a fundamental challenge and a valuable opportunity for technological advancement.[10,37] Among the various π-conjugated systems explored, perylenediimides (PDIs) are outstanding electron-deficient chromophores known for their strong absorption, photostability, and high electron mobility.[85,148,149] Their excited-state dynamics are highly sensitive to molecular packing, and recent studies have shown that PDIs organized into solid-state multichromophoric assemblies can undergo SB-CS through intermolecular pathways.[86,87,89,90] Notably, SB-CS has been observed in the solid-state in systems where PDIs adopt slip-stacked geometries that promote through-space electronic coupling while suppressing excimer formation, otherwise leading to non-radiative losses.[86]

Rational molecular design plays a crucial role in achieving such favourable packing geometries. Introducing bulky or directional substituents, tailoring the rigidity and conjugation of linkers, or using multimeric scaffolds can promote ordered slip-stacked aggregates in the solid-state.[89,90] These arrangements facilitate the electronic coupling necessary for SB-CS while simultaneously mitigating structural motifs that favour excimer formation.[86] Previously, we have shown that ultrafast intramolecular SB-CS can be achieved under the effect of polar solvents in angular PDI bichromophoric and trichromophoric structures through the modulation of intrachromophore electronic coupling.[111,181] Herein, we investigate the excited-state dynamics of two PDI-based multichromophoric assemblies (**PDI_2** and **PDI_3**) forming J-aggregated thin film structures. We demonstrate that such architectures enable ultrafast SB-CS even in a nonpolar polymethyl methacrylate (PMMA) polymer matrix, thus providing a framework for designing next-generation organic materials capable of efficient solid-state charge generation.

4.2. Results and Discussion

4.2.1 PDI Multimers and the Optimized Structures

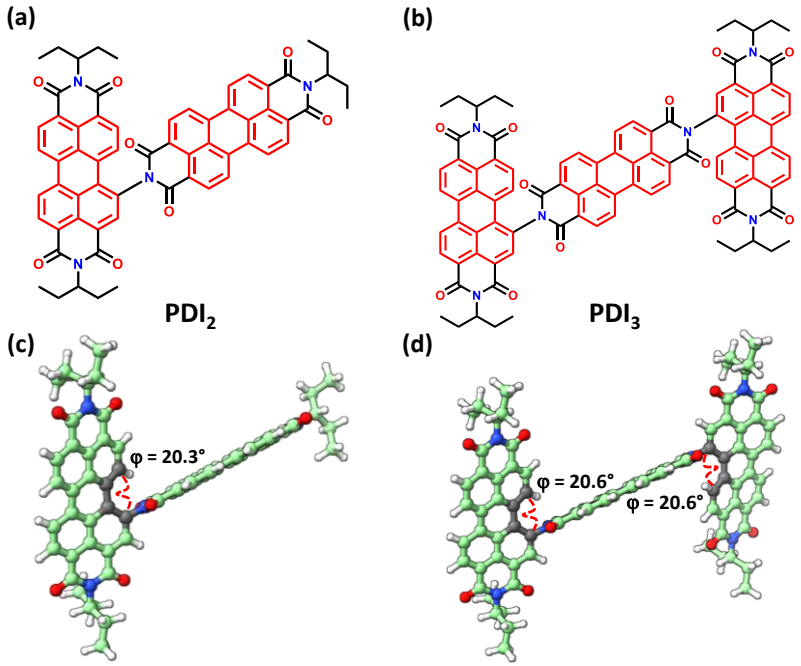

Figure 4.1: Molecular structures of a) **PDI₂** and b) **PDI₃**. Optimized structures of c) **PDI₂** and d) **PDI₃** showing the core-twist in the PDI multimers.

PDI₂ and **PDI₃** (Figures 4.1a, b) were synthesized following previously reported procedures.[106,107] Key insights into the aggregate stacking were obtained using multi-dimensional NMR analyses in $CDCl_3$, where ~12 molecules of **PDI₂** and **PDI₃** each were estimated to be stacked in the individual aggregate structure (refer to Figures A4.1, A4.2 and section 4.6.2 for more details). The **PDI₂** optimized ground-state geometry acquired at the B3LYP-D3/6-311+G(d,p) level of theory in vacuum, employing density functional theory (DFT), exhibited a core-twist of φ = 20.3° in the PDI fragment with bay-substitution (Figure 4.1c). Meanwhile, the **PDI₃** optimized structure displayed core-twisting of both the terminal PDI fragments with φ = 20.6° (Figure 4.1d).

4.2.2. Steady-State Photophysical Properties of the PDI Multimers in Thin Films in PMMA

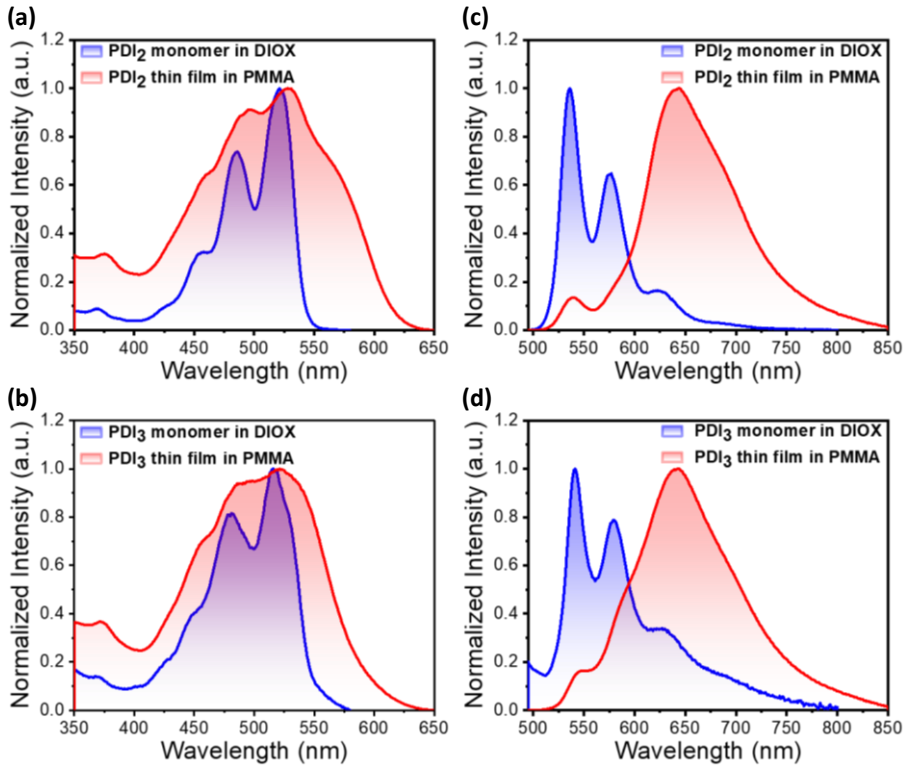

Figure 4.2: Fluorescence excitation spectra of a) **PDI₂** and b) **PDI₃**, and emission spectra of c) **PDI₂** and d) **PDI₃** in DIOX and thin films in PMMA.

The steady-state photophysical properties of **PDI₂** and **PDI₃** were investigated in thin films in a nonpolar PMMA matrix (ε = 2.80-3.20) in comparison to the photophysical properties at the monomer state in 1,4-dioxane (DIOX) at room temperature. The UV-vis absorption and fluorescence excitation spectra of **PDI₂** and **PDI₃** thin films reveal significantly broad red-shifted features compared to the **PDI₂** and **PDI₃** monomeric optical properties in DIOX (Figures 4.2, A4.1a). **PDI₂** thin film showed red-shifted broadened maxima in the excitation spectra (Figure 4.2a) with λ_{max}^{Exc} ≈ 528 nm (521 nm in DIOX), while **PDI₃** thin film exhibited broad maxima (Figure 4.2b) at λ_{max}^{Exc} ≈ 521 nm (516 nm in DIOX). The red-shifted excitation spectra of **PDI₂** and **PDI₃** thin films compared to the monomer excitation spectra in DIOX indicate the formation of J-type self-assembly in the aggregated state of **PDI₂** and **PDI₃**.[32,79,182] Moreover,

the fluorescence emission spectra recorded for the **PDI$_2$** and **PDI$_3$** thin films in PMMA at room temperature exhibited red-shifted featureless emission profiles compared to the well-defined monomeric emission observed in DIOX (Figures 4.2c, 4.2d and A4.1b).

Further, we have estimated the fluorescence quantum yields (ϕ_{FL}) of **PDI$_2$** and **PDI$_3$** to probe the emissive nature of the PDI dimers in a closely packed solid-state arrangement. **PDI$_2$** and **PDI$_3$** showed reduced ϕ_{FL} of 0.88% and 0.53% in the solid-state, respectively, compared to the ϕ_{FL} estimated in the solution-state in DIOX (16.20% for **PDI$_2$** and 3.77% for **PDI$_3$**). The lower ϕ_{FL} values of **PDI$_2$** and **PDI$_3$** in the solid-state indicate the presence of nonradiative decay channels involved in the excited-state dynamics of the PDI dimers in thin films.[181]

4.2.3. Femtosecond Transient Absorption Measurements of PDI$_2$ and PDI$_3$ Thin Films in PMMA

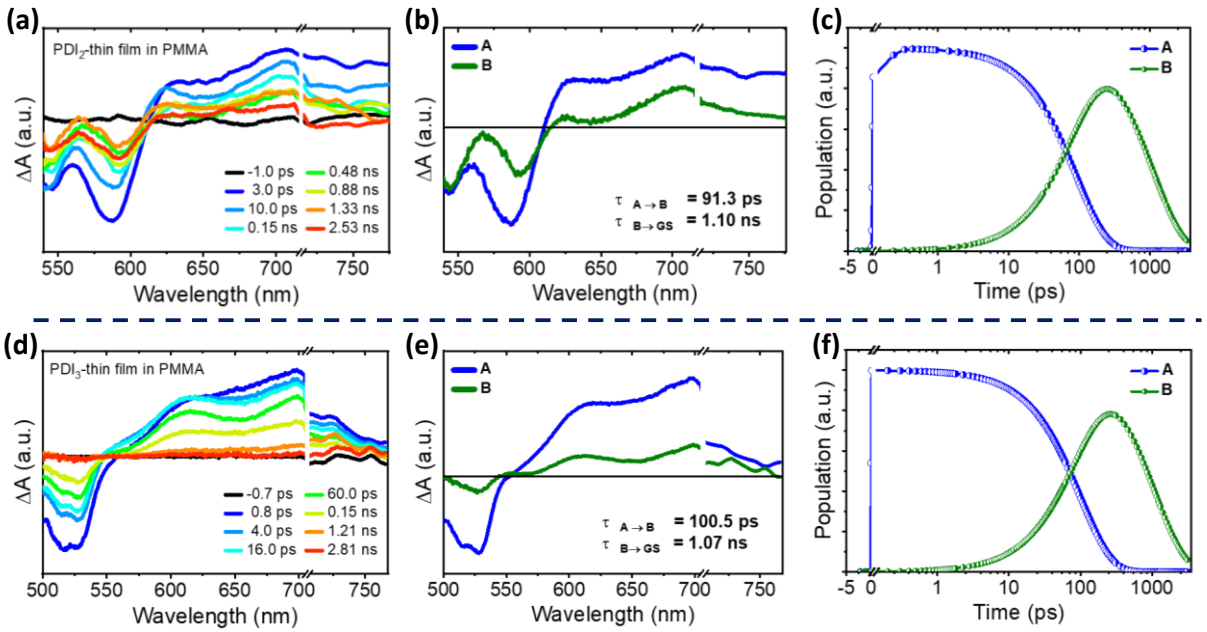

Figure 4.3: fsTA spectra of a) **PDI$_2$** and d) **PDI$_3$** in thin films in PMMA showing the excited-state dynamics upon photoexcitation. EAS reconstructed from global analysis of the fsTA data of b) **PDI$_2$** and e) **PDI$_3$** with the A → B → GS kinetic model, where A is the CSS, B is the CSS$_{rel}$, and GS is the ground-state (λ_{ex} = 480 nm). Relative population profile of the excited-states fitted using the above kinetic models in c) **PDI$_2$** and f) **PDI$_3$**.

To obtain critical insights into the nonradiative decay pathways governing the excited-state dynamics in the solid-state of the PDI multichromophoric assemblies, we performed femtosecond transient absorption (fsTA) spectroscopic measurements of **PDI$_2$** and **PDI$_3$** in thin films in PMMA (Figure 4.3). After photoexciting **PDI$_2$** thin film at 480 nm, the fsTA spectra depict negative GSB and/or SE at ~540 to 610 nm and two distinct positive ESA peaks centered at ~627 nm and ~707 nm (Figure 4.3a). The observed twin ESA peaks at ~627 nm and ~707 nm correspond to the characteristic spectral signature of the perylenediimide radical cation ($PDI^{\bullet+}$) and radical anion ($PDI^{\bullet-}$), respectively.[86,90] The simultaneous occurrence of $PDI^{\bullet+}$ and $PDI^{\bullet-}$ transient features represent the CSS, confirming the SB-CS process in thin films of **PDI$_2$** in a nonpolar PMMA polymer matrix (ε = 2.80). At longer time delays of ~150 ps, the CSS state decays to a relaxed CSS state (**CSS_{rel}**) with non-negligible blue-shifted ESA features. Similar excited-state dynamics were observed for **PDI$_3$** thin film in PMMA upon photoexcitation at 480 nm. The fsTA spectra of **PDI$_3$** thin film depict GSB and/or SE at ~500 to 555 nm and ESA peaks at ~619 nm and ~698 nm (Figure 4.3d). The two distinct ESA peaks characterize the unique spectral feature of $PDI^{\bullet+}$ and $PDI^{\bullet-}$, confirming SB-CS in thin films of **PDI$_3$** in PMMA.[86,90] The CSS state in **PDI$_3$** decays to a **CSS_{rel}** state with blue-shifted ESA peaks at higher time delays of ~150 ps.

Global analysis was applied to the fsTA data of **PDI$_2$** and **PDI$_3$** thin films to extract the EAS and the corresponding population dynamics of the excited-states involved in the above-mentioned transformations. Representative kinetic traces at selected wavelengths, along with the globally fitted curves, are shown in Figures A4.2a, A4.2b to illustrate the accuracy of the fit. The EAS and the relative population profile of **PDI$_2$** demonstrated two principal components (Figures 4.3b, c). The first component (A) is assigned to the CSS state formed due to SB-CS. The CSS state undergoes rapid vibrational relaxation (τ_{VR} = 91.3 ps) to form the second principal component (B). The component (B) is assigned to a **CSS_{rel}** state, which decays to the ground-state via charge recombination (CR) with a time constant of τ_{CR} = 1.10 ns. Likewise, the EAS and the relative population profile of **PDI$_3$** exhibited two principal components (Figures 4.3e, f). The first principal component (A) is attributed to the CSS state. The CSS state in **PDI$_3$** decays via vibrational relaxation (τ_{VR} = 100.5 ps) to form the **CSS_{rel}**. Further, the **CSS_{rel}** decays to the ground-state via CR within τ_{CR} = 1.07 ns. The immediate

appearance of the CSS feature upon photoexcitation shows that ultrafast CS occurs for **PDI$_2$** and **PDI$_3$** in the solid-state within the ~110 fs instrument response.[86,89,90] Recently, we have reported SB-CS in monomeric solutions of **PDI$_2$** and **PDI$_3$** in a polar solvent like ACE.[111,181] The experimentally determined CS time constants in ACE were τ_{CS} = 6.3 ps and 3.7 ps for **PDI$_2$** and **PDI$_3$**, respectively. Notably, the SB-CS dynamics observed in the solid-state for both molecules in this work are approximately an order of magnitude faster than those measured in solution. This could be due to the angular molecular design of **PDI$_2$** and **PDI$_3$**, with core-twisted PDI units, which compels the molecules to arrange in a J-aggregate type solid-state packing, promoting the long-range quadrupolar effects[86,89,183] and short-range intermolecular π-π interactions [88,90,184] necessary for efficient charge separation in the solid-state. Additionally, to understand the matrix effects modulating the aggregation process, favouring ultrafast SB-CS in the solid-state, we probed the feasibility of SB-CS in **PDI$_2$** and **PDI$_3$** in another nonpolar (ε = 2.60) polymer matrix, polystyrene (PS). The deconvoluted fsTA spectra showed the population of a broad singlet excited-state with partial charge transfer character (Figure A4.5). The absence of the distinct ESA features of the CSS in the fsTA spectra confirmed the infeasibility of SB-CS in **PDI$_2$** and **PDI$_3$** thin films in PS (refer to section 4.6.3 for more details). The above result sheds light on the crucial role played by PMMA in providing an optimum dielectric environment and promoting favourable solid-state packing necessary for ultrafast SB-CS.

4.2.4. Fluorescence Lifetime Measurements of PDI$_2$ and PDI$_3$ Thin Films in PMMA

Further, we measured the fluorescence lifetimes of **PDI$_2$** and **PDI$_3$** thin films in PMMA (Figures A4.6, A4.7). The major fluorescence lifetime component in **PDI$_2$** (τ_{FL}^{PDI2} = 2.63 ns (71%)) and **PDI$_3$** (τ_{FL}^{PDI3} = 2.60 ns (73%)) is in reasonable agreement with the decay constants for the $\mathbf{CSS_{rel}}$ state in **PDI$_2$** and **PDI$_3$** obtained from the global analysis fits of the solid-state fsTA data in PMMA (refer to section 4.6.4 for more details).

4.2.5. Aggregate Geometry Optimization and Excitonic Coupling Calculations

To understand the arrangement and packing of the individual monomers in the aggregate structure contributing to the experimentally observed SB-CS dynamics, we optimized the **PDI$_2$** and **PDI$_3$** aggregate ground-state geometries using DFT at the B3LYP-D3/6-31G level of theory in Gaussian 16. The optimizations were carried out employing a dimer model in vacuum. The optimized structure of **PDI$_2$** aggregate exhibited a slip-stacked orientation between the monomers, where the two planar PDI fragments are forced to arrange in a head-to-tail fashion due to the ineffective stacking of the core-twisted PDI fragments (Figure 4.4a). Comparably, the optimized structure of **PDI$_3$**

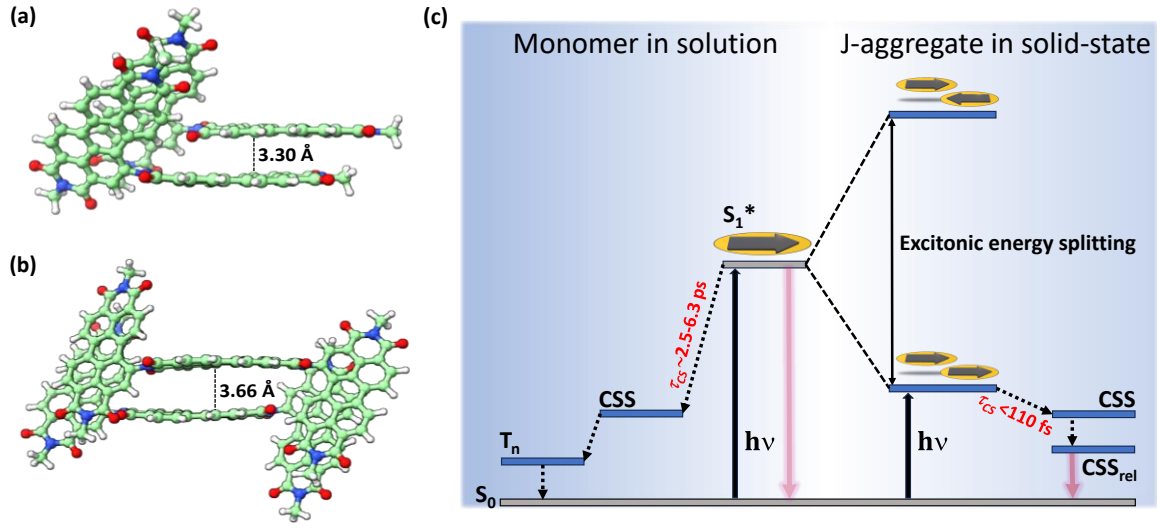

Figure 4.4: The optimized structures of a) **PDI$_2$** aggregate and b) **PDI$_3$** aggregate were obtained using a dimer model at the B3LYP-D3/6-31G level of theory in a vacuum (3-pentyl group substituted with methyl group to minimize computational cost). c) Schematic energy profile diagram summarizing the excited-state dynamics of **PDI$_2$** and **PDI$_3$** in (left) solution as monomer and (right) thin films in PMMA; S_0 = ground-state, S_1* = singlet excited-state; CSS = charge separated state; CSS_{rel} = relaxed charge separated state; T_n = triplet excited-state. N.B.- The solution-state photophysics is adapted from the previously reported energy profile diagrams in sections 2.2.12 and 3.2.10.

aggregate showed a slip-stacked arrangement between the central PDI fragments (Figure 4.4b). The interplanar distance between the slip-stacked PDI fragments was computed to be $d_{interplanar}$ = 3.30 Å and 3.66 Å in **PDI$_2$** and **PDI$_3$** aggregates, respectively (Figures 4.4a, b).

To comprehend the role of intermolecular excitonic interactions intrinsic to the spatial chromophore arrangement and packing in the aggregate structure, we theoretically computed the long-range J_{Coul} and the short-range J_{CT} interactions in **PDI$_2$** and **PDI$_3$** aggregates (Table A4.1). The J_{Coul} interactions were computed for the singlet excited-state with highest oscillator strength (f) at the CAM-B3LYP-D3/DEF2-TZVP level of theory using excitation energy transfer (EET) method in Gaussian 16 (Figures A4.3a, A4.3b and Table A4.2).[24,133] **PDI$_2$** and **PDI$_3$** exhibited comparable J_{Coul} values of -732.76 cm^{-1} and -710.30 cm^{-1}, respectively. The negative J_{Coul} values reinstate the J-type dipole-dipole excitonic interactions operative in the self-assembled aggregate structures of **PDI$_2$** and **PDI$_3$**.[20,21,32] In molecular aggregates, charge transfer (CT) plays a critical role in excitonic coupling and dictating the optical properties of the aggregates.[185,186] J_{CT} was calculated according to the equation Eq 1.2 given in section 1.2. **PDI$_2$** aggregate showed a significant J_{CT} of -85.22 cm^{-1}, whereas **PDI$_3$** aggregate exhibited weaker CT interactions, amounting to a J_{CT} of 37.92 cm^{-1}. The smaller $d_{interplanar}$ of 3.30 Å (Figure 4.4a) and the effective HOMO-HOMO/LUMO-LUMO overlap (Figure A4.4) between the J-type dimer stacks in **PDI$_2$** aggregate structure contribute to the theoretically observed higher strength of CT interactions. On the contrary, the larger $d_{interplanar}$ of 3.66 Å (Figure 4.4b) and the poor HOMO-HOMO/LUMO-LUMO overlap (Figure A4.5) between the J-type dimer stacks in **PDI$_3$** aggregate structure could be responsible for the lower strength of CT interactions.[32] According to equation Eq 1.3 given in section 1.2, the total excitonic coupling (J_{Total}), was estimated to be -817.98 cm^{-1} and -672.38 cm^{-1} in **PDI$_2$** and **PDI$_3$** aggregates, respectively.

4.2.6. Proposed Jablonski Diagram

A plausible schematic Jablonski diagram summarizing the mechanism of the SB-CS dynamics in **PDI$_2$** and **PDI$_3$** upon photoexcitation is shown in Figure 4.4c. Compared to the S_1* state energy in solution, **PDI$_2$** and **PDI$_3$** exhibit a J-type excitonic energy splitting upon aggregation

in the solid-state. The initially populated excited-state shows an order of magnitude faster charge separation in the solid-state compared to solution, populating the CSS via SB-CS. In the solid-state, the CSS relaxes to a lower vibrational energy level (CSS_{rel}), which recombines radiatively to repopulate the ground-state, whereas in solution, triplet excited-states are populated.

4.3. Conclusion

In summary, we have demonstrated ultrafast symmetry-breaking charge separation (SB-CS) in angularly oriented PDI multimers in the solid-state. A perylenediimide dimer (**PDI_2**) and a trimer (**PDI_3**) were prepared with systematic enhancement of core-twisted PDI fragments. Excitation and emission spectra of **PDI_2** and **PDI_3** thin films in a nonpolar polymethyl methacrylate (PMMA) polymer matrix exhibited broad red-shifted excitation and emission bands compared to the monomer photophysical properties in DIOX solvent. The red-shifted excitation spectra of **PDI_2** and **PDI_3** thin films relative to their monomeric counterparts in DIOX, suggest the emergence of J-type aggregates in the solid-state assemblies of these chromophores. Solid-state fsTA measurements of **PDI_2** and **PDI_3** in thin films in PMMA matrix exhibited ultrafast charge separation within the instrument response function (τ_{CS} <110 fs). The optimized dimer structures of the PDI aggregates corroborated the formation of J-type slip-stacked architectures. Theoretical calculations substantiated the role of through-space long-range intermolecular excitonic communication and short-range π-π interactions in the solid-state molecular packing driving the ultrafast charge separation process. Therefore, this investigation could be beneficial for designing SB-CS materials capable of solid-state charge separation for advanced optoelectronic devices.

4.4. Experimental Section

4.4.1. Syntheses and Characterization

The synthesis procedure and characterization of **PDI_2** and **PDI_3** is detailed in the previous sections 2.4.1 and 3.4.1 (*vide supra*).[111,181]

4.5. Additional Figures and Tables

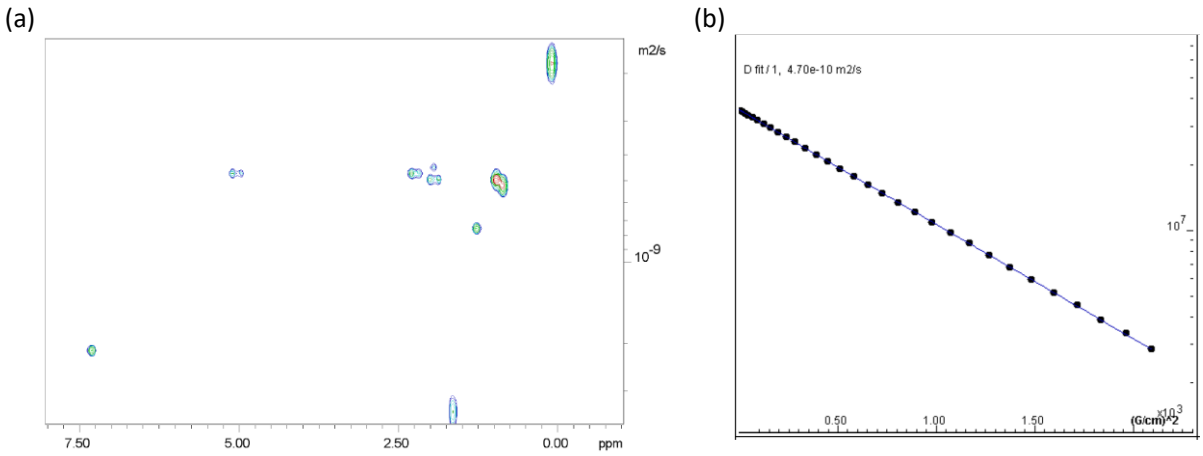

Figure A4.1: a) 2D-DOSY NMR spectrum and b) diffusion coefficient fit obtained from DOSY NMR spectrum of **PDI$_2$** in $CDCl_3$.

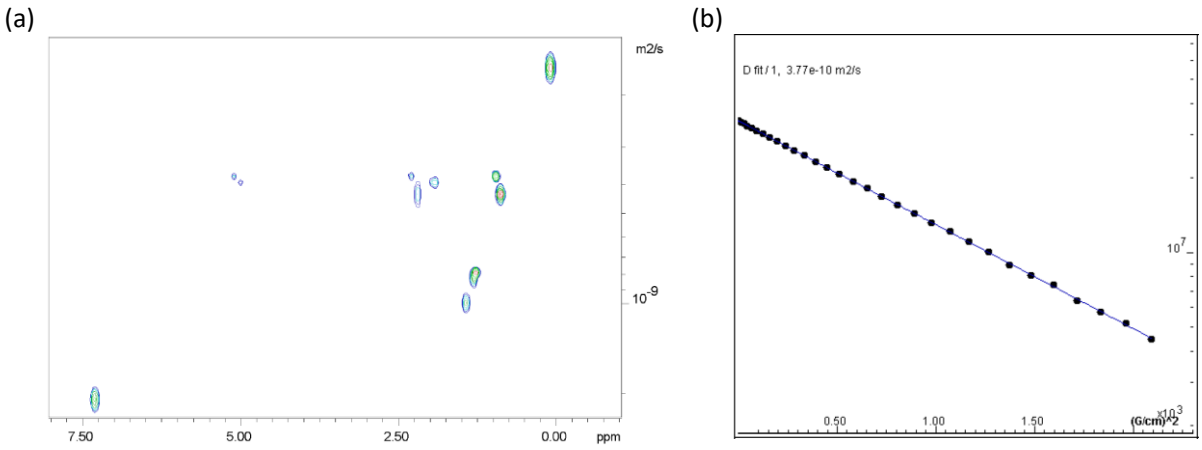

Figure A4.2: a) 2D-DOSY NMR spectrum and b) diffusion coefficient fit obtained from DOSY NMR spectrum of **PDI$_3$** in $CDCl_3$.

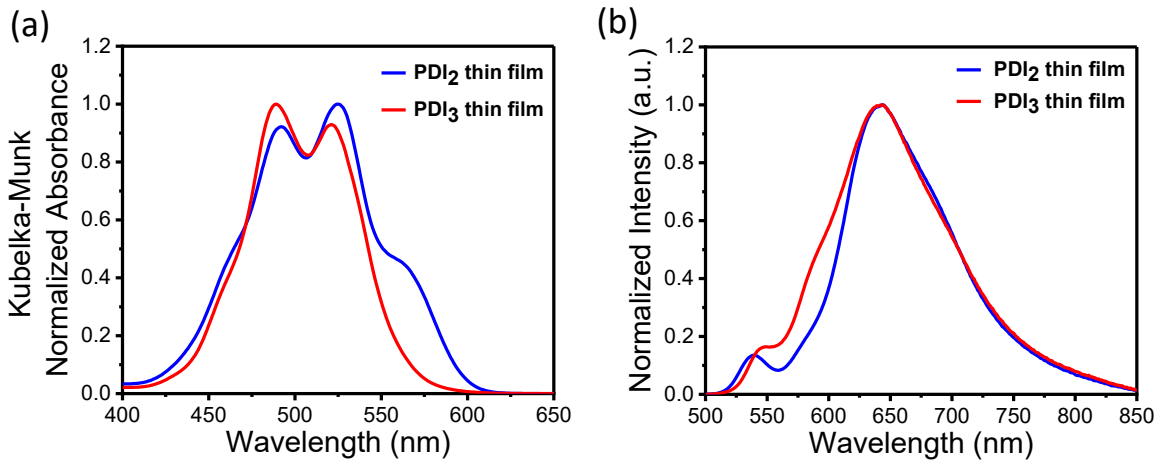

Figure A4.3: a) Kubelka-Munk transformed normalized absorption spectra of **PDI₂** and **PDI₃** thin films in PMMA matrix. b) Normalized emission spectra of **PDI₂** and **PDI₃** thin films in PMMA matrix.

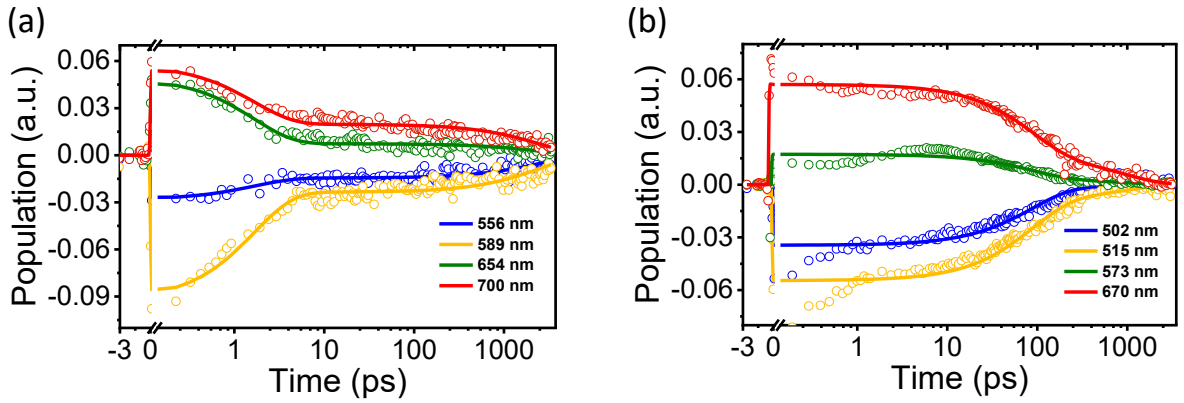

Figure A4.4: Global analysis fits for selected fsTA wavelengths (λ_{ex} = 480 nm) of a) **PDI₂** and b) **PDI₃** thin films in PMMA matrix using A → B → GS kinetic model. Fits are shown as solid lines.

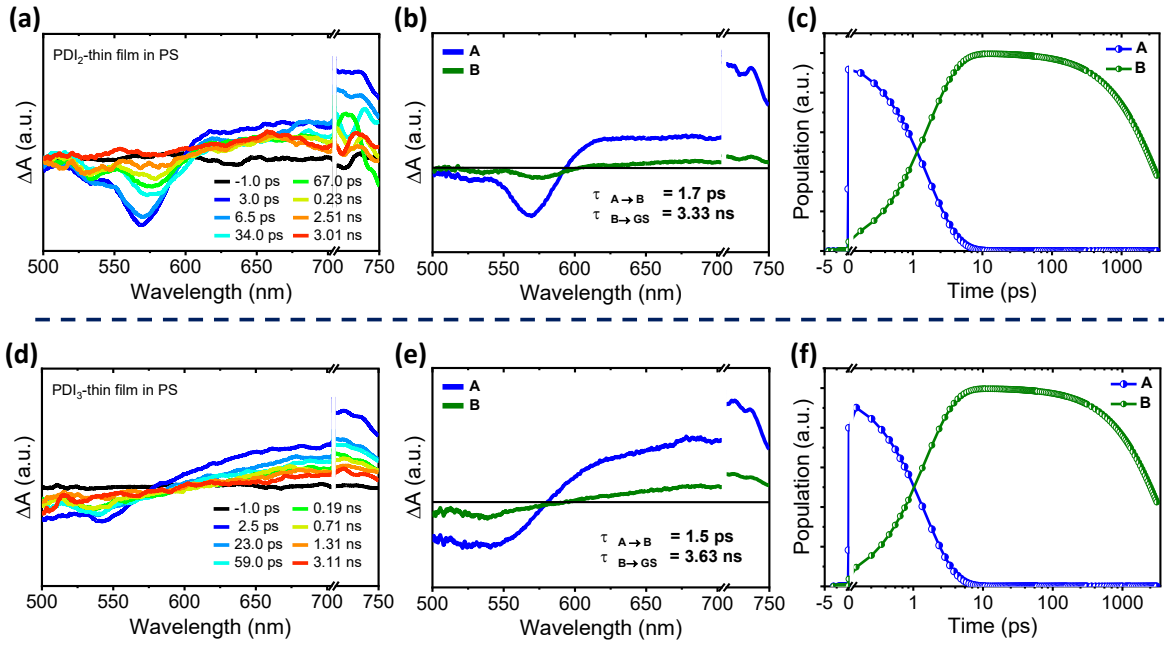

Figure A4.5: fsTA spectra of a) **PDI₂** and d) **PDI₃** in thin films in PS showing the excited-state dynamics upon photoexcitation. EAS reconstructed from global analysis of the fsTA data of b) **PDI₂** and e) **PDI₃** with the A → B → GS kinetic model, where A is the hot S_1 state, B is the $(S_1)_{rel}$ state, and GS is the ground-state (λ_{ex} = 480 nm). Relative population profile of the excited-states fitted using the above kinetic models in c) **PDI₂** and f) **PDI₃**.

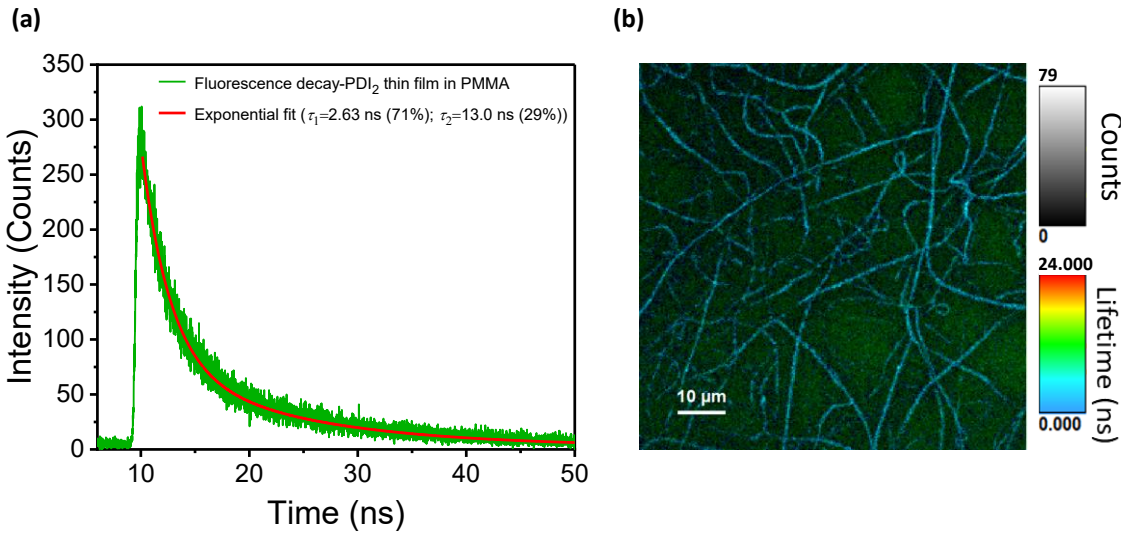

Figure A4.6: a) Fluorescence lifetime decay and b) FLIM image of **PDI₂** thin film.

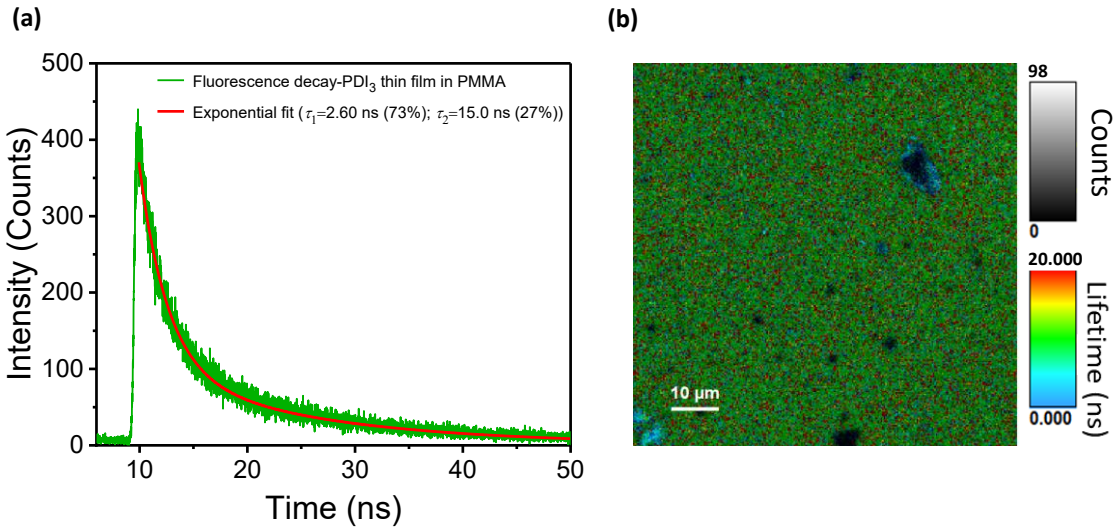

Figure A4.7: a) Fluorescence lifetime decay and b) FLIM image of **PDI₃** thin film.

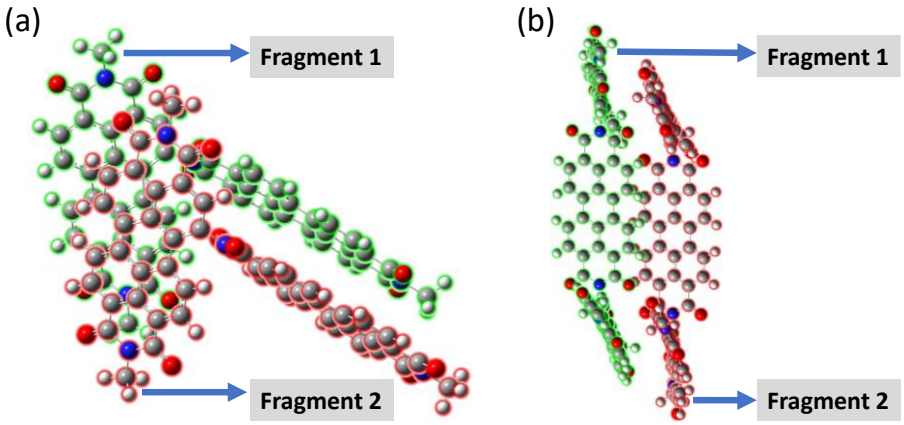

Figure A4.8: a) **PDI₂** and b) **PDI₃** dimer fragments used for the Coulombic coupling calculations.

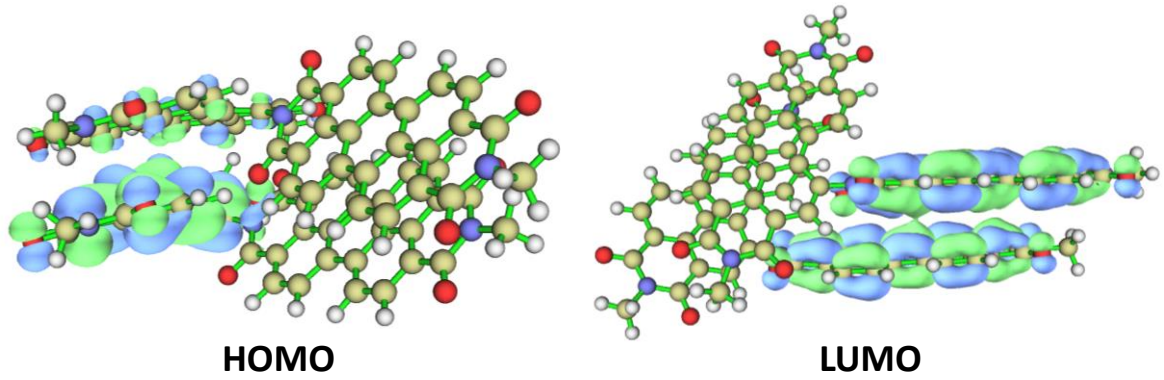

Figure A4.9: HOMO and LUMO isosurfaces of **PDI_2** aggregate, obtained from the ground-state optimized dimer geometry. N.B.- isovalue = 0.02 a.u.

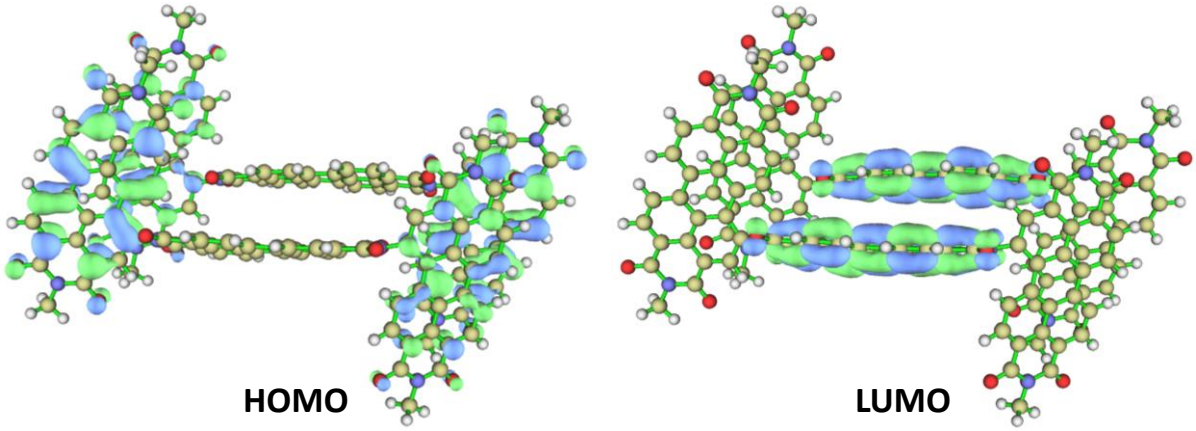

Figure A4.10: HOMO and LUMO isosurfaces of **PDI_3** aggregate, obtained from the ground-state optimized dimer geometry. N.B.- isovalue = 0.02 a.u.

Table A4.1: The theoretically computed J_{Coul}, J_{CT} and J_{Total} interaction values in **PDI_2** and **PDI_3** aggregates.

Aggregate	J_{Coul} (cm^{-1})	t_e (cm^{-1})	t_h (cm^{-1})	J_{CT} (cm^{-1})	J_{Total} (cm^{-1})
PDI_2	-732.76	-712.85	-226.58	-85.22	-817.98
PDI_3	-710.30	407.91	-151.44	37.92	-672.38

Table A4.2: The computed low-lying singlet excited-state energies and the corresponding oscillator strengths (*f*) in **PDI_2** and **PDI_3** aggregates at the CAM-B3LYP-D3/DEF2-TZVP level of theory.

State	PDI_2 aggregate		PDI_3 aggregate	
	Energy (eV)	Oscillator strength (*f*)	Energy (eV)	Oscillator strength (*f*)
S_1	2.55	0.7115	2.52	1.0630
S_2	2.63	0.8733	2.60	0.0210
S_3	2.98	0.0307	2.63	1.4571
S_4	3.54	0.0056	2.89	0.0087
S_5	3.59	0.0131	2.90	0.0170

4.6. Appendix

4.6.1. Materials and Methods

Detailed information regarding the materials and methods used is given in section 2.6.1.

Thin Film Preparation and Photophysical Measurements

For the thin film measurements, a square quartz substrate was cleaned and 5 mg/mL samples of **PDI$_2$** and **PDI$_3$** dissolved in PMMA polymer matrix in TOL (20 mg/mL) was uniformly drop casted. The thin films were subjected to vacuum drying and subsequently kept under a nitrogen environment until they were used for the experiments. The diffuse-reflectance spectra of the thin films were measured and the corresponding Kubelka-Munk transformed absorption spectra were calculated using UVProbe software by Shimadzu. The solution-state fluorescence quantum yield (ϕ_F) was measured relatively with respect to PDI as standard by exciting at 480 nm, whereas for the solid-state ϕ_F, it was measured using an integrating sphere by exciting at 480 nm in the Horiba Jobin Yvon Fluorolog spectrometer.

4.6.2. DOSY NMR Measurement

DOSY or Diffusion-Ordered Spectroscopy was employed to understand the aggregate stacking in **PDI$_2$** and **PDI$_3$** multimers. DOSY NMR experiments were performed at ≈3 mM concentration of PDI samples in $CDCl_3$. The diffusion coefficients (D) were estimated by fitting the DOSY NMR data, and D was found to be 4.70e-10 m^2/s and 3.77e-10 m^2/s for **PDI$_2$** and **PDI$_3$**, respectively. The molecular weight for the **PDI$_2$** and **PDI$_3$** aggregates was estimated from the experimentally obtained diffusion coefficients and was found to be MW^{DOSY} = 12235.37 g/mol and 16939.20 g/mol for **PDI$_2$** and **PDI$_3$** aggregates, respectively, with an average deviation of 11% and 23% maximum error. Dividing the MW^{DOSY} by the molecular weight of the PDI monomers, approximately 12 molecules of **PDI$_2$** and **PDI$_3$** each were estimated to be stacked in the individual aggregate structure.

4.6.3. Femtosecond Transient Absorption (fsTA) Measurement

The detailed fsTA instrumentation and experimental methods are provided in the previous section 2.6.5. For the fsTA measurements of **PDI$_2$** and **PDI$_3$** thin films, the samples were excited with 480 nm, 200 nJ, 100 fs laser pulse. Upon variations in laser intensity, the detected kinetic components remained unaffected, excluding singlet-singlet annihilation.[142] For fsTA measurements on thin films, a circular quartz cuvette was thoroughly cleaned by sonicating it sequentially in deionized water, isopropanol, and ACE for 10 minutes each, followed by drying under a stream of nitrogen.[187] Followingly, **PDI$_2$** and **PDI$_3$** sample (5 mg/mL) dissolved in PMMA polymer matrix in TOL (20 mg/mL) was uniformly dropcasted on the quartz cuvette. The films were dried in a vacuum and stored in a nitrogen atmosphere prior to the experiments.

The fsTA experiments of **PDI$_2$** and **PDI$_3$** in the solid-state were further recorded in another nonpolar (ε = 2.60) polystyrene (PS) polymer matrix, and the corresponding fsTA spectra is given in Figure A4.5. The deconvoluted evolution-associated spectra in both **PDI$_2$** and **PDI$_3$** demonstrates the population of a hot singlet excited-state (S_1) with partial charge transfer character (Figures A4.5b, A4.5e), as evident from the broadened and featureless excited-state absorption prominent in the first principal component (A). The first component (A) shows rapid vibrational relaxation (VR) to give rise to the relaxed singlet excited-state ($(S_1)_{rel}$) in **PDI$_2$** within τ_{VR} = 1.7 ps and **PDI$_3$** within τ_{VR} = 1.5 ps. The $(S_1)_{rel}$ state decays to the ground-state within 3.33 ns and 3.63 ns in **PDI$_2$** and **PDI$_3$**, respectively. Therefore, distinct ESA features of the radical cation and radical anion were not observed in the fsTA dynamics of **PDI$_2$** and **PDI$_3$** thin films in PS, which confirms the non-feasibility of SB-CS in PS. The samples for the thin film fsTA analysis in the PS matrix were made following the same procedure used for the PMMA matrix described previously.

4.6.4. Fluorescence Lifetime Imaging Microscopy

Fluorescence lifetime imaging microscopy (FLIM) images were obtained using the MicroTime 200 (MT200) time-resolved fluorescence microscope by PicoQuant. The inverted microscope (Olympus IX83) was equipped with a piezo scanning stage (P-733.2CD, PI). Sample excitation was achieved using a 512 nm pulsed laser (LDH-D-C-512, PicoQuant) with a repetition rate of

20 MHz, and scanning was performed with a dwell time of 0.4 ms. A water immersion objective (UplanSApo 60× NA 1.2) collected the photons. Spectral filtering utilized a major dichroic mirror (zt405-442/510 rpc-UF3, Chroma) and a 519 nm long-pass emission filter (FF01-519/LP, Semrock). A pinhole (50 μm) spatially filtered the photons, which were then directed to a SPCM-AQRH single-photon avalanche photodiode (SPAD) detector. The detector signals underwent postprocessing by the HydraHarp 400 time-correlated single-photon counting (TCSPC) data acquisition unit (PicoQuant). SymPhoTime64 software (PicoQuant) handled data recording and analysis. The thin film samples of **PDI$_2$** and **PDI$_3$** in PMMA matrix were prepared following the sample preparation technique mentioned in the fsTA measurement section under 4.6.3.

4.6.5. Computational Analysis

All the theoretical investigations were performed in Gaussian 16.[139] The ground-state optimized structures of **PDI$_2$** and **PDI$_3$** monomers were obtained at B3LYP-D3/6-311+G(d,p) level of theory.[111,181] Ground-state geometry optimization of the PDI aggregates (**PDI$_2$** and **PDI$_3$**) in vacuum was performed at B3LYP-D3/6-31G level of theory. HOMO-LUMO orbital isosurfaces for the **PDI$_2$** and **PDI$_3$** dimer model systems were generated using Multiwfn 3.8.[140]

4.6.6. Coulombic Coupling Calculation

The detailed Coulombic coupling estimation methodology is provided in section 2.6.4. TDDFT calculation was performed on **PDI$_2$** and **PDI$_3$** aggregate optimized geometries after defining each PDI monomer as a fragment (Figures A4.3a, A4.3b), and Coulombic coupling for the singlet excited-state with the highest oscillator strength (*f*) was procured at the CAM-B3LYP-D3/DEF2-TZVP level of theory.[23,24,133]

4.6.7. Charge Transfer-Mediated Coupling Calculation

Excitonic interactions are strongly influenced by short-range charge transfer (CT)-mediated coupling,[32,188] which arises from the extent of wavefunction overlap between neighbouring molecules and is quantified by the equation Eq 1.2 provided in section 1.2. The t_e and t_h values were calculated using the energy splitting in dimer method implemented in the Catnip tool. E_{CT} denotes the energy of the charge transfer state, while E_{S_1} corresponds to the energy of the first

Frenkel exciton state for the **PDI$_2$** and **PDI$_3$** monomers, as obtained from TDDFT calculations. The E_{CT} and E_{S_1} values for **PDI$_2$** and **PDI$_3$** molecules were obtained from the previously reported literature from our group (E_{CT} = 3.08 eV and E_{S_1}= 2.61 eV for **PDI$_2$**; E_{CT} = 2.99 eV and E_{S_1}= 2.59 eV for **PDI$_3$**).[111,181] The overall coupling between the adjacent molecules can be described by the equation Eq 1.3 provided in section 1.2.

Chapter 5

Conclusion and Outlook

Achieving a comprehensive understanding of the symmetry-breaking charge separation (SB-CS) process in organic chromophores is an emerging research area, driving potential applications in optoelectronic devices mimicking the efficient electron transfer process in natural photosynthesis. A fundamental understanding of the orientation-dependent excitonic coupling in π- conjugated organic multimers is essential to understanding the intramolecular and intermolecular electronic communication modulating the charge separation and charge recombination rates. The research work presented in this thesis provides extensive insights into the nature and strength of excitonic coupling as a function of the spatial orientation of the chromophoric assembly modulating the charge separation rates. The 2nd and 3rd chapters comprehensively demonstrated the acceleration of intramolecular SB-CS in an angular PDI dimer and trimer (**A-PDI$_2$** and **PDI-T**), respectively, in polar dielectric mediums. Weak excitonic coupling is rationalized as the crucial factor driving the SB-CS process in **A-PDI$_2$** and **PDI-T** in the isolated monomeric states. In the 4th chapter of this thesis, ultrafast SB-CS was realized for two PDI multimers (**PDI$_2$** and **PDI$_3$**) in thin films under the effect of a nonpolar polymer matrix. The strong π–π interactions and through-space excitonic coupling in the J-aggregated **PDI$_2$** and **PDI$_3$** thin films provide an excellent design strategy to achieve and accelerate SB-CS in the solid-state, having profound implications in optoelectronic devices.

This thesis demonstrates and establishes the acceleration of charge separation as a function of molecular geometry. Charge separation as fast as τ_{CS} < 110 fs was obtained in the solid-state for PDI chromophores. However, to harness the localized charges in a SB-CS material to enhance the photoconversion efficiency in organic solar cells, charge separation should be faster, whereas charge recombination should be slower. Therefore, novel molecular designs must be developed and investigated to push the charge recombination timescales to hundreds of nanoseconds or microseconds.

Bibliography

1 A. Marais, I. Sinayskiy, F. Petruccione and R. Van Grondelle, *Sci. Rep.*, 2015, **5**, 1–8.

2 M. Yang, A. Damjanović, H. M. Vaswani and G. R. Fleming, *Biophys. J.*, 2003, **85**, 140–158.

3 T. Mirkovic, E. E. Ostroumov, J. M. Anna, R. Van Grondelle, Govindjee and G. D. Scholes, *Chem. Rev.*, 2017, **117**, 249–293.

4 T. Brixner, R. Hildner, J. Köhler, C. Lambert and F. Würthner, *Adv. Energy Mater.*, 2017, **7**, 1700236.

5 M. T. Madigan and D. O. Jung, *Photosynth. Res.*, 2009, 1–15.

6 X. Zhou, S. Lin and H. Yan, *J. Nanobiotech.*, 2022, **20**, 1–23.

7 K. Sauer, R. J. Cogdell, S. M. Prince, A. Freer, N. W. Isaacs and H. Scheer, *Photochem. Photobiol.*, 1996, **64**, 564–576.

8 Bacterial Photosynthesis, http://www.photobiology.info/Jones.html, (accessed 23 July 2025).

9 J. Yang, M. C. Yoon, H. Yoo, P. Kim and D. Kim, *Chem. Soc. Rev.*, 2012, **41**, 4808–4826.

10 E. Sebastian and M. Hariharan, *ACS Energy Lett.*, 2022, **7**, 696–711.

11 E. Romero, R. Augulis, V. I. Novoderezhkin, M. Ferretti, J. Thieme, D. Zigmantas and R. Van Grondelle, *Nat. Phys.*, 2014, **10**, 676–682.

12 S. Savikhin and R. Jankowiak, *Biophys. Photosynth.*, 2014, 193–240.

13 E. E. Jelley, *Nature*, 1936, **138**, 1009–1010.

14 G. Scheibe, *Angew. Chem.*, 1937, **50**, 212–219.

15 B. Heyne, *Photochem. Photobiol. Sci.*, 2016, **15**, 1103–1114.

16 M. Kasha, *Radiat. Res.*, 1963, **20**, 55–70.

17 J. Gierschner, J. Shi, B. Milián-Medina, D. Roca-Sanjuán, S. Varghese, S. Y. Park, *Adv. Opt. Mater.*, 2021, **9**, 2002251.

18 E. Da Como and E. von Hauff, *Angew. Chem. Int. Ed.*, 2017, **56**, 4915–4916.

19 C. J. Bardeen, *Annu. Rev. Phys. Chem.*, 2014, **65**, 127–148.

20 A. S. Davydov, *Sov. Phys. Uspekhi*, 1964, **7**, 145–178.

21 M. Kasha, H. R. Rawls and M. A. El-Bayoumi, *Pure Appl. Chem.*, 1965, **11**, 371–392.

22 G. D. Scholes, K. P. Ghiggino, A. M. Oliver and M. N. Paddon-Row, *J. Am. Chem. Soc.*, 1993, **115**, 4345–4349.

23 B. P. Krueger, G. D. Scholes and G. R. Fleming, *J. Phys. Chem. B*, 1998, **102**, 5378–5386.

24 G. D. Scholes and K. P. Ghiggino, *J. Phys. Chem.*, 1994, **98**, 4580–4590.

25 F. Fassioli, R. Dinshaw, P. C. Arpin and G. D. Scholes, *J. R. Soc. Interface*, 2014, *11*.

26 M. K. Espinoza Cangahuala, S. R. Krishnaswamy, A. V. Kuevda, M. S. Pshenichnikov and T. L. C. Jansen, *J. Chem. Phys.*, 2025, **162**, 54311.

27 J. L. Bricks, Y. L. Slominskii, I. D. Panas and A. P. Demchenko, *Methods Appl. Fluoresc.*, 2017, **6**, 012001.

28 E. Sebastian, A. M. Philip, A. Benny and M. Hariharan, *Angew. Chem. Int. Ed.*, 2018, **57**, 15696–15701.

29 J. Zhou, W. Zhang, X. F. Jiang, C. Wang, X. Zhou, B. Xu, L. Liu, Z. Xie and Y. Ma, *J. Phys. Chem. Lett.*, 2018, **9**, 596–600.

30 M. P. Lijina, A. Benny, E. Sebastian and M. Hariharan, *Chem. Soc. Rev.*, 2023, **52**, 6664–6679.

31 H. Yamagata, C. M. Pochas and F. C. Spano, *J. Phys. Chem. B*, 2012, **116**, 14494–14503.

32 N. J. Hestand and F. C. Spano, *Chem. Rev.*, 2018, **118**, 7069–7163.

33 H. Yamagata, J. Norton, E. Hontz, Y. Olivier, D. Beljonne, J. L. Brédas, R. J. Silbey and F. C. Spano, *J. Chem. Phys.*, 2011, **134**, 204703.

34 J. Vura-Weis, M. A. Ratner and M. R. Wasielewski, *J. Am. Chem. Soc.*, 2010, **132**, 1738–1739.

35 A. Benny, D. Sasikumar and M. Hariharan, *J. Phys. Chem. C*, 2019, **123**, 26758–26768.

36 N. J. Hestand and F. C. Spano, *Acc. Chem. Res.*, 2017, **50**, 341–350.

37 R. M. Young and M. R. Wasielewski, *Acc. Chem. Res.*, 2020, **53**, 1957–1968.

38 E. Vauthey, *ChemPhysChem*, 2012, **13**, 2001–2011.

39 M. J. Álvaro-Martins, C. Billiaux, P. Godard, R. Oda, G. Raffy and D. M. Bassani, *Chem. Commun.*, 2023, **59**, 7963–7966.

40 A. N. Bartynski, M. Gruber, S. Das, S. Rangan, S. Mollinger, C. Trinh, S. E. Bradforth, K. Vandewal, A. Salleo, R. A. Bartynski, W. Bruetting and M. E. Thompson, *J. Am. Chem. Soc.*, 2015, **137**, 5397–5405.

41 J. M. Bradley, A. F. Coleman, P. J. Brown, Y. Huang, R. M. Young and M. R. Wasielewski, *Proc. Natl. Acad. Sci. U.S.A.*, 2023, **120**, e2313575120.

42 F. C. Spano, *J. Phys. Chem. C*, 2024, **128**, 248–260.

43 R. Roy, S. Chawla, V. Sharma, A. K. Pal, Y. Silori, A. Datta, A. K. De and A. L. Koner, *Chem. Sci.*, 2024, **15**, 6363–6377.

44 A. I. Ivanov, *J. Photochem. Photobiol.*, 2024, **58**, 100651.

45 X. Zhao, R. M. Young, C. Tang, G. Wu, K. R. Peinkofer, Y. Han, S. Yang, Y. K. Xing, H. Han, H. Wu, X. Li, Y. Feng, R. Zhang, C. L. Stern, M. R. Wasielewski and J. F. Stoddart, *Chem*, 2025, **11**, 102248.

46 L. A. Baker and S. Habershon, *Proc. R. Soc. A*, 2017, **473**, 1-25.

47 R. van Grondelle and V. Sundström, *Photosynthetic Light-Harvesting Systems. Organization and Function*, De Gruyter, 2019, 403–438.

48 V. Markovic, D. Villamaina, I. Barabanov, L. M. Lawson Daku and E. Vauthey, *Angew. Chem. Int. Ed.*, 2011, **50**, 7596–7598.

49 T. Van der Boom, R. T. Hayes, Y. Zhao, P. J. Bushard, E. A. Weiss and M. R. Wasielewski, *J. Am. Chem. Soc.*, 2002, **124**, 9582–9590.

50 C. Trinh, K. Kirlikovali, S. Das, M. E. Ener, H. B. Gray, P. Djurovich, S. E. Bradforth and M. E. Thompson, *J. Phys. Chem. C*, 2014, **118**, 21834–21845.

51 G. D. Scholes, T. Fournier, A. W. Parker and D. Phillips, *J. Chem. Phys.*, 1999, **111**, 5999–6010.

52 B. Dereka, D. Svechkarev, A. Rosspeintner, A. Aster, M. Lunzer, R. Liska, A. M. Mohs and E. Vauthey, *Nat. Commun.*, 2020, **11**, 1–11.

53 P. Roy, G. Bressan, J. Gretton, A. N. Cammidge, S. R. Meech, *Angew. Chem. Int. Ed.*, 2021, **60**, 10568–10572.

54 H. Khandelwal, A. R. Mallia, R. T. Cheriya and M. Hariharan, *Phys. Chem. Chem. Phys.*, 2012, **14**, 15282–15285.

55 M. Zhang, L. Zhu, G. Zhou, T. Hao, C. Qiu, Z. Zhao, Q. Hu, B. W. Larson, H. Zhu, Z. Ma, Z. Tang, W. Feng, Y. Zhang, T. P. Russell and F. Liu, *Nat. Commun.*, 2021, **12**, 1–10.

56 Z. Nilsson, M. Van Erdewyk, L. Wang and J. B. Sambur, *ACS Energy Lett.*, 2020, **5**, 1474–1486.

57 J. L. Brédas, E. H. Sargent and G. D. Scholes, *Nat. Mater.*, 2016, **16**, 35–44.

58 A. J. Gillett, A. Privitera, R. Dilmurat, A. Karki, D. Qian, A. Pershin, G. Londi, W. K. Myers, J. Lee, J. Yuan, S. J. Ko, M. K. Riede, F. Gao, G. C. Bazan, A. Rao, T. Q. Nguyen, D. Beljonne and R. H. Friend, *Nature*, 2021, **597**, 666–671.

59 V. Coropceanu, X. K. Chen, T. Wang, Z. Zheng and J. L. Brédas, *Nat. Rev. Mater.*, 2019, **4**, 689–707.

60 M. Kellogg, A. Akil, D. S. Muthiah Ravinson, L. Estergreen, S. E. Bradforth and M. E. Thompson, *Faraday Discuss.*, 2019, **216**, 379–394.

61 M. Silver, D. Olness, M. Swicord and R. C. Jarnagin, *Phys. Rev. Lett.*, 1963, **10**, 12.

62 F. Schneider and E. Lippert, *Ber. Bunsenges. Phys. Chem.*, 1968, **72**, 1155–1160.

63 N. Nakashima, M. Murakawa and N. Mataga, *Bull. Chem. Soc. Jpn.*, 1976, **49**, 854–858.

64 Y. Wu, R. M. Young, M. Frasconi, S. T. Schneebeli, P. Spenst, D. M. Gardner, K. E. Brown, F. Würthner, J. F. Stoddart and M. R. Wasielewski, *J. Am. Chem. Soc.*, 2015, **137**, 13236–13239.

65 P. D. Maret, D. Sasikumar, E. Sebastian and M. Hariharan, *J. Phys. Chem. Lett.*, 2023, **14**, 8667–8675.

66 A. Yahagh, R. R. Kaswan, S. Kazemi, P. A. Karr and F. D'Souza, *Chem. Sci.*, 2024, **15**, 906–913.

67 C. Lin, T. Kim, J. D. Schultz, R. M. Young and M. R. Wasielewski, *Nat. Chem.,* 2022, **14**, 786–793.

68 J. Strümpfer and K. Schulten, *J. Chem. Phys.*, 2009, **131**, 225101.

69 T. Cardona, A. Sedoud, N. Cox and A. W. Rutherford, *Biochim. Biophys. Acta - Bioenerg.*, 2012, **1817**, 26–43.

70 E. Sebastian and M. Hariharan, *J. Am. Chem. Soc.*, 2021, **143**, 13769–13781.

71 A. Aster, G. Licari, F. Zinna, E. Brun, T. Kumpulainen, E. Tajkhorshid, J. Lacour and E. Vauthey, *Chem. Sci.*, 2019, **10**, 10629–10639.

72 X. Niu, K. Tajima, J. Kong, M. Tao, N. Fukui, Z. Kuang, H. Shinokubo and A. Xia, *Phys. Chem. Chem. Phys.*, 2022, **24**, 14007–14015.

73 K. Wang, X. Chen, S. Peng, G. Liang, J. Xu, L. Zhang, D. Wu and J. Xia, *J. Chem. Phys.*, 2024, **160**, 164719.

74 X. Zhao, J. P. O'Connor, J. D. Schultz, Y. J. Bae, C. Lin, R. M. Young and M. R. Wasielewski, *J. Phys. Chem. B*, 2021, **125**, 6945–6954.

75 J. Wega, K. F. Zhang, J. Lacour and E. Vauthey, *J. Phys. Chem. Lett.*, 2024, **15**, 2834–2840.

76 Y. Liu, J. Zhao, A. Iagatti, L. Bussotti, P. Foggi, E. Castellucci, M. Di Donato and K. L. Han, *J. Phys. Chem. C*, 2018, **122**, 2502–2511.

77 I. Papadopoulos, M. J. Álvaro-Martins, D. Molina, P. M. McCosker, P. A. Keller, T. Clark, Á. Sastre-Santos and D. M. Guldi, *Adv. Energy Mater.*, 2020, **10**, 2001496.

78 J. M. Giaimo, A. V. Gusev and M. R. Wasielewski, *J. Am. Chem. Soc.*, 2002, **124**, 8530–8531.

79 F. Würthner, C. R. Saha-Möller, B. Fimmel, S. Ogi, P. Leowanawat and D. Schmidt, *Chem. Rev.*, 2016, **116**, 962–1052.

80 M. W. Holman, R. Liu, L. Zang, P. Yan, S. A. DiBenedetto, R. D. Bowers and D. M. Adams, *J. Am. Chem. Soc.*, 2004, **126**, 16126–16133.

81 D. Veldman, S. M. A. Chopin, S. C. J. Meskers, M. M. Groeneveld, R. M. Williams and R. A. J. Janssen, *J. Phys. Chem. A*, 2008, **112**, 5846–5857.

82 P. Spenst, R. M. Young, M. R. Wasielewski and F. Würthner, *Chem. Sci.*, 2016, **7**, 5428–5434.

83 K. Wang, G. Shao, S. Peng, X. You, X. Chen, J. Xu, H. Huang, H. Wang, D. Wu and J. Xia, *J. Phys. Chem. B*, 2022, **126**, 3758–3767.

84 G. Yu, L. Yang, Y. Gao, Z. Guo, Y. Tian, Y. Wang, Y. Wan, Y. Han, W. Yang, J. Song and X. Ma, *J. Phys. Chem. Lett.*, 2024, **15**, 12561–12570.

85 J. Kong, W. Zhang, G. Li, D. Huo, Y. Guo, X. Niu, Y. Wan, B. Tang and A. Xia, *J. Phys. Chem. Lett.*, 2020, **11**, 10329–10339.

86 C. E. Ramirez, S. Chen, N. E. Powers-Riggs, I. Schlesinger, R. M. Young and M. R. Wasielewski, *J. Am. Chem. Soc.*, 2020, **142**, 18243–18250.

87 G. Ran, J. Zeb, Y. Song, P. A. Denis, U. Ghani and W. Zhang, *J. Phys. Chem. C*, 2022, **126**, 3872–3880.

88 P. J. Brown, M. L. Williams, S. B. Tyndall, Y. Qi, R. M. Young and M. R. Wasielewski, *J. Phys. Chem. C*, 2024, **128**, 14185–14194.

89 A. Khan, N. A. Tcyrulnikov, R. Roy, R. M. Young, M. R. Wasielewski and A. L. Koner, *J. Phys. Chem. C*, 2024, **128**, 10474–10482.

90 J. Mao, Q. Fan, Z. Yan, X. Chen, S. Zhao, Y. Lu, S. Li, W. Jiang, Z. Xu, Z. Wang and J. Wang, *J. Am. Chem. Soc.*, 2025, **147**, 12730–12739.

91 R. Carmieli, Q. Mi, A. B. Ricks, E. M. Giacobbe, S. M. Mickley and M. R. Wasielewski, *J. Am. Chem. Soc.*, 2009, **131**, 8372–8373.

92 M. R. Wasielewski, *Chem. Rev.*, 1992, **92**, 435–461.

93 A. P. H. J. Schenning, J. V. Herrikhuyzen, P. Jonkheijm, Z. Chen, F. Würthner and E. W. Meijer, *J. Am. Chem. Soc.*, 2002, **124**, 10252–10253.

94 B. Rybtchinski, L. E. Sinks and M. R. Wasielewski, *J. Am. Chem. Soc.*, 2004, **126**, 12268–12269.

95 B. A. Gregg and R. A. Cormier, *J. Am. Chem. Soc.*, 2001, **123**, 7959–7960.

96 E. E. Neuteboom, S. C. J. Meskers, P. A. Van Hal, J. K. J. Van Duren, E. W. Meijer, R. A. J. Janssen, H. Dupin, G. Pourtois, J. Cornil, R. Lazzaroni, J. L. Brédas and D. Beljonne, *J. Am. Chem. Soc.*, 2003, **125**, 8625–8638.

97 X. Zhan, A. Facchetti, T. J. Marks, A. Ratner, M. R. Wasielewski, S. Barlow and S. R. Marder, *Adv. Mater.*, 2011, **23**, 268–284.

98 S. Rajaram, R. Shivanna, S. K. Kandappa and K. S. Narayan, *J. Phys. Chem. Lett.*, 2012, **3**, 2405–2408.

99 N. Renaud, P. A. Sherratt and M. A. Ratner, *J. Phys. Chem. Lett.*, 2013, **4**, 1065–1069.

100 Z. R. Grabowski, K. Rotkiewicz and W. Rettig, *Chem. Rev.*, 2003, **103**, 3899–4031.

101 W. Rettig, *Angew. Chem. In. Ed.*, 1986, **25**, 971–988.

102 B. Dereka, M. Koch and E. Vauthey, *Acc. Chem. Res.*, 2017, **50**, 426–434.

103 C. M. Pochas, K. A. Kistler, H. Yamagata, S. Matsika and F. C. Spano, *J. Am. Chem. Soc.*, 2013, **135**, 3056–3066.

104 Y. Guo, Z. Ma, X. Niu, W. Zhang, M. Tao, Q. Guo, Z. Wang and A. Xia, *J. Am. Chem. Soc.*, 2019, **141**, 12789–12796.

105 E. Sebastian, J. Sunny and M. Hariharan, *Chem. Sci.*, 2022, **13**, 10824–10835.

106 H. Langhals and W. Jona, *Angew. Chem. Int. Ed.*, 1998, **37**, 952– 955.

107 Z. Luo, K. Wu, Y. Zhao, B. Qiu, Y. Li and C. Yang, *Dyes Pigm.*, 2019, **163**, 356–362.

108 B. Zhang, H. Soleimaninejad, D. J. Jones, J. M. White, K. P. Ghiggino, T. A. Smith and W. W. H. Wong, *Chem. Mater.*, 2017, **29**, 8395–8403.

109 A. Austin, N. J. Hestand, I. G. McKendry, C. Zhong, X. Zhu, M. J. Zdilla, F. C. Spano and J. M. Szarko, *J. Phys. Chem. Lett.*, 2017, **8**, 1118–1123.

110 F. Gao, Y. Zhao and W. Liang, *J. Phys. Chem. B*, 2011, **115**, 2699–2708.

111 A. Mazumder, K. Vinod, P. D. Maret, P. P. Das and M. Hariharan, *J. Phys. Chem. Lett.*, 2024, **15**, 5896–5904.

112 J. J. Snellenburg, S. Laptenok, R. Seger, K. M. Mullen and I. H. M. van Stokkum, *J. Stat. Softw.*, 2012, **49**, 1–22.

113 Y. Hong, F. Schlosser, W. Kim, F. Würthner and D. Kim, *J. Am. Chem. Soc.*, 2022, **144**, 15539–15548.

114 H. Imahori, K. Hagiwara, M. Aoki, T. Akiyama, S. Taniguchi, T. Okada, M. Shirakawa and Y. Sakata, *J. Am. Chem. Soc.*, 1996, **118**, 11771–11782.

115 Y. Kobayashi, D. Fukuda, Y. Okayasu and Y. Nagai, *J. Chem. Phys.*, 2024, **161**, 34308.

116 D. J. Gibbons, A. Farawar, P. Mazzella, S. Leroy-Lhez and R. M. Williams, *Photochem. Photobiol. Sci.*, 2020, **19**, 136–158.

117 N. J. Turro, V. Ramamurthy, J. C. Scaiano, *Principles of Molecular Photochemistry: An Introduction*; University Science Books, 2009.

118 H. Dreeskamp, E. Koch and M. Zander, *Chem. Phys. Lett.*, 1975, **31**, 251–253.

119 W. E. Ford and P. V. Kamat, *J. Phys. Chem.*, 1987, **91**, 6373–6380.

120 J. Sunny, E. Sebastian, S. Sujilkumar, F. Würthner, B. Engels and M. Hariharan, *Phys. Chem. Chem. Phys.*, 2023, **25**, 28428–28436.

121 F. Gotardo, L. H. Z. Cocca, T. V. Acunha, A. Longoni, J. Toldo, P. F. B. Gonçalves, B. A. Iglesias and L. De Boni, *Chem. Phys. Lett.*, 2017, **674**, 48–57.

122 S. Medina Rivero, M. J. Alonso-Navarro, C. Tonnelé, J. M. Marín-Beloqui, F. Suárez-Blas, T. M. Clarke, S. Kang, J. Oh, M. M. Ramos, D. Kim, D. Casanova, J. L. Segura and J. Casado, *J. Am. Chem. Soc.*, 2023, **145**, 27295–27306.

123 R. Ringström, Z. W. Schroeder, L. Mencaroni, P. Chabera, R. R. Tykwinski and B. Albinsson, *J. Phys. Chem. Lett.*, 2023, **14**, 7897–7902.

124 Y. Bo, P. Hou, J. Wan, H. Cao, Y. Liu, L. Xie, D. M. Guldi, Y. Bo, D. M. Guldi, P. Hou, J. Wan, H. Cao, L. Xie and Y. Liu, *Adv. Mater.*, 2023, **35**, 2302664.

125 M. Lv, X. Lu, Y. Jiang, M. E. Sandoval-Salinas, D. Casanova, H. Sun, Z. Sun, J. Xu, Y. Yang and J. Chen, *Angew. Chem. Int. Ed.*, 2022, **61**, e202113190.

126 K. Nagarajan, A. R. Mallia, K. Muraleedharan and M. Hariharan, *Chem. Sci.*, 2017, **8**, 1776–1782.

127 A. Weller, *Z. Phys. Chem.*, 1982, **133**, 93–98.

128 F. Plasser, *J. Chem. Phys.*, 2020, **152**, 84108.

129 F. Plasser and H. Lischka, *J. Chem. Theory Comput.*, 2012, **8**, 2777–2789.

130 D. Lee, J. Lee, D. H. Sin, S. G. Han, H. Lee, W. Choi, H. Kim, J. Noh, J. Mun, W. Sung, S. W. Kim, B. G. Jeong, S. H. Kim, J. Rho, M. S. Jeong and K. Cho, *J. Phys. Chem. C*, 2022, **126**, 3171–3179.

131 Z. Guan, H. W. Li, J. Zhang, Y. Cheng, Q. Yang, M. F. Lo, T. W. Ng, S. W. Tsang and C. S. Lee, *ACS Appl. Mater. Interfaces*, 2016, **8**, 21798–21805.

132 B. F. Emad Aziz, A. Vollmer, S. Eisebitt, W. Eberhardt, P. Pingel, D. Neher and N. Koch, *Adv. Mater.*, 2007, **19**, 3257–3260.

133 Z. Q. You and C. P. Hsu, *Int. J. Quantum Chem.*, 2014, **114**, 102–115.

134 T. F. Hinrichsen, C. C. S. Chan, C. Ma, D. Paleček, A. Gillett, S. Chen, X. Zou, G. Zhang, H. L. Yip, K. S. Wong, R. H. Friend, H. Yan, A. Rao and P. C. Y. Chow, *Nat. Commun.*, 2020, **11**, 1–10.

135 X. Wang, L. Martínez-Fernández, Y. Zhang, K. Zhang, R. Improta, B. Kohler, J. Xu and J. Chen, *Chem. Eur. J.*, 2021, **27**, 10932–10940.

136 L. Dordević, D. Milano, N. Demitri and D. Bonifazi, *Org. Lett.*, 2020, **22**, 4283–4288.

137 A. Mazumder, E. Sebastian and M. Hariharan, *Chem. Sci.*, 2022, **13**, 8860–8870.

138 T. M. Wilson, M. J. Tauber and M. R. Wasielewski, *J. Am. Chem. Soc.*, 2009, **131**, 8952–8957.

139 Gaussian 16, Revision C.01, M. J. Frisch, G. W. Trucks, H. B. Schlegel, G. E. Scuseria, M. A. Robb, J. R. Cheeseman, G. Scalmani, V. Barone, G. A. Petersson, H. Nakatsuji, X. Li, M. Caricato, A. V. Marenich, J. Bloino, B. G. Janesko, R. Gomperts, B. Mennucci, H. P. Hratchian, J. V. Ortiz, A. F. Izmaylov, J. L. Sonnenberg, D. Williams-Young, F. Ding, F. Lipparini, F. Egidi, J. Goings, B. Peng, A. Petrone, T. Henderson, D. Ranasinghe, V. G. Zakrzewski, J. Gao, N. Rega, G. Zheng, W. Liang, M. Hada, M. Ehara, K. Toyota, R. Fukuda, J. Hasegawa, M. Ishida, T. Nakajima, Y. Honda, O. Kitao, H. Nakai, T. Vreven, K. Throssell, J. A. Montgomery, Jr., J. E. Peralta, F. Ogliaro, M. J. Bearpark, J. J. Heyd, E. N. Brothers, K. N. Kudin, V. N. Staroverov, T. A. Keith, R. Kobayashi, J. Normand, K. Raghavachari, A. P. Rendell, J. C. Burant, S. S. Iyengar, J. Tomasi, M. Cossi, J. M. Millam, M. Klene, C. Adamo, R. Cammi, J. W. Ochterski, R. L. Martin, K. Morokuma, O. Farkas, J. B. Foresman, and D. J. Fox, Gaussian, Inc., Wallingford CT, 2016.

140 T. Lu and F. Chen, *J. Comput. Chem.*, 2012, **33**, 580–592.

141 W. Humphrey, A. Dalke and K. Schulten, *J. Mol. Graph*, 1996, **14**, 33–38.

142 Y. L. Wu, K. E. Brown and M. R. Wasielewski, *J. Am. Chem. Soc.*, 2013, **135**, 13322–13325.

143 M. Kasha, *Chem. Rev.*, 1947, **41**, 401–419.

144 Y. Kobayashi and J. Abe, *Chem. Soc. Rev.*, 2022, **51**, 2397–2415.

145 D. Sasikumar, A. T. John, J. Sunny and M. Hariharan, *Chem. Soc. Rev.*, 2020, **49**, 6122–6140.

146 B. D. Ravetz, A. B. Pun, E. M. Churchill, D. N. Congreve, T. Rovis and L. M. Campos, *Nature*, 2019, **565**, 343–346.

147 A. Kamkaew, S. H. Lim, H. B. Lee, L. V. Kiew, L. Y. Chung and K. Burgess, *Chem. Soc. Rev.*, 2012, **42**, 77–88.

148 A. Nowak-Król and F. Würthner, *Org. Chem. Front.*, 2019, **6**, 1272–1318.

149 C. Huang, S. Barlow and S. R. Marder, *J. Org. Chem.*, 2011, **76**, 2386–2407.

150 C. M. Marian, *Wiley Interdiscip. Rev. Comput. Mol. Sci.*, 2012, **2**, 187–203.

151 M. B. Smith and J. Michl, *Chem. Rev.*, 2010, **110**, 6891–6936.

152 D. Casanova, *Chem. Rev.*, 2018, **118**, 7164–7207.

153 B. Carlotti, I. K. Madu, H. Kim, Z. Cai, H. Jiang, A. K. Muthike, L. Yu, P. M. Zimmerman and T. Goodson, *Chem. Sci.*, 2020, **11**, 8757–8770.

154 B. J. Walker, A. J. Musser, D. Beljonne and R. H. Friend, *Nat. Chem.*, 2013, **5**, 1019–1024.

155 T. Mikulchyk, S. Karuthedath, C. S. P. De Castro, A. A. Buglak, A. Sheehan, A. Wieder, F. Laquai, I. Naydenova and M. A. Filatov, *J. Mater. Chem. C*, 2022, **10**, 11588–11597.

156 C. Kaufmann, W. Kim, A. Nowak-Król, Y. Hong, D. Kim and F. Würthner, *J. Am. Chem. Soc.*, 2018, **140**, 4253–4258.

157 M. B. Smith and J. Michl, *Annu. Rev. Phys. Chem*., 2013, **64**, 361– 386.

158 L. Estergreen, A. R. Mencke, D. E. Cotton, N. V. Korovina, J. Michl, S. T. Roberts, M. E. Thompson and S. E. Bradforth, *Acc. Chem. Res.*, 2022, **55**, 1561–1572.

159 H. Halperin, K. Dejong, R. E. W Adams, C. C. Coggins, N. Hammond, D. S. Gotufried, M. A. Steffen and S. G. Boxer, *Science*, 1991, **251**, 662–665.

160 A. Y. Chan, A. Ghosh, J. T. Yarranton, J. Twilton, J. Jin, D. M. Arias-Rotondo, H. A. Sakai, J. K. McCusker and D. W. C. MacMillan, *Science*, 2023, **382**, 191–197.

161 A. Issac, R. Hildner, C. Hippius, F. Würthner and J. Köhler, *ACS Nano*, 2014, **8**, 1708–1717.

162 S. J. Hauschildt, Z. Wu, D. Uersfeld, P. Schmid, C. Götz, V. Engel, B. Engels, K. Müllen and T. Basché, *J. Chem. Phys.*, 2022, **156**, 044304.

163 P. A. J. De Witte, J. Hernando, E. E. Neuteboom, E. M. H. P. Van Dijk, S. C. J. Meskers, R. A. J. Janssen, N. F. Van Hulst, R. J. M. Nolte, M. F. García-Parajó and A. E. Rowan, *J. Phys. Chem. B*, 2006, **110**, 7803–7812.

164 J. P. Hoogenboom, E. M. H. P. Van Dijk, J. Hernando, N. F. Van Hulst and M. F. García-Parajó, *Phys. Rev. Lett.*, 2005, **95**, 097401.

165 T. Vosch, M. Cotlet, J. Hofkens, K. Van Der Biest, M. Lor, K. Weston, P. Tinnefeld, M. Sauer, L. Latterini, K. Müllen and F. C. De Schryver, *J. Phys. Chem. A*, 2003, **107**, 6920–6931.

166 Q. Zheng, M. F. Juette, S. Jockusch, M. R. Wasserman, Z. Zhou, R. B. Altman and S. C. Blanchard, *Chem. Soc. Rev.*, 2014, **43**, 1044–1056.

167 M. R. Wasielewski, *Acc. Chem. Res.*, 2009, **42**, 1910–1921.

168 M. Hariharan and G. D. Scholes, *J. Phys. Chem. Lett.*, 2022, **13**, 8365–8368.

169 S. Das, W. G. Thornbury, A. N. Bartynski, M. E. Thompson and S. E. Bradforth, *J. Phys. Chem. Lett.*, 2018, **9**, 3264–3270.

170 R. Gronheid, A. Stefan, M. Cotlet, J. Hofkens, J. Qu, K. Müllen, M. Van der Auweraer, J. W. Verhoeven and F. C. De Schryver, *Angew. Chem. Int. Ed.*, 2003, **42**, 4209–4214.

171 D. Bouchet, E. Lhuillier, S. Ithurria, A. Gulinatti, I. Rech, R. Carminati, Y. De Wilde and V. Krachmalnicoff, *Phys. Rev. A*, 2017, **95**, 1–7.

172 T. Basché, W. E. Moerner, M. Orrit and H. Talon, *Phys. Rev. Lett.*, 1992, **69**, 1516.

173 M. Koch, M. Myahkostupov, D. G. Oblinsky, S. Wang, S. Garakyaraghi, F. N. Castellano and G. D. Scholes, *J. Am. Chem. Soc.*, 2017, **139**, 5530–5537.

174 T. Kim, W. Kim, O. Vakuliuk, D. T. Gryko and D. Kim, *J. Am. Chem. Soc.*, 2020, **142**, 1564–1573.

175 T. F. Hinrichsen, C. C. S. Chan, C. Ma, D. Paleček, A. Gillett, S. Chen, X. Zou, G. Zhang, H. L. Yip, K. S. Wong, R. H. Friend, H. Yan, A. Rao and P. C. Y. Chow, *Nat. Commun.*, 2020, **11**, 1–10.

176 H. Imahori, Y. Kobori and H. Kaji, *Acc. Mater. Res.*, 2021, **2**, 501–514.

177 J. Zhao, J. Xu, H. Huang, K. Wang, D. Wu, R. Jasti and J. Xia, *Angew. Chem. Int. Ed.*, 2024, **63**, e202400941.

178 A. Goun, K. Glusac and M. D. Fayer, *J. Chem. Phys.*, 2006, **124**, 84504.

179 M. W. Holman, R. Liu and D. M. Adams, *J. Am. Chem. Soc.*, 2003, **125**, 12649–12654.

180 E. K. Vishnu, A. A. Kumar Nair and K. G. Thomas, *J. Phys. Chem. C*, 2021, **125**, 25706–25716.

181 A. Mazumder, K. Vinod, A. C. Thomas and M. Hariharan, *J. Phys. Chem. Lett.*, 2025, **16**, 4819–4827.

182 M. Hecht and F. Würthner, *Acc. Chem. Res.*, 2021, **54**, 18.

183 S. Seetharaman, N. Zink-Lorre, D. Gutiérrez-Moreno, P. A. Karr, F. Fernández-Lázaro and F. D'Souza, *Chem. Eur. J.*, 2022, **28**, e202104574.

184 R. R. Kaswan, D. Molina, L. Ferrer-López, J. Ortiz, P. A. Karr, Á. Sastre-Santos and F. D'Souza, *Angew. Chem. Int. Ed.*, 2025, **64**, e202502516.

185 M. Mandal, S. Mardanya, A. Saha, M. Singh, S. Ghosh, T. Chatterjee, R. Patra, S. Bhunia, S. Mandal, S. Mukherjee, R. Debnath, C. M. Reddy, M. Das and P. K. Mandal, *Chem. Sci.*, 2025, **16**, 901–909.

186 X. Chang, M. Balooch Qarai and F. C. Spano, *J. Phys. Chem. C*, 2022, **126**, 18784–18795.

187 K. N. Prajapati, B. Johns, K. Bandopadhyay, S. R. P. Silva and J. Mitra, *J. Chem. Phys.*, 2020, **152**, 064704.

188 N. J. Hestand and F. C. Spano, *J. Chem. Phys.*, 2015, **143**, 244707.

List of Publications

Published

1. **Mazumder, A.**; Vinod, K.; Tharamel, A.; Maret, P. D.; Rajendran, A.; Hariharan, M.* Ultrafast Symmetry-Breaking Charge Separation in Thin Films of J-Aggregated Perylenediimide Multimers in a Nonpolar Solid-State Environment. ***Chem. Commun.*** 2025, *61*, 17641–17644.
2. **Mazumder, A.**; Vinod, K.; Thomas, A. C.; Hariharan, M.* Accelerating Symmetry-Breaking Charge Separation in an Angular versus Linear Perylenediimide Dimer through the Modulation of Coulombic Coupling. ***J. Phys. Chem. Lett.*** 2025, *16*, 4819–4827.
3. **Mazumder, A.**; Panthakkal Das, P.; Vinod, K.; Maret, P. D.; Lijina, M. P.; Engels, B.;* Hariharan, M.* Core-Twist Modulated Intersystem Crossing in a π-Fused Single-Molecule. **J. *Phys. Chem. Lett.*** 2025, *16*, 4643–4651.
4. **Mazumder, A.**; Vinod, K.; Maret, P. D.; Panthakkal Das, P.; Hariharan, M.* Symmetry-Breaking Charge Separation Mediated Triplet Population in a Perylenediimide Trimer at the Single-Molecule Level. ***J. Phys. Chem. Lett.*** 2024, *15*, 5896–5904.
5. **Mazumder, A.**;† Mathew, R.;† Kumara, P.; Matula, J.; Mohamed, S.;* Brazda, P.;* Hariharan, M.;* Thomas, B.* Unveiling the Topology of Partially Disordered Micro-Crystalline Nitroperylenediimide with X-aggregate Stacking: An Integrated Approach. ***Chemical Science*** 2024, *15*, 490–499.
6. **Mazumder, A.**;† Panthakkal Das, P.;† Rajeevan, M.; Swathi, R. S.;* Hariharan, M.* Energy Landscape of Perylenediimide Chromophoric Aggregates. ***Phys. Chem. Chem. Phys.*** 2024, *26*, 2007–2015.
7. Mondal, M.; Giri, I.; **Mazumder, A.**; Patra, R.; Vijayaraghavan, R. K.* Tailored Energy Landscape to Foster Reverse Intersystem Crossing and Radiative Rates in TADF Emitters. ***J. Phys. Chem. C*** 2024, *128*, 21208–21219.
8. **Mazumder, A.**;† Suriyakumar, S.;† Dilip, P. S.; Hariharan, M.;* Shaijumon, M. M.* Synergistically Improving the Stability and Operating Potential of Organic Cathodes for Sodium-Ion Battery. ***Batteries & Supercaps*** 2023, *6*, e202300111.
9. **Mazumder, A.**; Sebastian, E.; Hariharan, M.* Solvent Dielectric Delimited Nitro–Nitrito Photorearrangement in a Perylenediimide Derivative. ***Chemical Science*** 2022, *13*, 8860–8870.

Submitted

1. Maret, P. D.; **Mazumder, A.**; Hariharan, M.* Photoinduced Symmetry-Breaking Charge Separation: Ensemble to Single-Molecule Level.

†Equal contribution.

Workshops and Conferences

1. Participated in the **International Research Training Group (IRTG) 2991 Startup Meeting** at IISER Thiruvananthapuram, India (February 25-28, 2025)
2. Presented a poster in the **12th International Symposium on Dynamic Exciton (ISDyEx 2024)**, Thiruvananthapuram, India (December 14-15, 2024).
3. Presented a poster in the **ChemSci 2024 LITF Symposium**, IISER Thiruvananthapuram, India (December 9-11, 2024).
4. Presented a poster in the **29th IUPAC Symposium on Photochemistry (PhotoIUPAC 2024)**, Valencia, Spain (July 14-19, 2024).
5. Presented a poster in the **Inter IISER/NISER Chemistry Meet 2024**, IISER Kolkata, India, (February 23-25, 2024).
6. Presented a poster in the **National Workshop on Fluorescence and Raman Spectroscopy (FCS XIV)**, IISER Mohali, India (December 09-15, 2023).
7. Presented a poster in the **12th Asian Photochemistry Conference (APC 2023)**, Melbourne, Australia (November 27- December 01, 2023).
8. Facilitator at **Yusuf Hamied Chemistry Camp**, IISER Thiruvananthapuram, India (July 19-21, 2023).
9. Presented a poster in the **3rd Edition of the Annual Symposium, Frontier Symposium in Chemistry 2023 (FS-CHM 2023)**, IISER Thiruvananthapuram, India (January 13-15, 2023).
10. Presented a poster in the **13th National workshop on Fluorescence and Raman Spectroscopy (FCSXIII)**, Fluorescence Chemical Society, IISER Thiruvananthapuram and RGCB, India (January 06-11, 2023).
11. Presented a poster in the **9th Theme meeting on Ultrafast Sciences (UFS 2022)**, IISER Thiruvananthapuram, India (November 03-05, 2022).
12. Presented a poster in the **2nd Edition of the Annual Symposium, Frontier Symposium in Chemistry 2022 (FS-CHM 2022)**, IISER Thiruvananthapuram, India (April 08-10, 2022).
13. Participated in the **12th National workshop on Fluorescence and Raman Spectroscopy (FCS 2021)**, Fluorescence Chemical Society, IISER Thiruvananthapuram and RGCB, India (November 29-December 4, 2021).

14. Participated in the **Light-matter Interactions from scratch: Theory and Experiments at the Border with Biology**, International Centre for Theoretical Physics, Italy (November 22-25, 2021).

15. Participated in the **Virtual Chemistry Course "Functional π-Systems – Organic Materials Design by Molecular and Supramolecular Engineering"**, Department of Chemistry & Pharmacy at the Julius-Maximilians-Universität Würzburg, Germany (July 19- 23, 2021).

16. Participated in the **International Conference on Ultrafast Spectroscopy (ICUS 2020)**, IISER TVM, Kerala, India February 21-22, 2020).

17. Participated in the **IISERTVM-RSC Symposium on Advances in Chemical Sciences**, IISER TVM, Kerala, India (February 4, 2020).

Achievements in Workshops and Conferences

1. **Best Oral Presentation** at ChemSci 2024 LITF, IISER Thiruvananthapuram, India (December 9-11, 2024).

2. **Best Poster Award** at ChemSci 2024 LITF Symposium, IISER Thiruvananthapuram, India (December 9-11, 2024).

3. **Best Poster Award** at Inter IISER/NISER Chemistry Meet 2024, IISER Kolkata, India, (February 23-25, 2024).

4. **Best Poster Award** at 3rd Edition of the Annual Symposium, Frontier Symposium in Chemistry 2023 (FS-CHM 2023), IISER Thiruvananthapuram, India (January 13-15, 2023).

5. **Fluorescence Society Award for the Best Poster** at FCSXIII, IISER Thiruvananthapuram and RGCB, India, January 2023.

Copyrights and Permissions

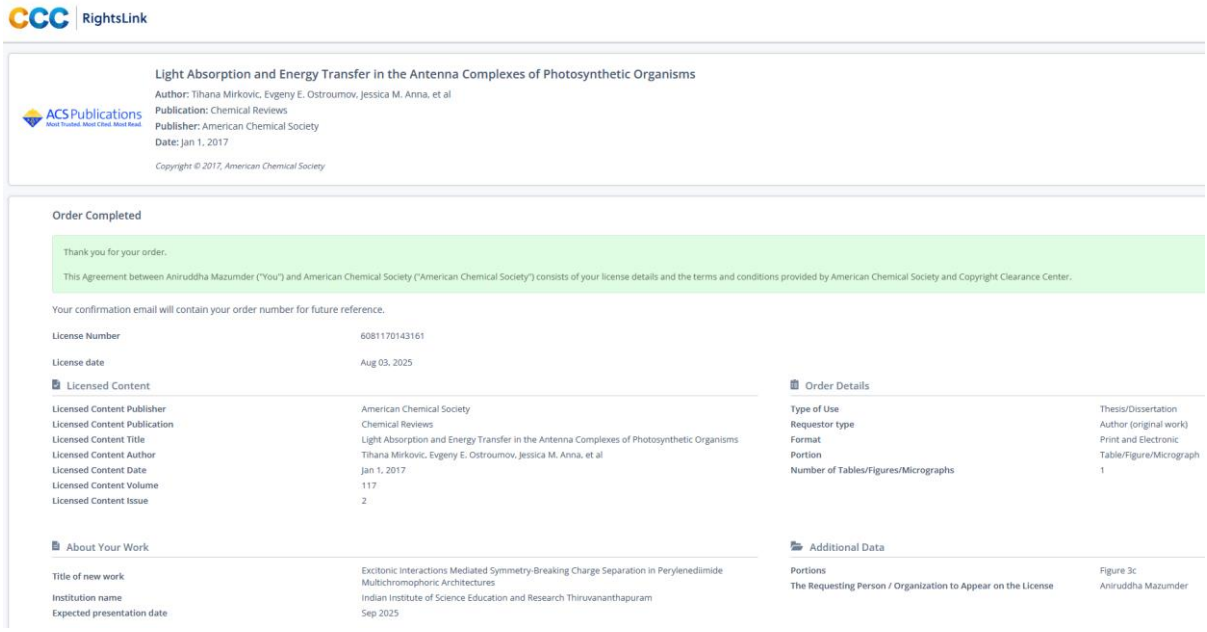

CCC RightsLink

ACS Publications
Most Trusted. Most Cited. Most Read.

Light Absorption and Energy Transfer in the Antenna Complexes of Photosynthetic Organisms

Author: Tihana Mirkovic, Evgeny E. Ostroumov, Jessica M. Anna, et al
Publication: Chemical Reviews
Publisher: American Chemical Society
Date: Jan 1, 2017

Copyright © 2017, American Chemical Society

Order Completed

Thank you for your order.

This Agreement between Aniruddha Mazumder ("You") and American Chemical Society ("American Chemical Society") consists of your license details and the terms and conditions provided by American Chemical Society and Copyright Clearance Center.

Your confirmation email will contain your order number for future reference.

License Number	6081170143161
License date	Aug 03, 2025

Licensed Content

Licensed Content Publisher	American Chemical Society
Licensed Content Publication	Chemical Reviews
Licensed Content Title	Light Absorption and Energy Transfer in the Antenna Complexes of Photosynthetic Organisms
Licensed Content Author	Tihana Mirkovic, Evgeny E. Ostroumov, Jessica M. Anna, et al
Licensed Content Date	Jan 1, 2017
Licensed Content Volume	117
Licensed Content Issue	2

Order Details

Type of Use	Thesis/Dissertation
Requestor type	Author (original work)
Format	Print and Electronic
Portion	Table/Figure/Micrograph
Number of Tables/Figures/Micrographs	1

About Your Work

Title of new work	Excitonic Interactions Mediated Symmetry-Breaking Charge Separation in Perylenediimide Multichromophoric Architectures
Institution name	Indian Institute of Science Education and Research Thiruvananthapuram
Expected presentation date	Sep 2025

Additional Data

Portions	Figure 3c
The Requesting Person / Organization to Appear on the License	Aniruddha Mazumder

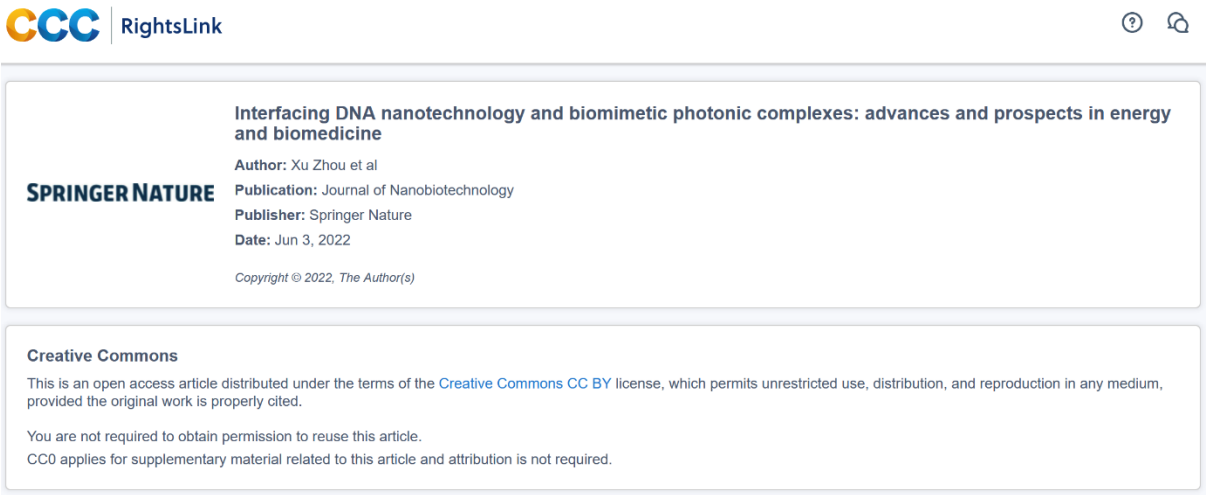

CCC RightsLink

SPRINGER NATURE

Interfacing DNA nanotechnology and biomimetic photonic complexes: advances and prospects in energy and biomedicine

Author: Xu Zhou et al
Publication: Journal of Nanobiotechnology
Publisher: Springer Nature
Date: Jun 3, 2022

Copyright © 2022, The Author(s)

Creative Commons

This is an open access article distributed under the terms of the Creative Commons CC BY license, which permits unrestricted use, distribution, and reproduction in any medium, provided the original work is properly cited.

You are not required to obtain permission to reuse this article.
CC0 applies for supplementary material related to this article and attribution is not required.

CCC | RightsLink

ACS Publications
Most Trusted. Most Cited. Most Read.

Through-space and through-bond effects on exciton interactions in rigidly linked dinaphthyl molecules

Author: Gregory D. Scholes, Kenneth P. Ghiggino, Anna M. Oliver, et al
Publication: Journal of the American Chemical Society
Publisher: American Chemical Society
Date: May 1, 1993

Order Completed

Thank you for your order.

This Agreement between Aniruddha Mazumder ("You") and American Chemical Society ("American Chemical Society") consists of your license details and the terms and conditions provided by American Chemical Society and Copyright Clearance Center.

Your confirmation email will contain your order number for future reference.

License Number	6081210307030
License date	Aug 03, 2025

Licensed Content

Licensed Content Publisher	American Chemical Society
Licensed Content Publication	Journal of the American Chemical Society
Licensed Content Title	Through-space and through-bond effects on exciton interactions in rigidly linked dinaphthyl molecules
Licensed Content Author	Gregory D. Scholes, Kenneth P. Ghiggino, Anna M. Oliver, et al
Licensed Content Date	May 1, 1993
Licensed Content Volume	115
Licensed Content Issue	10

Order Details

Type of Use	Thesis/Dissertation
Requestor type	Author (original work)
Format	Print and Electronic
Portion	Table/Figure/Micrograph
Number of Tables/Figures/Micrographs	1

About Your Work

Title of new work	Excitonic Interactions Mediated Symmetry-Breaking Charge Separation in Perylenediimide Multichromophoric Architectures
Institution name	Indian Institute of Science Education and Research Thiruvananthapuram
Expected presentation date	Sep 2025

Additional Data

Portions	Figure 3
The Requesting Person / Organization to Appear on the License	Aniruddha Mazumder

CCC | RightsLink

Null Exciton Splitting in Chromophoric Greek Cross ( ) Aggregate

Author: Ebin Sebastian, Abbey M. Philip, Alfy Benny, et al
Publication: Angewandte Chemie International Edition
Publisher: John Wiley and Sons
Date: Nov 7, 2018

Order Completed

Thank you for your order.

This Agreement between Aniruddha Mazumder ("You") and John Wiley and Sons ("John Wiley and Sons") consists of your license details and the terms and conditions provided by John Wiley and Sons and Copyright Clearance Center.

Your confirmation email will contain your order number for future reference.

License Number	6081210756251
License date	Aug 03, 2025

Licensed Content

Licensed Content Publisher	John Wiley and Sons
Licensed Content Publication	Angewandte Chemie International Edition
Licensed Content Title	Null Exciton Splitting in Chromophoric Greek Cross ( ) Aggregate
Licensed Content Author	Ebin Sebastian, Abbey M. Philip, Alfy Benny, et al
Licensed Content Date	Nov 7, 2018
Licensed Content Volume	57
Licensed Content Issue	48
Licensed Content Pages	6

Order Details

Type of use	Dissertation/Thesis
Requestor type	University/Academic
Format	Print and electronic
Portion	Figure/table
Number of figures/tables	1
Will you be translating?	No

About Your Work

Title of new work	Excitonic Interactions Mediated Symmetry-Breaking Charge Separation in Perylenediimide Multichromophoric Architectures
Institution name	Indian Institute of Science Education and Research Thiruvananthapuram
Expected presentation date	Sep 2025

Additional Data

Portions	Scheme 1
The Requesting Person / Organization to Appear on the License	Aniruddha Mazumder

Requestor Location

Requestor Location	Mr. Aniruddha Mazumder IISER TVM, Maruthamala, Thiruvananthapuram, Kerala, India Thiruvananthapuram, 695551 India

Tax Details

Publisher Tax ID	EU826007151

CCC Marketplace

This is a License Agreement between Aniruddha Mazumder ("User") and Copyright Clearance Center, Inc. ("CCC") on behalf of the Rightsholder identified in the order details below. The license consists of the order details, the Marketplace Permissions General Terms and Conditions below, and any Rightsholder Terms and Conditions which are included below.

All payments must be made in full to CCC in accordance with the Marketplace Permissions General Terms and Conditions below.

Order Date	03-Aug-2025	Type of Use	Republish in a thesis/dissertation
Order License ID	1637135-1	Publisher	IOP Publishing
ISSN	2050-6120	Portion	Image/photo/illustration

LICENSED CONTENT

Publication Title	Methods and Applications in Fluorescence	Country	United Kingdom of Great Britain and Northern Ireland
Date	01/01/2013	Rightsholder	IOP Publishing, Ltd
Language	English	Publication Type	e-Journal

REQUEST DETAILS

Portion Type	Image/photo/illustration	Distribution	Worldwide
Number of Images / Photos / Illustrations	1	Translation	Original language of publication
Format (select all that apply)	Electronic	Copies for the Disabled?	No
Who Will Republish the Content?	Academic institution	Minor Editing Privileges?	No
Duration of Use	Life of current edition	Incidental Promotional Use?	No
Lifetime Unit Quantity	Up to 499	Currency	USD
Rights Requested	Main product		

NEW WORK DETAILS

Title	Excitonic Interactions Mediated Symmetry-Breaking Charge Separation in Perylenediimide Multichromophoric Architectures	Institution Name	Indian Institute of Science Education and Research Thiruvananthapuram
Instructor Name	Mahesh Hariharan	Expected Presentation Date	2025-10-01

ADDITIONAL DETAILS

Order Reference Number	N/A	The Requesting Person / Organization to Appear on the License	Aniruddha Mazumder

REQUESTED CONTENT DETAILS

Title, Description or Numeric Reference of the Portion(s)	Figure 1	Title of the Article / Chapter the Portion Is From	Fluorescent J-aggregates of cyanine dyes: basic research and applications review
Editor of Portion(s)	N/A	Author of Portion(s)	Julia L. Bricks, Yuri L. Slominskii, Ihor D. Panas and Alexander P. Demchenko
Volume / Edition	N/A	Issue, if Republishing an Article From a Serial	N/A
Page or Page Range of Portion	3	Publication Date of Portion	2017-12-21

CCC Marketplace

This is a License Agreement between Aniruddha Mazumder ("User") and Copyright Clearance Center, Inc. ("CCC") on behalf of the Rightsholder identified in the order details below. The license consists of the order details, the Marketplace Permissions General Terms and Conditions below, and any Rightsholder Terms and Conditions which are included below.

All payments must be made in full to CCC in accordance with the Marketplace Permissions General Terms and Conditions below.

Order Date	03-Aug-2025	Type of Use	Republish in a thesis/dissertation
Order License ID	1637136-1	Publisher	ROYAL SOCIETY OF CHEMISTRY
ISSN	1460-4744	Portion	Image/photo/illustration

LICENSED CONTENT

Publication Title	Chemical Society reviews	Publication Type	e-Journal
Article Title	Keeping the chromophores crossed: evidence for null exciton splitting.	Start Page	6664
		End Page	6679
		Issue	19
Author / Editor	Royal Society of Chemistry (Great Britain)	Volume	52
Date	01/01/1972	URL	http://pubs.rsc.org/en/journals/journalissues/cs#!recentarticles&adv
Language	English		
Country	United Kingdom of Great Britain and Northern Ireland		
Rightsholder	Royal Society of Chemistry		

REQUEST DETAILS

Portion Type	Image/photo/illustration	Distribution	Worldwide
Number of Images / Photos / Illustrations	1	Translation	Original language of publication
		Copies for the Disabled?	No
Format (select all that apply)	Electronic	Minor Editing Privileges?	No
Who Will Republish the Content?	Academic institution	Incidental Promotional Use?	No
		Currency	USD
Duration of Use	Life of current edition		
Lifetime Unit Quantity	Up to 499		
Rights Requested	Main product		

NEW WORK DETAILS

Title	Excitonic Interactions Mediated Symmetry-Breaking Charge Separation in Perylenediimide Multichromophoric Architectures	Institution Name	Indian Institute of Science Education and Research Thiruvananthapuram
		Expected Presentation Date	2025-10-01
Instructor Name	Mahesh Hariharan		

ADDITIONAL DETAILS

Order Reference Number	N/A	The Requesting Person / Organization to Appear on the License	Aniruddha Mazumder

REQUESTED CONTENT DETAILS

Title, Description or Numeric Reference of the Portion(s)	Figure 3	Title of the Article / Chapter the Portion Is From	Keeping the chromophores crossed: evidence for null exciton splitting.
Editor of Portion(s)	Lijina, M P; Benny, Alfy; Sebastian, Ebin; Hariharan, Mahesh	Author of Portion(s)	Lijina, M P; Benny, Alfy; Sebastian, Ebin; Hariharan, Mahesh
Volume / Edition	52 / ONLINE		

CCC | RightsLink

ACS Publications

Molecular Aggregate Photophysics beyond the Kasha Model: Novel Design Principles for Organic Materials

Author: Nicholas J. Hestand, Frank C. Spano
Publication: Accounts of Chemical Research
Publisher: American Chemical Society
Date: Feb 1, 2017

Order Completed

Thank you for your order.

This Agreement between Aniruddha Mazumder ("You") and American Chemical Society ("American Chemical Society") consists of your license details and the terms and conditions provided by American Chemical Society and Copyright Clearance Center.

Your confirmation email will contain your order number for future reference.

License Number	6081221015312
License date	Aug 03, 2025

Licensed Content

Licensed Content Publisher	American Chemical Society
Licensed Content Publication	Accounts of Chemical Research
Licensed Content Title	Molecular Aggregate Photophysics beyond the Kasha Model: Novel Design Principles for Organic Materials
Licensed Content Author	Nicholas J. Hestand, Frank C. Spano
Licensed Content Date	Feb 1, 2017
Licensed Content Volume	50
Licensed Content Issue	2

Order Details

Type of Use	Thesis/Dissertation
Requestor type	Author (original work)
Format	Print and Electronic
Portion	Table/Figure/Micrograph
Number of Tables/Figures/Micrographs	1

About Your Work

Title of new work	Excitonic Interactions Mediated Symmetry-Breaking Charge Separation in Perylenediimide Multichromophoric Architectures
Institution name	Indian Institute of Science Education and Research Thiruvananthapuram
Expected presentation date	Sep 2025

Additional Data

Portions	Figure 4
The Requesting Person / Organization to Appear on the License	Aniruddha Mazumder

CCC | RightsLink

ACS Publications

Symmetry-Breaking Charge Separation in Molecular Constructs for Efficient Light Energy Conversion

Author: Ebin Sebastian, Mahesh Hariharan
Publication: ACS Energy Letters
Publisher: American Chemical Society
Date: Feb 1, 2022

Order Completed

Thank you for your order.

This Agreement between Aniruddha Mazumder ("You") and American Chemical Society ("American Chemical Society") consists of your license details and the terms and conditions provided by American Chemical Society and Copyright Clearance Center.

Your confirmation email will contain your order number for future reference.

License Number	6081221476304
License date	Aug 03, 2025

Licensed Content

Licensed Content Publisher	American Chemical Society
Licensed Content Publication	ACS Energy Letters
Licensed Content Title	Symmetry-Breaking Charge Separation in Molecular Constructs for Efficient Light Energy Conversion
Licensed Content Author	Ebin Sebastian, Mahesh Hariharan
Licensed Content Date	Feb 1, 2022
Licensed Content Volume	7
Licensed Content Issue	2

Order Details

Type of Use	Thesis/Dissertation
Requestor type	Author (original work)
Format	Print and Electronic
Portion	Table/Figure/Micrograph
Number of Tables/Figures/Micrographs	2

About Your Work

Title of new work	Excitonic Interactions Mediated Symmetry-Breaking Charge Separation in Perylenediimide Multichromophoric Architectures
Institution name	Indian Institute of Science Education and Research Thiruvananthapuram
Expected presentation date	Sep 2025

Additional Data

Portions	Figure 1, Figure 2
The Requesting Person / Organization to Appear on the License	Aniruddha Mazumder

CCC RightsLink

Ultrafast Excimer Formation and Solvent Controlled Symmetry Breaking Charge Separation in the Excitonically Coupled Subphthalocyanine Dimer

Author: Stephen R. Meech, Andrew N. Cammidge, Jacob Gretton, et al
Publication: Angewandte Chemie International Edition
Publisher: John Wiley and Sons
Date: Mar 30, 2021

CCC RightsLink

ACS Publications
Most Trusted. Most Cited. Most Read.

Symmetry-Breaking Charge Separation in a Chiral Bis(perylenediimide) Probed at Ensemble and Single-Molecule Levels

Author: Philip Daniel Maret, Devika Sasikumar, Ebin Sebastian, et al
Publication: Journal of Physical Chemistry Letters
Publisher: American Chemical Society
Date: Sep 1, 2023

Order Completed

Thank you for your order.

This Agreement between Aniruddha Mazumder ("You") and American Chemical Society ("American Chemical Society") consists of your license details and the terms and conditions provided by American Chemical Society and Copyright Clearance Center.

Your confirmation email will contain your order number for future reference.

License Number	6081230411436
License date	Aug 03, 2025

Licensed Content

Licensed Content Publisher	American Chemical Society
Licensed Content Publication	Journal of Physical Chemistry Letters
Licensed Content Title	Symmetry-Breaking Charge Separation in a Chiral Bis(perylenediimide) Probed at Ensemble and Single-Molecule Levels
Licensed Content Author	Philip Daniel Maret, Devika Sasikumar, Ebin Sebastian, et al
Licensed Content Date	Sep 1, 2023
Licensed Content Volume	14
Licensed Content Issue	38

Order Details

Type of Use	Thesis/Dissertation
Requestor type	Author (original work)
Format	Print and Electronic
Portion	Table/Figure/Micrograph
Number of Tables/Figures/Micrographs	2

About Your Work

Title of new work	Excitonic Interactions Mediated Symmetry-Breaking Charge Separation in Perylenediimide Multichromophoric Architectures
Institution name	Indian Institute of Science Education and Research Thiruvananthapuram
Expected presentation date	Sep 2025

Additional Data

Portions	Figure 1, Figure 3
The Requesting Person / Organization to Appear on the License	Aniruddha Mazumder

Tuning symmetry breaking charge separation in perylene bichromophores by conformational control

A. Aster, G. Licari, F. Zinna, E. Brun, T. Kumpulainen, E. Tajkhorshid, J. Lacour and E. Vauthey, *Chem. Sci.*, 2019, **10**, 10629 **DOI:** 10.1039/C9SC03913A

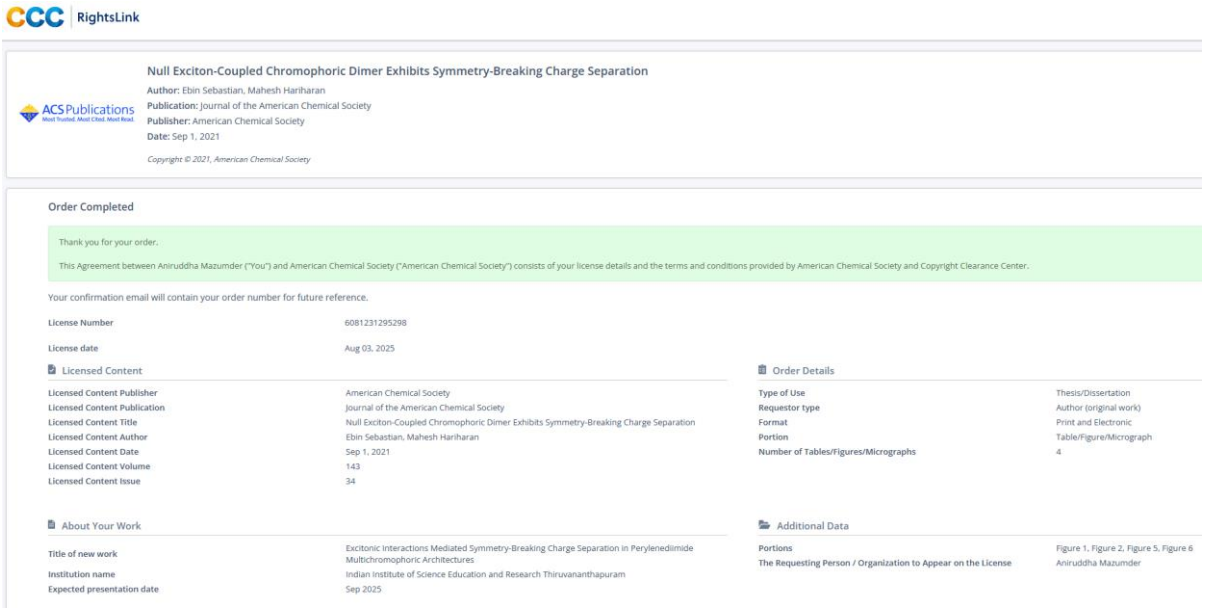

CCC RightsLink

ACS Publications

Null Exciton-Coupled Chromophoric Dimer Exhibits Symmetry-Breaking Charge Separation

Author: Ebin Sebastian, Mahesh Hariharan
Publication: Journal of the American Chemical Society
Publisher: American Chemical Society
Date: Sep 1, 2021

Copyright © 2021, American Chemical Society

Order Completed

Thank you for your order.

This Agreement between Aniruddha Mazumder ("You") and American Chemical Society ("American Chemical Society") consists of your license details and the terms and conditions provided by American Chemical Society and Copyright Clearance Center.

Your confirmation email will contain your order number for future reference.

License Number	6081231295298
License date	Aug 03, 2025

Licensed Content

Licensed Content Publisher	American Chemical Society
Licensed Content Publication	Journal of the American Chemical Society
Licensed Content Title	Null Exciton-Coupled Chromophoric Dimer Exhibits Symmetry-Breaking Charge Separation
Licensed Content Author	Ebin Sebastian, Mahesh Hariharan
Licensed Content Date	Sep 1, 2021
Licensed Content Volume	143
Licensed Content Issue	34

Order Details

Type of Use	Thesis/Dissertation
Requestor type	Author (original work)
Format	Print and Electronic
Portion	Table/Figure/Micrograph
Number of Tables/Figures/Micrographs	4

About Your Work

Title of new work	Excitonic Interactions Mediated Symmetry-Breaking Charge Separation in Perylenediimide Multichromophoric Architectures
Institution name	Indian Institute of Science Education and Research Thiruvananthapuram
Expected presentation date	Sep 2025

Additional Data

Portions	Figure 1, Figure 2, Figure 5, Figure 6
The Requesting Person / Organization to Appear on the License	Aniruddha Mazumder

CCC Marketplace

This is a License Agreement between Aniruddha Mazumder ("User") and Copyright Clearance Center, Inc. ("CCC") on behalf of the Rightsholder identified in the order details below. The license consists of the order details, the Marketplace Permissions General Terms and Conditions below, and any Rightsholder Terms and Conditions which are included below.

All payments must be made in full to CCC in accordance with the Marketplace Permissions General Terms and Conditions below.

Order Date	03-Aug-2025	Type of Use	Republish in a thesis/dissertation
Order License ID	1637139-1	Publisher	ROYAL SOCIETY OF CHEMISTRY
ISSN	1463-9084	Portion	Image/photo/illustration

LICENSED CONTENT

Publication Title	Physical chemistry chemical physics	Publication Type	e-Journal
Article Title	Symmetry-Breaking Charge Separation in Nitrogen-Bridged Naphthalene Monoimide Dimer	Start Page	14007
		End Page	14015
		Issue	22
Author / Editor	Royal Society of Chemistry (Great Britain)	Volume	24
		URL	http://firstsearch.oclc.org/journal=1463-9076;screen=info;ECOIP
Date	01/01/1999		
Language	English		
Country	United Kingdom of Great Britain and Northern Ireland		
Rightsholder	Royal Society of Chemistry		

REQUEST DETAILS

Portion Type	Image/photo/illustration	Distribution	Worldwide
Number of Images / Photos / Illustrations	2	Translation	Original language of publication
		Copies for the Disabled?	No
Format (select all that apply)	Electronic	Minor Editing Privileges?	No
Who Will Republish the Content?	Academic institution	Incidental Promotional Use?	No
		Currency	USD
Duration of Use	Life of current edition		
Lifetime Unit Quantity	Up to 499		
Rights Requested	Main product		

NEW WORK DETAILS

Title	Excitonic Interactions Mediated Symmetry-Breaking Charge Separation in Perylenediimide Multichromophoric Architectures	Institution Name	Indian Institute of Science Education and Research Thiruvananthapuram
		Expected Presentation Date	2025-10-01
Instructor Name	Mahesh Hariharan		

ADDITIONAL DETAILS

Order Reference Number	N/A	The Requesting Person / Organization to Appear on the License	Aniruddha Mazumder

REQUESTED CONTENT DETAILS

Title, Description or Numeric Reference of the Portion(s)	Figure 1, Figure 7	Title of the Article / Chapter the Portion Is From	Symmetry-Breaking Charge Separation in Nitrogen-Bridged Naphthalene Monoimide Dimer
Editor of Portion(s)	Xia, Andong; Niu, Xinmiao; Tajima, Keita; Kong, Jie; Tao, Min; Fukui, Norihito; Kuang, Zhuoran; Shinokubo, Hiroshi		

CCC | RightsLink

SPRINGER NATURE

Accelerating symmetry-breaking charge separation in a perylenediimide trimer through a vibronically coherent dimer intermediate

Author: Chenjian Lin et al
Publication: Nature Chemistry
Publisher: Springer Nature
Date: Apr 25, 2022

Order Completed

Thank you for your order.

This Agreement between Aniruddha Mazumder ("You") and Springer Nature ("Springer Nature") consists of your license details and the terms and conditions provided by Springer Nature and Copyright Clearance Center.

Your confirmation email will contain your order number for future reference.

License Number	6081240100233
License date	Aug 03, 2025

Licensed Content

Licensed Content Publisher	Springer Nature
Licensed Content Publication	Nature Chemistry
Licensed Content Title	Accelerating symmetry-breaking charge separation in a perylenediimide trimer through a vibronically coherent dimer intermediate
Licensed Content Author	Chenjian Lin et al
Licensed Content Date	Apr 25, 2022

Order Details

Type of Use	Thesis/Dissertation
Requestor Type	academic/university or research institute
Format	print and electronic
Portion	figures/tables/illustrations
Number of figures/tables/illustrations	2
Would you like a high resolution image with your order?	no
Will you be translating?	no
Circulation/distribution	1 - 29
Author of this Springer Nature content	no

About Your Work

Title of new work	Excitonic Interactions Mediated Symmetry-Breaking Charge Separation in Perylenediimide Multichromophoric Architectures
Institution name	Indian Institute of Science Education and Research Thiruvananthapuram
Expected presentation date	Sep 2025

Additional Data

Portions	Figure 2, Figure 4
The Requesting Person / Organization to Appear on the License	Aniruddha Mazumder